

AD-R160 465

PIEZOELECTRIC AND ELECTROSTRICTIVE MATERIALS FOR
TRANSDUCER APPLICATIONS(U) PENNSYLVANIA STATE UNIV
UNIVERSITY PARK MATERIALS RESEARCH LAB

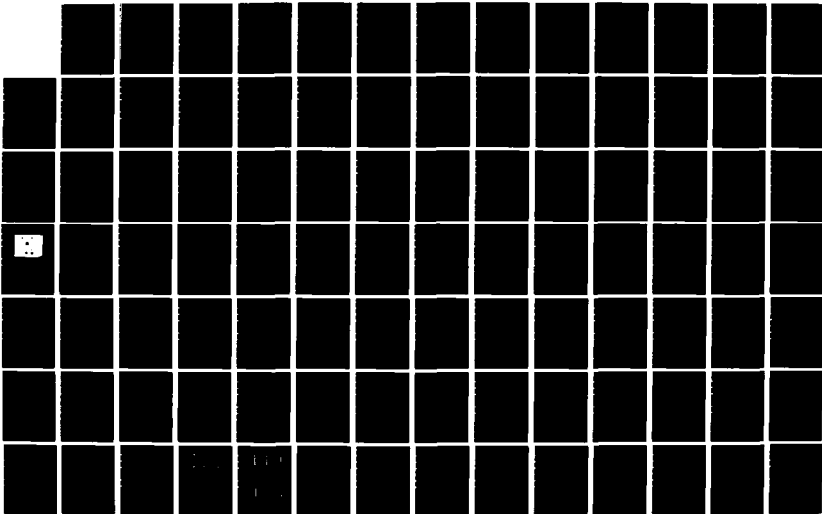
1/4

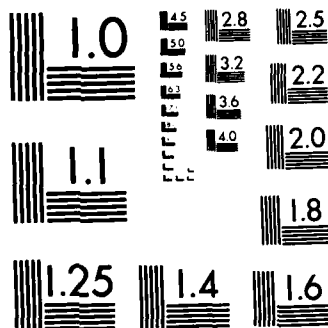
UNCLASSIFIED

L E CROSS ET AL. MAY 85 N00014-82-K-0339

F/G 9/1

NL





MICROCOPY RESOLUTION TEST CHART
NATIONAL BUREAU OF STANDARDS-1963-A

AD-A160 465

12

PIEZOELECTRIC AND ELECTROSTRICTIVE MATERIALS
FOR TRANSDUCER APPLICATIONS

Period January 1 to December 31, 1984

Annual Report

OFFICE OF NAVAL RESEARCH

Contract No. N00014-82-K0339

APPROVED FOR PUBLIC RELEASE - DISTRIBUTION UNLIMITED

Reproduction in whole or in part is permitted for
any purpose of the United States Government

L.E. Cross
R.E. Newnham
G.R. Barsch
J.V. Biggers

MAY 1985

DTIC
OCT 18 1985
A

DTIC FILE COPY



MATERIALS RESEARCH LABORATORY
THE PENNSYLVANIA STATE UNIVERSITY
UNIVERSITY PARK, PENNSYLVANIA 16802

85 10 10 1985

REPORT DOCUMENTATION PAGE		READ INSTRUCTIONS BEFORE COMPLETING FORM
1. REPORT NUMBER	2. GOVT ACCESSION NO.	3. RECIPIENT'S CATALOG NUMBER
	AD-A160465	
4. TITLE (and Subtitle) PIEZOELECTRIC AND ELECTROSTRICTIVE MATERIALS FOR TRANSDUCER APPLICATIONS		5. TYPE OF REPORT & PERIOD COVERED Annual Report Jan. 1 to Dec. 1, 1984
		6. PERFORMING ORG. REPORT NUMBER
7. AUTHOR(s) L.E. Cross, R.E. Newnham, G.R. Barsch, J.V. Biggers		8. CONTRACT OR GRANT NUMBER(s) N00014-82-K0339
9. PERFORMING ORGANIZATION NAME AND ADDRESS Materials Research Laboratory The Pennsylvania State University University Park, PA 16802		10. PROGRAM ELEMENT, PROJECT, TASK AREA & WORK UNIT NUMBERS
11. CONTROLLING OFFICE NAME AND ADDRESS Office of Naval Research Ballston Tower, 800 N. Quincy Street Arlington, VA 22217		12. REPORT DATE July, 1985
		13. NUMBER OF PAGES 322
14. MONITORING AGENCY NAME & ADDRESS (if different from Controlling Office)		15. SECURITY CLASS. (of this report)
		15a. DECLASSIFICATION/DOWNGRADING SCHEDULE
16. DISTRIBUTION STATEMENT (of this Report) Reproduction in whole or in part is permitted for any purpose of the United States Government This document has been approved for public release and sale; its distribution is unlimited.		
17. DISTRIBUTION STATEMENT (of the abstract entered in Block 20, if different from Report)		
18. SUPPLEMENTARY NOTES		
19. KEY WORDS (Continue on reverse side if necessary and identify by block number)		
20. ABSTRACT (Continue on reverse side if necessary and identify by block number) This report covers work accomplished on the second year of contract No. N00014-82-K0339 for the study of "Piezoelectric and Electrostrictive Materials for Transducer Applications. The work accomplished covers a rather wide range of topics and for convenience, it is divided into four major sub-topics. (1) Composite Materials, The major emphasis this year has been upon 0:3 type connected composites in polymer:ceramic systems, seeking new lower permittivity high anisotropy		

piezoceramic powders and new poling procedures. It was shown that solid solutions in the $\text{PbTiO}_3:\text{BiFeO}_3$ system near the 50:50 ratio provide a superior ceramic component over PZT and pure PbTiO_3 . An 0:0:3 structure using a dispersed conductive component trapped between the piezoceramic grains has been shown to improve poling and a simple theoretical cubes model has been invoked to explain this improvement.

Initial tests of a pseudo 1:3 $\text{PbZn}_{1/3}\text{Nb}_{2/3}\text{O}_3:\text{PbTiO}_3$ ceramic:epoxy composite shows unusual promise with d_{33} values up to 1,000 pc/i.

(2) Electrostriction

Theoretical calculations have been extended to the fluorite structure halides CaF_2 , SrF_2 , and BaF_2 . This work has been most important in confirming new data for the converse measurement technique. Using the new uniaxial compressometer described last year, the full electrostriction tensor has been measured for CaF_2 , SrF_2 , and BaF_2 . The values are all lower than earlier direct measurement, but in good agreement with theory. The instrument is now being used to characterize electrostriction in sodium silicate and aluminosilicate glasses.

For high permittivity relaxors, work has been completed which clearly demonstrates the electrostrictive origin of elastic changes in the relaxor PLZTs.

In a cooperative study with the Dielectrics Center Program, electrostriction has been used to confirm the superparaelectric origin of the permittivity in strontium barium niobate and to measure the fluctuating component of the polarization above the mean Curie temperature.

(3) Conventional Piezoelectrics

A phenomenology for the single cell structure phases in the $\text{PbTiO}_3:\text{PbZrO}_3$ solid solution family has been completed. The theory has now been extended to the multicell structures involving tilts of the oxygen octahedra. A simple fourth order expansion in tilt angle permits a qualitative description of observed properties and a full sixth order presentation gives close quantitative fitting of polarization and tilt behavior.

(4) Preparative Studies

In single crystal growth, work has been concentrated upon the $\text{Pb}_{0.6}\text{Ba}_{0.4}\text{Nb}_2\text{O}_6$ bronze compositions close to the morphotropic phase boundary. New crystals of KMgF_3 and KInF_3 have been grown for electrostriction and third order elastic constant measurement. The fresnoite structure analogue $\text{Ba}_2\text{TiGe}_2\text{O}_8$ is also being grown to permit study of the unusual ferroic phase change in this crystal near 0°C .

In ceramic preparation, studies of liquid salt techniques for developing acicular powders of $\text{Pb}(\text{K})\text{Nb}_2\text{O}_6$ have been completed. In cooperation with the Dielectrics Center programs, techniques are being developed for very rapid firing of relaxor type electrostrictors.

TABLE OF CONTENTS

	<u>Page</u>
1.0 INTRODUCTION.	1
2.0 SUMMARY OF ACCOMPLISHMENTS.	1
2.1 Piezoelectric Composites for Transducer Applications	1
2.2 Electrostriction	2
2.2.1 Theoretical Studies	2
2.2.2 Experimental Studies.	2
2.3 Conventional Piezoelectrics.	3
2.3.1 Practical Studies	3
2.3.2 Phenomenological Studies.	3
2.4 Preparative Studies.	4
2.4.1 Single Crystal Growth	4
2.4.2 Ceramic Studies	5
3.0 PUBLICATIONS, PRESENTATIONS, HONORS, AND AWARDS	5
3.1 Publications	5
3.2 Presentations at National and International Meetings	8
3.2.1 Invited Papers.	8
3.2.2 Contributed Papers.	9
3.3 Honors, Awards and Prizes.	10
3.4 Degrees Earned	11
3.4.1 Graduate Degrees (M.S., Ph.D.).	11
3.4.2 Undergraduate Thesis Projects (B.S.)0	12
4.0 APPLIED SCIENCE APPRENTICESHIPS IN THE CENTER FOR DIELECTRIC STUDIES.	12
 PIEZOELECTRIC COMPOSITES OF PZT AND SOME SEMI-CRYSTALLINE POLYMERS - J. Runt and E.C. Galgoci	
 POLYMER/PIEZOELECTRIC CERAMIC COMPOSITES: POLYSTYRENE AND POLY (METHYL METHACRYLATE) WITH PZT - J. Runt and E.C. Galgoci	
 COMPOSITE PIEZOELECTRIC SENSORS - R.E. Newnham, A. Safari, J. Giniewicz, and B.H. Fox	
 POLAR GLASS CERAMICS FOR SONAR TRANSDUCERS - R.Y. Ting, A. Halliyal, and A.S. Bhalla	
 GRAIN-ORIENTED GLASS-CERAMICS FOR PIEZOELECTRIC DEVICES - A. Halliyal, A. Safari, A.S. Bhalla, R.E. Newnham, and L.E. Cross	

Table of Contents (Continued)

RESONANT MODES OF VIBRATION IN PIEZOELECTRIC PZT-POLYMER COMPOSITES WITH TWO DIMENSIONAL PERIODICITY - T.R. Gururaja, W.A. Schulze, L.E. Cross, B.A. Auld, Y.A. Shui, and Y. Wang

PYROELECTRIC AND PIEZOELECTRIC PROPERTIES OF SbsI COMPOSITES - A.S. Bhalla and R.E. Newnham

FLEXIBLE COMPOSITE PIEZOELECTRIC SENSORS - R.E. Newnham, A. Safari, G. Sa-Gong, and J. Giniewicz

FINITE ELEMENT MODELING OF PERFORATED PZT-POLYMER COMPOSITES - S. DaVanzo, A. Safari, and R.E. Newnham

ELECTROSTRICTION TENSOR COMPONENT OF ALKALINE-EARTH FLUORIDE SINGLE CRYSTALS - Z.Y. Meng, Y.M. Sun, and L.E. Cross

POLARIZATION AND DEPOLARIZATION BEHAVIOR OF HOT PRESSED LEAD LANTHANUM ZIRCONATE TITANATE CERAMICS - Yao Xi, Chen Zhili, and L.E. Cross

ELECTRON MICROSCOPY OF ORDERED DOMAINS IN LEAD SCANDIUM TANTALATE $Pb(Sc_{0.5}Ta_{0.5})O_3$ - M.P. Harmer, A. Bhalla, B. Fox, and L.E. Cross

PRESSURE DEPENDENCE OF THE REFRACTIVE INDEX AND DIELECTRIC CONSTANT IN A FLUOROPEROVSKITE, $KMgF_3$ - Kenji Uchino, Shoichiro Nomura, K. Vedam, Robert E. Newnham, and Leslie E. Cross

ELECTROSTRICTION IN LEAD LANTHANUM ZIRCONATE TITANATE (PLZT) CERAMICS - Z.Y. Meng, U. Kumar, and L.E. Cross

DIELECTRIC, PIEZOELECTRIC, AND FERROELECTRIC COMPONENTS - L.E. Cross

A PHENOMENOLOGICAL THEORY FOR PHASE TRANSITIONS IN PEROVSKITE FERROELECTRICS WITH OXYGEN OCTAHEDRON TILTS - T.R. Halemane, M.J. Haun, L.E. Cross, and R.E. Newnham

A PHENOMENOLOGICAL GIBBS FUNCTIONS FOR THE SINGLE CELL REGION OF THE $PbZrO_3:PbTiO_3$ SOLID SOLUTION SYSTEM - A. Amin, M.J. Haun, B. Badger, H. McKinstry, and L.E. Cross

PIEZOELECTRIC COMPOSITE MATERIALS FOR ULTRASONIC TRANSDUCER APPLICATIONS PART I. RESONANT MODES OF VIBRATION OF PZT ROD-POLYMER COMPOSITES - T.R. Gururaja, W.A. Schulze, L.E. Cross, and R.E. Newnham

PIEZOELECTRIC COMPOSITE MATERIAL FOR ULTRASONIC TRANSDUCER APPLICATIONS: PART II. EVALUATION FOR ULTRASONIC MEDICAL APPLICATIONS - T.R. Gururaja, W.A. Schulze, L.E. Cross, and R.E. Newnham

Ph.D. Thesis - STUDY OF THE PIEZOELECTRIC AND PYROELECTRIC PROPERTIES OF POLAR GLASS CERAMICS - A. Halliyal

Table of Contents (Continued)

Ph.D. Thesis - PIEZOELECTRIC COMPOSITE MATERIALS FOR ULTRASONIC
TRANSDUCER APPLICATIONS - T.R. Gururaja

Ph.D. Thesis - ELECTROSTRICTION IN CUBIC HALIDE COMPOUNDS - Kurt M.
Rittenmyer

M.S. Thesis - AN ANALYSIS OF THE REACTION OF PbO and Nb₂O₅ IN THE
PRESENCE OF MOLTEN SALTS FOR USE IN GRAIN-ORIENTED PIEZOELECTRIC
0/3 COMPOSITES - Mary Bliss



SEARCHED	INDEXED
SERIALIZED	FILED
APR 1964	
FBI - MEMPHIS	
RECEIVED	
FOR THE DIRECTOR	
OFFICE OF THE ATTORNEY GENERAL	
U.S. DEPARTMENT OF JUSTICE	
WASHINGTON, D.C.	

1.0 INTRODUCTION

This report delineates work carried out on the second year of Contract No. N00014-82-K-0339, Piezoelectric and Electrostrictive Materials for Transducer Applications, which is Task II of the contract award. Task I, which was performed to further development of the Center for Dielectric Studies, is submitted as a separate report.

In keeping with earlier reports in this sequence, there is a brief narrative description of the major advances which have been accomplished on contract funds, the bulk of the work has, however, been published or is being submitted for publication and is carried as appendices to the report in the form of reprints and preprints of these papers. Again for convenience, the work is divided into four major sections:

- (1) COMPOSITE MATERIALS FOR TRANSDUCER APPLICATIONS
- (2) ELECTROSTRICTION
- (3) CONVENTIONAL PIEZOELECTRICS
- (4) PREPARATIVE STUDIES.

2.0 SUMMARY OF ACCOMPLISHMENTS

2.1 Piezoelectric Composites for Transducer Applications

(a) The development of new water quenched piezoelectric powders in the $\text{PbTiO}_3:\text{BiFeO}_3$ solid solution system for the active phase in 0:3 ceramic:polymer composites. The best samples give $g_h \sim 100$ mVm/N and $d_h \sim 50$ pC/N comparable to the best 0:3 composites produced by NGK in Japan.

(b) Diced capped PZT polymer composites having $d_h g_h$ values up to 20,000 m^2/N have been fabricated and tested in MRL and at NRL Orlando.

(c) Poling studies have been extended to 0:0:3 composites incorporating a conductive filler phase and a cubes type model developed to describe the behavior.

(d) Preliminary evaluation of pseudo 1:3 composites using a lead zinc niobate $\text{PbZn}_{1/3}\text{Nb}_{2/3}\text{O}_3$ active phase have shown values of d_{33} up to 1,000 pC/N.

(e) Finite element methods applied to analysis of the stress and polarization distribution in 3:0 ceramic:polymer composites have yielded values for d_h and g_h coefficients within 10% of measured data.

2.2 Electrostriction

2.2.1 Theoretical Studies

(a) Calculations of electrostriction constant Q_h and Q_{44} for BaF_2 , SrF_2 and CaF_2 show good agreement with experimental determinations using the indirect method, and tend to support these data over the larger values determined by direct measurement. Reasonable accord is also observed with the numerically larger third order elastic constants. The theory still has problems accounting for the electrostrictive shear constant $Q_s = Q_{11} - Q_{12}$ probably due to many body effects in the short range overlap forces.

2.2.2 Experimental Studies

(a) The compressometer discussed in last year's report has been used to measure electrostriction in BaF_2 , CaF_2 , SrF_2 single crystals.

(b) The system is now being used to characterize electrostriction in sodium trisilicate and sodium aluminosilicate glasses to observe the effect of sodium ion relaxation on the electrostrictive behavior. The question which is to be resolved is whether the equality between direct and converse electrostriction effects which is based on reversible thermodynamics will breakdown for the highly dissipative glass system.

(c) A detailed study of the PLZT family compositions near the 65:35 morphotropic phase boundary have confirmed the electrostrictive nature of the

strain which accompanies polarization and suggested a new type of current controlled "dial a displacement transducer."

(d) In cooperation with the Dielectric Center programs, electrostriction measurements have been combined with thermal expansion and birefringence studies to sort out the fluctuating component of polarization in the relaxor ferroelectrics $\text{Ba}_{0.39}\text{Sr}_{0.61}\text{Nb}_2\text{O}_6$ and $\text{Pb}(\text{Mg}_{1/3}\text{Nb}_{2/3})\text{O}_3$.

2.3 Conventional Piezoelectrics

2.3.1 Practical Studies

(a) In a series of studies aimed at stabilizing the perovskite structure phase in $\text{PbZn}_{1/3}\text{Nb}_{2/3}\text{O}_3$ ceramics, solid solutions incorporating BaTiO_3 and PbTiO_3 are being explored. With only 5 mole% BaTiO_3 excellent sintered ceramics have been obtained and studies are now exploring composition near the morphotropic boundary between rhombohedral and tetragonal ferroelectric phases.

(b) Cooperative studies with North American Philips Laboratories are exploring the low temperature properties of the highly anisotropic $\text{PbTiO}_3:\text{Sm}$ piezoelectric compositions.

2.3.2 Phenomenological Studies

(a) The studies initiated by A. Amin in our group to delineate a phenomenological Gibbs function to describe the whole family of simple proper ferroelectrics in this solid solution system has now been completed and published.

(b) Following on from this work a simple model was proposed for the multicell rhombohedral phase, describing the contribution to the free energy by oxygen octahedron rotation as an expansion using the tilt angle as the order parameter. A simple expansion up to the 4th power terms permitted a

rigorous family of solutions and clearly delineated possible descriptions from the model. One such description is in qualitative agreement with the observed PZT behavior.

(c) To improve the simple 4th power model, which only permits second order rotational transitions, a 6th power term has been added. The simplicity of the solutions is lost and computer solution is necessary but the fitting to experimental rotation and polarization data is excellent.

(d) The objective of the initial exercise in the multicell system is now in sight. By adding the cross terms which couple polarization and strain (electrostriction) and rotation and strain (rotostriction) the shape changes associated with the polarized rotated states, i.e. the multicell states, can be properly described.

2.4 Preparative Studies

2.4.1 Single Crystal Growth

(a) Focus of effort is single crystal pulling has remained with $\text{Pb}_{1/x}\text{Ba}_x\text{Nb}_2\text{O}_6$ tungsten bronze crystals at compositions close to but on the tetragonal side of the $\text{Pb}_{0.6}\text{Ba}_{0.4}\text{Nb}_2\text{O}_6$ composition.

To aid in the study of the unusual phase change near room temperature, single crystals of the fresnoite structure $\text{Ba}_2\text{TiGe}_2\text{O}_8$ are being pulled from the stoichiometric melt.

(b) In Bridgeman growth, a sealed ampule technique is being used to grow crystals of the fluoride analogue perovskite KMnF_3 and KMgF_3 . These crystals are needed for compressometer studies of the electrostriction behavior and for measurements of third order elastic constants.

(c) Flux growth has been used to produce mm cube crystals of the perovskite form of $\text{PbZn}_{1/3}\text{Nb}_{2/3}\text{O}_3$ using excess PbO and B_2O_3 as fluxes. The

program to improve the growth of $\text{PbMg}_{2/3}\text{O}_3$ and $\text{PbMg}_{1/3}\text{Nb}_{2/3}\text{O}_3:\text{PbTiO}_3$ compositions is continuing.

Small (mm) size single crystals of $\text{PbTiO}_3:\text{Sm}$ have also been grown with samarium content up to 10 mole%.

2.4.2 Ceramic Studies

(a) Preparation of acicular powders by liquid salt processing has been carried through for compositions in the $\text{PbNb}_2\text{O}_6:\text{KNbO}_3$ system.

(b) In cooperation with the Dielectric Center programs, a new computer controlled furnace system has been developed which permits rapid firing of small low thermal inertia samples in highly controlled reproducible firing cycles.

(c) Efforts have continued to improve preparation facilities for the many types of ceramic compositions required in both Piezoelectric and Dielectric programs. New Swako vibratory mill, and a new attritor mill have been installed, a high energy sonicator for dispersing soft agglomerates in tape casting formulations is also in use, and new particle size characterization equipment is on order.

3.0 PUBLICATIONS, PRESENTATIONS, HONORS, AND AWARDS

3.1 Publications

Over the contract period from January 1 to December 31, 1984.

1. J. Runt, E.C. Galgoci. Piezoelectric Composites of PZT and Some Semi-Crystalline Polymers. Mat. Res. Bull. 19:253 (1984).
2. J. Runt, E.C. Galgoci. Polymer/Piezoelectric Ceramic Composites: Polystyrene and Poly (Methyl Methacrylate) with PZT. J. Appl. Polymer Sci 29:611 (1984).

3. R.E. Newnham, A. Safari, J. Giniewicz, B.H. Fox. Composite Piezoelectric Sensors. Ferroelectrics 60:15-21 (1984).
4. R.Y. Ting, A. Halliyal, A. Bhalla. Polar Glass Ceramics for Sonar Transducers. Appl. Phys. Letters 44:852-854 (1984).
5. A. Halliyal, A. Safari, A.S. Bhalla, R.E. Newnham, L.E. Cross. Grain Oriented Glass Ceramics for Piezoelectric Devices. J. Amer. Ceram. Soc. 67(5):305 (1984).
6. T.R. Gururaja, W.A. Schulze, L.E. Cross, B.A. Auld, Y.A. Shui, Y. Wang. Resonant Modes of Vibration in Piezoelectric PZT-Polymer Composites with Two-Dimensional Periodicity. Ferroelectrics 54:183-186 (1984).
7. A.S. Bhalla, R.E. Newnham. Pyroelectric and Piezoelectric Properties of SbSI Composites. Ferroelectrics Letters 3:59 (1984).
8. R.E. Newnham, A. Safari, J. Giniewicz, G. SaGong. Flexible Composite Piezoelectric Sensors. Proc. IEEE Ultrasonics Symposium Vol. 501 (1984).
9. S. DaVanzo, A. Safari, R.E. Newnham. Finite Element Modeling of Perforated PZT Polymer Composites. Ferroelectrics Letters 3:109 (1985).
10. Z.Y. Meng, Y.M. Sun, L.E. Cross. Electrostriction Tensor Components of Alkaline-Earth Fluoride Single Crystals. Mat. Lett. 2(6a,b):544-546 (1984).
11. Y. Xi, Z. Chen, L.E. Cross. Polarization and Depolarization Behavior of Hot Pressed Lead Lanthanum Zirconate Titanate Ceramics. Ferroelectrics 54:163-166 (1984).
12. M.P. Harmer, A. Bhalla, B.H. Fox, L.E. Cross. Electron Microscopy of Ordered Domains in Lead Scandium Tantalate $Pb(Sc_{0.5}Ta_{0.5})O_3$. Mat. Lett. 2:278 (1984).
13. K. Uchino, S. Nomura, K. Vedam, R.E. Newnham, L.E. Cross. Pressure Dependence of the Refractive Index and Dielectric Constant in a Fluoroperovskite $KMgF_3$. Phys. Rev. B 29:6921 (1984).

14. Z.Y. Meng, U. Kumar, L.E. Cross. Electrostriction in Lead Lanthanum Zirconate Titanate (PLZT) Ceramics. J. Amer. Ceram. Soc. (in press).
15. T.R. Halemane, M.J. Haun, L.E. Cross, R.E. Newnham. Phenomenology for First Order Transitions with Tilted Octahedra. Ferroelectrics (in press).
16. L.E. Cross. Dielectric, Piezoelectric, and Ferroelectric Components. Ceram. Bull. 4:586 (1984).
17. T.R. Halemane, M.J. Haun, L.E. Cross, R.E. Newnham. A Phenomenological Theory for Phase Transitions in Perovskite Ferroelectrics with Oxygen Octahedron Tilts. Ferroelectrics 62(3/4):149 (1985).
18. A. Amin, M.J. Haun, B. Badger, H.A. McKinstry, L.E. Cross. A Phenomenological Gibbs Function for the Single Cell Region of the $\text{PbZrO}_3:\text{PbTiO}_3$ Solid Solution System. Ferroelectrics (in press).
19. T.R. Gururaja, W.A. Schulze, L.E. Cross, R.E. Newnham. Piezoelectric Composites for Ultrasonic Transducer Applications. Part I. IEEE Trans. on Sonics and Ultrasonics (in press).
20. T.R. Gururaja, W.A. Schulze, L.E. Cross, R.E. Newnham. Piezoelectric Composite for Ultrasonic Transducer Applications. Part II. IEEE Trans. on Sonics and Ultrasonics (in press).
21. A. Halliyal. Study of the Piezoelectric and Pyroelectric Properties of Polar Glass Ceramics. Ph.D. Thesis in Solid State Science, The Pennsylvania State University (May, 1984).
22. T.R. Gururaja. Piezoelectric Composite Materials for Ultrasonic Transducer Applications. Ph.D. Thesis in Solid State Science, The Pennsylvania State University (May, 1984).

23. M. Bliss. An Analysis of the Reaction of PbO and Nb₂O₅ in Molten Salt for Use in Grain Oriented Piezoelectric 0:3 Composites. M.S. Thesis in Ceramic Science and Engineering, The Pennsylvania State University (August, 1984).
24. K. Rittenmyer. Electrostriction in Cubic Halide Compounds. Ph.D. Thesis in Solid State Science, The Pennsylvania State University (May, 1984).

3.2 Presentations at National and International Meetings

3.2.1 Invited Papers

1. J.N. Kim, S.J. Jang, L.E. Cross. Dielectric and Piezoelectric Properties of PZT Ceramics from Liquid Helium Temperature to Room Temperature. 86th Annual Meeting American Ceramic Society, Pittsburgh, PA, April 29 to May 3, 1985.
2. R.E. Newnham. Composite Piezoelectric Transducers. Acoustical Society American Meeting, Norfolk, VA, May 7-9.
3. R.E. Newnham. Structure Property Relations in Multilayer Capacitors. American Cryst. Assoc. Meeting, Lexington, KY, May 21-25.
4. R.E. Newnham. Structure Property Relations in Sensor Materials. International Union of Crystallography Meeting, Hamburg, Germany, August 9-18.
5. R.E. Newnham. Composite Electroceramics. Lehigh University Kraner Symposium, September 17.
6. R.E. Newnham. Composite Electroceramics. 2nd U.S.:Japan Seminar on Dielectric and Piezoelectric Ceramics. Williamsburg, VA, November 4-7.

3.2.2 Contributed Papers

86th Annual Meeting of the American Ceramics Society, Pittsburgh, PA,
April 29 - May 3, 1985

1. A. Halliyal, A.S. Bhalla. Glass-Ceramics: New Materials for Hydrophone Applications.
2. J.R. Giniewicz, A. Safari, R.E. Newnham. $\text{PbTiO}_3\text{-BiFeO}_3$ as a Piezoelectric Composite Material.
3. G. SaGong, A. Safari, S.J. Jang, R.E. Newnham. Poling Study on Ceramic-Polymer Composites.
4. S. DaVanzo, A. Safari, R.E. Newnham. Finite Element Modelling of PZT Composites.
5. A. Safari, L.E. Cross, R.E. Newnham. Diced PZT Composites for Hydrophone Applications.
6. Z. Meng, U. Kumar, L.E. Cross. High Field Dielectric and Electrostrictive Behavior in PLZT Ceramics with Zr/Ti Ratio 65/35.
7. K. Rittenmyer, Z. Meng, A.S. Bhalla, L.E. Cross. Determination of the Electrostriction Coefficients Q_{11} , Q_{12} , Q_{44} for Single Crystals of Calcium Fluoride.
8. C. Sundius, M. Shishineh, S.J. Jang, L.E. Cross. Electrostriction Measurements on Single Crystals of BaTiO_3 and $(\text{Sr}_{0.61}\text{Ba}_{0.39})\text{Nb}_2\text{O}_6$ (SBN).
9. G.O. Dayton, B.H. Fox, J.V. Biggers. Unconventional Profile Sintering Systems.
10. M. Bliss, R.E. Newnham, W.A. Schulze. Processing Effects on the Piezoelectric Properties of Lead Metaniobate Compounds.
11. D. Christopher, W.R. Xue, J.V. Biggers. Agglomerate Characteristics of Oxide Powders Used in Production of Electronic Ceramics.
12. L.C. Veitch, S. Swartz, R.E. Newnham. Processing of Lead Nickel Niobate.

13. W.R. Xue, R.E. Newnham, L.E. Cross. The Temperature Behavior of Electromechanical Properties of Modified PbTiO_3 Ceramic.

2nd U.S.:Japan Seminar on Dielectric and Piezoelectric Ceramics, Williamsburg, VA, November 4-7, 1984
14. L.E. Cross, C. Sundius, T. Shrout. Polarization Mechanisms in Relaxor Ferroelectrics.
15. L.E. Cross, C. Sundius, T.R. Shrout. Elastic and Optical Effects from Polarization Fluctuations in Relaxor Ferroelectrics.
16. L.J. Bowen, J. McColl, A. Halliyal, A. Bhalla. Properties and Applications of Piezoelectric Glass-Ceramics.
17. D.G. Christopher, W.R. Xue, G.O. Dayton, J.V. Biggers. Agglomeration Characterization of Oxide Powders Used in Production of Electronic Ceramics.
18. D. Bonnema, J.N. Kim, M. Haun, S.J. Jang, L.E. Cross. Low Temperature Properties of Lead-Titanate Based Ceramics.
19. A. Halliyal, A.S. Bhalla, L.E. Cross. Phase Transitions, Dielectric, Piezoelectric and Pyroelectric Properties of Barium Titanium Germanate $\text{Ba}_2\text{TiGe}_2\text{O}_8$ Single Crystals.
20. T.R. Halemane, M.J. Haun, L.E. Cross, R.E. Newnham. A Phenomenological Theory for Phase Transitions in Perovskite Ferroelectrics Exhibiting Oxygen Octahedron Tilts with Application to PZT Materials.

3.3 Honors, Awards and Prizes

Dr. L.E. Cross Elected to the National Academy of Engineers

 Elected Fellow of the I.E.E.E.

 Presented with the John Jeppson Medal and Award of the
 American Ceramic Society

Dr. R.E. Newnham Elected President of the American Crystallographic Assn.
Presented with the Faculty Scholars Medal in Science and Engineering at Penn State

*Dr. T. Gururaja Xerox Award Winner for Ph.D. in Materials Subject at Penn State, August, 1984

*Dr. A. Safari Xerox Award Winner for Ph.D. in Materials Subject at Penn State, August, 1984.

*Dr. M. Haun Xerox Award Winner for M.S. in Materials Subject at Penn State, August, 1984.

*The Xerox Awards are presented on the judgement of an independent committee drawn from the Departments of Electrical Engineering, Physics, Materials Science and Materials Research Laboratory for the best Ph.D., M.S. and B.S. thesis work in materials at Penn State, judged from the quality of the thesis and associated published works. Only two Ph.D. and two M.S. prizes are awarded each year, and it is a signal honor to this ONR sponsored program that three of the four top awardees were associated with studies on this program.

3.4 Degrees Earned

3.4.1 Graduate Degrees (M.S., Ph.D.)

1. K. Rittenmyer Ph.D. Thesis in Solid State Science, May 1984.
"Electrostriction in Cubic Halide Compounds"
2. T. Gururaja Ph.D. Thesis in Solid State Science, May 1984.
"Piezoelectric Composite Materials for Ultrasonic Transducer Applications"
3. A. Halliyal Ph.D. Thesis in Solid State Science, May 1984.
"Study of the Piezoelectric and Pyroelectric Properties of Polar Glass Ceramics."
4. M. Bliss M.S. Thesis in Ceramic Science and Engineering, Aug. 1984
"An Analysis of the Reaction of PbO and Nb₂O₅ in Molten

Salt for Use in Grain Oriented Piezoelectric 0:3
Composites"

3.4.2 Undergraduate Thesis Projects (B.S.)

- Phillip Gilmour B.S. Ceramic Science and Engineering, May 1984.
"Domain Size and Microstrain Determination in Ultrasonic
Transducers Using X-Ray Diffraction"
- Thomas Chiesa B.S. Ceramic Science and Engineering, May 1984.
"Study of $\text{LiNbO}_3:\text{NaNbO}_3$ Solid Solutions"
- Stephen Costantino B.S. Ceramic Science and Engineering, May 1984.
"Characteristics of Japanese Multilayer Ceramic
Capacitors"
- Kevin Dietz B.S. Ceramic Science and Engineering, May 1984.
"Leucite Structure Ferroelastic Silicates"
- Alan Hain, Jr. B.S. Engineering Science, May 1984.
"New Bimorph Structures with High Flexural Resonance
Frequency"
- Eric Rothdeutsch B.S. Engineering Science, December 1984.
"Electrical Characteristics of BaPbO_3 Filled Epoxy
Composite Conductors"

4.0 APPLIED SCIENCE APPRENTICESHIPS IN THE CENTER FOR DIELECTRIC STUDIES

It is the purpose of this program to provide opportunity for high school students to become acquainted, during their summer break, with the workings of a major research laboratory and the fascination of research and discover. The objective is to have a maximum of three students in this category who could work closely with the postdoctoral fellows and graduate assistants in the Materials Research Laboratory on problems associated with our ONR program in

the Center for Dielectric Studies and on the program of research on Piezoelectric and Electrostrictive Materials for Transducer Applications. These program which encompasses the preparation, characterization, and measurement of properties of a wide range of new electroceramic and ceramic-plastic composites offer many opportunities in which the "extra pair of hands" and quick perceptions of a well motivated high school student provides invaluable assistance.

We believe that the relaxed atmosphere and constant interchange between faculty, postdoctoral fellows, graduate assistants, and technical aides, and the continuous presence of many eminent foreign visiting scientists provides a very stimulating environment for the young student who may be at a critical juncture in making decisions as to longer range career plans.

It is our belief that if the very bright young students are to be encouraged to choose careers in science and engineering, it must be through acquaintance with some of the less obvious, intangible intellectual benefits of the profession, since legal, medical and business careers can almost always offer more immediate financial reward and more obvious ladders for advancement.

A secondary but not insignificant advantage of the program is in the additional component which it provides in the education of our graduate students. Most of these young men and women will go out into responsible positions in Government and Industry where they will be called upon to organize and supervise the work of many junior engineers and technicians. This program, which attaches the technical aid to a graduate assistant, gives him the chance to organize the work of a second person to speed his own program, but also the responsibility of the associated human problems of scheduling and humane management. We believe it has been a most valuable experience for the graduate assistants who have participated and has given

them very useful insights into both the problems and the rewards of "people management."

For the last two years, we have developed a much closer relationship with the University's Upward Bound Program, who are able to draw well motivated black students from the Philadelphia School System. Over the years it has become our custom to issue each student participant a certificate on completion of the term, at a small internal ceremony in MRL. Copies of certificates given to our last three successful apprentices are appended.

THE·MATERIALS·RESEARCH·LABORATORY

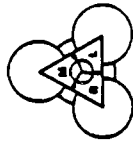
PENNSYLVANIA · STATE · UNIVERSITY
·1984·

Office of Naval Research
Apprentice Program Certification
for successful completion of the ten week project/study program
in Electronic Ceramics

Winston L. Edwards


L. E. Choss
Associate Director

August 10, 1984
Date Signed



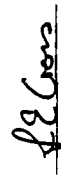
Funded by Modification P00006
to Contract N000014-82-K-0339

THE·MATERIALS·RESEARCH·LABORATORY

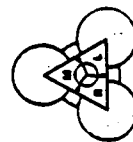
PENNSYLVANIA · STATE · UNIVERSITY
·1984·

Office of Naval Research
Apprentice Program Certification
for successful completion of the ten week project/study program
in Electronic Ceramics

Dennette E. Gibson


L. E. Choss
Associate Director

August 10, 1984
Date Signed

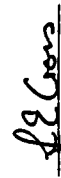


THE·MATERIALS·RESEARCH·LABORATORY

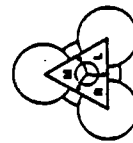
PENNSYLVANIA · STATE · UNIVERSITY
·1984·

Office of Naval Research
Apprentice Program Certification
for successful completion of the ten week project/study program
in Electronic Ceramics

Tanya M. Stafford


L. E. Choss
Associate Director

August 10, 1984
Date Signed



PIZOELECTRIC COMPOSITES OF PZT AND SOME SEMI-CRYSTALLINE POLYMERS

J. Runt and E.C. Galgoci

PIEZOELECTRIC COMPOSITES OF PZT AND SOME SEMI-CRYSTALLINE POLYMERS

J. Runt and E. C. Galgoci
Polymer Science Program
Department of Materials Science and Engineering
The Pennsylvania State University
University Park, PA 16802

(Received August 17, 1983; Refereed)

ABSTRACT

Piezoelectric composites of PZT ceramics and several semi-crystalline polymers have been produced by embedding slender PZT rods (4 volume percent) in the polymers. The observed dielectric constants were considerably lower than that of pure PZT. The hydrostatic piezoelectric voltage coefficients of the composites were larger than PZT, even though the composite hydrostatic piezoelectric strain coefficients were lower. Composite figures of merit ranged from one-third to six times that of PZT.

Introduction and Background

By careful choice of design, multiphase materials may be produced which possess ultimate properties which are superior to the sum of those of the individual components (1). With this idea in mind, novel piezoelectric transducers have been produced and tested for applications such as hydrophones and medical ultrasound (2). One of the most successful designs to date consists of slender, extruded fibers of lead zirconate titanate (PZT) aligned normal to two electrode surfaces and surrounded by a polymer matrix (3,4,5). These composites are referred to as 1-3 composites in the

nomenclature adopted by Newham, et al. (6), where the numbers refer to the total orthogonal directions (in an orthogonal axis system) in which each phase is self-connected. Since the PZT rods are continuous from one electrode surface to the other, saturation poling can be accomplished; thereby ensuring the maximum piezoelectric sensitivity.

The hydrostatic piezoelectric response can be defined by the piezoelectric strain (d_h) and voltage (g_h) coefficients. d_h is a measure of the polarization produced as a result of applying a hydrostatic stress and is given by:

$$d_h = d_{33} + 2d_{31} \quad (1)$$

where the subscripts refer to directions in an orthogonal axis system according to the common reduced notation. The 3-direction is defined as the direction parallel to the PZT fiber axis. Charge which develops on the electrode surface as a result of stresses parallel and perpendicular to the poling axis is governed by d_{33} and d_{31} , respectively. The voltage coefficient is related to d_h by:

$$g_h = \frac{d_h}{K_{33}\epsilon_0} \quad (2)$$

where K_{33} is the dielectric constant in the poling direction and ϵ_0 is the permittivity of free space. Since, for PZT, d_{33} is opposite in sign to and about twice the value of d_{31} , and K_{33} is large, both d_h and g_h are relatively low.

For piezoelectric 1-3 composites a simple parallel-series model developed by Skinner, et al. (7) predicts that the d_{33} (\bar{d}_{33}) of a composite containing a very compliant matrix is equal to the d_{33} of PZT. The composite d_{31} (\bar{d}_{31}) is given by:

$$\bar{d}_{31} = v^1 d_{31} \quad (3)$$

where v is the volume fraction and the superscript 1 refers to the PZT phase. The composite hydrostatic piezoelectric coefficient (\bar{d}_h) can then be expressed as:

$$\bar{d}_h = d_{33} + v^1 d_{31} \quad (4)$$

Also, the composite voltage coefficient, which is important for hydrophones, is given by:

$$\bar{g}_h = \frac{\bar{d}_h}{v^1 K_{33} \epsilon_0} \quad (5)$$

Therefore, the simple model predicts large increases in \bar{d}_h and \bar{g}_h over PZT as the amount of PZT in the composite is decreased.

However, recent experimental work (4,5,8) has shown that the quantitative predictions of the Skinner, et al. scheme are not realized if flexible electrodes are used for 1-3 composites. Several explanations have been proposed to account for these discrepancies. These include: the effective matrix region of influence (8), internal stresses arising from differences in the Poisson's strain between the ceramic and polymer (9), and relic processing stresses (5). In the case of glassy thermoplastic polymer matrices, annealing the composites at temperatures near the glass transition temperature (T_g) of the matrix was found to improve their piezoelectric response (5). This is presumably due to relief of some of the residual processing stresses.

All 1-3 composites studied to date have used amorphous polymers as the matrix phase. Semi-crystalline polymer matrices have never been employed in these types of piezoelectric composites. Low T_g , semi-crystalline polymers such as polyethylene and the Hytrel poly(ester/ether) block copolymers have mechanical properties which are intermediate between glassy and elastomeric materials. Also, it is possible to conveniently alter the degree of crystallinity of these materials by thermal annealing at temperatures approaching the melting point or, in the case of the Hytrels, by varying the crystallizable-segment content. This allows one to investigate the effect of matrix compliance on composite performance. This paper reports some of our initial studies on 1-3 PZT/semi-crystalline polymer composites.

Experimental

A. Composite Fabrication

The PZT rods used in this study were prepared by a technique described previously (3). All composites contained rods which were 12-mil (305 μm) in diameter and were prepared from PZT 501A powder (obtained from Ultrasonic Powders, Inc.). The sintered PZT fibers were aligned in racks which consisted of two parallel plates of aluminum foil separated by ~2 cm. Each plate had an array of perforations through which the rods were inserted so as to be held in place during polymer processing. This was done to insure the proper volume fraction (4%) of PZT for all composites.

(a) PZT/Poly(butylene terephthalate) Composites

Poly(butylene terephthalate) (PBT) is a semi-crystalline polymer with a melting point (T_m) of -220°C and a $T_g = 70^\circ\text{C}$. Therefore, PBT is a glassy semi-crystalline material and possesses mechanical properties characteristic of rigid polymers (e.g. Young's modulus (E) = 10^9 N/m^2). PBT is polymerized by condensation methods and has a relatively low molecular weight (ca. 20,000-30,000 gm/mole). Its melt viscosity is therefore also comparatively low, making small scale melt composite processing feasible without the use of high pressures.

PZT/PBT composites were prepared by placing filled racks of PZT rods and dried PBT pellets (obtained from Scientific Polymer Products, Inc.) into glass molds which were then purged with nitrogen and immersed in a 250°C oil bath until the pellets melted and no voids were present in the melt. The system was allowed to cool to room temperature over a 5 hour period.

(b) PZT/Nylon 11 Composites

Like PBT, nylon 11 is a glassy, semi-crystalline polymer ($T_m \approx 185^\circ\text{C}$, $T_g \approx 45^\circ\text{C}$, $E \approx 10^9 \text{ N/m}^2$) and has a relatively low melt viscosity. However, in order to avoid the problem of polymer degradation at high temperatures, we decided to prepare these composites by insitu polymerization of the monomer.

Racks of PZT in glass molds were surrounded by 11-aminoundecanoic acid ($T_m \approx 190^\circ\text{C}$) and the molds (under a continuous nitrogen purge) were placed in a 220°C silicone oil bath. Water vapor which formed during the polymerization was forced through an exit tube by the gas pressure. The polymerization was terminated by cooling for one hour after water formation ceased.

(c) PZT/Hytrel Composites

The Hytrels (E. I. duPont de Nemours and Co., Inc.) are a series of thermoplastic elastomers composed of polyester "hard" segments which are crystallizable and non-crystallizable, low T_g polyether "soft" segments. By varying the concentration of polyester units, the degree of crystallinity and, hence, the modulus of the resultant copolymer can be adjusted. Some characteristics of the three Hytrels used in this study are shown in Table 1(10). Note that all the Hytrels have moduli which are significantly lower than both PBT and nylon 11.

TABLE 1
Properties of Hytrel Copolymers (10)

Hytrel	Wt. % Polyester segments	T_m ($^\circ\text{C}$)	T_g ($^\circ\text{C}$)	Density (gm/cc)	Modulus (10^8 N/m^2)
4056	30	150	-80	1.17	0.34
1000	49	186	-65	1.19	1.48
995	81	218	-5	1.23	4.00

Composites were prepared in the same manner as the PZT/PBT materials except that the oil bath was heated to 220°C and cooling to room temperature was done over a 48 hour period.

After solid composites were fabricated, the molds were broken and the composites were sectioned perpendicular to the rod axis using an electric diamond saw or a hacksaw. The as-cut slugs were then sanded with 60 grit garnet paper followed by polishing using 200 grit garnet paper. All composites were 4mm thick in the fiber direction.

Air-dry silver electrodes were applied to the two faces perpendicular to the rods and the composites were poled at 75°C in an oil bath with a field of 22kV/cm for 5 min. After the composites were removed from the bath, they were allowed to cool in air under a field of 7.5 kV/cm for 10 minutes to prevent depoling during cooling. The poled composites were aged for at least 24 hours prior to piezoelectric and dielectric measurements

B. Measurement of Dielectric and Piezoelectric Properties

Dielectric measurements were performed with a Hewlett Packard 4270A Automatic Capacitance Bridge at 1kHz and 1 volt. \bar{d}_{33} was measured using a Berlincourt Piezo d_{33} -Meter with rounded rams. The ratio of the diameter of the rams to the center-to-center distance of the PZT rods was 0.74. The \bar{d}_{33} was taken as the average of 20 random measurements (10 on each electroded surface of the composite) at a ram pressure of approximately 55 psi. The hydrostatic piezoelectric coefficients (\bar{d}_h and \bar{g}_h) were measured by a dynamic method (11). The apparatus consisted of an oil-filled chamber in which the samples and a PZT standard of known d_h and g_h were immersed. The pressure inside the vessel was raised to 100 psi and alternating sinusoidal pressure cycles (amplitude ± 0.1 psi) were imposed using an AC stress generator driven by a function generator adjusted to the proper frequency. The sample (or standard) voltage was recorded on an oscilloscope display.

Results and Discussion

Comparison of composite dielectric and piezoelectric properties with conventional single phase materials can be found in Table 2. As expected, the composite dielectric constants are low compared to that of PZT but, except for the PZT/Hytrel 4056 composite, K_{33} values are greater than that predicted by the rule of mixtures (theoretical $K_{33} = 64$). Since applied compressive stress is known to increase the dielectric constant of PZT (12), radial compression between the rods and the matrix may be responsible for these results (5). Radial stresses may have originated from thermal expansion mismatches, mechanical processing conditions, or polymer crystallization shrinkage.

TABLE 2
Piezoelectric Properties of 1-3 Composites and Single Phase Materials

Material	Density* (g/cc)	\bar{K}_{33}	\bar{d}_{33}^{**} (10^{-12} C/N)	\bar{d}_h^{***} (10^{-12} C/N)	\bar{g}_h^{***} (10^{-3} V-m/N)	$\bar{d}_h \bar{g}_h^{***}$ (10^{-15} m ² /N)
PZT/PBT	1.35	97	110 ±20	29	34	990
PZT/nylon 11	1.31	105	128 ±27	32	34	1090
PZT/Hytrel 4056	1.44	62	174 ±43	6	10	60
PZT/Hytrel 1000	1.46	94	215 ±50	11	13	140
PZT/Hytrel 995	1.49	94	141 ±25	32	38	1220
PZT	7.9	1600	400	50	4	200
PVDF	1.4	12	24	11	104	1140

* Calculated for composites

** Errors are ± standard deviation.

*** Estimated errors are: $\bar{d}_h \pm 12\%$, $\bar{g}_h \pm 16\%$, and $\bar{d}_h \bar{g}_h \pm 20\%$

For a more compliant polymer, stress transfer from the matrix to the PZT rods should be more efficient than for a stiffer matrix. Thus, \bar{d}_{33} would be expected to increase as matrix compliance increases and this is seen to be the general trend for the polymers examined in this study with the PZT/Hytrel 4056 and PZT/Hytrel 1000 composites exhibiting \bar{d}_{33} 's which are larger than some of the higher modulus composites.

A somewhat surprising result is that \bar{d}_h increases as polymer modulus increases. Since \bar{d}_{33} increases as the matrix stiffness decreases, $|\bar{d}_{31}|$ must increase accordingly. In general, as the compliance of a polymer increases, its Poisson's ratio (ν) increases and the enhancement of $|\bar{d}_{31}|$ is thought to arise from stresses due to differences in Poisson's contraction between the phases (9). Although one cannot alter the characteristic modulus and ν independently in solid polymers, one can lower both simultaneously through matrix foaming. Such compliant, foamed composites would be expected to have outstanding hydrostatic figures of merit. This has, in fact, been shown to be the case by Klicker, et al. for PZT/foamed polyurethane composites (13).

The hydrostatic piezoelectric coefficients (\bar{d}_h) for the PBT, nylon 11 and Hytrel 995 composites are smaller than those of PZT but similar to those observed previously for 1-3 composites with rigid matrices (5,11). \bar{d}_h for the Hytrel 4056 and 1000 composites are comparable to that of PVDF but considerably smaller than the other composites presumably due to Poisson's ratio stresses. The voltage coefficients of all composites are greater than that of PZT because the permittivities of the composites are much lower than the values for PZT alone. \bar{E}_h for the composites with relatively stiff matrices (PBT, nylon 11 and Hytrel 995) are about an order of magnitude larger than PZT but, because of their low \bar{d}_h , the Hytrel 4056 and 1000 composites exhibit significantly lower \bar{E}_h 's. This results in $\bar{E}_h \bar{d}_h$ for the composites with stiff matrices being about five times larger than that of PZT and comparable to that of PVDF while the figures of merit of the more compliant matrix composites are somewhat less than PZT. Finally, no frequency dependence of \bar{d}_h was observed for any composite from 30 to 160 Hz (Figure 1).

Conclusions

The piezoelectric figures of merit for composites with stiff polymer matrices are about five times larger than PZT and comparable to PVDF. The primary reason for the enhancement of $\bar{d}_h \bar{E}_h$ over PZT is that the composites have much lower \bar{k}_{33} values than PZT. An unexpected result was the decrease in \bar{d}_h as matrix modulus decreased. Since \bar{d}_{33} was found to increase as the matrix modulus decreases, $|\bar{d}_{31}|$ must be increasing as the polymer stiffness decreases. The enhanced component of $|\bar{d}_{31}|$ presumably results from differences in Poisson's contraction between the phases and ultimately results in relatively low figures of merit for composites with compliant polymer matrices.

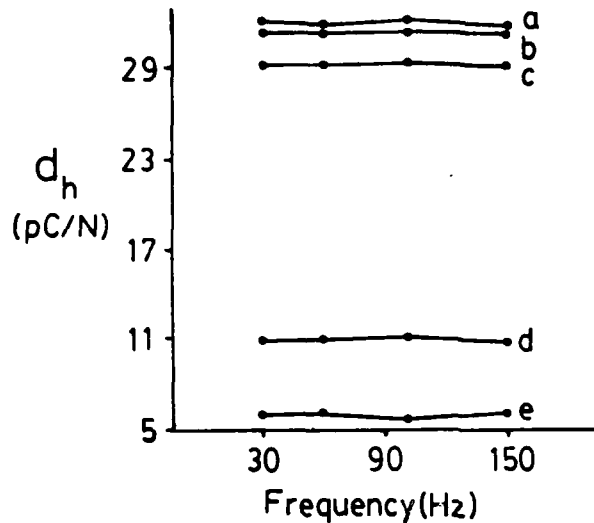


FIG. 1

\bar{d}_h of Composites as a
Function of Test Frequency

- a. PZT/Nylon 11
- b. PZT/Hytrel 995
- c. PZT/PBT
- d. PZT/Hytrel 1000
- e. PZT/Hytrel 4056

Acknowledgements

The authors would like to thank the Office of Naval Research for partial support of this work through contract N00014-82-K-0339.

References

1. R. E. Newnham, D. P. Skinner and L. E. Cross, *Mat. Res. Bull.* **13**, 525 (1978).
2. R. E. Newnham, L. J. Bowen, K. A. Klicker and L. E. Cross, *Mater. Eng.* **2**, 93 (1980).
3. K. A. Klicker, J. V. Biggers and R. E. Newnham, *J. Amer. Ceram. Soc.* **64**, 5 (1981).
4. S. Y. Lynn, R. E. Newnham, K. A. Klicker, K. Rittenmeyer, A. Safari and W. A. Schulze, *Ferroelectrics* **38**, 955 (1981).
5. J. Runt and E. C. Galgoci, *J. Appl. Polym. Sci.* (in press).
6. R. E. Newnham, D. P. Skinner and L. E. Cross, *Mat. Res. Bull.* **13**, 525 (1978).
7. D. P. Skinner, R. E. Newnham and L. E. Cross, *Mat. Res. Bull.* **13**, 599 (1978).
8. K. A. Klicker, Ph.D. Dissertation, The Pennsylvania State University (1980).
9. M. Haun, M.S. Thesis, The Pennsylvania State University (1983).
10. R. J. Cella, "Encyclopedia of Polymer Science and Technology", supplement Volume II, p. 485, John Wiley and Sons, Inc., New York (1977).
11. S. Y. Lynn, M.S. Thesis, The Pennsylvania State University (1981).
12. B. Jaffe, W. R. Cook and H. Jaffe, "Piezoelectric Ceramics", Academic Press, London (1971).
13. K. A. Klicker, W. A. Schulze and J. V. Biggers, *Ceram. Amer. Ceram. Soc.* **65**, 208 (1982).

POLYMER/PIEZOELECTRIC CERAMIC COMPOSITES:
POLYSTYRENE AND POLY(METHYL METHACRYLATE) WITH PZT

J. Runt and E.C. Galgoci

Polymer/Piezoelectric Ceramic Composites: Polystyrene and Poly(methyl Methacrylate) with PZT

J. RUNT* and E. C. GALGOCI, *Polymer Science Program, Department of Materials Science and Engineering, The Pennsylvania State University, University Park, Pennsylvania 16802*

Synopsis

Lead zirconate-titanate (PZT)/polymer composites have been prepared by *in situ* polymerization of styrene and methyl methacrylate around aligned, thin PZT rods. Hydrostatic piezoelectric coefficients (\bar{d}_h and \bar{g}_h) measured by a dynamic technique yielded figures of merit ($\bar{d}_h\bar{g}_h$) roughly four times that of homogeneous PZT for as-polymerized composites. When these composites were annealed at a temperature slightly below the glass transition temperature of the matrix polymer and repoled, $\bar{d}_h\bar{g}_h$ increased nearly twofold due primarily to a reduction of the composite dielectric constant. The piezoelectric response was found to be essentially independent of frequency from 30 to 160 Hz.

INTRODUCTION

Piezoelectric composites have been the center of much recent study¹ because of their possible advantages over single phase piezoelectrics [e.g., poly(vinylidene fluoride) (PVDF) and lead zirconate-titanate (PZT)] for hydrophone applications. The phase connectivity² is a particularly important parameter, which ultimately determines the properties of a composite solid. For piezoelectric composites made from PZT and polymers, designs which allow the ceramic to be poled to saturation produce relatively large piezoelectric coefficients even for low PZT concentrations.

One such motif studied by Klicker et al.³ consisted of slender PZT rods aligned perpendicular to the electrode surface and surrounded by a thermosetting polymer (epoxy). These diphasic materials are designated 1-3 composites in the notation adopted by Newnham et al.² The numbers refer to the total orthogonal directions in which each phase is continuous throughout the object. In this case the active phase (PZT) extends continuously in one direction, while the polymer matrix spans the composite in all three orthogonal directions. Klicker et al.'s PZT/epoxy composites have hydrostatic "figures of merit" about an order of magnitude larger than homogeneous PZT.³ In addition, these materials have low densities ($\rho < 1.8 \text{ g/cm}^3$), which provide for better acoustic coupling to water than PZT ($\rho = 7.8 \text{ g/cm}^3$), and are flexible relative to PZT ceramics.

Even though the major improvements in properties for these composites over PZT ceramics can be traced to the polymeric phase, few polymer systems have been studied as possible matrix materials. Furthermore, only thermosetting polymers (e.g., epoxies and polyurethanes) have been employed previously in

* To whom correspondence should be addressed.

1-3 composites. Because the mechanical and physical properties of polymers can vary widely, and because theory⁴ suggests that matrix mechanical properties should strongly affect composite piezoelectric response, we have fabricated composites with a variety of thermoplastic polymers. This paper describes our initial studies on polystyrene (PS)/PZT and poly(methyl methacrylate) (PMMA)/PZT 1-3 composites.

BACKGROUND—THEORY

Piezoelectric materials experience a polarization (P) due to an applied stress (σ). The piezoelectric coefficient (d) is a measure of the polarization produced per unit stress. Under hydrostatic conditions, the piezoelectric coefficient is given by

$$d_h = d_{33} + 2d_{31} \quad (1)$$

where the subscripts are the reduced notation for designated directions in an orthogonal axis system. The d_{33} and d_{31} coefficients refer to polarizations which develop along the poling axis (i.e., the 3-direction) due to applied stresses parallel and transverse to the poling direction, respectively. For PZT, d_{31} is opposite in sign to and approximately one-half of d_{33} ; therefore, d_h is small. The hydrostatic voltage coefficient (g_h) is related to d_h by

$$g_h = d_h/\epsilon_{33} \quad (2)$$

where ϵ_{33} is the dielectric permittivity. Since d_h is low and the permittivity is high for PZT, the voltage coefficient, which is important for hydrophone applications, is very low. For a hydrostatic transducer material the $d_h g_h$ product is considered to be an all-encompassing "figure of merit."

A simple theory to describe the piezoelectric coefficients of composites with 1-3 connectivity has been described by Skinner et al.⁴ The theoretical piezoelectric and dielectric coefficients are given by

$$\bar{d}_{33} = \frac{{}^1v {}^1d_{33} {}^2J_{33} + {}^2v {}^2d_{33} {}^1J_{33}}{{}^1v {}^2J_{33} + {}^2v {}^1J_{33}} \quad (3)$$

$$\bar{d}_{31} = {}^1v {}^1d_{31} + {}^2v {}^2d_{31} \quad (4)$$

$$\bar{\epsilon}_{33} = {}^1v {}^1\epsilon_{33} + {}^2v {}^2\epsilon_{33} \quad (5)$$

where v and J are the volume fraction and elastic compliance, respectively. The superscripts refer to phase 1 (PZT) or phase 2 (polymer), and the bar represents the average composite coefficient.

Equations (3)–(5) can be reduced by considering that most polymers are nonpiezoelectric (i.e., ${}^2d_{33} = {}^2d_{31} = 0$), and possess relatively low dielectric permittivities (${}^1\epsilon_{33} \gg {}^2\epsilon_{33}$). Therefore, eqs. (3)–(5) become

$$\bar{d}_{33} = \frac{{}^1v {}^1d_{33} {}^2J_{33}}{{}^1v {}^2J_{33} + {}^2v {}^1J_{33}} \quad (6)$$

$$\bar{d}_{31} = {}^1v {}^1d_{31} \quad (7)$$

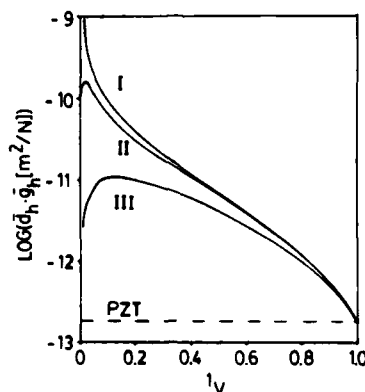


Fig. 1. Theoretical plot of $\log(\bar{d}_h \bar{g}_h)$ as a function of volume fraction of PZT (v_1). Curve I corresponds to ${}^2J_{33} = 10^{-7} \text{ m}^2/\text{N}$; for curve II, ${}^2J_{33} = 10^{-9} \text{ m}^2/\text{N}$; and for curve III, ${}^2J_{33} = 10^{-10} \text{ m}^2/\text{N}$. The broken line represents the $d_h g_h$ for homogeneous PZT.

$$\bar{\epsilon}_{33} = v_1 \epsilon_{33} \quad (8)$$

Since most polymers are much more compliant than PZT (i.e., ${}^2J_{33} \gg {}^1J_{33}$), eq. (6) further reduces to

$$\bar{d}_{33} = {}^1d_{33} \quad (9)$$

In this case, all of the force in the fiber direction is borne by the ceramic rod elements. However, if $v_1 \ll v_2$, this approximation to eq. (6) is invalid.

By combining eqs. (1), (6), and (7), the hydrostatic piezoelectric coefficient is obtained

$$\bar{d}_h = \frac{v_1 {}^1d_{33} {}^2J_{33}}{v_1 {}^2J_{33} + v_2 {}^1J_{33}} + 2 v_1 {}^1d_{31} \quad (10)$$

Figure 1 shows how $\bar{d}_h \bar{g}_h$ varies as a function of v_1 according to eqs. (2), (8) and (10) for several values of matrix compliance. For low concentrations of PZT, $\bar{d}_h \bar{g}_h$ is predicted to vary significantly as the matrix compliance changes.

Several modifications to the model of Skinner et al. have been suggested.^{5,6} Klicker⁶ has shown that \bar{d}_{33} is not necessarily equal to the d_{33} of PZT, but is a function of the PZT rod diameter and volume fraction, composite thickness, and matrix compliance. Additionally, the internal forces arising from a difference in constriction between the phases through Poisson's ratio produce an enhancement of $|\bar{d}_{31}|$ over that predicted by eqs. (4) or (7).⁵ These considerations lead to the conclusion that \bar{d}_h predictions based on the Skinner et al. approach are overestimates for 1-3 PZT/polymer composites.

Another important internal stress is that which is due to a mismatch in thermal expansion (or contraction) between the constituent phases.^{7,8} Polymers have coefficients of thermal expansion which are at least an order of magnitude larger than PZT ceramics. Therefore, large compressive stresses can develop at the interface of the resin and the PZT rods. These stresses may alter the piezoelectric and dielectric response of composite piezoelectrics. Furthermore, stresses related to curing or polymerization may also be of consequence.

EXPERIMENTAL

The preparation of the PZT rods used in this study has been described elsewhere.³ All rods were 12-mil (305- μm) in diameter and were prepared from PZT 501A (Ultrasonic Powders, Inc. South Plainfield, N. J.). The sintered rods were aligned in racks which consisted of two parallel plates of aluminum foil separated by ~ 2 cm. Each plate had an array of perforations through which the rods were inserted to be held in place during polymerization of the matrix in order to insure the proper volume fraction (4%) of PZT for all composites.

In situ polymerization of liquid monomers was the most convenient method to prepare composites because of the fragile nature of the PZT rods. The liquid monomers (styrene and methyl methacrylate) were purified by vacuum distillation prior to use. Polymerization was initiated by 0.5 wt % benzoyl peroxide. Prepolymer syrups (polymer in monomer) were prepared by heating the monomer-initiator systems at 80°C for 15 min and then cooling the mixture to room temperature. By using a prepolymer, the resulting composites were found to be essentially void free.

Composites were then fabricated by placing filled racks of PZT rods into glass molds and pouring a given prepolymer into the mold until the rods were submerged in the liquid and covered over by ~ 1 cm. The molds were then placed in an oven maintained at 50°C until the polymer solidified. Additional heating to 90°C for 1 h completed the polymerizations. After the molds were removed from the oven and allowed to cool, the glass mold was broken and the composites were sectioned perpendicular to the rod axis using an electric diamond saw or a hacksaw. The as-cut slugs were then sanded with 60-grit garnet paper followed by polishing using 200-grit garnet paper. All composites were 4 mm thick in the fiber direction. The glass transition temperatures (T_g) of the matrices were determined with a Perkin-Elmer DSC-2 equipped with a Thermal Analysis Data Station. The T_g of both the PS and PMMA was found to be approximately 100°C.

Air-dry silver electrodes were applied to the two faces perpendicular to the rods, and the composites were poled at 75°C in an oil bath with a field of 22 kV/cm for 5 min. After the composites were removed from the bath, they were allowed to cool in air under a field of 7.5 kV/cm for 10 min to prevent depoling during cooling. The poled composites were aged for at least 24 h prior to piezoelectric and dielectric measurements.

Dielectric measurements were performed with a Hewlett-Packard 4270A Automatic Capacitance Bridge at 1 kHz and 1 V. \bar{d}_{33} was measured using a Berlincourt Piezo d_{33} -Meter with rounded rams. The ratio of the diameter of the rams to the center-to-center distance of the PZT rods was 0.74. The \bar{d}_{33} was taken as the average of 20 random measurements (10 on each electroded surface of the composite) at a ram pressure of approximately 55 psi. The hydrostatic piezoelectric coefficients (\bar{d}_h and \bar{g}_h) were measured by a dynamic⁹ method. The apparatus consisted of an oil-filled chamber in which the samples and a PZT standard of known d_h and g_h were immersed. The pressure inside the vessel was raised to 100 psi and alternating sinusoidal pressure cycles (amplitude ± 0.1 psi) were imposed using an AC stress generator driven by a function generator adjusted to the proper frequency. The sample (or standard) voltage was recorded on an oscilloscope display.

TABLE I
Piezoelectric Properties of 1-3 Composites and Single Phase Materials

Material	Density (g/cm ³)	K_{33}	\bar{d}_{33}^a (10 ⁻¹² C/N)	\bar{d}_h^b (10 ⁻¹² C/N)	\bar{g}_h^b (10 ⁻³ V·m/N)	$\bar{d}_h\bar{g}_h^b$ (10 ⁻¹⁵ m ² /N)
PZT/PS	1.32	70	110 ± 16	22	36	790
PZT/PS (annealed)	1.32	54	130 ± 18	26	54	1400
PZT/PMMA	1.46	131	110 ± 18	28	25	700
PZT/PMMA (annealed)	1.46	100	125 ± 21	35	39	1370
PZT	7.9	1600	400	50	4	200
PVDF	1.8	12	30	11	104	1140
PZT/epoxy (Ref. 9)	1.4	97	—	32	51	1630

^a Errors are ± 1 standard deviation.

^b Estimated errors are $\bar{d}_h \pm 12\%$, $\bar{g}_h \pm 16\%$, and $\bar{d}_h\bar{g}_h \pm 20\%$.

After the composites were tested, they were annealed at 95°C for 15 h under vacuum followed by slow cooling to room temperature. The annealed composites were repoled in order to ensure saturation poling of the PZT rods and then retested as described above.

RESULTS AND DISCUSSION

The dielectric and piezoelectric properties of the PZT/PS and PZT/PMMA composites are summarized in Table I. As expected, the composite dielectric constants (K_{33}) were considerably less than that of PZT ($K_{33} \approx 1600$). The value of K_{33} predicted by the simple parallel model for a 4% PZT/polymer, 1-3 composite is 64. The PZT/PS composites approached the theoretical value; however, the PZT/PMMA materials far exceeded the prediction. One possible explanation for this discrepancy may involve cracking or crazing of the PS matrix. Examination of unannealed PZT/PS composites under a light microscope revealed crazes (or cracks) emanating radially away from each rod into the PS matrix at the electrode surface. No such cracks were observed in PZT/PMMA samples. Since applied compressive stress is known to increase the dielectric constant of PZT,¹⁰ one would expect K_{33} of the PZT/PS composites to be less than K_{33} of the PZT/PMMA materials if the cracks acted to relieve interfacial compressive stresses.

The presence of internal stresses in these composites is further supported by the decrease in the dielectric constant after they were annealed. If the annealing process acts to relieve some radial compression between the rods and the matrix, then the dielectric constant would be expected to be lower than the K_{33} before annealing. Presumably, the radial stresses resulted from thermal expansion mismatches, mechanical processing (cutting and polishing), or polymerization shrinkage.

The simple Skinner et al. model predicts that the \bar{d}_{33} for composites with matrices of the same stiffness should be the same. Since PS and PMMA have roughly the same elastic modulus ($\sim 3 \times 10^9$ N/m²), it is not surprising that \bar{d}_{33} is similar for both composite materials. However, the predicted \bar{d}_{33} values are three times greater than those observed. Clearly, transfer of applied stress from matrix to rods is more complex than allowed for by the simple parallel model. If the effective matrix region of influence on the rods is less than the total matrix

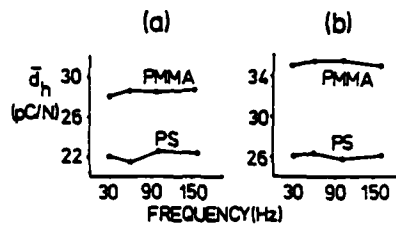


Fig. 2. Piezoelectric response of PZT/PS and PZT/PMMA composites as a function of frequency: (a) unannealed; (b) annealed.

area, then the amount of stress experienced by the rods would be less than predicted by the Skinner et al. model.⁶ This would act to decrease \bar{d}_{33} relative to the predicted value.

The standard deviations of \bar{d}_{33} values obtained from a d_{33} -meter using rounded probes gives an indication of the relative piezoelectric homogeneity of the composites. For the composites tested here the standard deviations of the \bar{d}_{33} measurements were similar. Again, considering that the matrices used in this work have similar mechanical properties, this result is not unexpected.

The hydrostatic piezoelectric coefficients (\bar{d}_h) reported in Table I are smaller than those of PZT but similar to that observed by Lynn⁹ for the PZT/epoxy system. The voltage coefficients are roughly an order of magnitude larger than PZT because the permittivities of the composites are much lower than the values for PZT alone. This results in $\bar{d}_h \bar{g}_h$ being significantly larger than that of PZT and comparable to that of PVDF. Also, no frequency dependence of \bar{d}_h was observed from 30 to 160 Hz (Fig. 2). Annealing was found to improve the piezoelectric coefficients (especially \bar{g}_h) due to a significant decrease in K_{33} .

Composite densities are roughly 1.4 g/cm³ (calculated), which is considerably lower than the 7.8 g/cm³ of PZT. Low density materials provide better acoustic coupling to an aqueous environment than ones of high density. Therefore, these types of composites may be useful as shallow-water hydrophones or for medical ultrasound applications.

CONCLUSIONS

Composites of uniaxially oriented, continuous PZT rods embedded in polystyrene or poly(methyl methacrylate) matrices possess hydrostatic piezoelectric coefficients somewhat lower than that of homogeneous PZT. However, hydrostatic voltage coefficients for these materials are approximately an order of magnitude larger than the ceramic element. Enhancement of \bar{g}_h is primarily due to the reduction of K_{33} over PZT. Further enhancement of the piezoelectric response can be accomplished by annealing which further reduces K_{33} . The \bar{d}_{33} values and the standard deviation of the d_{33} measurements are similar for both types of composites. Predictions of the composite piezoelectric coefficients based on the Skinner et al. model are qualitatively correct but quantitatively overestimated.

The authors would like to thank the Office of Naval Research for partial support of this work through contract N00014-82-K-0339. We would also like to thank Drs. R. E. Newnham and L. E. Cross for stimulating our interest in this subject.

References

1. R. E. Newnham, L. J. Bowen, K. A. Klicker, and L. E. Cross, *Mater. Eng.*, **2**, 93 (1980).
2. R. E. Newnham, D. P. Skinner, and L. E. Cross, *Mater. Res. Bull.*, **13**, 525 (1978).
3. K. A. Klicker, J. V. Biggers, and R. E. Newnham, *J. Am. Ceram. Soc.*, **64**, 5 (1981).
4. D. P. Skinner, R. E. Newnham, and L. E. Cross, *Mater. Res. Bull.*, **13**, 599 (1978).
5. M. Haun, M.S. thesis, The Pennsylvania State University, 1983.
6. K. A. Klicker, Ph.D. thesis, The Pennsylvania State University, 1980.
7. J. Selsing, *J. Am. Ceram. Soc.*, **44**, 419 (1961).
8. W. H. Haslett and F. J. McGarry, *Modern Plastics*, **40**, 135 (1962).
9. S. Y. Lynn, M.S. thesis, The Pennsylvania State University, 1981.
10. B. Jaffe, W. R. Cook, and H. Jaffe, *Piezoelectric Ceramics*, Academic, London, 1971.

Received April 27, 1983

Accepted July 28, 1983

COMPOSITE PIEZOELECTRIC SENSORS

R.E. Newnham, A. Safari, J. Giniewicz and B.H. Fox

COMPOSITE PIEZOELECTRIC SENSORS

R. E. NEWNHAM, A. SAFARI, J. GINIEWICZ and B. H. FOX

*Materials Research Laboratory, The Pennsylvania State University, University
Park, PA 16802*

Various types of composite piezoelectric transducers are reviewed with emphasis on the hydrophone figure of merit $d_h g_h$. Composites containing piezoceramic fibers, or skeletons in a polymer matrix, are superior to single-phase polymer or ceramic transducers.

INTRODUCTION

Lead zirconate titanate (PZT) is used extensively as a piezoelectric transducer material, but suffers from several disadvantages when used as a sensor of hydrostatic pressure waves. The hydrostatic piezoelectric coefficient $d_h (= d_{33} + 2d_{31})$ of PZT is small because d_{33} and d_{31} differ in sign. The voltage coefficients $g_{33} (= d_{33}/\epsilon)$ and $g_h (= d_h/\epsilon)$ are also small because of its high permittivity ϵ .

To improve the magnitudes of d_h and g_h , we have fabricated a number of different diphasic composites made from polymers and PZT, utilizing the concept of phase connectivity (Figure 1). Based on these studies it is clear that in a composite, the electric flux pattern and the mechanical stress distribution together with the resulting physical and piezoelectric properties depend strongly on the manner in which the individual phases are interconnected. Composites of PZT and polymer with different connectivity patterns have been prepared in which the d_h and g_h coefficients are an order of magnitude larger than those of solid PZT. In addition, some of the composites have high mechanical compliances and low density, making it easier to obtain good impedance matching with water. The properties of some of these composites are summarized in Table I.

Connectivity¹ is the key feature in designing the microstructure of PZT-polymer composites. Each phase in a composite may be self-connected in zero, one, two, or three dimensions. Using an orthogonal axis system, for diphasic composites, there are ten connectivities designated as 0-0, 1-0, 2-0, 3-0, 1-1, 2-1, 3-1, 2-2, 3-2, and 3-3. A 2-1 connectivity pattern, for example, has one phase self-connected in two dimensional layers, the other self-connected in one dimensional chains or fibers. The connectivity patterns are not geometrically unique. In the case of 2-1 patterns, the fibers of the second phase might be perpendicular to the layers of the first phase or might be parallel to the layers. In the notation used here, the piezoelectric phase appears first. Thus a 1-3 composite consists of PZT fibers embedded in a polymer matrix, and a 3-1 composite is a solid piece of PZT with parallel holes filled with polymer.

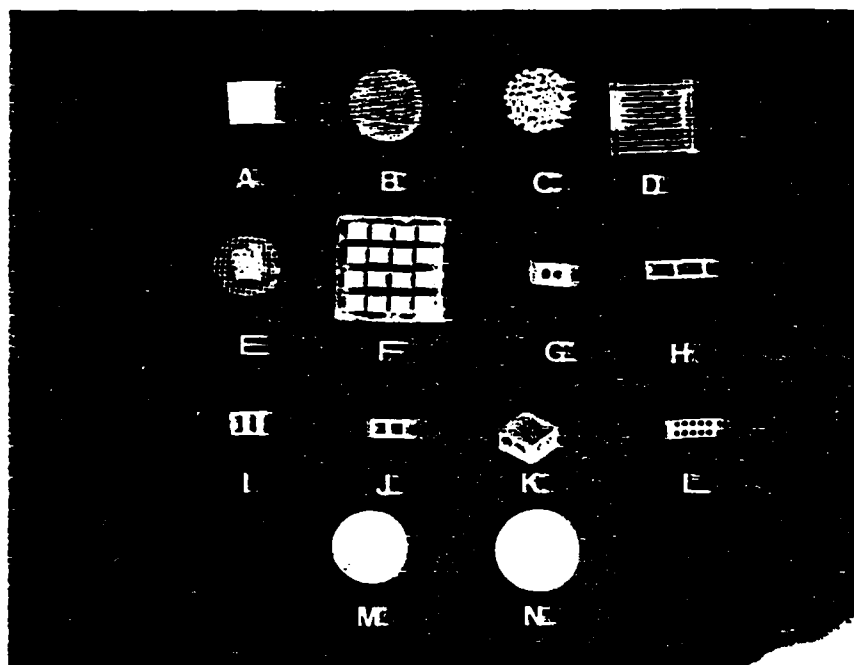


FIGURE 1 A selection of the various composite types produced in the recent past: (A) Lead titanate composite (0-3), (B) PZT rods-spurrs epoxy composite (1-3), (C) PZT spheres-polymer composite (1-3), (D) PZT tape laminate composite (2-2), (E) Honeycomb configuration PZT-polymer composite (3-1), (F) Array of perforated PZT composites (3-1), (G), (H), (I), and (J) Perforated PZT-polymer with 3-1 connectivity, (K) Perforated PZT-polymer with 3-2 connectivity, (L) Perforated PZT composite with 2 perforated layers, (M) Replamine composite with 3-3 connectivity and (N) Burps composite with 3-3 connectivity.

PIEZOELECTRIC 3-3 COMPOSITES

In a 3-3 composite each of the constituent phases is continuously self-connected in three dimensions to give two interlocking skeletons in intimate contact with one another. This type of structure is exhibited by certain polymer foams, by some phase-separated metals and glasses, by three-dimensional waves, and by natural substances such as wood and coral. The piezoelectric and pyroelectric properties of 3-3 composites have been investigated with some rather remarkable results. For certain coefficients, dramatic improvements can be made over the best single-phase piezoelectrics.

Piezoelectric ceramic-polymer composites with 3-3 connectivity were first made by Skinner² using a lost-wax method with coral as a starting material. Among the advantages of these composites are high hydrostatic sensitivity, low dielectric constant, low density for improved acoustic impedance matching with water, high compliance to provide damping, and the mechanical flexibility needed to develop conformable transducers. Shrouf³ developed a simpler method for fabricating a three-dimensionally interconnected lead zirconate-titanate (PZT) and polymer com-

posite with properties similar to the coral-based composites. The simplified preparation method involves mixing plastic spheres and PZT powder in an organic binder. When carefully sintered, a porous PZT skeleton is formed, and later back-filled with polymer to form a 3-3 composite. This technique is commonly referred to as the BURPS process, an acronym for burned-out plastic spheres. Since the process involves the generation and emission of gaseous hydrocarbons, the name BURPS is highly appropriate.

Recently⁴ we measured the electromechanical properties of 3-3 composites having a wide range of PZT/polymer ratios, and compared the results with other piezoelectric materials, including some earlier Japanese work^{5,6} on similar composites. Dielectric and piezoelectric properties were measured on samples ranging from 30 to 70 volume % PZT, and compared with a rectangular skeleton model for 3-3 composites. Composites containing 50% PZT-50% silicone rubber appear especially useful for hydrophone applications with $d_h g_h$ products a hundred times larger than PZT.

Further studies of porous PZT were reported last year at the International Symposium on Applications of Ferroelectrics.⁷ Scientists at Mitsubishi Mining and Cement have developed several techniques for introducing connected porosity in PZT ceramics: reactive sintering, foaming agents, organic additives, and careful control of particle size and firing conditions. Measurements on unfilled ceramic skeletons with 60% interconnected porosity gave d_{33} coefficients near 150 pC/N and g_{33} coefficients of 0.15 Vm/N.

PERFORATED PZT-POLYMER COMPOSITES

Composites of PZT and polymer with 3-1 and 3-2 connectivity patterns have been fabricated⁸ by drilling holes in sintered PZT blocks and filling the holes with epoxy.

TABLE I

Representative dielectric and piezoelectric coefficients of important hydrophone component materials and composites. K = dielectric constant, d_{33} = linear piezoelectric charge coefficient (pC/N), g_h = hydrostatic voltage coefficient (mV-m/N), d_h = hydrostatic charge coefficient (pC/N), $g_h d_h$ = hydrostatic figure of merit ($\times 10^{-15}$ m²/N), all measurements 50 Hz, 25°C

Material	K	d_{33}	g_h	d_h	$g_h d_h$
Pb(Zr, Ti)O ₃ = PZT	1800	450	2.5	40	100
(CH ₂ CF ₂) _n = PVF ₂	12	20	100	11	1100
PbNb ₂ O ₆	225	85	35	65	2300
3-3 PZT-Epoxy	620	150	18	100	1800
3-3 PZT-Rubber	450	200	45	180	8100
3-2 PZT-Epoxy	410	320	55	200	11000
3-2-0 Hollow 3-2	400	380	65	230	15000
3-1 PZT-Epoxy	750	350	24	160	3800
3-1-0 Hollow 3-1	730	370	28	185	5300
1-3 PZT-Epoxy	70	150	50	30	1500
1-3-0 PZT-Epoxy-spheres	80	180	60	40	2400
1-3-0 Fcamed 1-3	75	200	135	85	10000
0-3 PZT-Rubber	40	60	40	15	600
0-3 PbTiO ₃ -Rubber	40	30	100	35	3500

The influence of hole size and volume fraction PZT on the hydrostatic properties of the composite was evaluated. By decoupling the piezoelectric d_{33} and d_{31} coefficients in the composite, the hydrostatic coefficients are greatly enhanced. On samples optimized for hydrophone performance, the dielectric constants of 3-1 and 3-2 composites are 600 and 300 respectively. For two typical composites, the piezoelectric coefficients d_h , g_h , and $g_h d_h$ for 3-1 composites are 160 (pC/N), $24 (\times 10^{-3} \text{ Vm/N})$, and $3800 (10^{-15} \text{ m}^2/\text{N})$ respectively, and the corresponding values for 3-2 composites are 200 (pC/N), $55 (10^{-3} \text{ Vm/N})$, and $11000 (10^{-15} \text{ m}^2/\text{N})$.

These composites are extremely rugged and show no pressure dependence. Similar composites can be made⁹ by extruding the ceramic rather than drilling. Composites with 3-1 connectivity were fabricated by impregnating an extruded, sintered honeycomb configuration of PZT with epoxy. The composites had lower density ($\approx 3000 \text{ Kg/m}^3$) and lower dielectric constant (≈ 400) than that of solid PZT. The maximum piezoelectric d_{33} coefficient of the composites was 350 pC/N, and the maximum hydrostatic d_h , 220 pC/N. g_h and $d_h g_h$ of the composites were an order of magnitude higher than that of solid PZT.

PIEZOELECTRIC COMPOSITES BASED ON 1-3 CONNECTIVITY

Composites in which the polymer phase is self-connected three-dimensionally and the piezoelectric ceramic is self-connected one-dimensionally were developed by Klicker.¹⁰ In a 1-3 composite, PZT rods are embedded in a continuous polymer matrix. Under the idealized situation in which the polymer phase is far more compliant than PZT, the stress on the polymer will be transferred to the PZT rods. The stress amplification on the PZT phase along with the reduced permittivity greatly enhances the piezoelectric voltage coefficient. To provide a better understanding of the composites, the piezoelectric properties were studied as a function of volume fraction PZT, rod diameter, and sample thickness.

The magnitude of the $d_h g_h$ product of 1-3 composites with PZT rods in polymer matrix is large, but far less than the theoretical value. Part of the reason is that the Poisson ratio of the polymer used is fairly high thus an internal stress exists which opposes the applied stress, and the stress amplification of a 1-3 connectivity model is greatly reduced. One way to reduce the Poisson ratio of a polymer is to introduce porosity into it. The fabrication of 1-3 composites with porous polyurethanes was developed by Klicker¹¹ who showed that porosity in the polyurethane matrix has a dramatic effect on d_h . Composites made with 4 volume % PZT rods 240 μm in diameter in a foamed polyurethane with 45% porosity had a $d_h g_h$ product close to $50,000 \times 10^{-15} \text{ m}^2/\text{N}$, which is more than an order of magnitude greater than the $d_h g_h$ product of composites with a non-porous epoxy matrix. But this porous polyurethane composite is very pressure dependent above 200 psi. Other types of 1-3-0 composites were studied by Lynn.¹² Porosity was introduced into different types of polymer matrix either by adding a foaming agent or by mixing commercial hollow glass spheres with the polymer. Using a foamed REN epoxy, composites with 4 volume % of 280 μm diameter rods showed a three-fold increase in d_h above the unfoamed REN Epoxy. When hollow glass spheres of an average diameter of 80 μm and 2 μm wall thickness were mixed in REN and Spurr's epoxy, d_h increased about

twice that of the plain epoxy composites. For all the composites with glass spheres, no pressure dependences were found, while in foamed REN epoxy composites, the pressure dependence remains a problem.

Transverse reinforcement is another technique used to enhance the hydrostatic piezoelectric coefficient.^{13,14} These composites were made by mounting two types of fibers in the polymer matrix: PZT rods parallel to the poling direction and stiff glass fibers in the two transverse directions. The glass fibers carry most of the transverse stress thereby decreasing d_{31} without appreciable reduction in d_{33} . Transversely reinforced composites have 1-2-3 connectivity, or 1-2-3-0 connectivity if the polymer matrix is foamed. In many of these polymer ceramic composites a coupling agent is required to achieve good stress transfer.

Savakus¹⁵ developed a simplified preparation technique for making composites with 1-3 connectivity pattern. Composite piezoelectric transducers have been constructed by partially dicing PZT ceramics and back-filling with epoxy. Composites containing 10 to 70 volume percent PZT were prepared with several different rod diameters. Measured dielectric constants ranged from 200 to 1000, longitudinal piezoelectric coefficients d_{33} from 200 to 350 pC/N, and hydrostatic piezoelectric coefficients d_h from 40 to 80 pC/N.

Another interesting variation on the 1-3 composite is the use of solid-porous-solid sandwiches of PZT.¹⁶ The g_h and $d_h g_h$ of these composites were about 0.3 Vm/N and 50×10^{-12} m²/N respectively.

COMPOSITES WITH 0-3 CONNECTIVITY

The simplest type of piezoelectric composite consists of a polymer matrix loaded with ceramic powder. Early attempts to fabricate flexible composites of piezoelectric ceramic particles and polymers were made by Kitayama,¹⁷ Pauer,¹⁸ and Harrison.¹⁹

This type of composite does not have the desirable stress concentration factor found in other connectivity patterns, so the hydrostatic figure of merit is not large. In many ways the 0-3 composite is similar to polyvinylidene fluoride (PVF₂). Both consist of a crystalline phase embedded in an amorphous matrix, and both are reasonably flexible.

An improved version of the 0-3 composite was synthesized by Safari.²⁰ Flexible piezoelectric composites made from PZT spheres and polymers with 0-3 connectivity were fabricated using several types of polymers. Two techniques were developed for making spheres 0.4 to 4 mm in diameter. The dielectric constant of the composites were 300-400 and the piezoelectric voltage coefficients g_{33} were $45-55 \times 10^{-3}$ Vm/N. The high frequency properties of the composites were measured in both the thickness and radial mode of resonance. The frequency constants and the coupling coefficients of the composites for the thickness mode of resonance are comparable with the corresponding values for PZT. Possible applications of the composites as band-pass filters have been developed.

But an even better suggestion has been put forward by Banno.²¹ Rather than using PZT as the ceramic filler, pure PbTiO₃ was employed because of its greater piezoelectric anisotropy. This type of 0-3 composite is capable of greater hydrostatic sensitivity than PVF₂, and although it is inferior to some of the other composites in $d_h g_h$, it is far easier to make.

CONTINUOUS POLING AND MUPPET DEVICES

Conventional poling methods are limited by the size of the power supply to dielectric thickness of 1 cm or less. For the continuous poling method²² there is no limit on length in the poling direction. The method utilizes the idea of gradually advancing thin PZT rods or ribbons past two electrical contacts maintained at the required potential difference. Electrical contact is achieved through conductive carbon foam attached to copper electrodes and it is not necessary to attach electrodes to the sample. It is important to note that thin PZT fibers pole easily relative to the solid ceramic because of the relaxed mechanical constraints on the PZT grains. In the devices to be described, an electric field 16–18 kV/cm was used to pole the rods to saturation at temperatures of only 80°C.

We are experimenting with composites in which pre-poled PZT fibers are arranged in other than a conventional 1-3 pattern. A triple-pillar composite with fibers oriented in three perpendicular directions is one such example.²³ This modified 3-3 sensor can be used as a polarization analyzer for acoustic waves in which the voltage signals from three orthogonal electrodes resolve the wave into its longitudinal component and two shear components.

Another example is an acoustic phase plate made by arranging pre-poled pieces in a selected target array. A simple type of annular phase plate was demonstrated by Farnow and Auld.²⁴ The pattern might conform, for instance, to the Fourier transform of the shape of an object, or perhaps the elements are phased to detect a target moving with a pre-selected speed and direction. We refer to these composites as MUPPETS, Multiply-Poled Piezoelectric Transducers. They come in as many odd shapes and sizes as the Muppet characters seen on television.

The DOFUSS (named for a comic strip dinosaur) is a composite device made from pre-poled PZT ribbon. By poling the ribbon parallel to its length, and later electroding the major faces of the ribbon, one obtains a shear sensor or generator based on piezoelectric coefficient d_{15} . For many perovskite crystals and ceramics, coefficient d_{15} is very large. DOFUSS is an acronym for D-One-Five (d_{15}) Ultrasonic Shear Sensor. A number of interesting MUPPET and DOFUSS devices are under study.

REFERENCES

1. R. E. Newnham, D. P. Skinner and L. E. Cross, *Mat. Res. Bull.*, **13**, 525 (1978).
2. D. P. Skinner, R. E. Newnham and L. E. Cross, *Mat. Res. Bull.*, **13**, 599–607 (1978).
3. T. R. Shrout, W. A. Schulze and J. V. Biggers, *Mat. Res. Bull.*, **14**, 1553 (1979).
4. K. Rittenmyer, T. R. Shrout and R. E. Newnham, *Ferroelectrics*, **41**, 189–195 (1982).
5. K. Nagata, H. Igarashi, K. Okazaki and R. C. Bradt, *Japan J. Appl. Phys.*, **19**, L37-L40 (1980).
6. M. Miyashita, K. Takano and T. Toda, *Ferroelectrics*, **28**, 397–401 (1980).
7. H. Hikita, K. Yamada, M. Nishioka and M. Ono, *Ferroelectrics*, **49**, 265–272 (1983).
8. A. Safari, R. E. Newnham, L. E. Cross and W. A. Schulze, *Ferroelectrics*, **41**, 197–205 (1982).
9. A. Safari, A. Halliyal, R. E. Newnham and I. M. Lachman, *Mat. Res. Bull.*, **17**, 301 (1982).
10. K. A. Klicker, *Ph. D. Thesis*, The Pennsylvania State University (1980).
11. K. A. Klicker, J. V. Biggers and R. E. Newnham, *J. Amer. Ceram. Soc.*, **64**, 5–9 (1982).
12. S. Y. Lynn, *M.S. Thesis*, The Pennsylvania State University (1982).
13. M. Haun, P. Moses, T. R. Gururaja and W. A. Schulze, *Ferroelectrics*, **49**, 259–264 (1983).
14. N. M. Shorrocks, M. E. Brown and R. W. Whitmore, *E.M.F. 5 Paper*, P1D35 (1983).
15. H. P. Savakus, K. A. Klicker and R. E. Newnham, *Mat. Res. Bull.*, **16**, 677–680 (1981).

16. Y-Q Zhuang, Y-G He, Q-C Xu, *Ferroelectrics*, **49**, 241-249 (1983).
17. T. Kitayama and S. Sugawara, *Rep. Prof. Gr. Inst. Elec. Comm. Eng. Japan*, CPM27-17 (1972).
18. L. A. Pauer, *IEEE Int. Conv. Rec.*, pp. 1-5 (1973).
19. W. B. Harrison, *Proc., Workshop on Sonar Transducer Materials*, Naval Res. Labs., p. 257 (1975).
20. A. Safari, A. Halliyal, L. J. Bowen and R. E. Newnham, *J. Amer. Ceram. Soc.*, **65**, 207-209 (1982).
21. H. Banno, *Ferroelectrics*, **50**, 329-338 (1983).
22. T. R. Gururaja, L. E. Cross and R. E. Newnham, *J. Amer. Ceram. Soc.*, **64**, C8-C9 (1982).
23. T. R. Gururaja, D. Christopher, R. E. Newnham, *Ferroelectrics*, **47**, 193-200 (1983).
24. S. A. Farnow and B. A. Auld, *Appl. Physics Lett.*, **25**, 681 (1974).

POLAR GLASS CERAMICS FOR SONAR TRANSDUCERS

R.Y. Ting, A. Halliyal and A.S. Bhalla

Polar glass ceramics for sonar transducers

R. Y. Ting

Underwater Sound Reference Detachment, Naval Research Laboratory, P. O. Box 8337, Orlando, Florida 32856

A. Halliyal and A. S. Bhalla

Materials Research Laboratory, The Pennsylvania State University, University Park, Pennsylvania 16802

(Received 10 January 1984; accepted for publication 21 February 1984)

Glass ceramics are shown in this study to be a new class of transduction materials for application in sonar transducers. It is found that glass ceramics of $Ba_2TiSi_2O_8$ have high hydrostatic voltage sensitivity, low dielectric loss, and low dielectric constant. These properties are also shown to be practically independent of pressure up to 35 MPa. The free-field voltage sensitivity of a glass-ceramic prototype hydrophone is higher than that based on a commonly used lead zirconate titanate ceramic element.

PACS numbers: 43.30.Yj, 43.88.Fx, 77.60.+v, 77.20.+y

Since the discovery of ferroelectric barium titanate ($BaTiO_3$) and lead zirconate titanate (PZT),^{1,2} ceramics have been rapidly replacing conventional piezoelectric crystals for hydrophone applications, and now PZT ceramics are used almost exclusively in the U.S. Navy's sonar transducers. However, PZT ceramics suffer several disadvantages: the values of their hydrostatic piezoelectric constants are relatively low, and dielectric constants very high. The density of these ceramics is also very high. Furthermore, PZT exhibits depoling or aging problems, commonly encountered in most ferromagnetic materials.³ Therefore, there has been a great deal of interest in recent years in developing new transduction materials that offer improved sensitivity and aging characteristics. Several different approaches such as PZT polymer composites⁴ and piezoelectric polymer⁵ have been investigated. Recently a new family of materials (polar glass ceramics) has been studied for pyroelectric and piezoelectric applications.⁶⁻¹¹ Glass ceramics containing the crystalline phases of Li_2SiO_3 , $Li_2Si_2O_5$, $Ba_2TiSi_2O_8$, $Ba_2TiGe_2O_8$, and $Li_2B_4O_7$ were shown to exhibit large pyroelectric responses comparable to those of respective single crystals. These materials also have low dielectric constant in the range of 10-20 and attractive piezoelectric properties. In this letter, grain-oriented $Ba_2TiSi_2O_8$ glass ceramics (BST) are proposed as new materials for potential applications in sonar transducers.

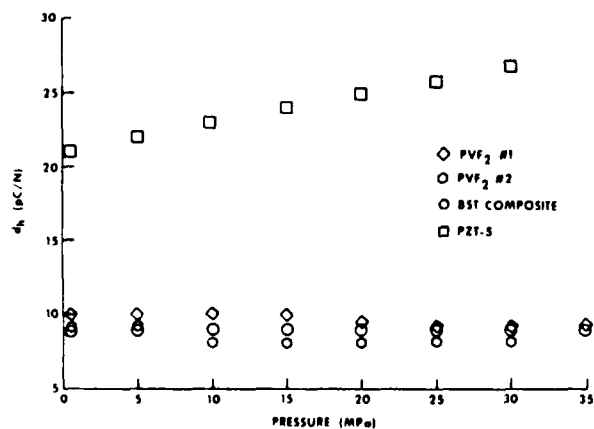


FIG. 1. Hydrostatic piezoelectric strain coefficient d_h as a function of pressure (at 24.5 °C).

Glass ceramic samples with oriented $Ba_2TiSi_2O_8$ crystallites were prepared by recrystallizing the glasses of compositions in the $BaO-TiO_2-SiO_2$ system in a temperature gradient. Detailed procedure for the preparation of glass ceramic samples was described in earlier references.⁶⁻¹¹ After the recrystallization of the glasses, oriented plates were cut normal to the temperature gradient and then polished to thickness ≈ 0.04 cm. Silver-paint electrodes were applied on both surfaces of each sample for testing. The piezoelectric and dielectric properties of the samples were characterized by using an acoustic reciprocity technique.¹² The theory of this calibration method has been well documented¹³ and will not be repeated here. The experiments were carried out in a castor-oil-filled acoustic coupler with temperature and pressure controlled to within ± 0.1 °C and ± 0.02 MPa, respectively, and a sinusoidal acoustic pressure applied at 1 kHz. The glass ceramic specimen was a circular disk approximately 1.2 cm in diameter and 0.04 cm thick. A PZT-5 sample, 1.3 cm in diameter and 0.6 cm thick, was tested as a reference. The properties of two commercially available piezoelectric polymer PVF_2 samples, obtained from two different sources, were also measured for comparison. Each PVF_2 sample was a 1.2×1.2 cm square piece. Their thicknesses were 0.056 and 0.070 cm, respectively.

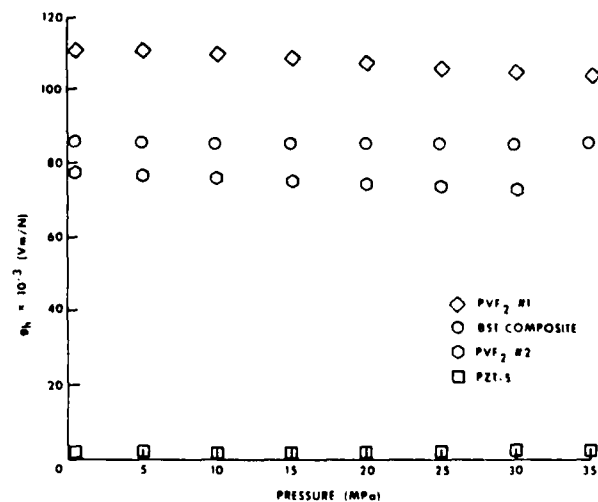


FIG. 2. Hydrostatic piezoelectric voltage coefficient g_h as a function of pressure (at 24.5 °C).

TABLE I. Properties^a of glass ceramic in comparison with those of PZT, PVF₂, and Li₂SO₄.

Property	PZT-5	PVF ₂ No. 1	PVF ₂ No. 2	Glass ceramic (Ba ₂ TiSi ₂ O ₈)	Li ₂ SO ₄ ^b
$D (\times 10^{-2})$	1.73	1.05	1.81	0.003-0.06	...
K_{33}^T	1688	10	12	12	10
d_h (pC/N)	21	10	9	9	14
$g_h (\times 10^{-3} \text{ Vm/N})$	1.5	112	78	83	148
Thickness (mm)	6	0.56	0.7	0.4	6.4
FFVS (dB re 1 V/ μ Pa)	-222	-202	-207	-211	-187

^a Measured at 1 kHz, 0.5 MPa, and 24.5 °C.

^b Data from Ref. 16.

The experiments were performed over the temperature range of 5–45 °C. A pressure cycle was carried out for each sample by increasing the static pressure in the coupler from ambient to 35 MPa at 5-MPa intervals, then followed with decreasing pressure at the same rate. During such a pressure cycle, the temperature of the system was carefully controlled at 24.5 °C.

The hydrophone characteristics of the glass ceramic sample were also evaluated in a prototype design using a standard NRL-USRD H23 oil filled hydrophone assembly. The element was placed in the H23 mount with a rubber window attached to the face. The device was tested at the NRL-USRD Lake Facility to obtain its free-field voltage sensitivity (FFVS) as a function of frequency.

Figure 1 shows the hydrostatic d constant¹⁴ of the materials tested as a function of pressure. The PZT-5 sample exhibited a d_h value of 21 pC/N at the ambient pressure, which also increased slowly with increasing pressure. The d_h values for both PVF₂ samples and the glass ceramic composite fall in the range of 9–10 pC/N. PVF₂ sample No. 1 showed a 1-dB reduction in d_h when the pressure was increased from 0.5 to 35 MPa, whereas the reduction for the PVF₂ sample No. 2 slightly exceeded 2 dB. The d_h of the glass ceramic material, however, was constant over the range of hydrostatic pressure of 0–35 MPa. During the decreasing portion of the pressure cycle, the d_h value also remained independent of pressure. This is in contrast to some ceramic polymer composites which showed very large pressure hysteresis effects.¹⁵ The piezoelectric voltage constant g_h of the glass ceramic material, shown in Fig. 2, was also found to be independent of pressure up to 35 MPa. The g_h value of 83×10^{-3} V m/N is an improvement over that of PZT-5 by nearly two orders of magnitude. PVF₂ sample No. 1 exhibited an initial g_h value of 112×10^{-3} V m/N which was decreased to 104×10^{-3} V m/N at 35 MPa, representing a reduction of 0.6 dB. PVF₂ sample No. 2 gave a g_h less than that of the

glass ceramic. It was also somewhat pressure sensitive; a 0.5-dB reduction was found at 35 MPa. The d_h and g_h properties of these materials were also measured at 0.5 MPa over the temperature range between 5 and 45 °C. The d_h value of the glass ceramic sample was independent of the test temperature, but g_h increased linearly with temperature by about 0.4 dB from 5 to 45 °C. The results on these samples are summarized in Table I.

The dielectric dissipation of these samples was also measured at 1 kHz. It can be seen from Table I that both the PZT and PVF₂ material have dissipation in the range of 0.01–0.02. But the glass ceramic samples have extremely low dissipation, varying from 0.00003 to 0.0006 depending on the sample composition. This would be very important if one would consider the material for active transduction applications.

The FFVS of the glass ceramic prototype hydrophone is shown in Fig. 3. A -211-dB sensitivity referenced to 1 V/ μ Pa was measured, and over the frequency range of 10–100 kHz, the response was reasonably flat. The PVF₂ elements gave a sensitivity of -202 and -207 dB, respectively. Although the FFVS of the glass ceramic is less than those of PVF₂, it should be noted that this sensitivity parameter depends on both the g_h constant of the material and the thickness of the sample. The thickness of the glass ceramic sample is only 0.04 cm, as compared to 0.056 and 0.070 cm for the PVF₂ samples. Because of the high voltage required for poling, the thickness of poled PVF₂ that can be fabricated will be severely limited. On the other hand, thick glass ceramics can be readily prepared by routine glass fabrication techniques, and the FFVS then can be easily increased. As is, the glass ceramic sample is more sensitive than the 0.6-cm-thick PZT-5, which gives a FFVS of -222 dB re 1 V/ μ Pa. Furthermore, the glass ceramics have low density (3–4 g/cc) and thus lower mechanical impedance compared to that of PZT ceramics.

Finally, it is noted that the properties of the glass ceramics are approaching those of lithium sulphate crystals (see Table I). Lithium sulphate has been used in underwater transducers, and is still a favorite piezoelectric material for use in many of the Navy's standard transducers. However, the availability of lithium sulphate from commercial sources has declined rapidly in recent years. The glass ceramic would be a good candidate for its replacement.

Arvind Halliyal and Amar S. Bhalla acknowledge the support of the National Science Foundation (grant No. DMR-8303906) for part of this work.

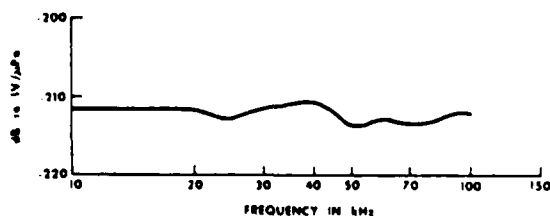


FIG. 3. Free-field voltage sensitivity (FFVS) of the glass ceramic hydrophone as a function of frequency (at 24.5 °C).

- ¹S. Roberts, *Phys. Rev.* 71, 890 (1947).
- ²B. Jaffe, R. S. Roth, and S. Marzullo, *J. Appl. Phys.* 25, 809 (1954).
- ³R. W. Timme, "Low Electrical Field Characteristics of Piezoelectric Ceramic Rings," NRL Report 7528, 1973.
- ⁴R. E. Newnham, L. J. Bowen, K. A. Klicker, and L. E. Cross, *Mater. Eng.* 2, 93 (1980).
- ⁵B. Woodward, *Acoustica* 38, 264 (1977).
- ⁶G. J. Gardopoe, R. E. Newnham, A. G. Halliyal, and A. S. Bhalla, *Appl. Phys. Lett.* 36, 817 (1980).
- ⁷G. J. Gardopoe, R. E. Newnham, and A. S. Bhalla, *Ferroelectrics* 33, 155 (1981).
- ⁸A. Halliyal, A. S. Bhalla, R. E. Newnham, and L. E. Cross, *J. Mater. Sci.* 16, 1023 (1981).
- ⁹A. Halliyal, A. S. Bhalla, R. E. Newnham, and L. E. Cross, *Ferroelectrics* 38, 871 (1981).
- ¹⁰A. Halliyal, A. S. Bhalla, R. E. Newnham, and L. E. Cross, *IEEE Ultrasonics Symposium* 1, 315 (1981).
- ¹¹A. Halliyal, A. S. Bhalla, R. E. Newnham, and L. E. Cross, *J. Appl. Phys.* 53, 2871 (1982).
- ¹²C. C. Sims and T. A. Henriquez, *J. Acoust. Soc. Am.* 36, 1704 (1964).
- ¹³R. J. Bobber, *Underwater Electroacoustic Measurements* (GPO, Washington, D.C., 1970), pp. 27-41.
- ¹⁴*IEEE Standard on Piezoelectricity*, IEEE Standards (IEEE, New York, 1978), p. 176.
- ¹⁵R. Y. Ting, *Ferroelectrics* 49, 251 (1983).
- ¹⁶T. A. Henriquez and L. E. Ivey, *J. Acoust. Soc. Am.* 47, 276 (1970).

GRAIN-ORIENTED GLASS-CERAMICS FOR PIEZOELECTRIC DEVICES

A. Halliyal, A. Safari, A.S. Bhalla, R.E. Newnham, and L.E. Cross

Grain-Oriented Glass-Ceramics for Piezoelectric Devices

A. HALLIYAL, A. SAFARI, A. S. BHALLA,* R. E. NEWNHAM,* and L. E. CROSS*

Materials Research Laboratory, The Pennsylvania State University, University Park, Pennsylvania 16802

Grain-oriented glass-ceramics of $\text{Li}_2\text{Si}_2\text{O}_7$, fresnoite ($\text{Ba}_2\text{TiSi}_2\text{O}_8$), and its isomorphs $\text{Sr}_2\text{TiSi}_2\text{O}_8$ and $\text{Ba}_2\text{TiGe}_2\text{O}_8$, were prepared by recrystallizing glasses in a temperature gradient. Electromechanical and hydrostatic piezoelectric properties of these glass-ceramics were measured. Piezoelectric voltage coefficients g_{33} and hydrostatic voltage coefficient g_h of these glass-ceramics are comparable to those of polyvinylidene fluoride and an order of magnitude higher than the corresponding values of lead zirconate-titanate. These glass-ceramics seem to be attractive candidate materials for hydrophones and several piezoelectric devices. Hydrostatic piezoelectric properties of $\text{Ba}_2\text{TiSi}_2\text{O}_8$ and $\text{Ba}_2\text{TiGe}_2\text{O}_8$ single crystals were also measured. The unusually high values of g_h in fresnoite single crystals and glass-ceramics are supposed to be due to positive d_{31} in these materials. A composite model is proposed to explain the positive sign of d_{31} in fresnoite based on its crystal structure and internal Poisson's ratio stress.

I. Introduction

A WIDE range of ferroelectric materials is available at present in a single-crystal or ceramic form for use in piezoelectric and pyroelectric devices. In the polycrystalline ceramic form, the polar axes in individual crystallites are randomly oriented. An essential feature of the ferroelectric ceramics which makes them usable for piezoelectric and pyroelectric applications is the ability to reorient the polar axis in individual crystallites under a high electric field so as to impart a long-range remnant polar order. In polar but nonferroelectric ceramics this orientability is not present, so that randomly axed ceramics of these materials have no piezoelectric or pyroelectric properties and thus they are of no use in this area. Since many of the nonferroelectric materials have interesting properties in single-crystal form, e.g., quartz which is the basic resonant time standard, an exploration of processing techniques which might be used to impart a polar texture during the formation of an ensemble of crystallites could be most interesting.

Glass-ceramics as a class of materials have several properties quite different from both single crystals and conventionally sintered ceramics. Because of their special characteristics, glass-ceramics may offer some advantages in the fabrication of piezoelectric and pyroelectric devices. Even though glass-ceramics are used extensively in electronic industry, not much attention seems to have been paid to developing glass-ceramics for piezoelectric and pyroelectric devices. Recently a new technique for preparing glass-ceramics with oriented crystallites was studied extensively.¹⁻⁵ In this technique, glasses are recrystallized in a temperature gradient. It was shown in earlier studies that the technique is suitable for preparing inexpensive, large-area pyroelectric detectors and piezoelectric resonators. Using this method, we have prepared glass-ceramics with both crystallographic and polar orientation.

The glass-forming systems studied include $\text{Li}_2\text{O-SiO}_2$, $\text{Li}_2\text{O-SiO}_2\text{-B}_2\text{O}_3$, $\text{BaO-SiO}_2\text{-TiO}_2$, $\text{SrO-SiO}_2\text{-TiO}_2$, and $\text{BaO-GeO}_2\text{-TiO}_2$. Among the crystalline phases recrystallized from the glasses within these systems are $\text{Li}_2\text{Si}_2\text{O}_7$, $\text{Li}_2\text{B}_4\text{O}_7$, $\text{Ba}_2\text{TiSi}_2\text{O}_8$, $\text{Sr}_2\text{TiSi}_2\text{O}_8$, and $\text{Ba}_2\text{TiGe}_2\text{O}_8$. One or more of these crystalline phases are obtained, depending on the composition of the glasses. All of these crystalline phases are nonferroelectric and belong to one of the ten polar point groups. The compositions of the glasses

were optimized by compositional variations and by the addition of various modifying oxides to obtain glass-ceramics with good physical properties. Extensive studies have been carried out to optimize the piezoelectric and pyroelectric properties of the glass-ceramics by adjusting the composition of the glasses and the crystallization conditions.¹⁻⁵

It has also been shown that the polar growth behavior of the crystallites from the glass matrix depends on the original composition of the glass. A glass-ceramic is essentially a composite of a glassy phase and one or more crystalline phases. For glass-ceramics containing two crystalline phases, a connectivity model has been developed⁶ based on the principles of series and parallel connectivity models^{6,7} to predict the piezoelectric and pyroelectric properties of glass-ceramic composites.

In the present study, the hydrostatic piezoelectric properties of glass-ceramics of fresnoite ($\text{Ba}_2\text{TiSi}_2\text{O}_8$) and its isomorphs $\text{Sr}_2\text{TiSi}_2\text{O}_8$ and $\text{Ba}_2\text{TiGe}_2\text{O}_8$ are reported. These glass-ceramics offer several advantages for hydrophone applications, as will be discussed in a later section. The hydrostatic piezoelectric properties of $\text{Ba}_2\text{TiSi}_2\text{O}_8$ and $\text{Ba}_2\text{TiGe}_2\text{O}_8$ single crystals were also measured. The hydrostatic piezoelectric coefficient d_h , hydrostatic voltage coefficient g_h , and acoustic impedances of these materials are compared with commonly used piezoelectric materials like lead zirconate titanate (PZT) and polyvinylidene fluoride ($(\text{CH}_2\text{F}_2)_n = \text{PVF}_2$). The advantages of these materials for application in piezoelectric devices are discussed. Finally, a simplified model based on the principles of series and parallel mixing of phases⁶ is proposed to explain the high value of g_h in fresnoite single crystals and glass-ceramics.

II. Experimental Procedure

Glasses of several different compositions were prepared by mixing reagent-grade chemicals and melting them in a platinum crucible. Glass-ceramic samples (approximately 1 cm in diameter) with oriented crystallites were prepared by recrystallizing the glasses in a strong temperature gradient. The details of the sample preparation technique can be found in Refs. 1 to 5. X-ray diffraction and microstructure studies indicated that needlelike crystals grow from the surface into the bulk of the sample along the direction of temperature gradient.

For piezoelectric and hydrostatic measurements, sections were cut normal to the temperature gradient, then polished and coated with sputtered gold electrodes. The finished samples were approximately 1 cm in diameter and 0.5 mm thick.

The dielectric constant (K) and loss factors of the samples were measured at a frequency of 1 kHz using an automated capacitance bridge.* The piezoelectric d_{33} coefficient was measured with a d_{33} meter.† The hydrostatic voltage coefficient g_h was measured by a dynamic method⁸ which is basically a comparative technique. In this method, a PZT 501A sample of known g_h is used as a standard. After the sample and the standard are placed in the holder, the chamber is filled with oil and a static pressure is applied. A function generator set to the desired frequency drives an ac stress generator placed inside the test chamber. The voltage produced by the sample is displayed on an oscilloscope and compared to the voltage produced by the standard. By knowing the voltage responses and the dimensions of the sample and the standard, we can calculate the piezoelectric voltage coefficient g_h of the sample. Corrections were made for the stray capacitance of

Received July 18, 1983; revised copy received January 23, 1984; approved January 30, 1984.

*Member, the American Ceramic Society.

*Model 4270A, Hewlett-Packard, Inc., Palo Alto, CA.

†Model CPDT 3300, Channel Products, Chesterland, OH.

Table I. Compositions and Crystalline Phases

Composition	Crystallization Temp. (°C)	Crystalline phases
2BaO-3SiO ₂ -TiO ₂	930	Ba ₂ TiSi ₂ O ₈
(1.9BaO-0.1PbO)-3SiO ₂ -TiO ₂	920	Ba ₂ TiSi ₂ O ₈
2BaO-0.15CaO-2.9SiO ₂ -TiO ₂	920	Ba ₂ TiSi ₂ O ₈
1.6BaO-0.4CaO-2.8SiO ₂ -TiO ₂	930	Ba ₂ TiSi ₂ O ₈
1.6BaO-0.4SrO-3SiO ₂ -TiO ₂ -0.2CaO	930	Ba ₂ TiSi ₂ O ₈
2SrO-3SiO ₂ -TiO ₂	950	Sr ₂ TiSi ₂ O ₈
(1.8SrO-0.2BaO)-2.8SiO ₂ -TiO ₂ -0.1CaO	940	Sr ₂ TiSi ₂ O ₈
BaO-GeO ₂ -TiO ₂	800	Ba ₂ TiGe ₂ O ₈
Li ₂ O-1.8SiO ₂ -0.2B ₂ O ₃	605 680	Li ₂ Si ₂ O ₅ + Li ₂ B ₄ O ₇ + Li ₇ Si ₃

Table II. Electromechanical Properties

Composition	k ₃ (%)	k ₁ (%)	Q	Temp. coeff. of resonance (radial) (ppm/°C)
Li ₂ O-1.8SiO ₂ -0.2B ₂ O ₃	15	20-25	1000-2000	70-100
2BaO-3SiO ₂ -TiO ₂	14	20-25	1000-2000	100-120
BaO-TiO ₂ -GeO ₂	6	8-10	2000-4000	60
2SrO-3SiO ₂ -TiO ₂	11	25-30	1000-1500	50

the sample holder. From the measured values of d_{33} , g_h , and K , the piezoelectric voltage coefficient $g_{33} = d_{33}/\epsilon_0 K$ and hydrostatic piezoelectric coefficient $d_h = g_h \epsilon_0 K$ were calculated. The electromechanical properties were measured by a resonance-antiresonance technique using a spectrum analyzer.²

Single crystals (1 cm in diameter) of Ba₂TiSi₂O₈ and Ba₂TiGe₂O₈ were grown from the stoichiometric melts by the Czochralski method. Details concerning the growth procedure can be found in Refs. 9 to 11.

III. Results and Discussion

(1) Compositions and Crystalline Phases

The compositions and crystalline phases of the glass-ceramics are listed in Table I along with their crystallization temperatures determined from exothermic peaks in DTA runs.

It was not possible to obtain glass-ceramics with reasonable mechanical strength from a stoichiometric fiesonite glass composition (2BaO-2SiO₂-TiO₂). The glass composition giving glass-ceramics with good physical properties and optimized piezoelectric and pyroelectric properties was 2BaO-3SiO₂-TiO₂. Additions of a small percentage of PbO, CaO, and SrO helped in obtaining glass-ceramics with uniform crystallization and good mechan-

ical strength. Similarly, the optimized glass compositions for Sr₂TiSi₂O₈ and Ba₂TiGe₂O₈ phases were 2SrO-3SiO₂-TiO₂ and BaO-GeO₂-TiO₂, respectively. The optimized composition in the system Li₂O-SiO₂-B₂O₃ was Li₂O-1.8SiO₂-0.2B₂O₃. Crystallization temperatures of the glasses ranged from 600° to 950°C. The crystalline phases of all the glass compositions are also listed in Table I.

(2) Electromechanical Properties

A summary of electromechanical properties of optimized glass-ceramics is given in Table II. Values of the temperature coefficient of resonance, measured by studying the variation of resonance frequency with temperature for the radial mode, are also listed in the table. The possibility of tailoring the electromechanical properties by varying the composition and heat treatment make these glass-ceramics attractive candidate materials for piezoelectric devices. The temperature variation of resonance frequencies can be further reduced by suitably modifying the composition of the glasses.⁵

(3) Hydrostatic Measurements

The measured values of the dielectric constant, d_{33} , and g_h are listed in Table III, along with the calculated values of g_{33} , d_h , and $d_h g_h$. The properties of Ba₂TiSi₂O₈ and Ba₂TiGe₂O₈ single crystals are also presented in the table. A comparison of the dielectric and hydrostatic properties of glass-ceramics with the corresponding properties of PVF₂ and PZT 501A is given in Table IV. The values of g_h and $d_h g_h$ of glass-ceramics are comparable to PVF₂ and much higher than PZT. Although the values of d_{33} and d_h of glass-ceramics are comparatively low, the magnitudes of g_{33} and g_h are high because of their low dielectric constant.⁴⁻¹⁰ A discussion of the advantages of these glass-ceramics in hydrophone applications is given in Section III(5).

(4) Acoustic Impedance

Acoustic impedance Z can be calculated from the relation $Z = \rho c$, where ρ is the density of the material and c is the velocity of sound in the medium. By measuring the thickness mode frequency constant N_t of the material, the velocity c can be calculated by the relation $c = 2N_t$. The values of density, velocity, and acoustic impedance are listed in Table V. The corresponding properties of PZT, PVF₂, and a number of commonly used materials are also listed in the table for comparison. A discussion of these properties is presented in the next section.

(5) Application in Hydrophones

A hydrophone is a passive device used as a hydrostatic pressure sensor. For hydrophone applications, the commonly used figures of merit are the hydrostatic piezoelectric coefficient g_h and the product $d_h g_h$. For hydrophone applications, the desirable properties of a transducer material are (1) high d_h and g_h ; (2) a density suited for acoustic matching with the pressure-transmitting medium, usually water; (3) high compliance and flexibility such that the transducer can withstand mechanical shock, and can conform to any surface; and (4) no variation of g_h with pressure.

PZT ceramics are used extensively as piezoelectric transducers despite having several disadvantages. The values of g_h and $d_h g_h$ of

²Model 3585A, Hewlett-Packard, Inc., Loveland, CO.

Table III. Hydrostatic Measurements

Composition	K	d_{33} (pC/N)	g_{33} (10 ⁻³ V·m/N)	g_h (10 ⁻³ V·m/N)	d_h (pC/N)	$d_h g_h$ (10 ⁻³ m ² /N)
2BaO-3SiO ₂ -TiO ₂	9	7	38	110	3.8	970
(1.9BaO-0.1PbO)-3SiO ₂ -TiO ₂	10	7	80	110	9.7	1070
2BaO-0.15CaO-2.9SiO ₂ -TiO ₂	10	6	68	75	6.6	500
1.6BaO-0.4CaO-2.8SiO ₂ -TiO ₂	10.5	6	65	35	7.9	670
1.6BaO-0.4SrO-3SiO ₂ -TiO ₂ -0.2CaO	9.3	6	70	100	3.7	370
2SrO-3SiO ₂ -TiO ₂	11.5	14	138	35	3.7	740
(1.8SrO-0.2BaO)-2.8SiO ₂ -0.1CaO-TiO ₂	10.6	10	107	100	9.4	940
BaO-GeO ₂ -TiO ₂	15	6	45	70	9.3	650
Ba ₂ TiSi ₂ O ₈ (single crystal)	11	3	32	130	12.7	1650
Ba ₂ TiGe ₂ O ₈ (single crystal)	11.4	3	30	120	12.1	1450

PZT are low because of its high dielectric constant (≈ 1800). In addition, the high density of PZT ($\approx 7900 \text{ kg/m}^3$) makes it difficult to obtain good impedance matching with water. PZT is also a brittle ceramic and, for hydrophone applications, a more compliant material with better shock resistance would be desirable.

PVF₂ offers several advantages over PZT ceramic for hydrophone applications. It has a low density (1760 kg/m^3), is a flexible material, and, although it has low d_{33} and d_{31} , its dielectric constant is low enough that large values of piezoelectric voltage coefficients g_{33} and g_h are possible. Overall, this combination of properties seems to be very attractive and PVF₂ transducers are under intensive development.¹² However, a major problem in the use of PVF₂ is the difficulty in poling PVF₂ sheets. A very high voltage is necessary to pole PVF₂ (about 10 to 100 MV/m) and this puts a limitation on the thickness of PVF₂ that can be poled.

To overcome these problems, a number of composites of PZT and polymer have been studied in recent years. A detailed description of different kinds of composites and the principles involved can be found in Ref. 13. In a composite, the polymer phase lowers density and dielectric constant and increases elastic compliance. Very high values of g_h and d_{hg} have been achieved with the composite approach.

From Table IV, it is clear that the piezoelectric coefficients d_{33} and d_h of glass-ceramics are comparable to PVF₂, but much lower than that of PZT. However, because of the low dielectric constant of glass-ceramics, the values of g_{33} and g_h of glass-ceramics are much higher than for PZT. Hence, these glass-ceramics will be useful in passive devices like hydrostatic pressure sensors where g_h is more important. The variation of g_h with pressure was measured for glass-ceramics up to 8 MPa. There was no significant variation of g_h with pressure. In practical use, glass-ceramics may offer several advantages over PVF₂ and other ferroelectric materials for application in piezoelectric devices.

Since all these glass-ceramics are nonferroelectric, there is no poling step involved, which is a major problem with PVF₂. There will be no problem of depoling or aging which are encountered in many ferroelectric materials. Hence, the glass-ceramics can be used in devices operating at high temperatures. Large-area devices can be prepared by routine glass-preparation techniques, and hence the cost of the device can be significantly lowered. Since acoustic impedances of the glass-ceramics are in the range 18 to 20×10^9 rayls, good acoustic matching can be obtained with metals like aluminum. Nondestructive testing of aircraft metals over a wide temperature range is a possibility. These glass-ceramics also look attractive for use in devices in which glass fibers are used because of the good impedance matching.

IV. Explanation for the High Value of g_h in Ba₂TiSi₂O₈

The g_h values of Ba₂TiSi₂O₈ and Ba₂TiGe₂O₈ single crystals and glass-ceramics are unusually large compared to other piezoelectric materials. An explanation is offered here for the high value of g_h based on the crystal structure of fresnoite and an internal Poisson ratio stress.

The hydrostatic piezoelectric coefficient d_h is given by the equation

$$d_h = d_{33} - 2d_{31} \tag{1}$$

For PZT, the piezoelectric d_{33} coefficient is large ($\approx 450 \text{ pC/N}$), but d_h is low because the sign of d_{33} is positive and that of d_{31} is negative ($\approx -205 \text{ pC/N}$). Moreover, its high dielectric constant (≈ 1800) further reduces the voltage coefficients g_{33} and g_h (Table III). On the other hand, for fresnoite, even though d_{33} is low, d_h is slightly larger than d_{33} because of positive d_{31} . In addition, because the dielectric constant of fresnoite is very low (≈ 10), the value of g_h becomes exceptionally high. An explanation of the positive sign of d_{31} is given in Section IV(2) by considering the crystal structure of Ba₂TiSi₂O₈.

(1) Composite Model

For a composite consisting of two phases, one-dimensional solutions for dielectric and piezoelectric properties have been presented

Table IV. Comparison of Hydrostatic Properties

Property	Glass-ceramics	PVF ₂	PZT
K	10	13	1800
d_{33} (10^{-12} C/N)	8-10	30	450
d_{31} (10^{-12} C/N)	1.5	-18	-205
d_h (10^{-12} C/N)	8-10	10	40
g_{33} ($10^{-3} \text{ V}\cdot\text{m/N}$)	100	250	28
g_h ($10^{-3} \text{ V}\cdot\text{m/N}$)	100	100	2.5
$d_h g_h$ ($10^{-15} \text{ m}^2/\text{N}$)	1000	900	100

Table V. Comparison of Acoustic Impedances

Medium	Density (kg/m ³)	Velocity (m/s)	$Z \times 10^{-9}$ (kg/m ² ·s)*
Air	1.2	330	0.0004
Water	1000	1480	1.5
Lead zirconate-titanate	7600	4000	30
Polyvinylidene fluoride	1760	1450	2-3
Aluminum	2700	6300	17
Quartz	2640	5800	15.2
BaO-SiO ₂ -TiO ₂	4000	4700	18-20
BaO-GeO ₂ -TiO ₂	4780	5020	24
SrO-SiO ₂ -TiO ₂	3600	5000	18

*kg/m²·s = rayl.

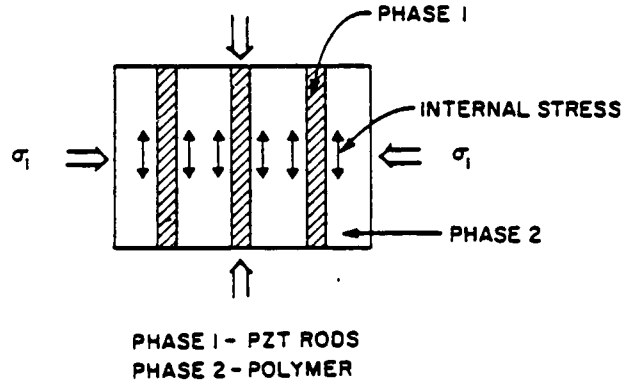


Fig. 1. Internal stress in composite of PZT fibers and polymer.

for both series and parallel connectivity.^{6,7} In a number of composites it has been shown, both theoretically and experimentally, that the hydrostatic piezoelectric coefficients d_h and g_h can be increased by an order of magnitude over that of single-phase PZT. Even though PZT-polymer composites are superior to single-phase piezoelectric materials, some of the composites were not as sensitive as expected theoretically. The reason for this is an internal stress arising from Poisson's ratio. As an example, consider the internal stress in composites prepared from PZT fibers and a stiff polymer.

In a 1-3 PZT-polymer composite (Fig. 1), the PZT fibers are aligned along the polar axis x_3 , and the polymer matrix phase is self-connected in all three directions. Further, the PZT and polymer phases are connected in series along x_1 and x_2 and in parallel along x_3 . Since the two phases are in series along x_1 and x_2 , they experience the same stress σ_1 . This assumes that the two phases do not exert forces on one another and hence internal stresses are zero. This assumption is not justified for composites with a small volume fraction of PZT, where interphase stress must be considered. Thus there are two contributions to d_{31} of composite: those arising from external stress σ_1 and those arising from internal stress. In the equations which follow, the piezoelectric coefficient d_{31} , volume fraction V , elastic compliances s_{11} and s_{33} , and Poisson's ratio ν

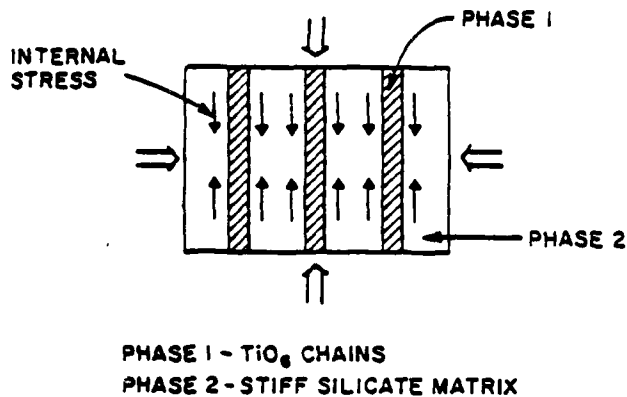


Fig. 2. Composite model for $\text{Ba}_2\text{TiSi}_2\text{O}_9$.

of PZT and polymer are designated with a superscript 1 and 2, respectively.

Considering only the external stress σ_1 , the polarization P_3 appearing in the polar direction is given by the following equation

$$P_3 = d_{31}\sigma_1 = {}^1V^1d_{31}'\sigma_1 \quad (2)$$

However, if internal stress is considered, a correction factor should be applied. This correction arises from Poisson's ratio and will be referred to as the Poisson's ratio stress.

When the composite is stretched along x_1 , it contracts along x_3 because of Poisson's ratio. This contraction is controlled by the compliance and Poisson's ratio. If the two constituent phases do not contract equally, an internal stress is generated. The magnitude of the internal stress can be estimated by assuming that the two phases remain mated together, or that the strains are equal along x_3 ($\epsilon_3^1 = \epsilon_3^2$). For simplicity it is assumed that both the phases are elastically isotropic ($s_{11} = s_{33}$). Under these assumptions, it can be shown that the internal stress on PZT phase (σ_3') is given by

$$\sigma_3' = \sigma_1 \frac{{}^1\nu^1 s_{11} - {}^2\nu^2 s_{11}}{s_{11} + ({}^1V/{}^2V)^2 s_{11}} \quad (3)$$

Since the polymer phase is generally far more compliant than PZT, ${}^2s_{11} \gg {}^1s_{11}$, whereas the Poisson's ratios are comparable. Equation (3) then reduces to

$$\sigma_3' = \frac{-{}^2\nu^2 s_{11} \sigma_1}{s_{11} + ({}^1V/{}^2V)^2 s_{11}} \quad (4)$$

The minus sign indicates that the internal Poisson's ratio stress acts oppositely to the applied stress. That is, when a tensile stress σ_1 is applied the internal stress σ_3' acting on PZT is compressive, and vice versa. The internal stress σ_3' produces a piezoelectric effect by coupling through coefficient d_{33} . If both the external stress σ_1 and the internal stress σ_3' are acting, the polarization along x_3 is given by

$$P_3 = {}^1V^1d_{31}'\sigma_1 + {}^1V^1d_{33}'\sigma_3' \quad (5)$$

The first term on the right is the normal stress contribution and the second term is due to Poisson's ratio stress. Coefficient d_{31} of the composite is given by

$$\bar{d}_{31} = \frac{P_3}{\sigma_1} = \frac{{}^1V^1d_{31}'\sigma_1 + {}^1V^1d_{33}'\sigma_3'}{\sigma_1} \quad (6)$$

It is clear from Eq. (6) that \bar{d}_{31} is greatly increased due to the internal Poisson ratio stress. Therefore, there will be a reduction in the magnitude of d_h (Eq. (1)), lessening hydrostatic piezoelectric sensitivity of the composite.

(2) Positive d_{31} in Fresnoite

The arguments concerning internal Poisson's ratio stress can be used to explain the positive sign of d_{31} in $\text{Ba}_2\text{TiSi}_2\text{O}_9$ single crys-

als, based on a knowledge of its crystal structure.

The $\text{Ba}_2\text{TiSi}_2\text{O}_9$ structure consists of $(\text{Si}_2\text{O}_7)^{4-}$ tetrahedral pairs and $(\text{TiO}_6)^{2-}$ square pyramids which are linked to give flat sheets parallel to $\{001\}$ planes.¹⁶ These sheets are bonded together by Ba^{2+} ions. The structure can be visualized as made up of chains of deformed TiO_6 octahedra linked together by a stiff silicate matrix. In the following discussion, the structure will be considered as a composite of two phases: a piezoelectric phase consisting of TiO_6 chains (phase 1) and a stiff silicate matrix which is nonpiezoelectric (phase 2), as shown in Fig. 2. All the properties with a superscript 1 and 2 refer to phases 1 and 2, respectively. Again for simplicity, elastic isotropy ($s_{33} = s_{11}$) is assumed and Poisson's ratios of phases 1 and 2 are assumed to be comparable. Further, it is assumed that the piezoelectric phase 1 is much more compliant than phase 2, so that

$${}^1s_{33} \approx {}^1s_{11} \gg {}^2s_{33} \approx {}^2s_{11} \quad (7)$$

and

$${}^1\nu \approx {}^2\nu \quad (8)$$

Under these assumptions, the internal stress due to Poisson's ratio, given by Eq. (3), reduces to

$$\sigma_3' = {}^1\nu\sigma_1 \quad (9)$$

The polarization along x_3 , due to both external and internal stresses, is given by

$$\begin{aligned} P_3 &= {}^1V^1d_{31}'\sigma_1 + {}^1V^1d_{33}'\sigma_3' \\ &= {}^1V({}^1d_{31} + {}^1\nu^1d_{33})\sigma_1 \end{aligned} \quad (10)$$

Hence d_{31} of the composite is given by

$$\bar{d}_{31} = ({}^1d_{31} + {}^1\nu^1d_{33})^1V \quad (11)$$

It is clear that \bar{d}_{31} of the composite can be positive if ${}^1\nu^1d_{33} > {}^1d_{31}$. If the preceding argument is true, the sign of d_{31} in fresnoite should be positive, but its magnitude should be very small. The positive sign of d_{31} in fresnoite was confirmed by measurements with a d_{33} meter and the magnitude of d_{31} was determined as 1.5 pC/N by standard resonance techniques. For most of the commonly used ferroelectric materials the value of d_{33}/d_{31} is approximately -3 , whereas for fresnoite it is approximately $+5$. From this discussion it is clear that the positive sign of d_{31} can be attributed to an internal Poisson's ratio stress acting in the same direction as external stress. This is the origin of the sizable hydrostatic sensitivity of $\text{Ba}_2\text{TiSi}_2\text{O}_9$ and $\text{Ba}_2\text{TiGe}_2\text{O}_9$ as well.

V. Conclusions

(1) It has been shown that grain-oriented glass-ceramics in the systems $\text{BaO-SiO}_2\text{-TiO}_2$, $\text{BaO-GeO}_2\text{-TiO}_2$, and $\text{SrO-SiO}_2\text{-TiO}_2$ can be prepared by crystallizing glasses of optimized compositions in a temperature gradient.

(2) Magnitudes of hydrostatic piezoelectric coefficient: d_h , piezoelectric voltage coefficient g_h , and the dielectric constant of glass-ceramics are comparable to the corresponding values of PVF₂.

(3) Acoustic impedances of these glass-ceramics are in the range 18 to 20×10^9 kg/m²·s and hence good acoustic matching can be obtained with metals such as aluminum and commonly used glasses.

(4) An explanation is given for the high value of g_h in fresnoite and its isomorphs, based on the principles of series and parallel mixing of phases and crystal structure of fresnoite. The reason for the high value of g_h in fresnoite is the positive sign of d_{31} , caused by an internal Poisson ratio stress.

References

- G. J. Gardoee, R. E. Newnham, and A. S. Bhalla, "Piezoelectric $\text{Li}_2\text{Si}_2\text{O}_7$ Glass-Ceramics," *Ferroelectrics*, **33**, 155-63 (1981).
- A. Halliyal, A. S. Bhalla, R. E. Newnham, and L. E. Cross, " $\text{Ba}_2\text{TiGe}_2\text{O}_9$ and $\text{Ba}_2\text{TiSi}_2\text{O}_9$ Piezoelectric Glass-Ceramics," *J. Mater. Sci.*, **16** (4) 1023-28 (1981).
- A. Halliyal, A. S. Bhalla, R. E. Newnham, and L. E. Cross, "Polar Glass-Ceramics," *Ferroelectrics*, **38**, 791-84 (1981).

- ⁴A. Halliyal, A. S. Bhalla, R. E. Newnham, and L. E. Cross. "Piezoelectric and Elastic Properties of Barium Germanium Titanate and Lithium Borosilicate Glass-Ceramics." *Ultrasonics Symp.*, 315-18 (1981).
- ⁵A. Halliyal, A. S. Bhalla, and R. E. Newnham. "Polar Glass-Ceramics — A New Family of Electroceramic Materials: Tailoring the Piezoelectric and Pyroelectric Properties." *Mater. Res. Bull.*, 18 (8) 1007-19 (1983).
- ⁶R. E. Newnham, D. P. Skinner, and L. E. Cross. "Connectivity and Piezoelectric-Pyroelectric Composites." *Mater. Res. Bull.*, 13 (5) 525-36 (1978).
- ⁷D. P. Skinner, R. E. Newnham, and L. E. Cross. "Flexible Composite Transducers." *Mater. Res. Bull.*, 13 (6) 599-607 (1978).
- ⁸S. Y. Lynn. "Polymer-Piezoelectric Ceramic Composites with 3-1-0 Connectivity for Hydrophone Applications". M. S. Thesis, The Pennsylvania State University, 1981.
- ⁹H. Schmid, P. Genequand, H. Tippmann, G. Pouilly, and H. Guedu. "Pyroelectricity and Related Properties in the Fresnoite Pseudobinary System Ba₂TiGe₂O₈-Ba₂TiSi₂O₈." *J. Mater. Sci.*, 13 (10) 2257-65 (1978).
- ¹⁰S. Haussühl. "Growth and Physical Properties of Fresnoite Ba₂TiSi₂O₈." *J. Cryst. Growth*, 40, 200-204 (1977).
- ¹¹M. Kimura, K. Doi, S. Nanamatsu, and T. Kawamura. "A New Piezoelectric Crystal Ba₂Ge₂TiO₈." *Appl. Phys. Lett.*, 23 (10) 531-32 (1973).
- ¹²G. M. Sessler. "Piezoelectricity in Polyvinylidene Fluoride." *J. Acoust. Soc. Am.*, 70 (6) 1596-1608 (1981).
- ¹³R. E. Newnham, L. J. Bowen, K. A. Klicker, and L. E. Cross. "Composite Piezoelectric Transducers." *Mater. Eng.*, 2 (12) 93-106 (1980).
- ¹⁴P. B. Moore and S. J. Louisnathan. "The Crystal Structure of Fresnoite, Ba₂TiO₂Si₂O₈." *Z. Krist.*, 130, 438-48 (1969).

RESONANT MODES OF VIBRATION IN PIEZOELECTRIC PZT-POLYMER
COMPOSITES WITH TWO DIMENSIONAL PERIODICITY

T.R. Gururaja, W.A. Schulze, L.E. Cross,
B.A. Auld, Y.A. Shui, and Y. Wang

RESONANT MODES OF VIBRATION IN PIEZOELECTRIC PZT-POLYMER COMPOSITES WITH TWO DIMENSIONAL PERIODICITY

T.R. GURURAJA, W.A. SCHULZE AND L.E. CROSS

Materials Research Laboratory, The Pennsylvania State University, University Park, PA 16802

B.A. AULD, Y.A. SHUI AND Y. WANG

Department of Applied Physics, Stanford University, Stanford, CA 94305

Abstract—High frequency resonance characteristics of piezoelectric PZT rod-polymer composites with 1-3 connectivity have been investigated. Electrical admittance plots and laser probe dilatometry of the dynamic displacement on the composite as a function of frequency are used to interpret the vibration pattern of resonant modes.

INTRODUCTION

Piezoelectric PZT-polymer composites of different connectivity pattern have been investigated to evaluate their adaptability as ultrasonic transducers for medical applications in the low megahertz frequency range¹. Among all the different composites, those with PZT-501A fibers embedded in Spurr's epoxy (Polysciences, Warrington, PA) matrix with regular periodicity (1-3 connectivity) appeared to be very promising for this application. The present paper is a brief report on the high frequency dynamic behavior of these composites in resonant configuration aimed at understanding their physics and possibly extending their usefulness in devices other than hydrophones.

Samples for the present study consisted of fired PZT-501A fibers (diameter = 0.45 mm) arranged in square lattice and impregnated in Spurr's epoxy matrix. Disc shaped composites (diameter = 1.9 cms) with 5, 10, 20, and 30 volume percent PZT were cut and ground to proper thickness and poled at 20 kV/cm.

THEORY

Resonance modes which can be expected in a cylindrically shaped composite are: fundamental radial and thickness modes and their overtones, and possible resonant lateral modes due to the regular periodicity of the PZT fibers in the composite.

Radial mode resonance is mainly determined by the effective modulus C_T normal to the fiber axis and the average density of the composite. The effective modulus C_T was calculated by the Reuss constant stress model². Similarly the thickness mode resonance is defined by the effective modulus C_L along the fiber axis and

the average density of the composite. The effective modulus C_L was estimated by the Voigt constant strain model². For the effective modulus calculations, elastic stiffness of the fiber perpendicular to the length was chosen to be $C_{11}^E = 12.1 \times 10^{10}$ N/m² and along the fiber axis Young's modulus $E = 1/S_{33}^D = 10.5 \times 10^{10}$ N/m² was chosen. For the epoxy, the modulus was determined to be 4.7×10^{10} N/m².

At wavelengths comparable to the unit cell dimensions of the array, the analysis is more complicated. A Brillouin theory of elastic wave propagation in a two dimensionally periodic lattice corresponding to composites with 1-3 connectivity has been developed³. For laterally propagating shear waves with polarization along the fibers, the lowest stop band frequencies have been calculated.

EXPERIMENTAL EVALUATION OF RESONANCE MODES

Absolute value of electrical admittance was measured on samples as a function of frequency in the ambients of air and water using a spectrum analyzer (HP-3585A). Here samples of different thickness and volume fraction were examined to identify the different resonances observed in the 0-2 MHz frequency range. The three major resonances of interest are designated as f_1 , f_{t1} , and f_{t2} as categorized in Table 1. To analyze the nature of vibration at these frequencies, detailed laser probe measurement of actual mechanical displacement on the composite was performed by laser heterodyne technique⁴. Frequency scans of the ultrasonic displacement at several points on the composite were combined with automated position scans across the diameter of the composite at frequencies f_1 , f_{t1} and f_{t2} to study the vibration pattern.

The resonance frequency f_1 was inversely proportional to thickness of the sample. The vibration on PZT fiber was in phase with that of the epoxy. For samples resonating at low frequencies (~ 300 KHz), the amplitude on the rod was only a little bit smaller than that on the epoxy. The resonance was heavily damped when the

Table 1. Resonant Modes in PZT Rod-Polymer Composites.

Volume % PZT	Periodicity d (mm)	Thickness t (mm)	Resonance Frequencies in KHz			$V_L = 2t f_1$ m/sec	$V_B = d f_{t1}$ m/sec	$V_B = \frac{d}{\sqrt{2}} f_{t2}$ m/sec
			f_1	f_{t1}	f_{t2}			
5	1.76	4.00	212	482	491	1248	472	359
		4.00	262	449	—	1227	790	—
		5.90	222	457	730	1209	769	902
10	1.27	3.44	410	462	1006	1492	840	902
		5.15	262	444	—	1249	817	—
		1.34	340	494	—	1271	804	—
20	0.90	3.05	453	430	—	1387	747	—
		3.95	348	420	—	1374	743	—
		4.60	294	406	—	1361	792	—
30	0.73	3.15	270	423	—	1390	742	—
		3.44	369	1123	—	1389	821	—
		5.15	274	1180	—	1424	867	—

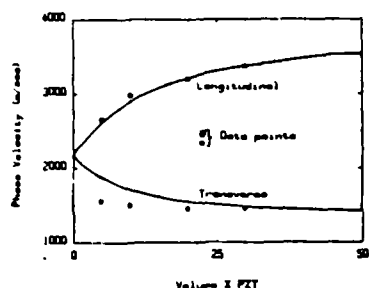


Figure 1. Phase velocities for PZT-fiber-polymer composites.

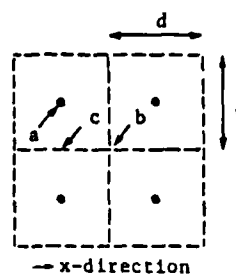


Figure 2. Unit cells in the composite.

resonator was immersed in water. Such a behavior suggests that this is the longitudinal thickness mode. Longitudinal velocities of sound along the fiber axis calculated using the resonance frequency agree very well with the theoretically estimated values for the composites of different volume fraction (Figure 1).

Resonances at f_{t1} and f_{t2} are quite similar in nature. For a certain volume fraction the resonances always occur at specified frequencies immaterial of the thickness. This observation indicates that the two resonances are due to transverse periodicity in the lattice.

The vibration pattern at f_{t1} can be explained by referring to Figure 2 which has four unit cells. At this frequency all the rods vibrate in phase. The vibration amplitude A at points a , b , and c in Figure 2 follows the relation $A_a \approx A_b \gg A_c$. The phase difference between points a and b was found to be 180° . The observed behavior can be explained by the superposition of two standing shear wave patterns of wavelength equal to the lattice periodicity (d) existing along both x and y axes. This resonance corresponds to one of the stop bands predicted by the theory. Velocity of transverse shear waves, $V_s = df_{t1}$, is tabulated in Table 1.

At frequency f_{t2} , the amplitude A at points a , b , and c follows the relation $A_b > A_a > A_c$. Points a and b vibrate in phase and there is 180° phase difference between the vibrations at points b and c . Superposition of standing shear waves along the two diagonals explain the observed vibration pattern. This lateral shear resonance along the diagonal fits a predicted stop band. Again the transverse shear velocity is calculated by the equation $V_s = df_{t2}/2$. The calculated shear velocity is about 25% lower than the measured velocity in epoxy by the transmission technique (1050-1100 m/sec). This is quite possibly due to the mass loading by PZT fibers.

The thickness coupling coefficient k_t and Q of the composites are given in Table 2. The data is mainly divided into two groups. Thin samples with thickness around 0.6 mm resonating around 2.25

MHz and thick samples with thickness above 2 mm with resonance frequency around 500 KHz. In thin samples, the resonance frequency is much higher than that of the strong lateral modes. Therefore, the PZT fibers can be pictured as vibrating independently resulting in k_t close to that of PZT. The low Q indicates that the PZT rods are partially damped by the surrounding polymer. For thick composites, the resonance is close to the lateral modes and the vibration of PZT fibers is laterally coupled through the epoxy as evidenced by the uniform mechanical displacement across the sample and is indicated by low k_t . The high Q for thick composites is a result of very low attenuation losses in the epoxy at around 0.5 MHz.

The radial mode coupling coefficient k_D was 22% for 5% PZT composites and increased to 27% for 30% PZT composites. The transverse longitudinal velocity V_T calculated using the resonance frequency and the diameter of the composite is compared with the theory in Figure 1. The large discrepancy between the calculated and measured velocities of transverse longitudinal wave is probably due to the finite diameter of the PZT fibers. Elastic stiffening by the PZT fibers is provided only at discrete points in the composite, and the approximations in the Reuss model are therefore not completely valid.

SUMMARY

PZT rod-polymer composites with 1-3 connectivity have, in addition to thickness and radial modes, complex lateral vibrational modes due to the periodicity of the lattice. The correspondence between the theory and experiment for the lateral modes is remarkably close. The thickness mode resonance in relatively thick composites follows the Voigt constant strain model.

REFERENCES

1. T.R. Gururaja, W.A. Schulze, T.R. Shrout, A. Safari, L. Webster and L.E. Cross, *Ferroelectrics* **39**, 1245 (1981).
2. S. Lees and C.L. Davidson, *IEEE Trans. on Sonics and Ultrasonics*, SU-24, 222 (1977).
3. B.A. Auld, Y.A. Shui and Y. Wang, International Conference on the Dynamics of Interfaces, France (Sept. 1983) (to be published in the *Journal de Physique*).
4. B.A. Auld and H.A. Kunkel, *Ferroelectrics*, **38**, 971 (1981).

Table 2. Thickness Mode Resonance.

Volume % PZT	Thickness t mm	k_t	Q
5	Thin	97.1	5.2
	Thick	27.5	31.6
10	Thin	68.2	7.0
	Thick	40.0	27.7
20	Thin	68.9	9.9
	Thick	55.1	18.1
30	Thin	--	--
	Thick	61.1	26.8

PYROELECTRIC AND PIEZOELECTRIC PROPERTIES OF SbsI COMPOSITES

A.S. Bhalla and R.E. Newnham

PYROELECTRIC AND PIEZOELECTRIC PROPERTIES OF SbSI COMPOSITES *

A.S. BHALLA AND R.E. NEWNHAM
Materials Research Laboratory
The Pennsylvania State University
University Park, PA 16802

(Received for Publication August 20, 1984)

Abstract—Antimony sulphur iodide (SbSI), in the ferroelectric phase below 20°C belongs to the orthorhombic point group symmetry $mm2$ and has very large pyroelectric coefficient, piezoelectric strain coefficients (d_{33}) and dielectric constant along the polar c -axis.

Composites of SbSI:polymer in (1:3) and (3:3) and SbSI:glass fibers in 3:1 connectivity modes have been prepared and electrical properties are measured. Pyroelectric and piezoelectric voltage sensitivities have substantially increased compared to those of pure SbSI single crystals.

Effects of doping on SbSI and the pyroelectric properties of the off c -axis cut composites will also be discussed.

† Communicated by Professor J. Gonzalo

*This paper was presented at the Fifth European Meeting on Ferroelectricity (EMF5) Benalmadena, Spain, September, 1983.

FLEXIBLE COMPOSITE PIEZOELECTRIC SENSORS

R.E. Newnham, A. Safari, G. Sa-Gong, and J. Giniewicz

FLEXIBLE COMPOSITE PIEZOELECTRIC SENSORS

R.E. Newham, A. Safari, G. Sa-gong and J. Glulwicz
Materials Research Laboratory
The Pennsylvania State University
University Park, PA 16802

Abstract

The piezoelectric properties of several different composites with 0-3 connectivity are reviewed. In these composites a piezoelectric ceramic powder such as $\text{PbZr}_{1-x}\text{Ti}_x\text{O}_3$ (PZT), PbTiO_3 or $\text{Pb}_{1-x}\text{Bi}_x\text{Ti}_{1-x}\text{Fe}_x\text{O}_3$ is used as a filler in a polymer matrix. The values of hydrostatic voltage coefficient g_h of these composites are higher than the corresponding properties of single phase materials. Composites with PbTiO_3 or $(\text{Pb,Bi})(\text{Ti,Fe})\text{O}_3$ as fillers have higher piezoelectric voltage coefficients than PZT-polymer composites because of the greater anisotropy and lower dielectric constants of these systems. By adding a small amount of carbon to the piezoelectric composite, poling can be carried out at much lower voltages and shorter poling times, making it possible to mass produce the composites. Fabrication of 0-3 composites is a relatively simple process which can be adapted to the production of piezoelectric fabrics, piezoelectric cables, and piezoelectric paint.

I. Introduction

A hydrophone is an underwater microphone or transducer used to detect underwater sound. The sensitivity of a hydrophone is determined by the voltage that is produced by a hydrostatic pressure wave. The hydrostatic voltage coefficient, g_h , relates the electric field appearing across a transducer to the applied hydrostatic stress, and is therefore a useful parameter for evaluating piezoelectric materials for use in hydrophones. Another piezoelectric coefficient frequently used is the hydrostatic strain coefficient, d_h , which describes the polarization resulting from a change in hydrostatic stress. The g_h coefficient is related to the d_h coefficient by the relative permittivity (K): $g_h = d_h/\epsilon_0 K$, where ϵ_0 is the permittivity of free space.

A useful 'figure of merit' for hydrophone materials is the product of hydrostatic strain coefficient d_h and hydrostatic voltage coefficient g_h . The product $d_h g_h$ has the units of $\text{m}^2 \text{N}^{-1}$. Other desirable properties for a hydrophone transducer include (i) low density for better acoustical matching with water, (ii) high compliance and flexibility so that the transducer can conform to any surface and withstand mechanical shock. Compliance also leads to large damping coefficients which prevent 'ringing' in a

passive transducer, and (iii) little or no variation of the g_h and d_h coefficients with pressure, temperature and frequency.

Lead zirconate titanate (PZT) is widely used as a transducer material because of its high piezoelectric coefficients. However for hydrophones, PZT is a poor choice for several reasons. PZT has a large piezoelectric d_{33} coefficient, but its hydrostatic strain coefficient $d_h (= d_{33} + 2d_{31})$ is small because d_{33} and $2d_{31}$ are opposite in sign, and almost cancel one another. Moreover, the high permittivity of PZT ($K \approx 1800$) lowers the voltage coefficient g_h to minuscule values. In addition, the density of PZT (7.9 g/cm^3) makes it difficult to obtain good impedance matching with water. PZT is also a brittle ceramic and for some applications a more compliant material with better shock resistance is desirable.

Other materials used for hydrophone applications are lead metaniobate PbNb_2O_6 (1) and PbTiO_3 (2). Their d_h values are slightly higher than that of PZT (Table 1) and the g_h values are an order of magnitude better because of their modest dielectric constants. Unfortunately, PbNb_2O_6 and PbTiO_3 are also dense, brittle ceramics, which undergo a large volume change at the Curie temperature, often causing fracture during preparation.

Polyvinylidene fluoride ($\text{PVF}_2 = (\text{CH}_2\text{-CF}_2)_n$) offers several advantages over PZT and other piezoelectric ceramics (2). It has low density, high flexibility, and although PVF_2 has low d_{33} and d_h , the piezoelectric voltage coefficient g_h is large because of its low relative permittivity.

There are, however, problems associated with the use of PVF_2 . The major problem is the difficulty in poling PVF_2 . A very high field is necessary to pole PVF_2 (1.2 MV/cm), and this limits the thickness that can be poled. Pyroelectric phenomena in PVF_2 also produces undesirably large polarization fluctuations with temperature.

It is clear that none of the single-phase materials are ideal for hydrophones and there is need for better piezoelectric materials.

II. Composite Piezoelectrics

One approach to the problem is to develop composite materials in which the desired properties can be incorporated through use of a combination of materials with different properties. In designing composite materials for hydrophone applications, a logical choice would be a piezoelectric ceramic and a compliant polymer. In such a composite, the ceramic produces a large piezoelectric effect, while the polymer phase lowers the density and permittivity and increases the elastic compliance.

In a composite the electric flux pattern and the mechanical stress distribution, and hence the resulting physical and electromechanical properties, depend strongly on the manner in which the individual phases are interconnected. In this regard the connectivity of a composite, defined as the number of dimensions in which each component phase is continuous⁽⁴⁾, is of crucial importance. When referred to in an orthogonal axis system, each phase in a composite may be self-connected in zero, one, two, or three directions. For diphasic composites, there are ten connectivity patterns designated as 0-0, 0-1, 0-2, 0-3, 1-1, 1-2, 1-3, 2-2, 2-3, and 3-3.

During the past few years, a number of investigators have examined piezoelectric ceramic-polymer composites with different connectivity patterns. The method of preparation of these composites covers a wide spectrum of ceramic fabrication processes, and the piezoelectric properties of the composites depend to a large extent, on the connectivity pattern. In this paper, a brief summary of the piezoelectric properties of flexible composites with 0-3 connectivity is presented. A more extensive description of the work on other PZT-polymer composites can be found in recent review papers^(5,6).

III. Dielectric Piezoelectric Properties of 0-3 Composites

The simplest type of piezoelectric composite consists of a polymer matrix loaded with ceramic powder. In a composite with 0-3 connectivity, the ceramic particles are not in contact with each other while the polymer phase is self-connected in all three dimensions (Fig. 1). This type of composite does not have the desirable stress concentration factor found in some other connectivity patterns⁽⁷⁾, so the hydrostatic figure of merit d_{hh} is not large. In many ways the 0-3 composite is similar to polyvinylidene fluoride (PVF₂). Both consist of a crystalline phase embedded in an amorphous matrix, and both are reasonably flexible.

The first flexible piezoelectric composites were made by embedding PZT particles 5-10 μm in size in a polyurethane film⁽⁷⁾. The d_{33} coefficient of these composites were comparable with PVF₂, but the d_h value was lower than those of solid PZT and PVF₂ polymer (Table 1).



Fig. 1. SEM micrograph of PZT-PVF₂ polymer composite with 0-3 connectivity.

A similar composite (T-flex) was developed at Honeywell⁽⁸⁾, using 120 μm particles in a silicone-rubber matrix. The d_{33} values obtained with these composites were again comparable to PVF₂. The measured piezoelectric voltage coefficient \bar{g}_h was low (Table 1) and further improvement of piezoelectric coefficients was necessary. One difficulty with this type of composite is that the piezoelectric particles are smaller in diameter than the thickness of polymer sheet, and poling of the PZT was very poor because the electrodes were not in direct contact with the particles. To improve the properties of these composites Harrison⁽⁸⁾ fabricated a composite with much larger PZT particles up to 2.4 mm. Here the particle size approaches the thickness of the composite, and since the PZT particles extend from electrode to electrode, near saturation poling can be achieved. The large rigid PZT particles can also transmit applied stress extremely well, leading to high d_{33} values when measurements are taken across the particles. Permittivity in this composite is lower than that of homogeneous PZT, resulting in an improved voltage coefficient. One problem with this type of composite is that complete poling cannot be achieved and the piezoelectric properties of the composite vary from point to point. An improved version of the 0-3 composite was synthesized by Safari⁽⁹⁾. Flexible piezoelectric composites made from PZT spheres and polymers with 0-3 connectivity were fabricated using several types of polymers. Two techniques were developed for making spheres 0.4 to 4 mm in diameter. The dielectric constant of the composites were 300-400 and the piezoelectric voltage coefficients g_{33} were $45.55 \times 10^{-3} \text{ Vm}^2/\text{N}$. The high frequency properties of the composites were measured in both the thickness and radial mode of resonance. The frequency constants and the coupling coefficients of the composites for

Table 1. Dielectric and Piezoelectric Properties of Single Phase and Composites

Description of	Dielectric Constant	d_{33} pCN ⁻¹	\bar{g}_{33} ($\times 10^{-3}$ VmN ⁻¹)	\bar{g}_h ($\times 10^{-3}$ VmN ⁻¹)	d_h (pCN ⁻¹)	$d_h \bar{g}_h$ ($\times 10^{-15}$ C ² N ⁻¹)	Reference
PZT 501 Ceramic	1800	450	28	2.5	40	100	6
Pb(Bb ₂ O ₆) Ceramic	225	85	42	33.	67	2300	1
PbTiO ₃ Ceramic	230	53	26	23	47	1080	2
PVF ₂ = (CH ₂ -CF ₂) _n	12	35	329	100	10	1000	3
PZT Particles-Polyurethane Composite	26	10	43	8	2	10	7
PZT Particles-Silicone Rubber Composite (T-flex)	41	8	22	--	--	--	8
Large PZT Particles-Silicone Rubber Composites (B-flex)	100	340	560	32	28	900	8
W ₃ Modified PZT-Chloroprene Rubber	45	--	--	14	5	70	11, 12
Bi ₂ O ₃ Modified PbTiO ₃ -Chloroprene Rubber	40	--	--	28	10	280	11, 12
Pure PbTiO ₃ -Chloroprene Composite	54	60	125	47	22	1000	11, 12
PZT-Eccogel Composite	100	45	51	9	10	90	17
Carbon Added PZT-Eccogel Composite	120	50	47	32	24	800	17
0.5 PbTiO ₃ -0.5 BiFeO ₃ Epox. Polymer Composite	20	40	225	85	16	1300	19

the thickness mode of resonance are comparable with the corresponding values for PZT. Possible applications of the composites as band-pass filters have been developed⁽¹⁰⁾.

But an even better suggestion has been put forward by Banno^(11,12). Rather than using PZT as the ceramic filler, pure or modified lead titanate was employed because of its greater piezoelectric anisotropy. The piezoelectric ceramic fillers used in these composites are PbTiO_3 , Bi_2O_3 -modified PbTiO_3 and WO_3 -modified PZT. Fine-grained ($\sim 5 \mu\text{m}$) particles of pure PbTiO_3 were made by water quenching sintered ceramics, while those of modified PbTiO_3 and PZT were made by grinding sintered ceramics. To fabricate the composite bodies, the piezoelectric powders and chloroprene rubber were mixed and rolled down into 0.5 mm thick sheets at 40°C using a hot roller, and then heated at 190°C for 20 minutes under a pressure of 13 kg/cm^2 . The composites were poled in a $100\text{--}150 \text{ kV/cm}$ for 30 minutes.

As shown in Table 1, the hydrostatic voltage coefficient \bar{g}_h of pure PbTiO_3 composites is comparable to that of PVF_2 . In Fig. 2 the \bar{g}_h and \bar{d}_h of these composites are plotted as a function of hydrostatic pressure up to 35 MPa. (5000 PSI). It is found that \bar{g}_h and \bar{d}_h are independent of pressure up to 35 MPa⁽¹³⁾.

Recently we have fabricated flexible composites with a more active piezoelectric material. The piezoelectric ceramic filler used in these composites is $\text{Pb}_{1-x}\text{Bi}_x\text{Ti}_{1-x}\text{Fe}_x\text{O}_3$ (BF-PT) which has a very large spontaneous strain.

There are two reasons why large spontaneous strain is advantageous. First, it makes it easy to obtain a loose ceramic powder of extremely fine-grain size. On cooling from high temperature, the BF-PT ceramic undergoes brittle fracture at the Curie point as it transforms from a cubic state to a tetragonal phase with c/a ratio as large as 1.18⁽¹⁴⁾. Water-quenching accelerates the fracture process, further reducing the particle size, and making it possible to fabricate very thin piezo-films. The second reason is that a large spontaneous strain promotes greater piezoelectric anisotropy. This increases the hydrostatic sensitivity by reducing the cancellation between piezoelectric coefficients d_{33} and d_{31} . Banno⁽¹¹⁾ found that in 0-3 composite ferroelectrics, pure PbTiO_3 has a larger hydrostatic piezoelectric effect than $\text{Pb}(\text{Zr},\text{Ti})\text{O}_3$.

The spontaneous strain in PbTiO_3 is about 6%. In PZT compositions near the morphotropic boundary, it is about 2%. And since in BF-PT, the spontaneous strain is as large as 18%, we were not surprised to find a substantial increase in the hydrostatic voltage coefficients of the composites.

To fabricate the composites, the filler powder is synthesized from the system $\text{Pb}_{1-x}\text{Bi}_x\text{Ti}_{1-x}\text{Fe}_x\text{O}_3$ for which there is a continuous solid solution across the entire composition range. The composition of

the powders synthesized in this study lie in the range $x = 0.5\text{--}0.7$. To prepare the filler powder, PbO , TiO_2 , Bi_2O_3 and Fe_2O_3 were mixed and ball-milled with zirconia media. The oxides were subjected to a low temperature (700°C – 800°C) primary calcination for 1.5 hours, followed by a second high temperature firing (950°C – 1050°C). Water quenching produces an average particle size of $5 \mu\text{m}$ (Fig. 1). To fabricate the composites, piezoelectric ceramic powders and eceogel polymer⁽¹⁵⁾ were mixed and calendared at 40°C . The calendared material is then cured at 80° under slight pressure. Composites were poled in an 80°C silicone oil bath by applying a field $100\text{--}120 \text{ kV/cm}$ for 20 minutes. The poled composite exhibits outstanding hydrostatic sensitivity attaining values of \bar{g}_h and \bar{d}_h well in excess of the values reported for pure PbTiO_3 composites (Table 1)⁽¹³⁾. The \bar{g}_h and \bar{d}_h values of these composites⁽¹³⁾ remain virtually constant over a broad pressure range (Fig. 2).

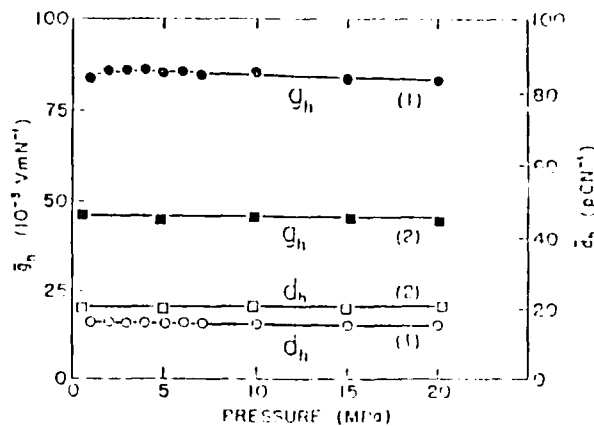


Fig. 2. Variation of \bar{g}_h and \bar{d}_h of composite (1) with pressure. \bar{g}_h and \bar{d}_h of composite (2) are also shown. (1) 0.3 PbTiO_3 – 0.7 BF-PT (average) (2) PbTiO_3 (control)

IV. Poling Method

As mentioned earlier, 0-3 composites prepared from PZT, PbTiO_3 and $(\text{Pb},\text{Bi})(\text{Ti},\text{Fe})\text{O}_3$ powders are poled at very large field strength ($100\text{--}150 \text{ kV/cm}$) in order to achieve sufficient poling. The reason for the necessity of such large fields will be clear from the following discussion.

For a 0-3 composite consisting of spherical grains embedded in a matrix, the electric field E_1 , acting on an isolated spherical grain is given by

$$E_1 = \frac{3K_2}{K_1 + 3K_2} E_0$$

In this equation, K_1 and K_2 are the dielectric constants of the spherical piezoelectric grains and polymer matrix, respectively, and E_0 is externally applied electric field. For a 0-3

composite of PbTiO_3 powder and polymer, $K_1 \sim 300$ and $K_2 \sim 5$. For such a composite with an external field of 100 kV/cm, the electric field acting on the piezoelectric particles is only about 5 kV/cm which is insufficient to pole the composite. According to the above equation $E_1 \sim E_0$ only when the dielectric constant of the piezoelectric phase approaches that of the polymer phase. Most of the ferroelectric materials have very high dielectric constants and hence the above condition cannot be satisfied.

The importance of conductivity to poling can be assessed by applying the Maxwell-Wagner model to the 0-3 composites⁽¹⁶⁾. The model leads to a relationship between the electric field strength and the conductivities of the two phases.

After applying a DC poling field to the sample for a time long compared to the sample relaxation time, the field distribution in a two-layer capacitor is given by $[E_1/E_2 = \sigma_2/\sigma_1]$. The field acting on the ceramic is controlled by σ_2/σ_1 , the ratio of the electrical conductivity of the polymer to that of the ceramic. Since the conductivity of the polymer matrix ($\sim 10^{-14} \Omega^{-1}\text{cm}^{-1}$) is about 100 times smaller than that of the PZT ceramic filler ($\sim 10^{-12} \Omega^{-1}\text{cm}^{-1}$) at room temperature, only a few percent of the poling field acts on the PZT particles. Under normal poling voltages, this is an insufficient field strength for poling the ferroelectric particles.

One way to increase poling is to increase the polymer conductivity close to that of the PZT filler. To do this, we have added a conducting third phase such as carbon to the PZT-polymer composite. In preparing these composites, 68.5 volume percent PZT 501 and 1.5 volume percent carbon were mixed and dry ball-milled. After ball-milling, the fillers were hand-mixed with eccogel polymer, and placed in a mold under pressure. It is found that the PZT-polymer composite with small amount of carbon additive can be poled in about five minutes under a field of 35-40 kV/cm at 100°C. Fig. 3 shows the effect of the poling voltage on the d_{33} values of the composites when poling is carried out at 120°C. It is observed that a duration of five minutes is sufficient for full poling of the composites. Piezoelectric and dielectric properties of some of these composites are calculated in Table 1 along with the properties of composites without conductive phase additive. Further details of the poling method will be reported elsewhere⁽¹⁷⁾.

Flexible 0-3 composite have also been developed at Bell Laboratories by Zipfel⁽¹⁸⁾. In this composite a polyurethane matrix material is mixed with 30-40 volume percent of a non-ferroelectric filler such as tartaric acid or lithium sulfate monohydrate. The liquid mixture is injected into an evacuated 3 inch diameter steel mold having two broad faces approximately 1.27 mm apart. While the polymer is undergoing polymerization, the composite is polarized by applying hydrostatic pressure and an electric field. In this way the piezoelectric crystals suspended in the liquid copolymer rotate until they are electrically

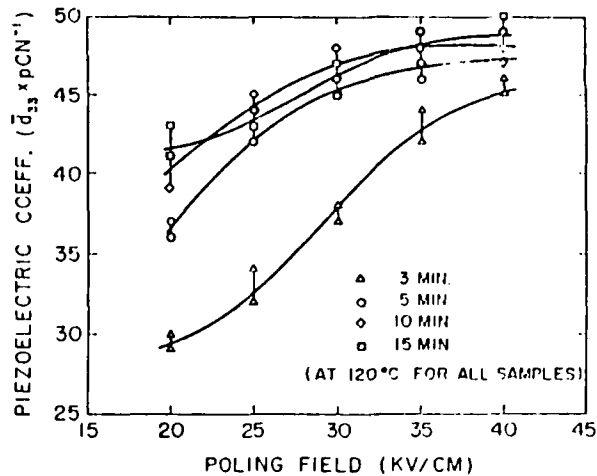


Fig. 3. Variation of d_{33} of PZT-carbon-polymer composites with poling voltage.

aligned. After polymerization, the resulting rubbery matrix holds the oriented particles in polar alignment for maximum sensitivity. The dielectric constant of this cable hydrophone is typically 4.2 and the piezoelectric sensitivity is stated to be 'comparable with most of the other piezoelectric materials.'

V. Summary

The dielectric and piezoelectric properties of several different types of flexible composites having 0-3 connectivity are described and their figure of merit for hydrophone applications ($d_{33}g_h$) are discussed. Hydrophones are used at low frequencies where the acoustic signal has a wavelength much larger than the scale of the macrostructure of the composite. It is shown that the hydrostatic voltage coefficient g_h and figure of merit $g_h d_{33}$ of ceramic-polymer composites are an order of magnitude higher than those of single phase materials. Composites fabricated with $(\text{Pb,Bi})(\text{Ti,Fe})\text{O}_3$ showed higher piezoelectric voltage coefficient than the other composites because of the large spontaneous strain in these systems. Difficulty of poling 0-3 composites can be eased by adding a small volume fraction of conductive phase.

VI. References

1. G. Goodman, *J. Am. Ceram. Soc.* 36, 368-72 (1953).
2. T.-Y. Tien and W.G. Carlson, *J. Am. Ceram. Soc.* 45, 567-71 (1962).
3. Y. Wada and R. Hayakawa, *Japan J. Appl. Phys.* 15, 2041 (1976).
4. R.E. Newnham, D.P. Skinner, and L.E. Cross, *Mat. Res. Bull.* 13, 525-536 (1978).
5. R.E. Newnham, L.J. Bowen, K.A. Klicker, and L.E. Cross, *Mat. in Eng.* 112, 93-106 (1980).
6. R.E. Newnham, A. Safari, J. Giniewicz, and B.H. Fox, *Ferroelectrics*, (to be published).
7. L.A. Pauer, *IEEE Int. Conf. Res.*, p. 1-5 (1973).
8. W.B. Harrison, *Proc. of the Workshop on Sonar Transducer Materials*, Naval Research Labs. (Feb. 1976).
9. A. Safari, A. Halliyal, L.J. Bowen, and R.F. Newnham, *J. Am. Ceram. Soc.* 65, 207-9 (1982).
10. L.J. Bowen and T.R. Gururaja, *J. Appl. Phys.* 51[11], 5661-66 (1980).
11. Hisao Banno, *Ferroelectrics*, Vol. 50, pp. 3-12 (1983).
12. Hisao Banno and Shigeo Saito, *Japan J. Appl. Phys.*, Vol. 22 (1983) Suppl. 22-2 pp. 67-69.
13. R. Tinge, Private Communication.
14. S.A. Fedulov, Yu. N. Venevtsev, G.S. Zhdanov, E.G. Smazhevskaya, and J.S. Roz, *Soviet Physics--Cryst.* Vol. 7, no. 1, p. 62, July-August 1962.
15. Eccogel 1365 Series (Emerson and Cumming, Dewey and Almy Chemical Division, W.R. Grace and Co.)
16. Arthur R. Von Hippel, *Dielectrics and Waves*, John Wiley and Sons, 1954, p. 228.
17. G. Sa-gong, A. Safari, R.F. Newnham, (to be published).
18. G.G. Zipfel, *Bell Labs Record*, Apr. 1983, p. 11-13.
19. J. Giniewicz, A. Safari and R.F. Newnham (applied for patent).

FINITE ELEMENT MODELING OF PERFORATED PZT-POLYMER COMPOSITES

S. DaVanzo, A. Safari, and R.E. Newnham

FINITE ELEMENT MODELING OF PERFORATED
PZT-POLYMER COMPOSITES

S. DaVanzo, A. Safari and R.E. Newnham
The Materials Research Laboratory
The Pennsylvania State University
University Park, Pennsylvania 16802

ABSTRACT

Perforated PZT-polymer composites with 3-1 connectivity patterns have been fabricated by drilling square holes perpendicular to the poling direction in prepoled PZT blocks and filling the holes with epoxy polymer. The influence of the separation between the holes on the dielectric and piezoelectric properties of the composite was studied. The finite element method has been used to calculate the stress distributions in this composite. The hydrostatic \bar{d}_h and \bar{g}_h coefficients have been calculated by summing the individual element polarization. The calculated values are compared with experimental results.

INTRODUCTION

PZT-polymer composites for hydrophone applications have been fabricated for a number of years using different macrosymmetry and interphase connectivity patterns¹⁻⁷. Safari and co-workers⁸ have investigated composites with 3-1 and 3-2 connectivity patterns. The connectivity pattern refers to the number of dimensions in which the individual phases within the composite are continuous. A 3-1 composite is one in which the PZT phase is continuous in three dimensions and the polymer is continuous in one dimension. The introduction of the polymer phase lowers the dielectric constant K_{33} from that of single phase PZT, and increases the hydrostatic piezoelectric charge coefficient d_h , the hydrostatic piezoelectric voltage coefficient g_h , and the figure of merit $g_h d_h$.

The 3-1 composites discussed in this study were fabricated by Safari⁸ by drilling holes perpendicular to the poling axis in prepoled PZT blocks. The holes were backfilled with Spurr's epoxy resin and the dielectric constant and piezoelectric coefficients measured. The 3-1 composites have a lower density than solid PZT which allows better acoustic coupling with water than does solid PZT. Depending on the geometry, the 3-1 composites show an increase in the hydrostatic figure of merit $d_h g_h$ of a factor of about 30.

It has been postulated that the increase in the hydrostatic piezoelectric coefficients is due to a favorable change in the stress distribution within the composite. In order to better understand the enhancement of the hydrostatic piezoelectric coefficients a simple series and parallel model was developed⁸. In the series and parallel model the composite was divided into three regions as shown in Figure 1. The two sections labeled A are solid segments of PZT. The section labeled B contains PZT regions in parallel with polymer regions. The three sections are connected in series to form the composite. The piezoelectric coefficients d_{33} , d_{31} and d_{32} were then calculated for the composite.

In calculating d_{33} and d_{32} it was assumed that the sections connected in parallel along the z direction would have equal strain, and those connected in series would be subject to a stress, equal to the applied stress. In estimating d_{31} only the constant stress conditions were used. The three coefficients were then combined to yield a hydrostatic coefficient $d_h = d_{31} + d_{32} + d_{33}$.

With the simple assumptions used to describe the stress distribution within the composite, the series and parallel model overestimated the hydrostatic piezoelectric coefficient d_h . In order to obtain a more realistic stress distribution within the composite the Finite Element Method (FEM) was used to calculate the coefficients.

THE FINITE ELEMENT METHOD

The Finite Element Method was used to calculate the stress distribution within the composites. FEM is a method of solving boundary value problems in which a continuous region is divided into a finite number of small regions. The differential equation used to describe the behavior of the continuous system is expanded on a set of simple basis functions termed "shape functions". The behavior of the continuous region is then described in terms of the behavior of a finite number of points within each element making up the region of interest. In the elastic problem the behavior of the region is described by the displacement of points within the region termed "nodes". The displacements of the nodes become the independent variables within a set of algebraic equations. The FEM calculates the displacements of the nodes to obtain a distribution of strains within the material. The stress distribution is then "recovered" from the strains.

The accuracy of the FEM is controlled by refining the element mesh. The FEM will converge uniformly* to the "exact" solution by using an increasingly

* Assuming isoparametric elements are used with other element types the FEM will converge but not always uniformly.

larger number of elements to describe the region. The method employed in the expansion of the differential equation places constraints on the displacements of the nodes, hence the model converges from a stiffer model. In terms of the present study, these constraints will imply that the calculated d_h coefficient will be underestimated by the FEM. The mesh size can be reduced to a point which will yield an error of less than 10% without the cost becoming prohibitively expensive.

The FEM was used to calculate the hydrostatic piezoelectric d_h coefficient for 3-1 perforated composites. The method involves the following five step procedure:

- STEP 1. Divide the composite into a large number of finite elements. A sample "grid" is shown in Figure 2. The elements used in this study are cubic blocks 0.25mm on a side. The nodes referred to earlier are the corners of the cube.
- STEP 2. Generate the elemental data for the grid. The elemental data consists of the positions of each node, the material making up the element (ie. polymer or PZT), and the mechanical load on the element. The way in which the nodes are arranged is important for minimizing computational cost and accuracy. The nodal arrangement is chosen to minimize the maximum difference between node numbers in any element.
- STEP 3. Calculate the stress distribution by the FEM. The FEM calculates the six components of the stress at the centroid of each element.
- STEP 4. Calculate the polarization at the centroid of each element using the relationship $P_i = d_{ijk} \sigma_{jk}$ for PZT.
- STEP 5. Sum the element polarizations and calculate the hydrostatic piezoelectric charge coefficient d_h . The composite polarization was calculated using a series and parallel model which assumes that the electrode surface is a constant potential surface.

The dielectric constant K_{33} was calculated by dividing the composite into the same Finite Element grid. The dielectric constant was then calculated using a similar series and parallel model, and summing the polarizations.

RESULTS AND DISCUSSION

The hydrostatic piezoelectric charge coefficient d_h was calculated for 3-1 perforated composites with 2 square holes. The hole size was 2.5mm on edge. Figure 3 shows the d_h coefficient plotted as a function of x (The center to center distance for adjacent holes). The figure compares calculated (solid line) and measured values (squares). The values calculated by the FEM fall below the measured values; this is to be expected as the FEM converges from a stiffer model.

Figure 4 shows the dielectric constant K_{33} as a function of x . The dielectric constant was calculated using the same FEM grid and the series and parallel model. There is good agreement between the calculated dielectric constant and the measured dielectric value.

The hydrostatic piezoelectric voltage coefficient g_h is shown plotted as a function of x , for both calculated and measured values, in Figure 5. The coefficient g_h was calculated from the relation $g_h = d_h / K_{33}$. The properties calculated using the FEM show good agreement with those measured in the laboratory.

In the process of calculating the hydrostatic piezoelectric coefficients the FEM calculates the distribution of the six components of stress tensor throughout the composite. The stress distribution is helpful in elucidating which composite designs will maximize the normal stress in the Z-direction while at the same time minimizing the X and Y components. The stress distribution will also show areas of stress concentration. Stress concentrations can be detrimental under high loads; causing depoling and fracture.

The stress distribution for a 3-1 perforated composite is shown in Figures 7-10. The applied load was a hydrostatic load of 689.5×10^3 Pa (100 psi). Each figure is a contour map of one of the six components of the stress tensor. The components are projected onto a plane parallel to the Y axis at a point 0.125 mm into the composite. The plane on which the contour plots are projected is shown in Figure 6. On each figure the contour lines follow paths of constant stress. By identifying the magnitude of each line it is possible to determine the stress at each point within the composite. As an example the rectangular region in the center of Figure 7 (XX-component) is enclosed by the 350×10^3 Pa (50 psi) contour. This same region is enclosed by the 950×10^3 Pa (135 psi) contour in Figure 8 (YY-component), and by the 1850×10^3 Pa (250 psi) contour in Figure 9 (ZZ-component).

Areas with a high density of lines represent regions with a large gradient of the particular component of the stress. For example the hole interface in Figure 7 shows a change from 750×10^3 Pa (120 psi) outside the hole to 350×10^3 Pa (50 psi) within the hole. The maximum in the XX and YY components of the stress occurs at the corners of the holes as is visible in Figures 7 and 8. The value of the maximum is only 2.3 and 1.5 times the applied load for the XX and YY components respectively. In Figure 9 the maximum stress occurs along the edge of the composite. This maximum is approximately 3.6 times the applied load. It is this increase in the ZZ component of the stress which is responsible for the increase in the hydrostatic piezoelectric coefficients but would also be responsible for fracture or depoling under high loads. The areas that would depole first are the regions surrounding the holes. Studying Figures 7 and 8 show that the normal components of the stress orthogonal to the poling direction are maximum at the hole interface. Fracture would occur first in the pillar regions between the holes and at the composite edge. Figure 9 shows that the maximum in the z component of the stress tensor is

approximately 3.6 times the applied load in these pillar regions. Care must be used in the design of these type of composites to make sure that the enhancement of the stress in the pillar regions is not great enough to degrade the mechanical integrity of the composite while at the same time maximizes the enhancement of the hydrostatic piezoelectric properties.

Studying Figures 7-9 show how the holes decrease the influence of the loads in the X and Y directions on the polarization in the Z direction. The goal of these composites is to reduce the influence of d_{31} and d_{32} on the hydrostatic coefficient d_h . Since it is not possible to change the coefficients of single phase PZT, the composite is designed to reduce the σ_1 and σ_2 components of the stress in the PZT phase. Figure 10 shows a contour map of the P_3 component of the polarization. It shows that the net effect is to increase the polarization in the pillar regions adjacent to the holes. It is this increase in the polarization which is responsible for the increase in the hydrostatic piezoelectric coefficient d_h of the composite from that of single phase PZT. The pillar regions shown in Figure 10 suggest that in designing composites for hydrophone applications the emphasis should be placed on maximizing pillar structures in the direction parallel to the poling axis.

The difference between the properties predicted by the series and parallel model and those predicted by the Finite Element technique can be attributed to the more realistic stress distribution. The simple assumptions used in the series parallel model do not hold for these composites. The Finite Element Method provide insights for future design criteria by allowing one to choose a geometry which will yield the desired stress distribution.

ACKNOWLEDGEMENT

We wish to thank the Office of Naval Research for their support of this work through Contract N00014-82-K-0339.

REFERENCES

1. R.E. Newnham, D.P. Skinner and L.E. Cross, Mat. Res. Bull., 13, 525 (1978).
2. D.P. Skinner, R.E. Newnham and L.E. Cross, Mat. Res. Bull., 13, 599-607 (1978).
3. T.R. Shrout, W.A. Schulze and J.V. Biggers, Mat. Res. Bull., 14, 1553 (1979).
4. K. Rittenmyer, T.R. Shrout and R.E. Newnham, Ferroelectrics, 41, 189-195 (1982).
5. A. Safari, A. Halliyal, R.E. Newnham and I.M. Lachman, Mat. Res. Bull., 17, 301 (1982).
6. R.E. Newnham, L.J. Bowen, K.A. Klicker and L.E. Cross, Mat. in Eng. 2, 93-106 (1980).
7. R.E. Newnham, A. Safari, J. Giniewicz and B.H. Fox, Ferroelectrics, (to be published).
8. A. Safari, Ph.D. Thesis, The Pennsylvania State University (1983).

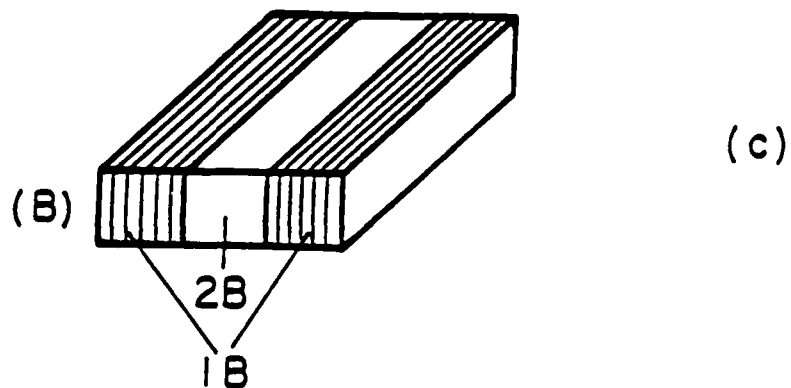
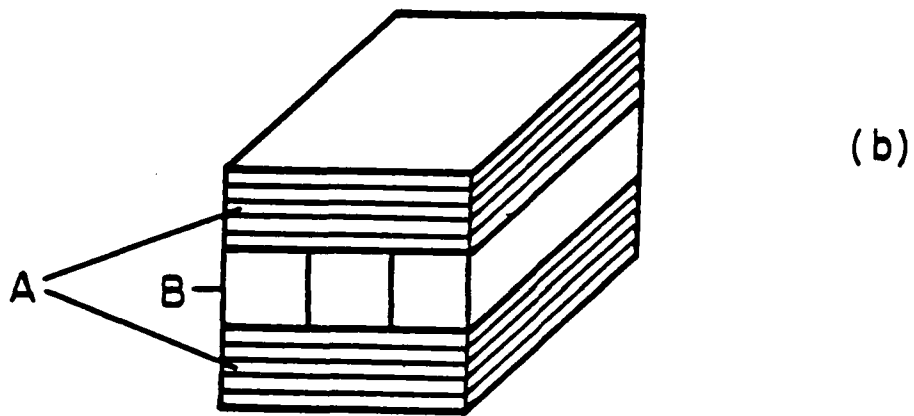
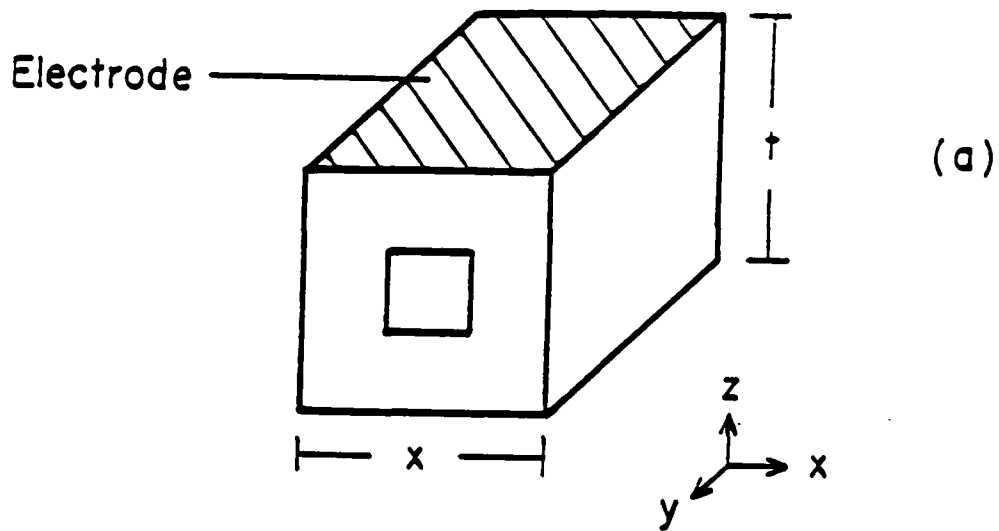


Fig. 1. Schematic diagram of perforated 3-1 composites.

(a) with square hole.

(b) with sectioning in two parts A and B.

(c) with sections 1B and 2B of part B of the composite.

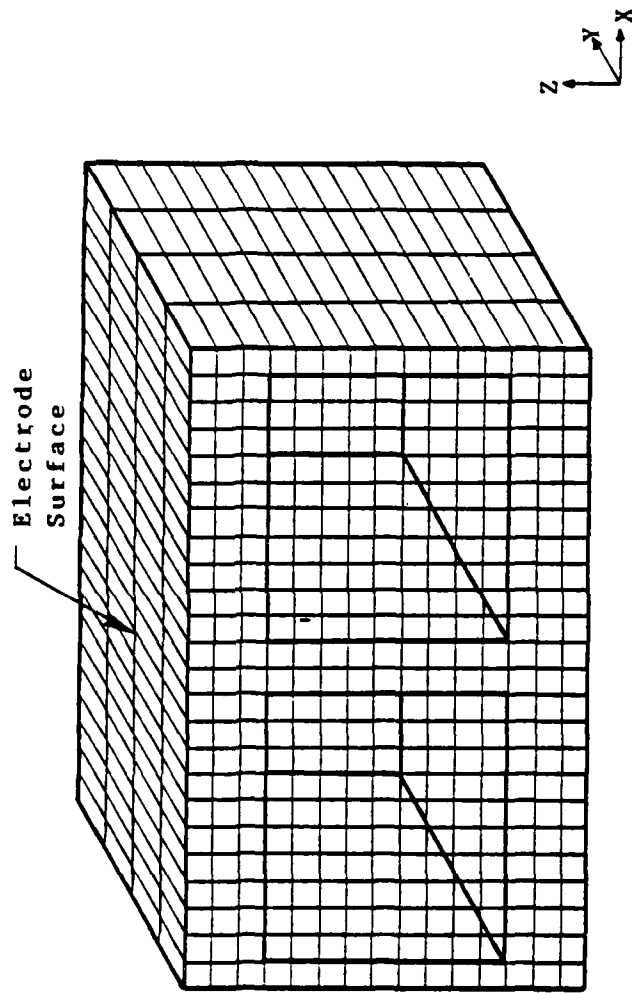


Fig. 2. A typical Finite Element Method grid for a 3-1 perforated PZT-polymer composite.

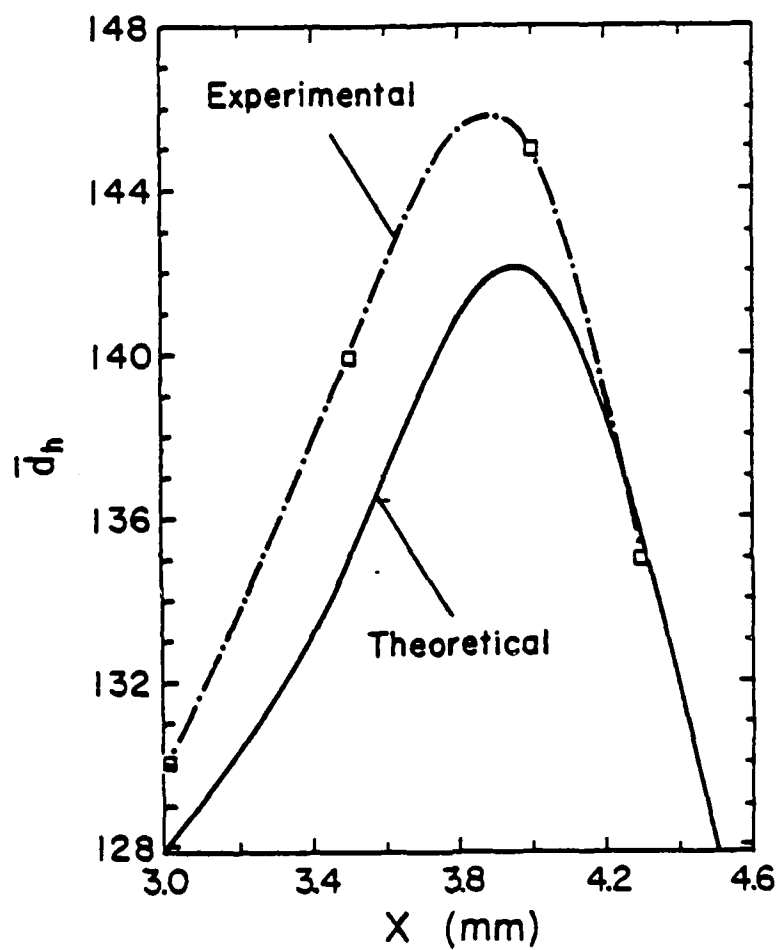


Fig. 3. Variation of hydrostatic charge coefficient \bar{d}_h as a function of x (the center to center distance for adjacent holes).

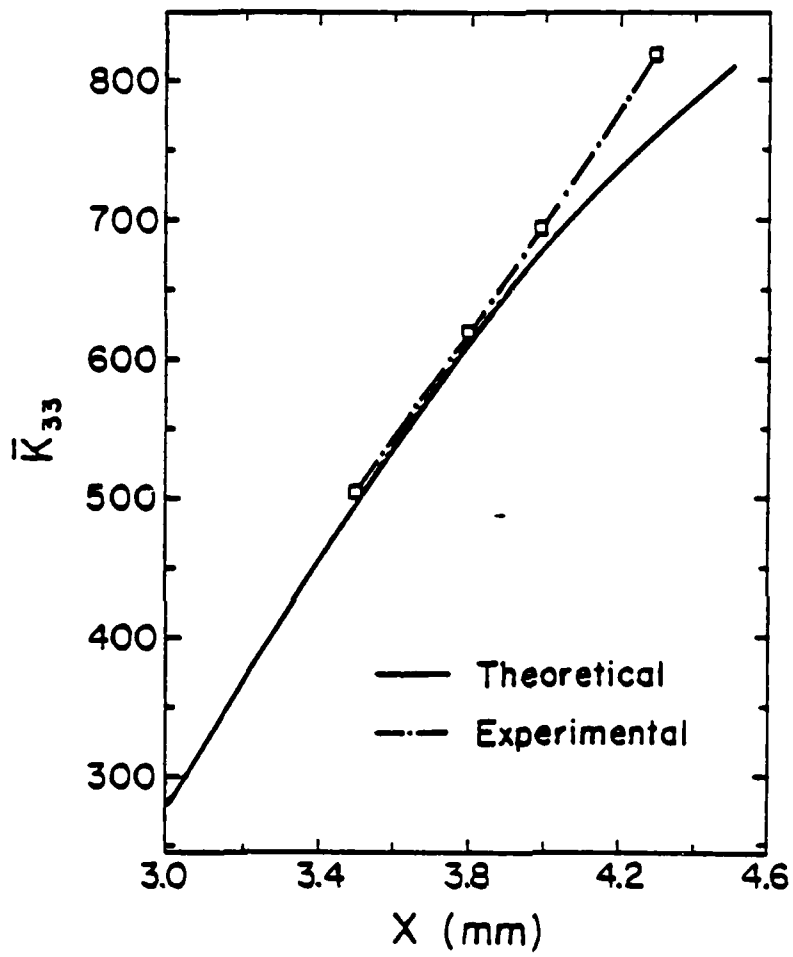


Fig. 4. Variation of dielectric constant \bar{K}_{33} as a function of x (the center to center distance for adjacent holes).

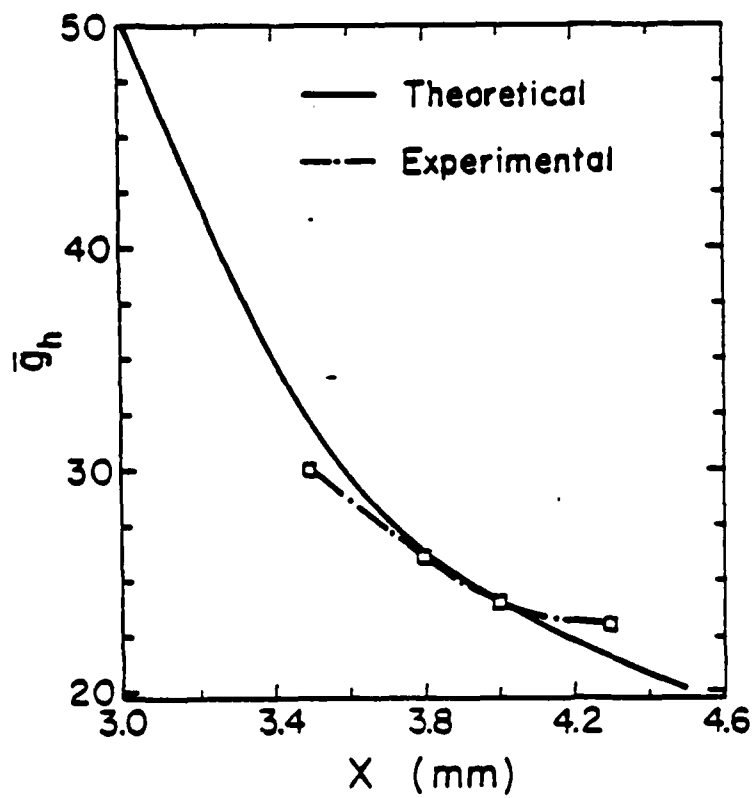


Fig. 5. Variation of the hydrostatic voltage coefficient \bar{g}_h as a function of x (the center to center distance for adjacent holes).

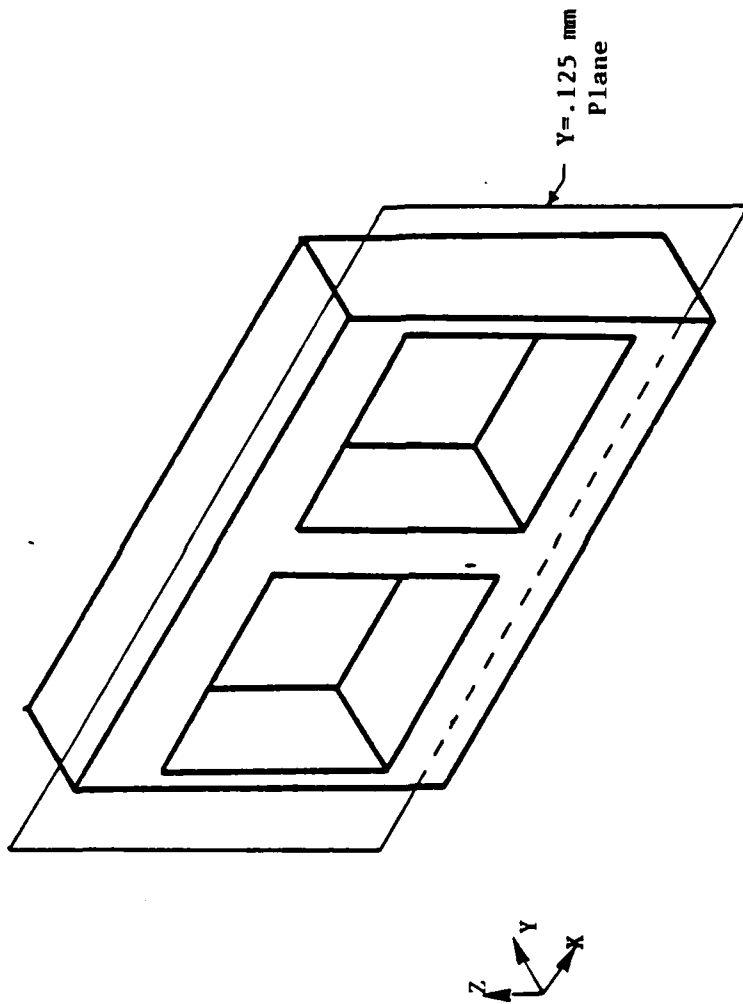


Fig. 6. An isometric view of a 3-1 perforated composite showing the Y=.125mm plane on which the stress is projected in Figures 8-10.

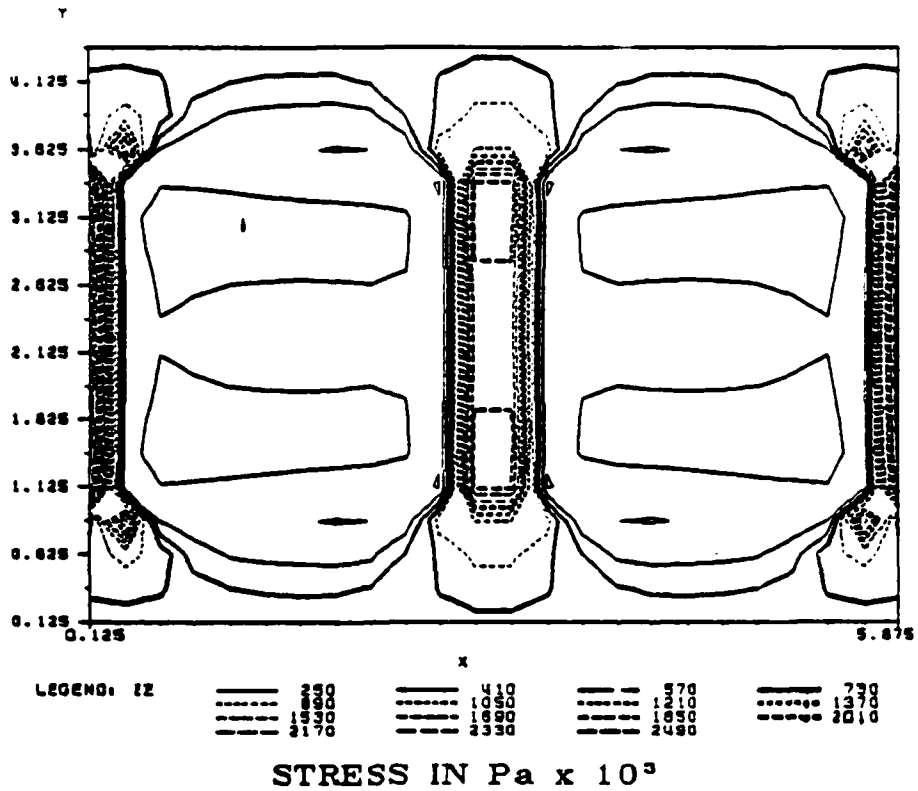


Fig. 9. A contour map of the ZZ component of the stress tensor projected onto the Y=.125mm plane.

POLARIZATION

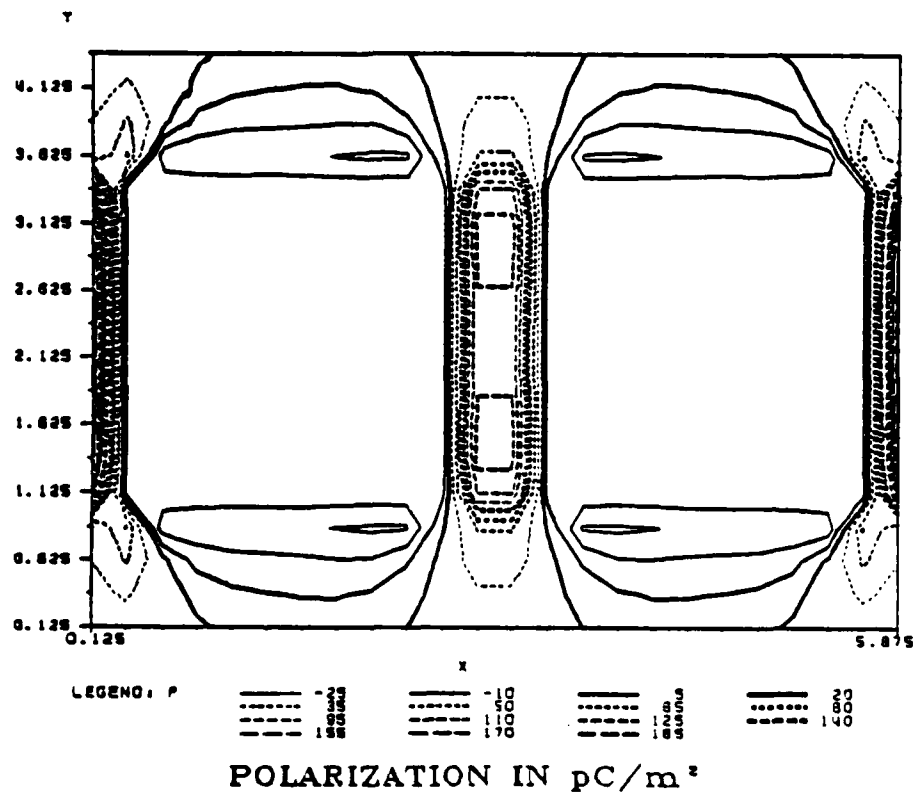


Fig. 10. A contour map of the polarization projected onto the Y=.125mm plane.

ELECTROSTRICTION TENSOR COMPONENTS OF
ALKALINE-EARTH FLUORIDE SINGLE CRYSTALS

Z.Y. Meng, Y.M. Sun, and L.E. Cross

ELECTROSTRICTION TENSOR COMPONENTS OF ALKALINE-EARTH FLUORIDE SINGLE CRYSTALS

Z.Y. MENG *, Y.M. SUN and L.E. CROSS **

*Materials Research Laboratory, The Pennsylvania State University,
University Park, PA 16802, USA*

Received 3 August 1984

The separated electrostriction tensor components for alkaline-earth fluoride single crystals have been measured by the converse method using the uniaxial stress dependence of the dielectric permittivity. Values obtained for the individual components of the electrostrictive voltage coefficients were $M_{11} = -0.116$, $M_{12} = 0.109$ and $M_{44} = 0.538$ for SrF_2 and $M_{11} = -0.107$, $M_{12} = 0.123$ and $M_{44} = 0.594$ for BaF_2 , respectively, in units of $10^{-20} \text{ m}^2/\text{V}^2$. The corresponding values for CaF_2 have been reported elsewhere.

In the space group O_h^F , CaF_2 , SrF_2 and BaF_2 are of interest as a set of isomorphous cubic crystals with the fluorite structure which are good electrical insulators. The separated quadratic electrostriction tensor components for calcium fluoride have been reported in ref. [1]. In this note, measured values of electrostriction coefficients for alkaline-earth fluoride single crystals SrF_2 and BaF_2 are given. Apparently there are no previous measurements of electrostriction tensor components for these crystals.

The measurements were made using the uniaxial stress dependence of the dielectric permittivity. The apparatus and procedures in the present experiment are the same as those described in a previous paper [1]. Samples of strontium and barium fluoride single crystals of high-purity optical grade were purchased from Harshaw Company and prepared in the form of flat cylindrical plates 23 mm in diameter, 1.5 mm in thickness. Plates with $\langle 100 \rangle$, $\langle 110 \rangle$, and $\langle 111 \rangle$ directions normal to the major surface were prepared.

From measurements for a sequence of different stress levels, the variations of electrical capacitance of

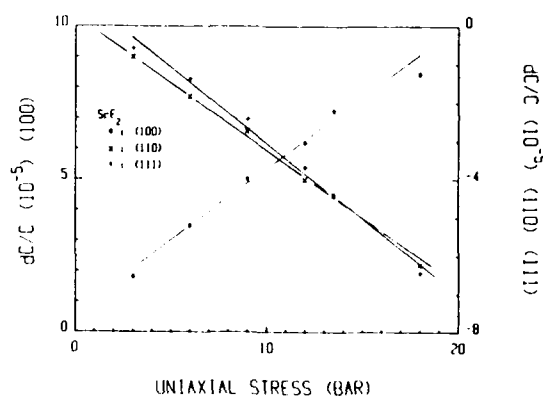


Fig. 1. Uniaxial stress dependence of capacitance change for SrF_2 .

the SrF_2 and BaF_2 samples shown in figs. 1 and 2 respectively were obtained. In order to facilitate comparison of the capacitance variations for CaF_2 , SrF_2 and BaF_2 in each crystal orientation, these results are plotted in figs. 3, 4 and 5 for $\langle 100 \rangle$, $\langle 110 \rangle$ and $\langle 111 \rangle$ orientations respectively. It is clear that there is an increase in the capacitance (and therefore the dielectric constants) with stress for $\langle 100 \rangle$ orientation, but a decrease for both $\langle 110 \rangle$ and $\langle 111 \rangle$ orientations. The plots for $\langle 100 \rangle$ and $\langle 110 \rangle$ orientated crystals are very similar

* On leave from the Department of Electronic Engineering, Xian Jiaotong University, Xian, Peoples Republic of China.

** Also affiliated with the Department of Electrical Engineering.

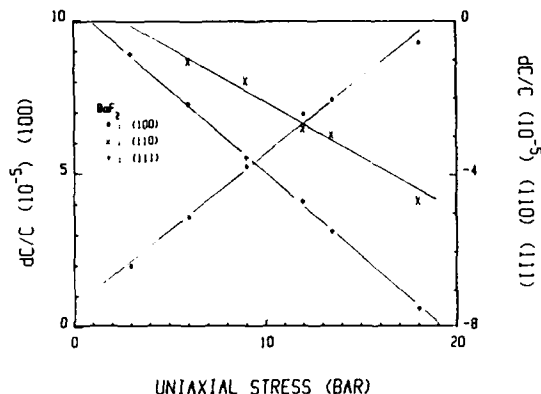


Fig. 2. Uniaxial stress dependence of capacitance change for BaF₂.

to those of alkali halides [3,4]. Under applied uniaxial stress, however, the capacitance changes for alkaline-earth fluorides are obviously lower than those of alkali halides.

When subjected to hydrostatic pressure, these crystals show a decrease in dielectric permittivity [5,6]. In order to calculate the electrostriction tensor components, the values for the hydrostatic M -coefficients were calculated from the data of ref. [6]. The values are $M_h = 0.1012 \pm 0.005$ for SrF₂ and $M_h = 0.1362 \pm 0.005$ for BaF₂ in units of $10^{-20} \text{ m}^2/\text{V}^2$ respectively. Using these values and the slopes of the curves in figs. 1 and 2, the values of the separated tensor components can be obtained and are summarized in table 1.

In the measurements, the major potential sources

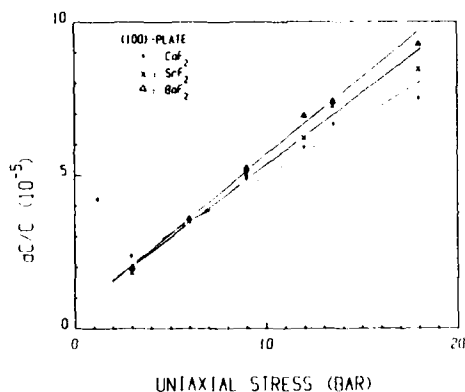


Fig. 3. Uniaxial stress dependence of capacitance change for (100) orientated CaF₂, SrF₂ and BaF₂.

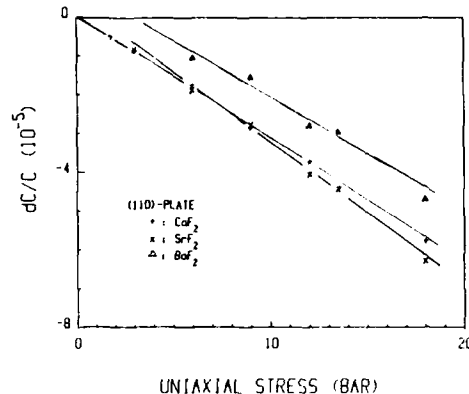


Fig. 4. Uniaxial stress dependence of capacitance change for (110) orientated CaF₂, SrF₂ and BaF₂.

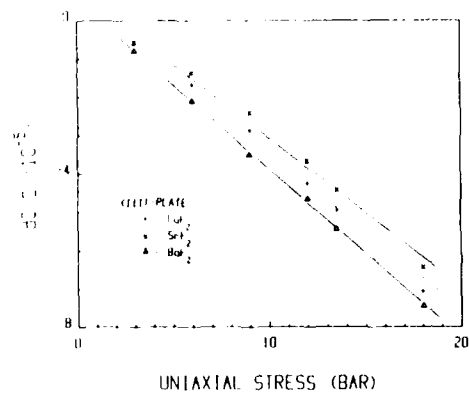


Fig. 5. Uniaxial stress dependence of capacitance change for (111) orientated CaF₂, SrF₂ and BaF₂.

of error have been discussed in the previous paper. The total error of measurement value from all sources is estimated to be less than $\pm 10\%$.

In view of the correlation expected between elastic compliance, thermal expansion and electrostrictive

Table 1
The electrostriction tensor coefficients for alkaline-earth fluoride single crystals in units of $10^{-20} \text{ m}^2/\text{V}^2$

Crystal	M_{11}	M_{12}	M_{44}	$(M_{1212})^a$
CaF ₂	-0.132	+0.117	+0.507	(+0.128)
SrF ₂	-0.116	+0.109	+0.538	(+0.138)
BaF ₂	-0.107	+0.123	+0.594	(+0.149)

a) $M_{44} = 4M_{1212}$.

behavior, the trends of the data with changing cation are as expected. The consistency and regularity of the data give added confidence to what is an exceedingly difficult experimental procedure, and suggest that the converse method of measurement may be more reliable than earlier attempts at direct measurement.

References

- [1] Z.Y. Meng and L.E. Cross, *J. Appl. Phys.*, to be published.
- [2] K. Rittenmeyer, Ph.D. Thesis, The Pennsylvania State University (1984).
- [3] G. Balakrishnan, K. Srinivasan and R. Srinivasan, *J. Appl. Phys.* 54 (1983) 2675.
- [4] P. Preu and S. Hanssuhl, *Solid State Commun.* 45 (1983) 619.
- [5] C. Andeen, D. Schnele and J. Fontanella, *Phys. Rev. B* 6 (1972) 591.
- [6] G.A. Samara, *Phys. Rev. B* 13 (1976) 4529.

POLARIZATION AND DEPOLARIZATION BEHAVIOR OF HOT PRESSED
LEAD LANTHANUM ZIRCONATE TITANATE CERAMICS

Yao Xi, Chen Zhili, and L.E. Cross

POLARIZATION AND DEPOLARIZATION BEHAVIOR OF HOT PRESSED LEAD LANTHANUM ZIRCONATE TITANATE CERAMICS

YAO XI, CHEN ZHILI, AND L.E. CROSS

Materials Research Laboratory, The Pennsylvania State University, University Park, PA 16802

Abstract—Studies have been made of the polarization and depolarization behavior for lead lanthanum zirconate titanate ceramics with zirconia:titanium ratio 0.65/0.35 and La_2O_3 content from 0.07 to 0.095 (7:65:35 to 9.5:65:35). Continuity of the dielectric dispersion on cooling unbiased freshly de-aged samples suggests that across this whole composition range for temperatures below the dielectric maxima, there are no macroscopic phase changes. Large remanent polarizations may be built up at low temperatures by cooling under suitable DC bias, but the ceramics will 'stand off' significant bias levels applied at low temperature and remain dispersive. Depoling on heating becomes progressively less abrupt with increasing La_2O_3 content but is always accomplished well below the temperature of the dielectric maximum. A model involving the ordering and disordering of polar micro-regions under electrical and thermal fields accounts well for the observed properties.

INTRODUCTION

The thermal depolarization behavior of electrically poled lead lanthanum zirconate titanate (PLZT) ceramics with compositions in the range of $\text{PbZr}_{0.65}\text{Ti}_{0.35}\text{O}_3$ with La_2O_3 additions of 6-, 7-, and 8-mole% La_2O_3 have been of interest for the behavior of the pyroelectric current, dielectric response, and electro-optic characteristics¹⁻³. It was clear from the early studies of Keve⁴ that depolarization of a short-circuited PLZT of composition 7:65:35 occurs at a temperature well below that of the dielectric permittivity maximum. Dielectric data of Salanek⁵ suggest that the K' maximum is strongly dispersive as in ferroelectrics with diffuse phase transitions (relaxors). More recent measurements by Kimura, Newnham, and Cross⁶ of the elastic shape memory effect suggest that the shape changing ferroelastic macrodomains are lost in these ceramics at the lower depoling temperature.

The present study was carried out to investigate more fully both poling and depoling characteristics of transparent hot pressed PLZTs covering the composition range from (7 to 9.5):65:35. Data for the 8% La_2O_3 composition have been presented earlier⁷, but some are reproduced again here to compare with the 8.8 and 9.5% La_2O_3 compositions.

SAMPLE PREPARATION AND EXPERIMENTAL PROCEDURE

Ceramics used in these studies were provided by the Shanghai

Institute of Ceramics in China. Wafers used in the present study were cut from boules of near theoretical density, high optical transparency and mean grain sizes in the range 2 to 5 μm .

Dielectric properties were measured on a computerized automatic measuring system using the HP LCR meters HP 4274A and 4275A under HP 9825 computer control. Pyroelectric currents were measured with an HP 4140B picoammeter. A Delta Design 2300 environment chamber covered the range -150 to 200°C and temperature were measured with a platinum resistance thermometer on a Fluke 8502A digital multimeter. Special software was developed for automatic measurement and all data were recorded on flexible magnetic disks.

EXPERIMENTAL RESULTS

The temperature dependence of dielectric permittivity in 8:65:35 PZT cooling under zero bias, and under a DC bias of 3 kV/cm for a cooling rate of $3^\circ\text{C}/\text{min}$ is shown in Figure 1a and 1b. Suppression of the dispersive behavior (relaxor character) under bias is clearly evident at temperatures below 55°C . Similarly for an 8:65:35 PLZT sample cooled to -75°C then biased to 3 kV/cm and heated at $3^\circ\text{C}/\text{min}$ (Fig. 2), the persistence of the dispersion up to a temperature T_f followed by a suppressed no dispersive region (2) a re-emergence of dispersion below T_m (3) and the conventional higher temperature non-dispersive regions (4) are quite evident. That T_f and T_m are poling and depoling temperatures is evidenced from the pyroelectric currents (Fig. 3), and the integrated current shows the corresponding build up and decay of macroscopic polarization.

Data has already been presented to show that T_f decreases with increasing bias field, and the kinetic nature of the change is evident from the dependence upon heating rate⁷.

In the 8.8/65/35 PZT, on cooling a freshly de-aged sample again the dispersive character of a relaxor ferroelectric is clearly evidenced (Fig. 4a). Here, however, under even high DC bias of 15 kV/cm the relaxation is not completely suppressed and there is no evidence of an abrupt change such as that seen in the 8/65/35 compositions (Fig. 4b). That the polarization builds up and decays in a rather similar manner to that in the ceramics of lower lanthanum content is, however, evident from the integrated pyroelectric response for a sample cooled under field (Fig. 5[2]) as compared to that of a sample cooled without field to -100°C then biased to 3 kV/cm and heated at a constant rate of $3^\circ\text{C}/\text{minute}$ (Fig. 5[1]).

It may be noted that the major changes with increased La_2O_3 content is that the polarization levels are lower, the changes are more gradual and occur at lower temperature.

In the 9.5:65:35 this trend is continued (Fig. 6) and here a higher field of 6.6 kV/cm was used to produce comparable polarization changes. Larger polarization levels can be induced in both 8.8 and 9.5% La_2O_3 compositions, but only by going to much higher field levels.

DISCUSSION

The continuity of the dispersion curves in all samples below T_m suggests that in the absence of a driving field none of the materials goes through a normal macroscopic phase change below T_m . This would appear to be confirmed by recent measurements in Shanghai of W. Yin and colleagues⁽⁸⁾ who show that in grain grown PLZTs of the 8:65:35 composition the individual grains have isotropic optical properties below T_m in the absence of an external field.

For the 8.8:65:35 and 9.5:65:35, the dispersion and poling: depoling behavior are remarkably similar to those observed in $Pb(Mg_{1/3}Nb_{2/3})O_3$, $Pb(Sc_{1/2}Ta_{1/2})O_3$ and other relaxor ferroelectrics. It is thus tempting to apply the model of ordering of polar micro regions under field, and disordering under temperature to describe the observed build up and decay of polarization. That the 8:65:35 composition is optically isotropic grain by grain on cooling again suggests the model of disordered polar micro-regions. However, in this composition the disordering is rather abrupt and has many of the features of a phase change.

We suggest in speculation, that in analogy to magnetism, the PMN, PST, 8.8:65:35 and 9.5:65:35 compositions may be superparaelectric but that in the 8:65:35 the phenomena may be more analogous to that of critical superparamagnetism.

REFERENCES

1. A.H. Meitzler and H.M. O'Bryan, *J. Am. Ceram. Soc.* **55**, 54 (1972).
2. G.H. Haertling and C.E. Land, *J. Am. Ceram. Soc.* **54**, 1 (1971).
3. G.H. Haertling, *J. Am. Ceram. Soc.* **54**, 303 (1971).
4. E.T. Keve and K.L. Bye, *J. Appl. Phys.* **46**, 810 (1975).
5. W.R. Salaneck, *J. Appl. Phys.* **43**, 4468 (1972).
6. T. Kimura, R.E. Newnham, and L.E. Cross, *Phase Transitions* **2**, 113 (1981).
7. Yao Xi, Chen Zhili, and L.E. Cross, *J. Appl. Phys.* **54**(6):339 (1983).
8. B.H. Chu, H.K. Ngao, X.S. Zheng, and Z.W. Yin, *Joint US:China Seminar on Microstructure and Properties of Ceramic Materials*, Shanghai, May, 1983 (to be published).

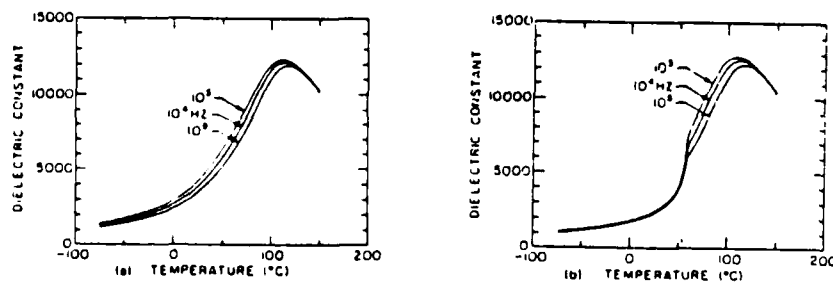


Figure 1. Temperature dependence of dielectric constant of PLZT 8:65:35 (a) without and (b) under dc bias of 3 kV/cm at cooling rate of 3°C/min.

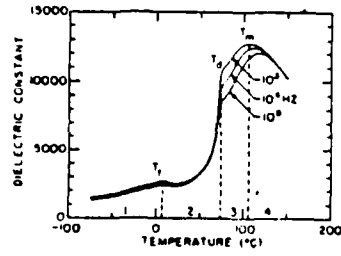


Figure 2. Temperature dependence of dielectric constant of PLZT 8:65:35 under dc bias of 3 kV/cm at heating rate of 3°C/min.

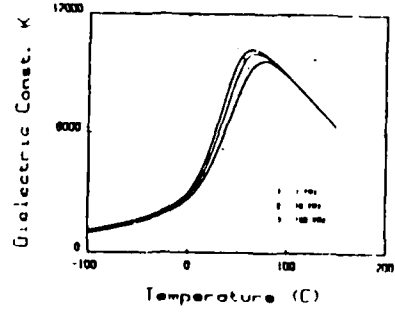


Figure 4(b). Dielectric permittivity in PLZT 8:8:65:35 ac field 100 V/cm, dc bias 15 kV/cm, cooling at 3°C/min.

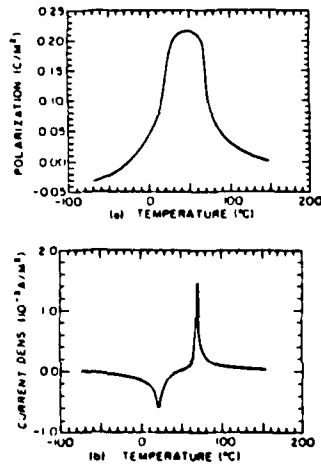


Figure 3. The buildup and decay of (a) the remanent polarization and (b) associated charging and discharging current of PLZT 8:65:35 under dc bias of 3 kV/cm at constant heating rate.

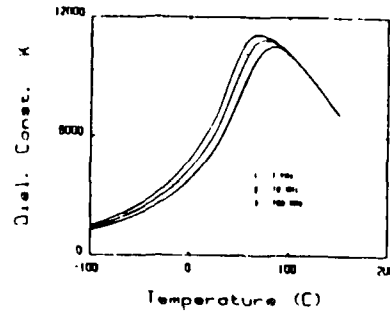


Figure 4(a). Dielectric permittivity in PLZT 8:8:65:35 E field 100 V/cm, cooling at 3°C/min.

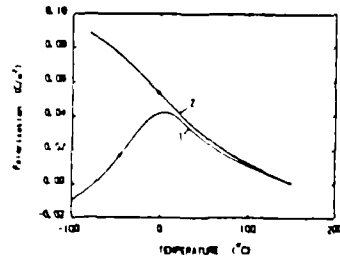


Figure 5. Polarization in PLZT 8:8:65:35 (1) Depoled sample heated at 3°C/min 3kV/cm (2) Cooling under a field of 3 kV/cm.

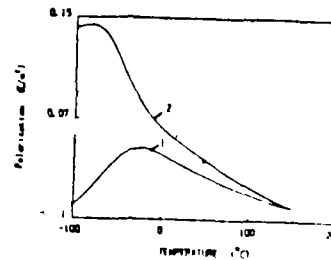


Figure 6. Poling and depoling in PLZT 9.5:65:15 (1) Depoled sample heating at 3°C/min under bias of 6.6 kV/cm (2) Depoling after pre-poling by cooling under 30 kV/cm dc bias 6.6 kV/cm heating rate 3°C/min.

AD-A160 465

PIEZOELECTRIC AND ELECTROSTRICTIVE MATERIALS FOR
TRANSDUCER APPLICATIONS(U) PENNSYLVANIA STATE UNIV
UNIVERSITY PARK MATERIALS RESEARCH LAB

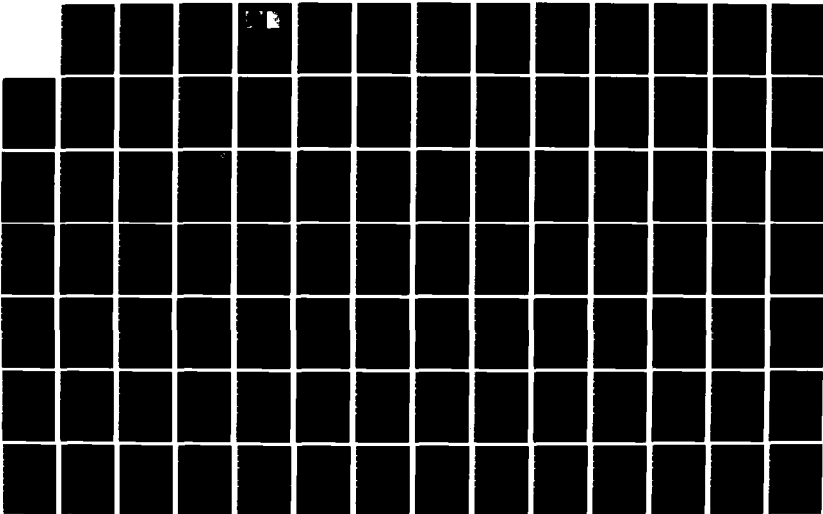
2/4

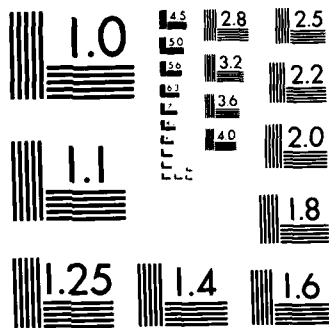
UNCLASSIFIED

L E CROSS ET AL. MAY 85 N00014-82-K-0339

F/G 9/1

NL





MICROCOPY RESOLUTION TEST CHART
NATIONAL BUREAU OF STANDARDS 1963 A

ELECTRON MICROSCOPY OF ORDERED DOMAINS IN
LEAD SCANDIUM TANTALATE $\text{Pb}(\text{Sc}_{0.5}\text{Ta}_{0.5})\text{O}_3$

M.P. Harmer, A. Bhalla, B. Fox, and L.E. Cross

ELECTRON MICROSCOPY OF ORDERED DOMAINS IN LEAD SCANDIUM TANTALATE



M.P. HARMER

Materials Research Center, Lehigh University, Bethlehem, PA 18015, USA

and

A. BHALLA, B. FOX and L.E. CROSS

Materials Research Laboratory, The Pennsylvania State University, University Park, PA 16802, USA

Received 3 February 1984; in final form 17 February 1984

In single crystal lead scandium tantalate micro-domains with an ordered arrangement of Sc:Ta have been observed directly in transmission electron microscopy. The scale of the ordered structures in the size range 35 to 120 nm agrees well with earlier indirect measurements from X-ray superlattice line broadening.

Lead scandium tantalate $\text{Pb}(\text{Sc}_{0.5}\text{Ta}_{0.5})\text{O}_3$ (PST) is a most interesting example of the mixed B cation lead containing PbBO_3 perovskites, materials which often show "relaxor-type" diffuse ferroelectric transition behavior. In PST, X-ray studies have shown that this material lies very close to the boundary between order and disorder in the $\text{Sc}^{3+}:\text{Ta}^{5+}$ arrangement on the B sites so that the degree of ordering can be controlled by suitable thermal treatment [1].

The key role of local compositional heterogeneity in the diffuse transition behavior is evidenced in PST by the fact that quenched disordered crystals and ceramics show classical relaxor character with a broad frequency-dependent maximum in dielectric permittivity over the Curie range whereas the annealed highly ordered material exhibits a sharp first-order phase change [2,3].

Heretofore, the size and shape of the ordered micro-regions in crystals and ceramics has been deduced indirectly by X-ray diffraction analysis of the intensity and profile of the superlattice reflections from ordered domains. The purpose of the present note is to present the first direct evidence for the existence of such ordered micro-domains using transmission electron microscopy (TEM).

Single crystals of $\text{Pb}(\text{Sc}_{0.5}\text{Ta}_{0.5})\text{O}_3$ for TEM study were grown by a flux technique which has been described elsewhere [4]. X-ray diffraction analysis indicated that the as grown crystals were 70% ordered. The degree of line broadening suggested that the micro-domain size was in the range of 10–100 nm. Electron transparent thin foils for TEM investigation were prepared by argon-ion-beam thinning using 6 kV argon ions incident 12° to the foil plane. The samples were examined using a Philips EM400 transmission electron microscope operating at 120 kV.

The ordered domain structure was visible in the TEM only when the foil was suitably oriented to include superlattice reflections in the diffraction pattern. A bright-field image of the ordered domains is shown in fig. 1. The micro-domains appear as ordered regions separated by antiphase domain boundaries (APBs) [5], and they can be seen to range in size from ≈ 35 nm to ≈ 120 nm consistent with the results of the X-ray diffraction studies. The APBs were visible in dark field only when a superlattice reflection was used to form the image.

The diffraction pattern corresponding to the bright-field image of fig. 1 is shown in fig. 2. The crystal was oriented with the electron beam parallel to the $\langle 211 \rangle$

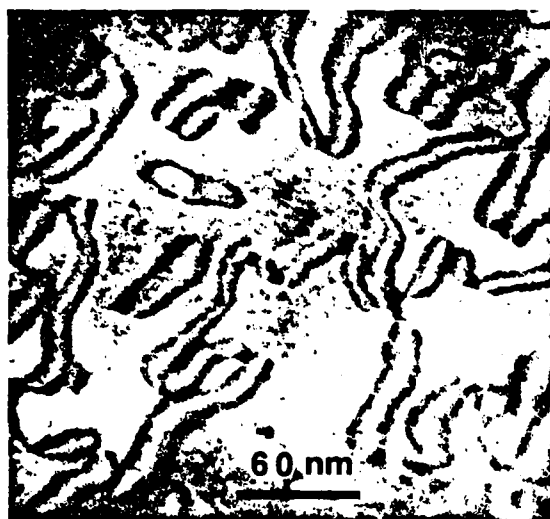


Fig. 1. Bright-field transmission electron micrograph showing antiphase domain boundaries in single crystal PST.

zone axis in order to excite strong superlattice reflections of the type $\{111\}$ and $\{311\}$. The diffraction pattern has been indexed so that the indices refer to the double-cell unit cell of PST ($a_0 = 0.813$ nm).

In a subsequent paper, we shall present a complete electron microscopy characterization of these materials including a comparison of single crystals and polycrystals and the effects of varying degrees of disorder induced by thermal annealing. Quantitative analytical electron microscopy will be used to study the microchemistry of the domains using STEM microanalysis.

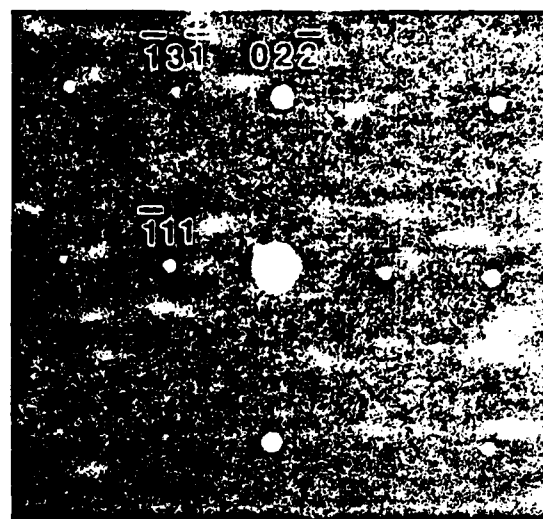


Fig. 2. Selected area diffraction pattern ($\langle 211 \rangle$ zone axis) corresponding to the bright-field image of fig. 1. Note the presence of superlattice reflections at $g = \bar{1}11$ and $\bar{1}3\bar{1}$.

The authors are grateful to the Office of Naval Research for financial support of this work.

References

- [1] N. Setter and L.E. Cross, *J. Mat. Sci.* 15 (1980) 2478.
- [2] N. Setter and L.E. Cross, *J. Appl. Phys.* 51 (1980) 4356.
- [3] N. Setter and L.E. Cross, *Phys. Stat. Sol.* 61a (1980) K71.
- [4] N. Sitter and L.E. Cross, *J. Crystal Growth* 50 (1980) 555.
- [5] J.W. Edington, *Practical electron microscopy in materials science* (Macmillan Press, London, 1975) p. 43.

PRESSURE DEPENDENCE OF THE REFRACTIVE INDEX AND
DIELECTRIC CONSTANT IN A FLUOROPEROVSKITE, KMgF_3

Kenji Uchino, Shoichiro Nomura,
K. Vedam, Robert E. Newnham, and Leslie E. Cross

Pressure dependence of the refractive index and dielectric constant in a fluoroperovskite, KMgF_3

Kenji Uchino and Shoichiro Nomura

Department of Physical Electronics, Tokyo Institute of Technology, Ookayama, Meguro-ku, Tokyo 152, Japan

K. Vedam, Robert E. Newnham, and Leslie E. Cross

Materials Research Laboratory, The Pennsylvania State University, University Park, Pennsylvania 16802

(Received 30 June 1983)

The hydrostatic-pressure dependence of the refractive index and the low-frequency dielectric constant of a perovskite-type single crystal, KMgF_3 , have been determined at room temperature. The refractive index n for $\lambda = 589.3$ nm increases monotonously in proportion to pressure p with a slope of $\partial n / \partial p = 2.46 \times 10^{-4} \text{ kbar}^{-1}$. On the other hand, the dielectric constant at 10 kHz decreases with increasing pressure, from which the electric-displacement-related electrostrictive coefficient Q_h ($= Q_{11} + 2Q_{12}$) is calculated as $0.24 \text{ m}^4 \text{ C}^{-2}$. These data are compared with the $\partial n / \partial p$ values and the Q_h coefficients of various alkali fluorides and perovskite oxides.

I. INTRODUCTION

The electric-displacement-related electrostrictive coefficients of a cubic perovskite-type or a rocksalt-type crystal ($m3m$) are defined by

$$Q_{11} = \frac{1}{2} \frac{\partial^2 x_1}{\partial D_1^2} \quad (1)$$

and

$$Q_{12} = \frac{1}{2} \frac{\partial^2 x_2}{\partial D_1^2}, \quad (2)$$

where x_1 and x_2 are the longitudinal and transverse-induced strains, respectively. By using a Maxwell relation, Eqs. (1) and (2) are transformed as follows:

$$Q_{11} = -\frac{1}{2} \frac{\partial(1/\epsilon_0 \epsilon_1)}{\partial X_1} \quad (3)$$

and

$$Q_{12} = -\frac{1}{2} \frac{\partial(1/\epsilon_0 \epsilon_1)}{\partial X_2}. \quad (4)$$

These equations indicate that the electrostrictive coefficients can be obtained by measuring the stress X dependence of the reciprocal dielectric permittivity ($1/\epsilon$). When a hydrostatic pressure p ($= -X_1 = -X_2 = -X_3$) is applied to a paraelectric crystal, the pressure dependence of the dielectric constant is represented by

$$\frac{\partial(1/\epsilon_1)}{\partial p} = 2\epsilon_0 Q_h, \quad (5)$$

where $Q_h = Q_{11} + 2Q_{12}$ and ϵ_0 is the permittivity of free space.

Recent investigations of perovskite-type oxides have clarified the relationship between the electrostrictive effect and crystal structure.¹⁻⁴ The electrostrictive coefficient Q_h differs by an order of magnitude depending on the degree of order in the cation arrangement of complex

perovskites. Because of these variations, it is interesting to examine perovskite-type halide crystals which are amenable to a rather simpler theoretical treatment than the oxides. This paper is concerned mainly with the electrostrictive properties of a perovskite-type fluoride, KMgF_3 . If we assume that a certain ionic shift causes the same elastic strain in fluorides and oxides on the basis of an intuitive "ion-rattling" model,⁵ then the electrostrictive Q coefficients in fluorides are expected to be larger than in oxides because the lower valences in fluorides result in smaller induced polarizations.

We have measured both the dielectric constant and the refractive index at room temperature as a function of hydrostatic pressure, so that the dielectric constant is separated experimentally into two parts, ϵ_{el} and ϵ_{ion} , which originate from the electronic polarizability and from the ionic shifts, respectively. It is also interesting to separate the contribution of the electronic polarizability to the electrostriction from that of the ionic polarizability, especially in simple low-permittivity dielectrics.

The fluoride used in this study, KMgF_3 , was first synthesized by van Arkel,⁶ and has a simple cubic perovskite-type structure with a lattice constant of $a = 3.973$ Å at room temperature.⁷ The elastic moduli have been measured precisely by the pulse superposition technique as a function of hydrostatic pressure and revealed no anomaly up to 2.5 kbars, showing only a gradual increase in stiffness.⁸

II. EXPERIMENTAL RESULTS

A. Pressure dependence of refractive index

Since the procedure for this measurement is the same as that described earlier,⁹ only a brief outline is described here. In principle, Ramchandran's interferometric method¹⁰ was adapted to an optical high-pressure cell. A schematic diagram of the experimental arrangement is shown in Fig. 1. A single-crystal plate of KMgF_3 with orientation $\langle 100 \rangle$ and dimensions of about $10 \times 10 \times 2$

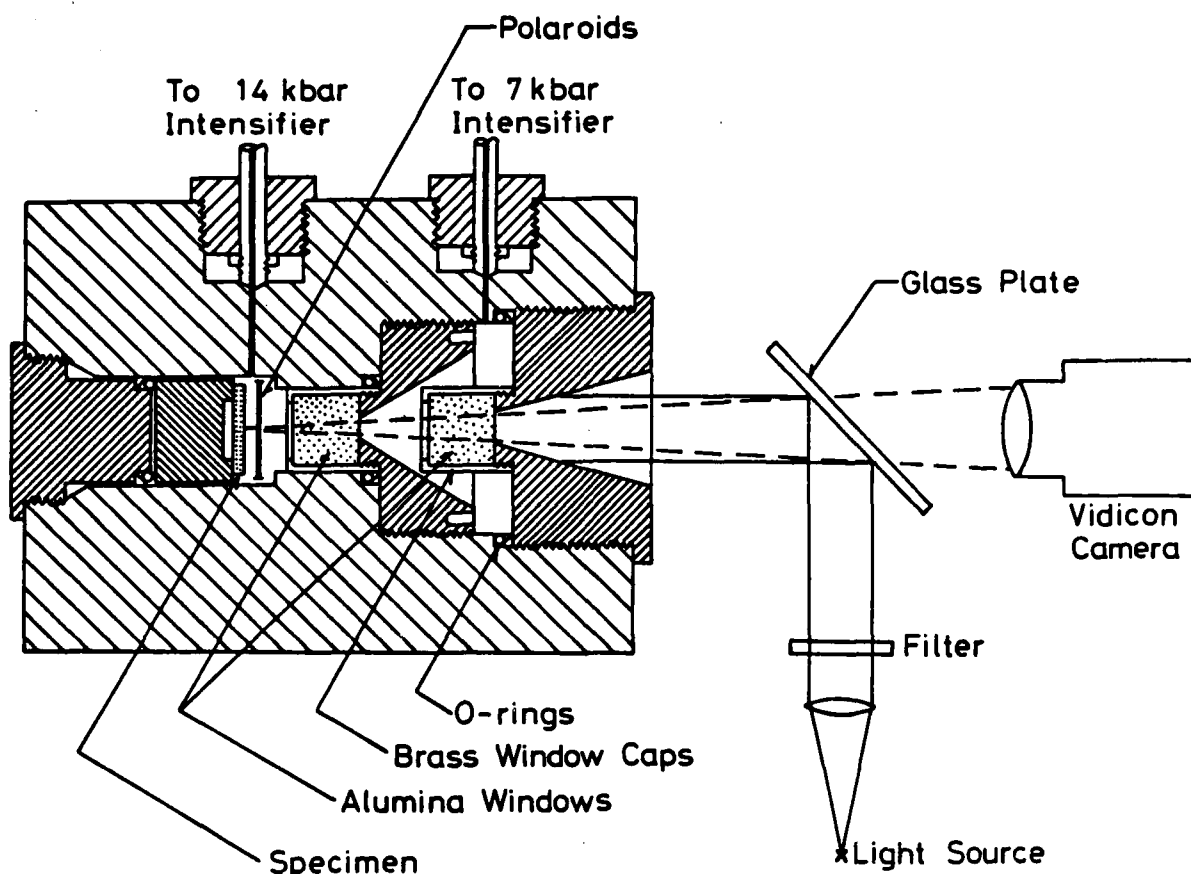


FIG. 1. Schematic drawing of the experimental arrangement for measuring the refractive-index change under high hydrostatic pressure.

mm³ was cut, ground, and polished to be nearly optically parallel, so that localized Newtonian interference fringes could easily be observed across the major faces of the crystal. The major surfaces were then coated with a thin film of aluminum to increase the sharpness of the fringes. The two-stage optical pressure vessel was of conventional design, with two single-crystal alumina windows whose optically flat surfaces were kept pressed against matching optically flat faces of two steel plugs. The two windows are positioned in such a way that neither window experiences a pressure difference greater than 10 kbars at any time. Two Harwood intensifiers with conventional hand pumps served as the pressure generating system. Pressures up to 7 kbars could be read off directly with the help of a calibrated Heise gauge accurate to ± 7 bars. For higher pressures a manganin resistance gauge was employed in conjunction with a Carey-Foster bridge. Plexol 262 [di-(2-ethylhexyl) adipate] marketed by Rohm and Haas Co. was used as the fluid-pressure medium.

The specimen suitably supported in the pressure cell was illuminated with collimated light from a sodium lamp ($\lambda = 589.3$ nm) and the localized fringes on the specimen could be observed through a telemicroscope or a vidicon camera coupled to a TV monitor. When the specimen is subjected to hydrostatic pressure, both the thickness and the refractive index of the crystal change, with consequent shift of the fringes across a fiducial mark on the specimen. The change in the refractive index Δn is

calculated from the interference formula

$$\Delta n = (m\lambda - 2n\Delta t) / 2t^0, \quad (6)$$

where m is the number of fringes shifted, t^0 is the initial thickness of the specimen, Δt is the change in thickness due to the compression, and λ is wavelength of the light. Elastic stiffnesses of $c_{11} = 138$ GPa and $c_{12} = 44$ GPa (Ref. 8) were used to evaluate Δt .

Figure 2 represents the variation of the refractive index n (the initial value $n^0 = 1.404$) of KMgF_3 at room temperature for hydrostatic pressures up to 14 kbars. The refractive index for $\lambda = 589.3$ nm increases linearly with a slope of 2.46×10^{-4} kbars⁻¹ up to about 9 kbars, and thereafter a clear departure from linearity is observed. This could be interpreted as either (a) nonlinear piezooptic behavior brought about by nonlinear elastic behavior at high pressures or (b) possible onset of a phase transition at 9 kbars causing a change in the slope $\Delta n / \Delta p$. Recent precision measurements by Jones⁸ on the elastic constants of KMgF_3 and their variation with pressure up to 2.5 kbars indicate that KMgF_3 behaves quite normally like most other crystals, whose compressibility decreases with increasing pressure. On the other hand, all the crystalline materials studied thus far^{9,11,12} exhibit either linear or sublinear $\Delta n / \Delta p$ relationships at high pressures, whereas KMgF_3 exhibits a superlinear $\Delta n / \Delta p$ relationship as shown in Fig. 2. Hence it is unlikely that this unusual

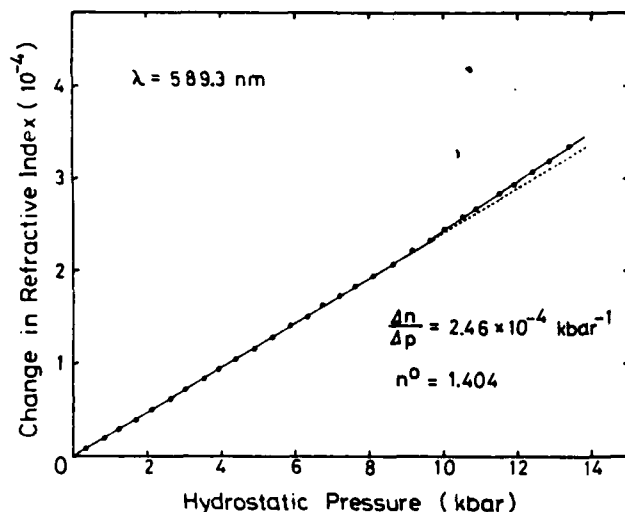


FIG. 2. Variation of the refractive index in KMgF_3 with hydrostatic pressure, measured with a sodium lamp ($\lambda = 589.3$ nm) at room temperature.

behavior is associated with the normal nonlinear piezo-optic behavior. At the same time it is felt that further optical, dielectric, and x-ray studies are necessary before we can definitely conclude that the unusual piezo-optic behavior above 9 kbars is due to a phase transition. Finally it may be mentioned that the pressure derivative of the refractive index $\partial n/\partial p$ is almost of the same magnitude as those of alkali fluorides such as LiF and NaF (see Table I).

B. Pressure dependence of dielectric constant

The effect of hydrostatic pressure on the dielectric constant has been investigated up to 1 kbar using a square

specimen $10 \times 10 \times 0.5$ mm³ in dimensions with gold-sputtered electrodes. Capacitance was measured by a three-terminal method with an automatic capacitance bridge (Yokogawa-Hewlett-Packard, 4192A) over the frequency range 1 to 100 kHz. The stray capacitance of the high-pressure cell used (manufactured by Riken Seiki Co, Ltd.) is about 0.2 pF, much less than the sample capacitance of 10 pF. No significant dielectric dispersion was observed in the above frequency range. The initial dielectric constant ϵ^0 is 6.97 at 10 kHz, measured at $p = 1$ bar. The value of hydrostatic pressure generated by a conventional oil-pressure hand pump was monitored by a Riken gauge with an accuracy of ± 8 bars.

Figure 3 shows the relative permittivity change $\Delta\epsilon/\epsilon^0$ of KMgF_3 with pressure, measured at room temperature at 10 kHz. The experimental error results mainly from the readout precision of the capacitance bridge with four decimal digits. The capacitance change due to the dimensional change with compression was calculated by using the elastic moduli of Jones.⁸ The dielectric permittivity decreases gradually with increasing hydrostatic pressure; this is quite similar to the behavior in alkali halides¹³ and cubic perovskite-type oxides.⁵ The electric-displacement-related electrostrictive coefficient Q_h is obtained from the pressure derivative of $\Delta\epsilon/\epsilon^0$ as $Q_h = 0.24$ m⁴C⁻², by using Eq. (5).

It is well known that the low-frequency dielectric constant ϵ ($\epsilon^0 = 6.97$) can be separated into two parts, ϵ_{el} and ϵ_{ion} , which originate from the electronic and the ionic polarizabilities, respectively. The high-frequency dielectric constant ϵ_{el} can be estimated from the optical refractive index n as

$$\epsilon_{el} = n^2 [\epsilon_{el}^0 = (1.404)^2]. \quad (7)$$

The pressure dependence of ϵ_{el} can, therefore, be derived from the experimental data in Sec. II A, and is inserted in

TABLE I. Refractive index n and its pressure derivative $\partial n/\partial p$, low-frequency dielectric constant ϵ , electrostrictive coefficient Q_h , and bulk modulus κ for several alkali fluorides, perovskite-type oxides, and fluorides at room temperature.

Material	Refractive index n ($\lambda = 589.3$ nm)	$\frac{\partial n}{\partial p}$ (10^{-4} kbar ⁻¹)	Relative permittivity ϵ	Electrostrictive coefficient Q_h (m ⁴ C ⁻²)	Bulk modulus κ (GPa)
LiF	1.392	1.9 ^b	9.06	0.32 ^c	65 ^a
NaF	1.328	2.17 ^b	5.08	0.46 ^c	46 ^a
KTaO ₃	2.252	-1.14 ^c	173 ^d	0.045 ^{d,f}	230 ^f
SrTiO ₃	2.407	-0.85 ^e	330	0.047 ^g	175 ^g
KMnF ₃	1.450 ^h		9.75	0.22 ^h	65 ⁱ
KMgF ₃	1.404	2.46	6.97	0.24	75 ^j

^a $\lambda = 632.8$ nm.

^bE. D. D. Schmidt, Ph.D. thesis, Solid State Science, Pennsylvania State University, 1972.

^cJ. L. Kirk, Ph.D. thesis, Solid State Science, Pennsylvania State University, 1972.

^dAt 450 K.

^eReference 13.

^fReference 14.

^gReference 15.

^hK. Gesi (private communication) and Ref. 16.

ⁱReference 17.

^jReference 18.

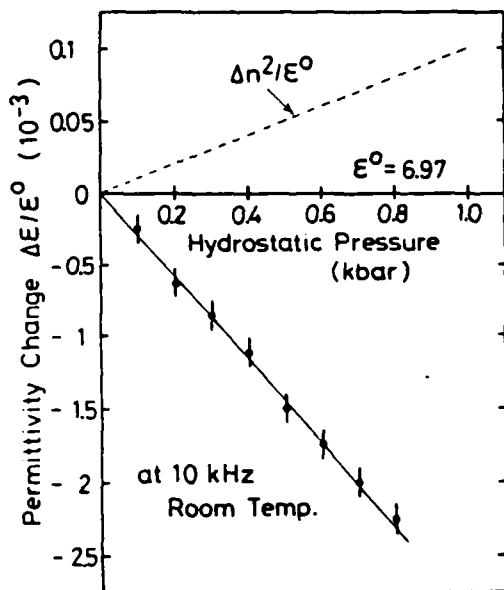


FIG. 3. Relative dielectric constant change $\Delta\epsilon/\epsilon^0$ in KMgF_3 with hydrostatic pressure, where ϵ^0 denotes the initial dielectric constant at $p=0$ kbar. The $\Delta n^2/\epsilon^0$ value which represents the dielectric constant $\Delta\epsilon_{el}/\epsilon^0$ originating from the electronic polarizability is also plotted with a dashed line.

Fig. 3 as a dashed line. The subtraction $\Delta\epsilon/\epsilon^0 - \Delta n^2/\epsilon^0$ gives $\Delta\epsilon_{ion}/\epsilon^0$. Taking account of the initial dielectric constants $\epsilon_{ion}^0=5$ and $\epsilon_{el}^0=2$, it is very interesting that the pressure derivative $(\partial\epsilon_{ion}/\partial p)$ is about 30 times as large as the $(\partial\epsilon_{el}/\partial p)$ value with the opposite sign. This leads to the conclusion that ionic shifts are the principal contribution to electrostriction rather than electronic polarizability.

III. DISCUSSION

The refractive index n and its pressure derivative $\partial n/\partial p$, the low-frequency dielectric constant ϵ , the electrostrictive coefficient Q_h , and the bulk modulus κ of the fluoroperovskite crystal KMgF_3 at room temperature are summarized in Table I, and compared with corresponding data for several alkali fluorides (LiF, NaF), perovskite oxides (KTaO_3 , SrTiO_3), and KMnF_3 .

The refractive indices of perovskite-type fluorides are similar to those of alkali fluorides, and are much smaller than those of perovskite oxides. Very similar pressure derivatives are observed for the fluoroperovskites and alkali fluorides, in marked contrast to the negative $\partial n/\partial p$ values in oxide perovskites. In conclusion, the high-frequency dielectric constant ϵ_{el} originating from the electronic polarizability depends mainly on the anion species (fluorine or oxygen¹¹) and is largely unaffected by the crystal structure (rocksalt or perovskite type).

On the other hand, the low-frequency dielectric con-

stant ϵ_{ion} is dependent on the crystal structure as well as the ionic species. It is concluded that the electrostrictive Q_h coefficient of fluoroperovskites lies near $0.23 \text{ m}^4 \text{ C}^{-2}$, intermediate between the Q_h values of alkali fluorides and perovskite oxides. In other words, it appears that the electrostrictive coefficient in fluorides is larger than in oxides, and that the Q_h value in perovskites is smaller than in rocksalt compounds. It is important to mention here that the bulk modulus κ in fluoroperovskites also lies between those in alkali fluorides and in perovskite oxides. This interrelation between the electrostrictive coefficients Q_h and the elastic moduli κ of fluorides and oxides can be understood on the basis of the discussion presented in our previous paper.¹⁹

Consider a rigid ion model of the rocksalt structure with $+q$ and $-q$ ion species as the simplest case, for which the ion-pair potential energy is represented by the following anharmonic function:

$$\Delta U = U(r) - U(r_0) = f(r - r_0)^2 - g(r - r_0)^3, \quad (8)$$

where r is a distance between a cation and the neighboring anion, and r_0 denotes the equilibrium position. Using a Boltzmann distribution, the averaged induced strain $\langle x_1 \rangle$ under an applied electric field E_1 is calculated to be

$$\langle x_1 \rangle = (3gq^2/4f^3r_0)E_1^2. \quad (9)$$

Taking account of the polarization P_1 per unit volume of the form

$$P_1 = (q^2/4fr_0^3)E_1, \quad (10)$$

the electrostrictive coefficient Q_{11} is given by

$$Q_{11} = 12gr_0^5/fq^2. \quad (11)$$

Note here that the hydrostatic Q_h is related to the Q_{11} coefficient through the Poisson ratio σ :

$$Q_h = (1 - 2\sigma)Q_{11}. \quad (12)$$

If we assume that f , g , and r_0 are of the same order of magnitude for the same crystal structure, the Q_h value will be nearly inversely proportional to the square of the valence q . Since the ratio of the valence of fluorides to that of oxides is about $\frac{1}{2}$, the electrostrictive coefficient of fluorides should be about four times larger than that of oxides. This rough estimation is comparable with the averaged ratio $0.23/0.046$ obtained experimentally for the fluoride and oxide perovskites (see Table I). In a similar manner a relation between the elastic modulus κ and the Q_h value,

$$\kappa \propto Q_h^{-1}, \quad (13)$$

can be obtained.

Detailed calculations taking into account the crystal-structure difference and the electronic polarizability (e.g., a shell model), will be required for further quantitative discussions.

- ¹K. Uchino, S. Nomura, L. E. Cross, and R. E. Newnham, *J. Phys. Soc. Jpn., Suppl. B* **49**, 45 (1980).
- ²K. Uchino, S. Nomura, L. E. Cross, R. E. Newnham, and S. J. Jang, *J. Mater. Sci.* **16**, 569 (1981).
- ³K. Uchino, S. Nomura, L. E. Cross, S. J. Jang, and R. E. Newnham, *J. Appl. Phys.* **51**, 1142 (1980).
- ⁴K. Uchino, L. E. Cross, R. E. Newnham, and S. Nomura, *J. Appl. Phys.* **52**, 1455 (1981).
- ⁵K. Uchino, L. E. Cross, R. E. Newnham, and S. Nomura, *Phase Transitions* **1**, 333 (1980).
- ⁶A. E. van Arkel, *Physica (Utrecht)* **5**, 166 (1925).
- ⁷H. Remy and F. Hansen, *Z. Anorg. Allg. Chem.* **283**, 277 (1956).
- ⁸L. E. A. Jones, *Phys. Chem. Miner.* **4**, 23 (1979).
- ⁹K. Vedam, E. D. D. Schmidt, J. L. Kirk, and W. C. Schneider, *Mater Res. Bull.* **4**, 573 (1969).
- ¹⁰G. N. Ramachandran, *Proc. Indian Acad. Sci.* **25A**, 208 (1947).
- ¹¹K. Vedam and E. D. D. Schmidt, *Phys. Rev.* **146**, 548 (1966).
- ¹²K. Vedam and E. D. D. Schmidt, *J. Phys. Chem. Solids* **27**, 1563 (1966); K. Vedam (private communication).
- ¹³J. Fontanella, C. Andeen, and D. Schuele, *Phys. Rev. B* **6**, 582 (1972); L. Bohaty and S. Haussuhl, *Acta Crystallog. Sect. A* **33**, 114 (1977).
- ¹⁴G. A. Samara and B. Morosin, *Phys. Rev. B* **8**, 1256 (1973).
- ¹⁵G. A. Samara, *Phys. Rev.* **151**, 378 (1966).
- ¹⁶K. Gesi and K. Ozawa, *J. Phys. Soc. Jpn.* **34**, 1698 (1973).
- ¹⁷K. S. Aleksandrov, L. M. Reshchikova, and B. V. Beznosikov, *Phys. Status Solidi* **18**, K17 (1966).
- ¹⁸L. M. Reshchikova, *Fiz. Tverd. Tela (Leningrad)* **10**, 2558 (1968) [*Sov. Phys.—Solid State* **10**, 2109 (1969)].
- ¹⁹K. Uchino and L. E. Cross, *Jpn. J. Appl. Phys.* **19**, L171 (1980).

ELECTROSTRICTION IN LEAD LANTHANUM ZIRCONATE TITANATE (PLZT) CERAMICS

Z.Y. Meng, U. Kumar, and L.E. Cross

ELECTROSTRICTION IN LEAD LANTHANUM ZIRCONATE TITANATE (PLZT) CERAMICS

Z.Y. Meng*, U. Kumar, and L.E. Cross**

Materials Research Laboratory
The Pennsylvania State University
University Park, PA 16802

ABSTRACT

Simultaneous measurements of electric polarization and elastic strain around the high electric field polarization loops in PLZTs of (7, 7.5, 8, 8.8, 9.5) 65:35 and in 8:70:30 show that for compositions where the base state is macroscopically nonpolar, the strains are dominantly electrostrictive. Both of the polarization related constants Q_{11} and Q_{12} are almost independent of temperature and of the same order as in other perovskites, but decrease in magnitude with increasing La_2O_3 content.

I. INTRODUCTION

The properties of lanthanum modified lead zirconate:lead titanate ceramics (PLZTs) have been mapped over a wide range of compositions by several authors¹⁻³. Much of this investigation has centered upon compositions with zirconia:titanium ratio 65/35 because of the interesting rhombohedral:tetragonal ferroelectric:ferroelectric phase change near this composition. However, data still appear to be lacking upon the shape changes accompanying polarization in these compositions, and their possible interpretation in terms of the electrostriction constants of the parent phase.

The present study is concerned with an examination of the elastic strains accompanying changes of polarization induced by electric fields in PLZT ceramics with compositions (7, 7.5, 8, 8.8, 9.5) 65:35 and 8/70/30. The longitudinal and transverse strains were measured as a function of applied electric field at various frequencies and temperatures. Polarization changes

induced by the field were measured at the same time. It was the objective of this study to see how well the strain changes could be modelled on the basis of a simple polarization related electrostriction, and if as in the relaxor ferroelectric lead magnesium niobate⁴, the constants Q_{11} and Q_{12} for longitudinal and transverse effects would be largely independent of temperature.

II. EXPERIMENTAL METHODS

The ceramic samples used in these studies were supplied from several different sources. Materials with composition (7, 7.5) 65:35 and 8:70:30 were from Honeywell Company. Fabricated by mixed oxide processing and uniaxial hot pressing⁵. The 8:65:35 and 8.8:65:35 compositions were from the Shanghai Institute of Ceramics and were chemically prepared and hot pressed to optical transparency⁶. The 9.5:65:35 is a standard Motorola Company slim loop ceramic fabricated by a part chemical mixing⁷, again being hot pressed to theoretical density and optical transparency.

All samples were cut to rectangular bar shape $\sim 4 \times 7 \times 12$ mm using a wire saw, then ground and polished to final dimensions. After processing and cleaning, the samples were annealed at 600°C for 2 hours to remove residual stress then slow cooled to room temperature. Electrodes used were of sputtered gold.

In order to explore electrostriction behavior strain and polarization were measured simultaneously under slow cyclic field drive. Both longitudinal and transverse strain were measured using a bonded strain gauge technique⁸. The polyimide foil gauge (Kyowa KFH-02-C1-11) was bonded to the sample surface using a Kyowa PC-6 cement. Gauge resistance was measured using a DC double bridge method. At room temperature, the transverse strain was checked by direct dilatometer methods using a linear variable differential transformer,

i.e. LVDT guage (Schaevitz 050 MHR 602). For all measurements, strain guage and LVDT methods agreed to better than $\pm 10\%$.

Dielectric polarization figures were measured using a modified Sawyer and Tower method⁹ reading out into a Nicolet sampling digital oscilloscope and strip chart recorder.

Before each measurement, at a specific temperature, the sample was freshly de-aged by heating to a temperature well above the dielectric maximum. This de-aging was found to be essential for obtaining reproducible measurements.

III. RESULTS AND DISCUSSION

Detailed polarization and strain data were recorded for several samples at each composition temperature and frequency. For brevity only representative data will be shown for samples exhibiting typical response. Such typical strain response curves for transverse strain s_{12} for PLZT 7.5:65:35 and longitudinal strain s_{11} for 8.8:65:35 are shown in Figures 1 and 2 for several fixed temperatures encompassing the permittivity maximum and the depoling transition temperature. Hysteresis loops for the same temperatures are shown in Figures 3 and 4.

When the temperature is well below the Curie range, the strain curves are the typical butterfly shape expected for polarization reversal in a normal ferroelectric. As the temperature approaches that of the Curie maximum, however, the loops become very thin, and the strain minima move together. In the region of temperature between the depoling transition (α - β change and the Curie maximum, the ceramics can be poled to a strong 'ferroelectric like' level, but there is no stable remanence, i.e. a high electric field can enforce a macroscopically ferroelectric state with a corresponding lattice

strain, but both strain and polarization decay to zero on removal of the field.

To obtain a measure of the electrostrictive Q constants induced longitudinal and transverse strains at room temperature are plotted in Figure 5 and 6, respectively, as a function of the square of the electric polarization read off from the hysteresis loop for 7.5 and 8.8:65:35 and 8:70:30 PLZTs. The straight lines evident, which pass through the origin clearly confirm the dominantly electrostrictive character of the strain with $s_{11} = Q_{11}P_1^2$ and $s_{12} = Q_{12}P_1^2$ yielding the values for Q_{11} and Q_{12} listed in Table 1. The values are in reasonable accord with the general order $1 \cdot 10^{-2}$ observed in most perovskite ferroelectrics and Q_{11} is 1 to 2 x Q_{12} as expected.

To check the temperature dependence of the Q_s , plots of polarization squared vs strain taken at a series of different temperatures are superposed in Figures 7 and 8 for 8.8:65:35 and 8:70:30 compositions respectively. Except for the temperature of -50°C and -80°C in the 8.8:65:35 composition, the curves superpose remarkably well and demonstrate the near temperature independence of both Q_{11} and Q_{12} across the whole relaxation region of the maximum in dielectric response as evidenced in Figure 9.

It may be noted that even in the low temperature curves for the 8.8:65:35 compositions in Figure 7, the slope is the same, but the zero of strain appears to have been offset. We believe that the enhanced strain at these temperatures may be due to a ferroelectric mechanism of polarization reorientation in which the P_s vector rotates through intermediate domain orientations. In this case the zero in measured P_1 may correspond to an array of domain polarizations which are dominantly in the 23 (yz) plane. Such a fan of polar domains would contribute a spurious elongation to the measured zero polarization base state in the 2 or 3 directions, and thus to an offset in the zero and an apparent increase in the measured contraction s_{12} induced by the

field. Indirect evidence that unlike the higher temperatures where polarization breaks up into random micro regions, the low temperature switching is by a direct ferroelectric domain reorientation.

Frequency dependence of the induced strain has been measured over the range from 0.02 to 0.3 Hz. Typical data for the 7.5:65:35 composition is given in Figure 10. Evidently there is no strong frequency dependence in the temperature range of the diffuse phase change for these low frequencies.

From the data in Table 1, there does appear to be a tendency for the Q constants to decrease with increasing La_2O_3 concentration in these PLZTs and this would be expected on the model of other relaxor compositions⁽¹⁰⁾.

IV. SUMMARY AND CONCLUSIONS

The most important results from these measurements are that the elastic strains associated with the development of polarization in this whole range of PLZT ceramics are electrostrictive in origin. It is startling to find that the electrostriction constants Q_{11} and Q_{12} are independent of temperature across the whole range of the diffuse phase transition about the maximum in dielectric permittivity. Only at low temperatures do these materials give evidence of departure from simple electrostrictive behavior which can be explained by 'normal' ferroelectric domain switching.

REFERENCES

1. G.H. Haertling and C.E. Land, 'Hot-Pressed (Pb,La)(Zr,Ti)O₃ Ferroelectric Ceramics for Electro-Optic Applications,' J. Amer. Ceram. Soc. 54:1-11 (1971).
2. G.H. Haertling, 'Improved Hot-Pressed Electro-Optic Ceramics in the (Pb,La)(Zr,Ti)O₃ System,' J. Amer. Ceram. Soc. 54:303-309 (1971).
3. C.E. Land and P.D. Thaeher, 'Electro-Optic Properties of Ba, Sn and La Modified Lead Zirconate Titanate Ceramics,' in the Physics of Opto-Electronic Materials, W.A. Albers, Jr., Ed., New York, Plenum Press, pp. 169-196 (1971).
4. S.J. Jang, K. Uchino, S. Nomura and L.E. Cross, 'Electrostrictive Behavior of Lead Magnesium Niobate Based Ceramic Dielectrics,' Ferroelectrics 27:31-34 (1980).
5. G.H. Haertling, 'Hot-Pressed Ferroelectric Lead Zirconate Titanate Ceramics for Electro-Optical Applications,' Amer. Ceram. Soc. Bull. 49:564-567 (1970).
6. Yao Xi, Chen Zhili and L.E. Cross, 'Polarization and Depolarization Behavior of Hot Pressed Lead Lanthanum Zirconate Titanate Ceramics,' J. Appl. Phys. 54:3399-3403 (1983).
7. G. Haertling, 'PLZT Reflective Displays,' Ferroelectrics 50:389 (1983).
8. K. Uchino, S. Nomura, L.E. Cross, S.J. Jang and R.E. Newnham, 'Electrostrictive Effect in Lead Magnesium Niobate Single Crystals,' J. Appl. Phys. 51:1142-1145 (1980).
9. J.K. Sinha, 'Modified Sawyer and Tower Circuit for Investigation of Ferroelectric Samples,' J. Phys. E: Sci. Instrum. 42:696-701 (1965).
10. K. Uchino, S. Nomura, A. Amin, Z.P. Chang, L.E. Cross and R.E. Newnham, 'Elastic Constants and Thermal Expansion of Cation Disordered Perovskites,' Jpn. J. Appl. Phys. 19:L398-L400 (1980).

Table I. Electrostrictive Coefficients for PLZT Ceramics at Room Temperature.

Compositions	Q_{11} ($10^{-3} \text{ M}^4/\text{C}^2$)	Q_{12} ($10^{-3} \text{ M}^4/\text{C}^2$)
7:65:35	22.5	-11.5
7.5:65:35	16.3	-8.7
8:65:35	18.3	-8.1
8.8:65:35	21.2	-9.5
9.5:65:35	21.0	-9.1
8:70:30	9.7	-7.5

Figure Captions

- Figure 1. Transverse strain s_{12} vs electric field for PLZT 7.5:65:35 for several fixed temperatures.
- Figure 2. Longitudinal strain s_{11} vs electric field for PLZT 8.8/65/35 for several fixed temperatures.
- Figure 3. Hysteresis loops for PLZT 7.5:65:35 corresponding to the strain curves shown in Figure 1.
- Figure 4. Hysteresis loops for PLZT 8.8:65:35 corresponding to the strain curves shown in Figure 2.
- Figure 5. Transverse strain s_{12} vs square of polarization P in 7.5:65:35, 8.8:65:35 and 8:70:30 compositions at room temperature.
- Figure 6. Longitudinal strain s_{11} vs square of polarization P in 7.5:65:35, 8.8:65:35 and 8:70:30 compositions at room temperature.
- Figure 7. Polarization squared P vs longitudinal strain s_{11} taken at a series of different temperatures for 8.8:65:35 composition.
- Figure 8. Polarization squared P vs transverse strain s_{12} taken at a series of different temperatures for 8:70:30 composition.
- Figure 9. Temperature dependence of the electrostriction Q_{11} and Q_{12} for 7.5:65:35 and 8:70:30 PLZTs.
- Figure 10. Frequency dependence of the induced strain for 7.5:65:35 composition.

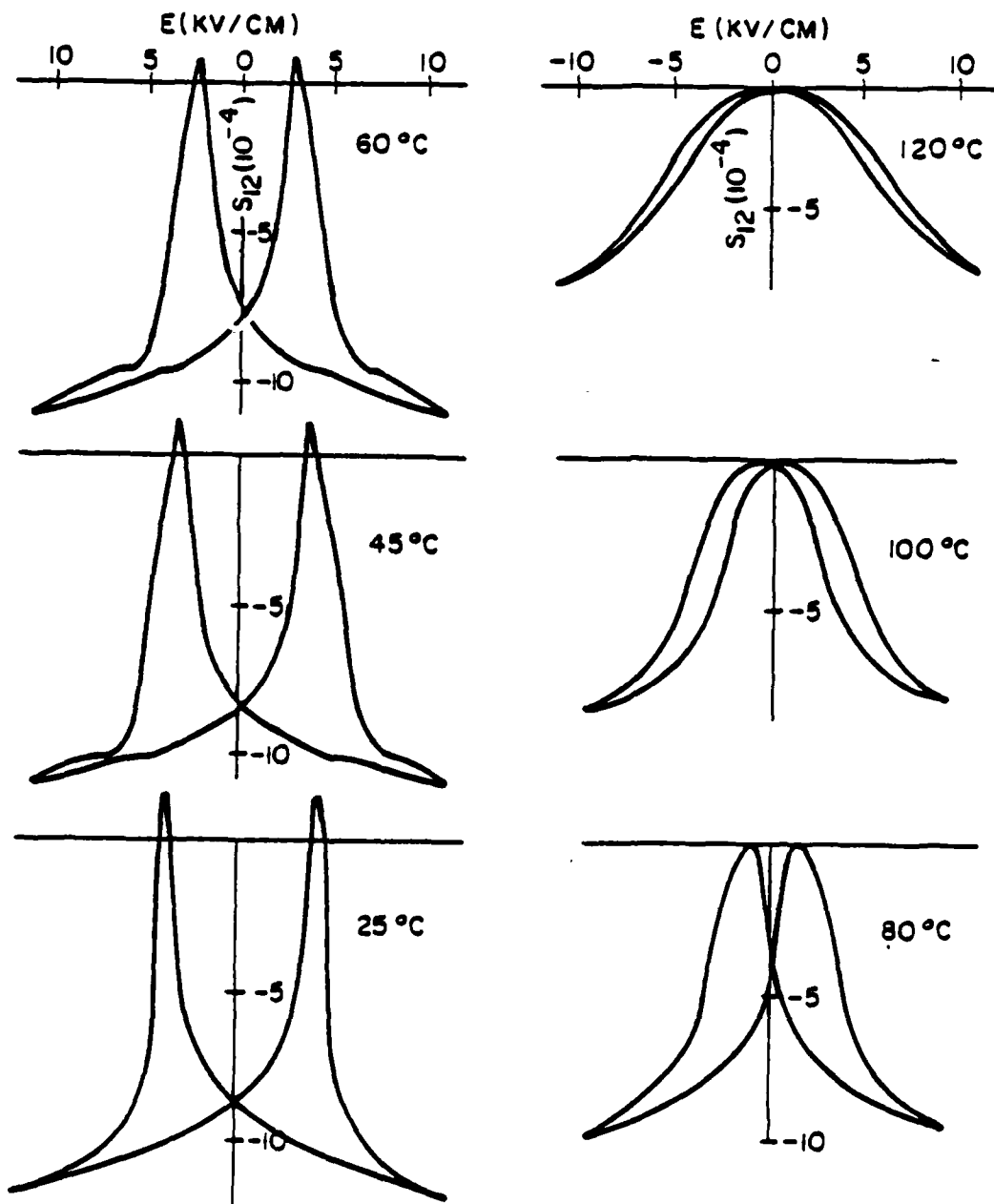
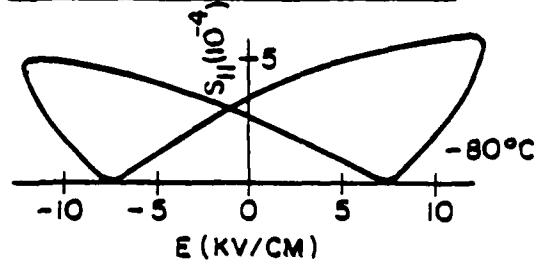
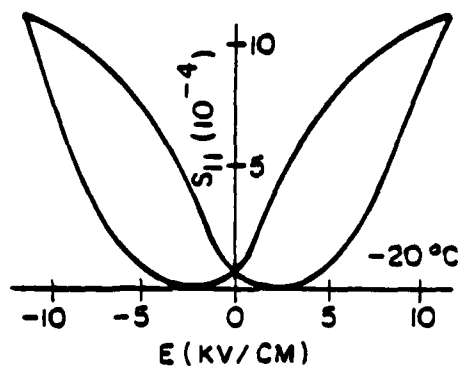
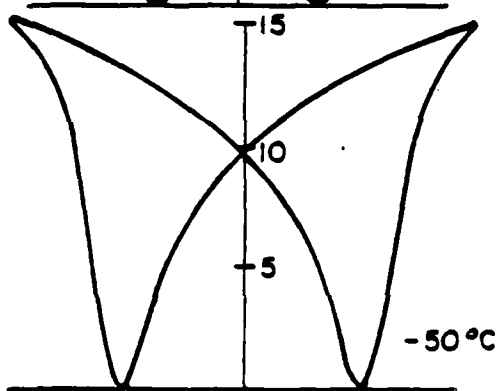
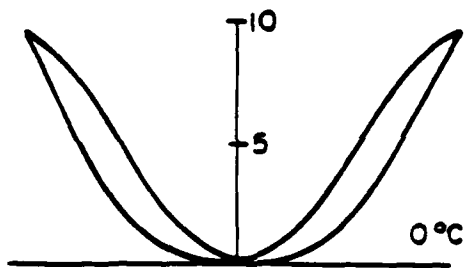
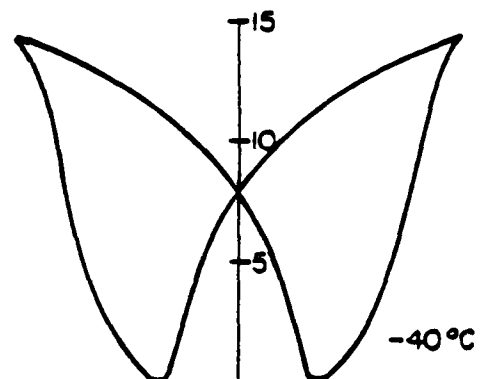
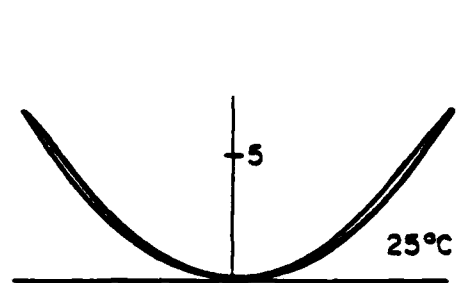
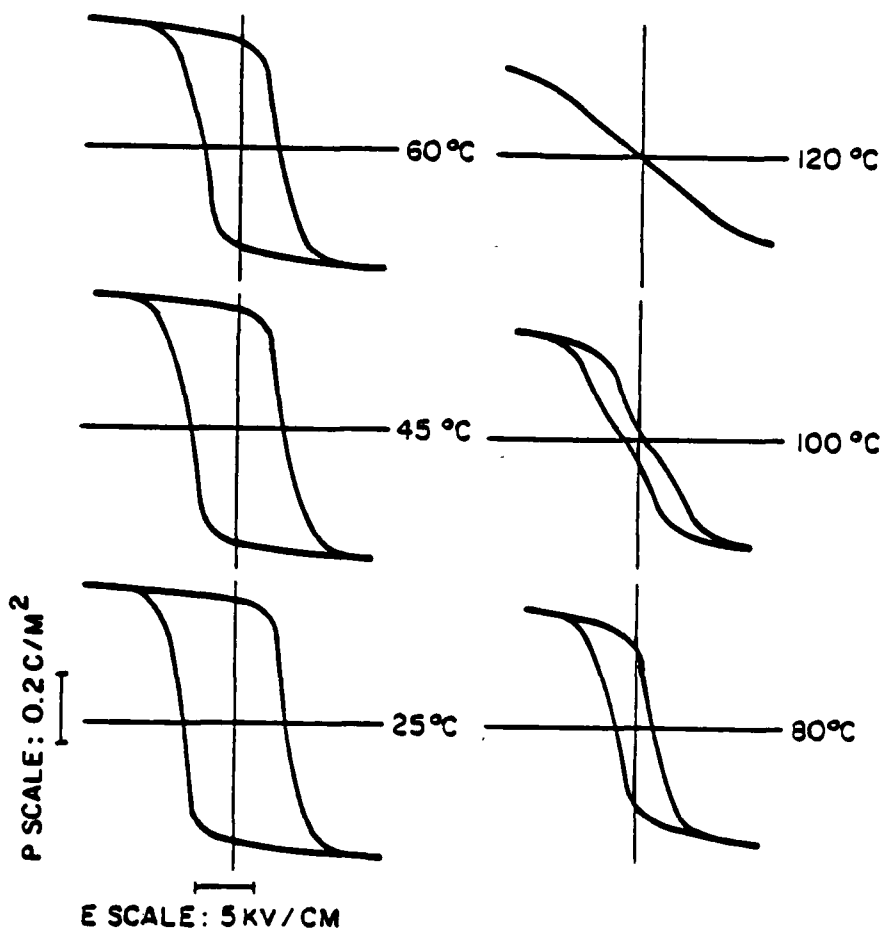


Fig. 1





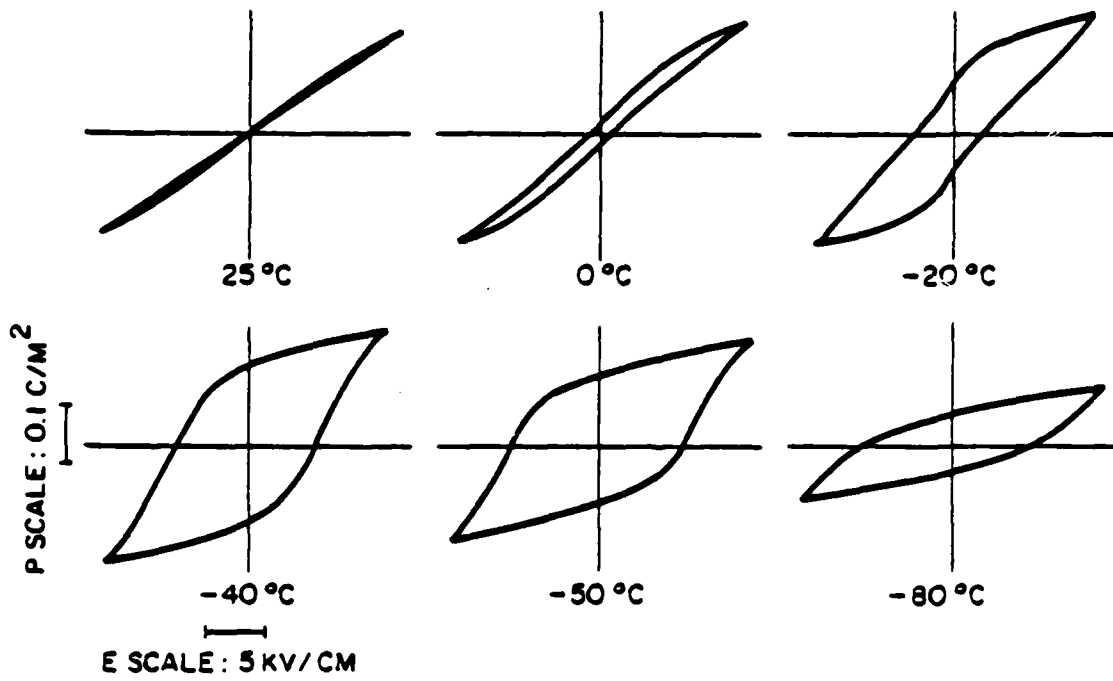


Fig 4

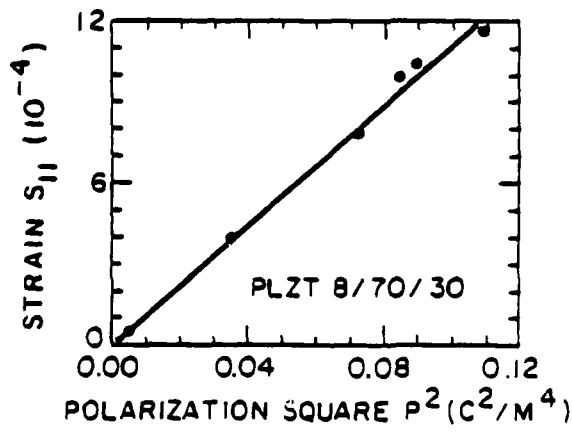
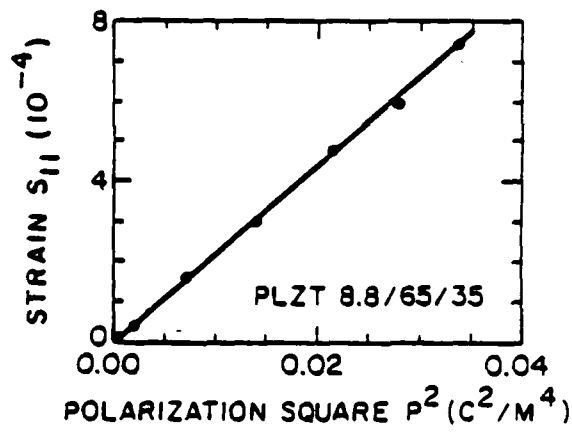
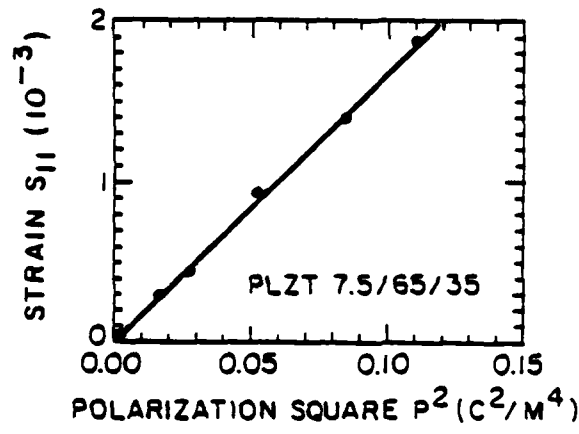
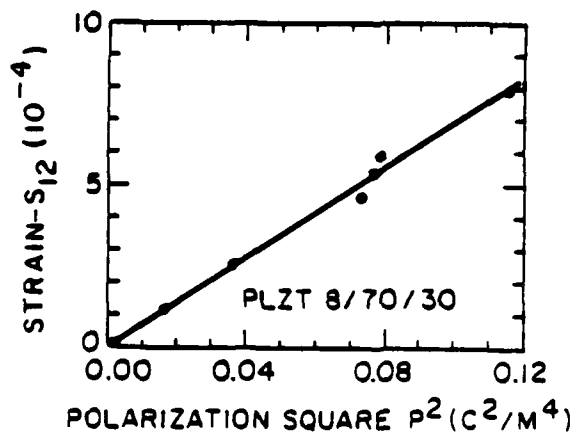
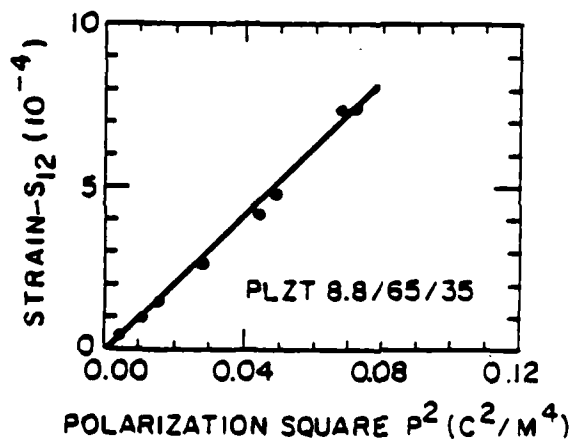
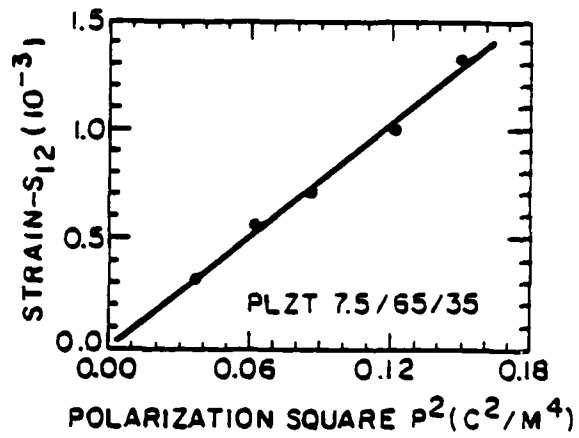
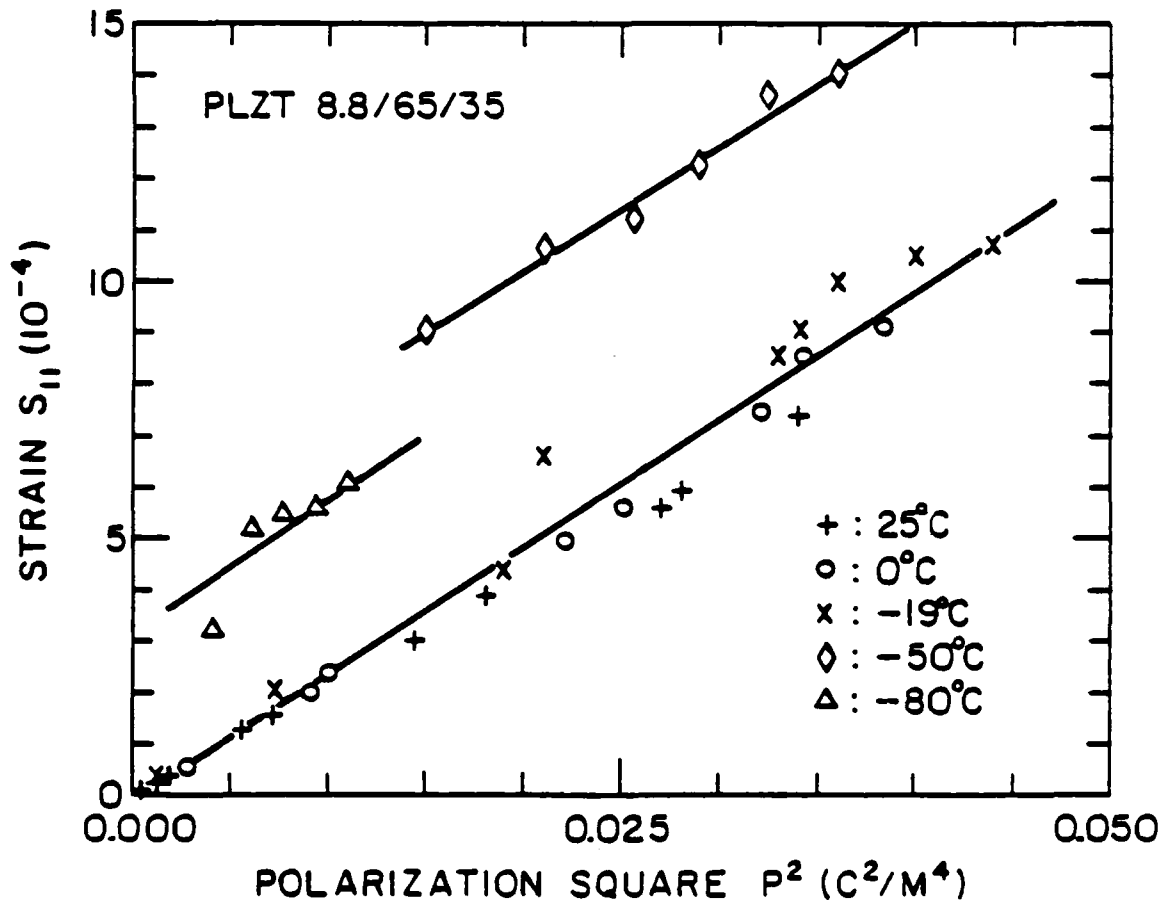


Fig -





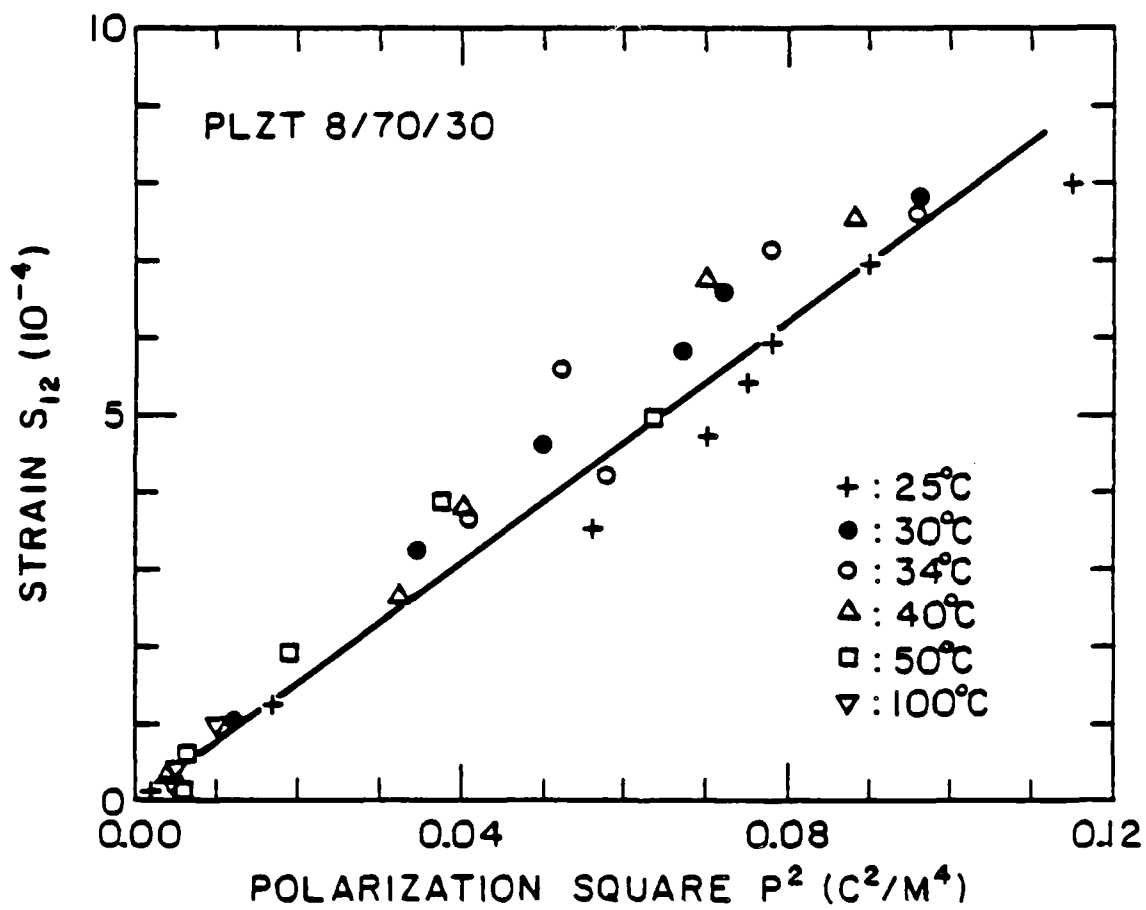
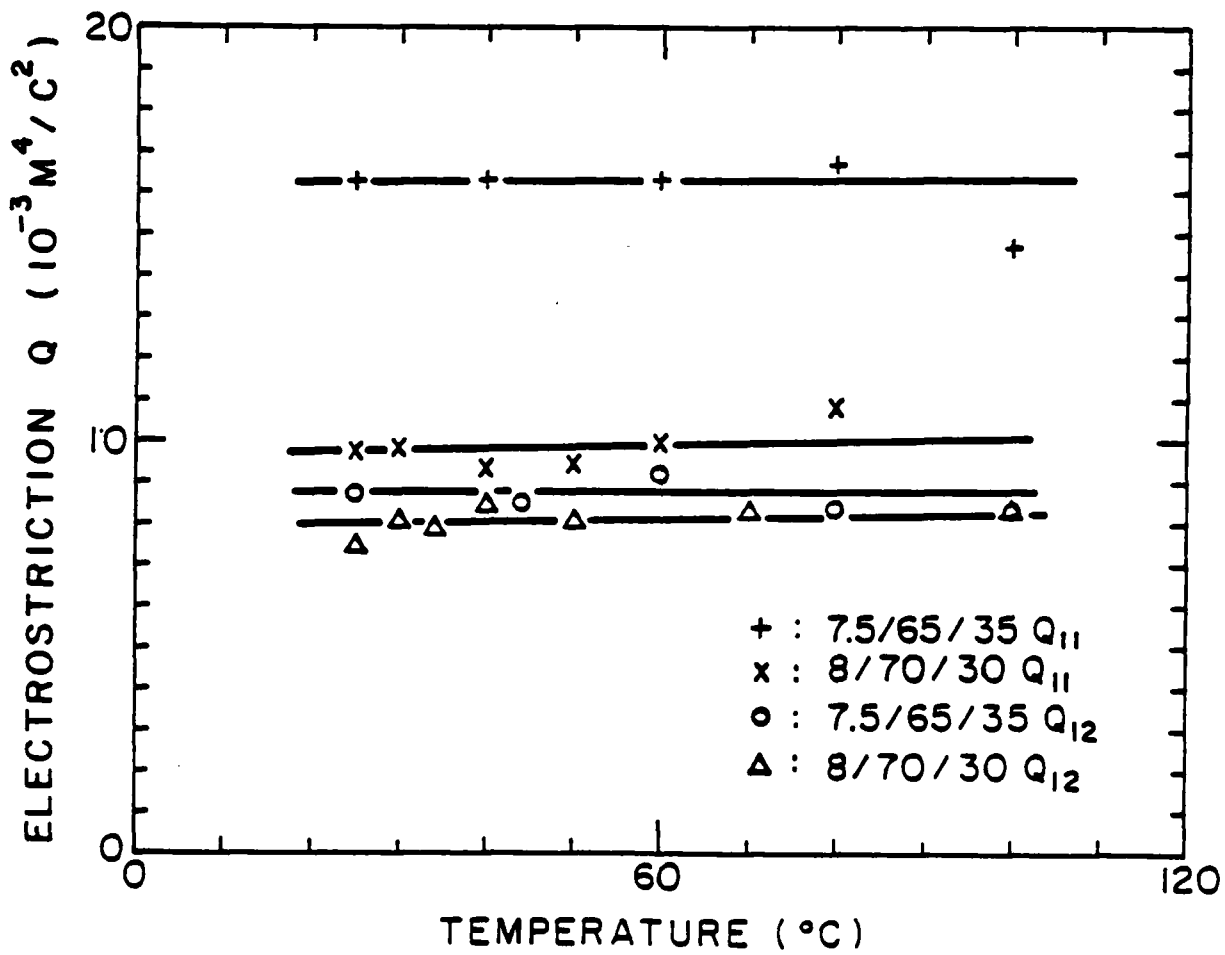


Fig. 1



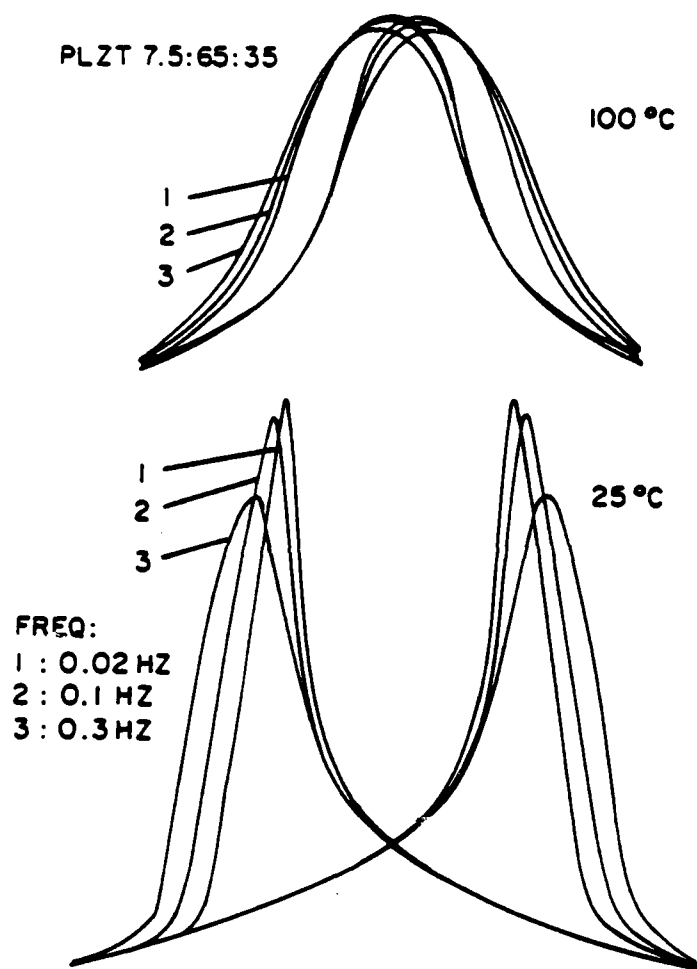


Fig. 10

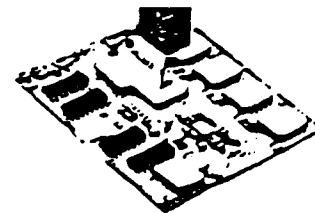
DIELECTRIC, PIEZOELECTRIC, AND FERROELECTRIC COMPONENTS

Leslie E. Cross

Dielectric, Piezoelectric, and Ferroelectric Components

LESLIE E. CROSS*

Pennsylvania State University, University Park, PA 16802



There are two major areas of application for ceramic dielectric materials in electronic ceramic components. In electrical capacitors, the focus is often upon storing maximum electrical energy in a minimum volume (volumetric efficiency) and thus the interest is in high permittivity dielectrics with ferroelectric or near ferroelectric properties. Current technology emphasizes the monolithic multilayer ceramic capacitor (MLC) in which a stacked very thin plate geometry is achieved by co-firing electrode and dielectric layers into a compact impervious monolithic chip.

For electrical insulation, which is the second major area of use, the ceramic dielectric is used to support and to separate electrical conductors. Often, the objective is to minimize the electrical energy stored in the dielectric so that materials of low permittivity are of major interest. Applications for insulators are as diverse as the packaging and support of interconnection structures for integrated circuits (ICs) and the mechanical and electrical support of high voltage power transmission lines.

In this paper, the emphasis is upon electronic components so that the larger insulator structures will not be considered. Packaging and interconnects are the subject of a separate article in this issue and thus will not be covered here. For both capacitors and insulators, the frequency range of maximum interest is from DC to high radio frequency (10^4 Hz). Recently with the broader use of satellite systems for TV and communications, the need has opened for special dielectric resonator materials with very stable low loss properties at 10^{10} Hz frequency. There are also signs of emerging needs for very high loss broad band dielectrics in radar absorbing materials and structures (RAM-RAS) and for filtering and interference suppression.

Capacitor Dielectrics

Historically, the ceramic capacitor has evolved from the simple disk and tube types of WW II vintage, through the more compact barrier layer structures with effective dielectric permittivities in the range 100,000 to 200,000 to the present generation multilayer monolithics with dielectric layers spacing now in the 25-12 μ meter range. Evolution has been from high towards lower voltages, following the trends in semiconductor integrated circuits, so consequently the capacitor has moved from thick towards much thinner effective dielectric layers.

It is interesting to note that the changes have been effected largely not by the phasing out of need for the higher voltage types, but by substantial growth and escalation of demand for the compact low voltage IC compatible capacitors, and this rapid growth is expected to continue. Over the whole period from 1945 to the present, ferroelectric barium titanate (BaTiO_3) in a number of modified or doped forms has dominated the field as the dielectric of choice in high permittivity (high K) applications.

Current Emphasis and Future Trends

In barrier layer type capacitors, current emphasis would appear to be on the grain-grain boundary rather than the surface barrier layer systems.^{1,2} Early units of the grain-grain boundary type were made from modified barium titanate compositions fired under reducing conditions to give a high conductivity grain core, then reoxidized to produce a narrow insulating boundary phase. Effective permittivity increases markedly with grain size, and commercial units have very large average grain size and consequently poor mechanical strength.

More recently, a reduced strontium titanate is often used as the conductive grain. Sintered with excess TiO_2 , the barrier in the SrTiO_3 is formed by infusing a bismuth oxide-lead oxide liquid phase to form a bismuth lead titanate insulating barrier phase.³ Under proper control the weak positive temperature coefficient of the bismuth oxide layer structure phase can be compensated by the negative coefficient of the reoxidized SrTiO_3 layer on the grain surface to give a remarkably flat capacitance temperature curve.⁴

The low base resistivity of the SrTiO_3 and the abrupt semiconductor-insulator transition afforded by the liquid phase infusion combine to lift the Maxwell-Wagner relaxation frequency towards 10^4 Hz giving a wide useful frequency range.⁵

To maintain high effective permittivity, the grain size must be large and the barrier phase thin, so that it is not yet possible to exploit the high effective K and low TC in a multilayer form, but a number of researchers are exploring possibilities in this direction.^{6,7}

The vast majority of MLC structures are still fabricated with BaTiO_3 based dielectrics, but developments are in progress towards other more versatile antiferroelectric and relaxor superparaelectric compositions. In the BaTiO_3 based systems, the high cost of precious metals has forced the change towards highly fluxed compositions which will densify at temperatures compatible with high silver palladium alloy electrodes^{8,9} or to heavily acceptor doped materials which can be co-fired at low oxygen partial pressure with nickel metal electrodes.¹⁰ In U.S. practice though, there are still doubts that these highly acceptor doped systems can be stabilized against DC degradation due to oxygen vacancy motion.

In Japan, it is evident that NEC has invested considerable effort upon the lead based perovskite relaxors and has materials which will densify at temperatures below 900°C with pure silver electrodes.^{11,12} Similarly, in the U.S. there is indication from Sorague Electric Company of a PLZT based MLC dielectric compatible with silver electrodes.¹³ The PLZT dielectric is in an antiferroelectric phase and appears to offer significant advantage in low power factor, high dielectric linearity and lower hysteresis loss under high fields.¹⁴

It would appear that both the base metal and the silver electrode units can be produced at a cost, and in sizes to begin to compete with larger electrolytics and to offer lower series resistance at high frequency.^{15,16}

An interesting newer contender in the field of MLCs in Japan offers a range of BaTiO_3 based compositions with controlled sub-micron grain size produced apparently by organic synthesis and again utilizing high silver palladium electrodes.^{17,18}

A technique which very neatly sidesteps many of the dielectric-electrode compatibility problems is the Corning ACE process in which the unit is fabricated with porous interleaving layers and the electrode injected by a separate low temperature step sinter firing.

In the near future, we may surmise that with the advancing speed of VLSI on silicon circuits, seal and interconnect inductance will become much more important parameters in MLCs and new sets of trade-offs may be required. Eventually one may suggest that in the very sophisticated systems the capacitor will become an integral part of the packaging and mounting structure.^{19,20}

Just from the perspective of basic physics, it is probable that the lead based perovskites and tungsten bronze structures may become of more importance as dielectrics since they offer a combination of antiferroelectric and superparaelectric phases which can have lower dielectric loss levels, higher permittivities, greater linearity

*Member, the American Ceramic Society.

high drive levels and lower processing temperatures, as compared to the traditional BaTiO₃ based systems.

Piezoelectrics

The device applications of piezoelectric ceramics fall naturally in two generically different categories. Piezoelectric transducers make direct use of the electromechanical coupling to convert electrical to mechanical energy and vice-versa. In mechanical to electrical change, the applications run the gamut of extremely low level signals such as in hydrophones and microphones where the weak sound field generates microvolts or less in electrical signal, to the shock excited phase change transducers which can generate hundreds of kilovolts or many kiloamps of current for special military fusing applications. In electrical to mechanical change, the range is equally large from the very small Å level changes in piezoelectrically controlled surface deformable mirrors to the very large deformations encountered in the power transducers of sonar or ultrasonic cleaning and sonification baths.

Piezoelectric resonators and filters make use of the fact that mechanical motion of the sample interacts through the electro-mechanical coupling to modify its electrical impedance. Thus the mechanical resonances of a regularly shaped solid gives rise to extrema in the impedance whose frequencies depend dominantly only upon the dimensions. Density and elastic properties, constants whose temperature characteristics can be much more easily controlled than the inductance and capacitance of an equivalent pure electrical resonator. These piezoelectric resonators can be designed to have exceedingly stable electrical impedance characteristics, and by multiple electroding and so called trapped energy configurations, very sharp square edged filtering characteristics can be achieved. Normal filters make use of sound waves in the bulk of the ceramic, however, by suitable electrode configurations it is possible to excite waves just on the surface (like waves on the ocean). There is now a complete science of these Surface Acoustic Waves, so called SAW devices, which again put new and interesting demands upon the materials designer and the ceramic engineer.

Piezoelectric Transducers

Polycrystal ceramic piezoelectric transducers stemmed from the immediate post WW II interest in ferroelectric barium titanate capacitors and the era was formally initiated by the R. B. Gray patent¹ in 1949 for a polarized BaTiO₃ ceramic transducer. A major 'quantum jump' in performance occurred with the discovery of the very strong piezoelectric activity in polarized lead zirconate titanate, by B. Jaffe and co-workers who correctly traced the very high activity to the important morphotropic phase boundary near the Pb(Zr_{0.12}Ti_{0.88})O₃ composition.² With the detailed assessment of the effect of donor and acceptor ion substitution upon coercivity and properties in the excellent studies at Clevite Corporation,³ the basis was established for the modern family of PZT transducers.

Current Activity and Future Projects

The lead zirconate titanate family still form the basis for most ceramic piezoelectric transducers. An immense amount of effort has been concentrated, particularly in Japan, upon modifications to the PZT compositions to trim properties and facilitate fabrication for specific device structures, and a wide range of options are now available, from very low coercivity (ultra-soft) high sensitivity compositions to heavily self-biased high coercivity hard compositions.⁴

For simple large area hydrophone applications, PZT is however far from ideal. The high density makes it a poor acoustic match to water, it is brittle and the cancellation between the positive piezoelectric d_{31} , and the negative d_{32} make the hydrostatic coefficient ($d_h = d_{31} + 2d_{32}$) uncomfortably small.⁵ Recently it has been shown, using composites of a PZT and a polymer phase with controlled phase interconnection, that a more nearly optimum internal stress can be generated and the hydrophone figure of merit ($d_h \rho$) improved by two orders of magnitude.⁶⁻⁸ It appears that

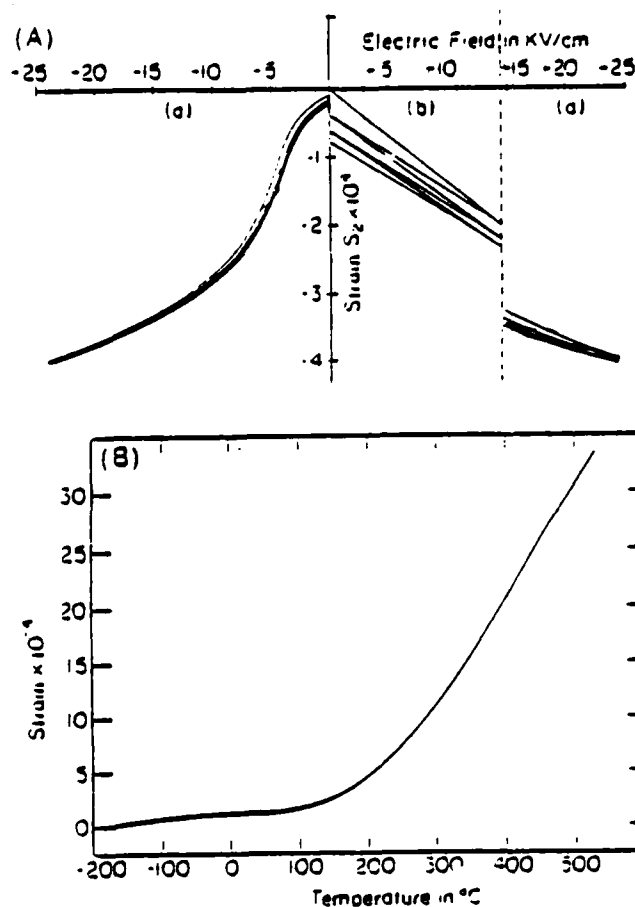


Fig. 1. (A) Transverse strain in a ceramic specimen of 0.9 PMN:0.1 PT (a) and in a typical hard PZT piezoceramic under slowly varying electric fields. Strain levels are comparable in the two materials but the relaxor is more reproducible because of field induced de-aging in the PZT. (B) Thermal strain in ceramic 0.9 PMN:0.1 PT. Linear expansion is about 10^{-4} C^{-1} at 400°C and less than 10^{-4} C^{-1} at room temperature.

these composites offer a new opportunity to the design engineer and may have important application also at higher frequency in biomedical and other N D E. systems.

For transducer arrays and acoustic imaging, there is considerable interest in the new lead titanate compositions modified with samarium (Sm) or calcium (Ca) ions. These materials, after suitable processing and poling, show high transverse but almost zero planar coupling.^{9,10} With different modifier ions, lead titanate also appears to offer interesting compositions with very low temperature coefficients of delay for inexpensive surface acoustic wave (SAW) materials.¹¹

In high power transducers, possibilities for impedance control using co-fired internal electrode fabrication, not unlike the MLC capacitor structures are being explored. The possible control of hardness by quite manageable external bias levels in such structures offer new intriguing consequences.

Aging of the poled state, and consequent drift of dimensions have always been a problem when using PZT type compositions for precise position control. New families of lead magnesium niobate based electrostrictive materials appear now to offer an interesting alternative with better reproducibility, lower drift, larger force and much lower thermal expansion.^{12,13} Typical data for a lead magnesium niobate based relaxor composition is shown in Fig. 1. For infra-red wavelength surface deformable mirrors, these materials are already finding important application.

Piezoelectric Resonators and Filters

The piezoelectric resonator was one of the earliest device structures exploiting electromechanical coupling in crystals,¹⁴ and right from the outset in the early 1920's to the present time single crystal quartz in its temperature compensated cuts has taken the bulk of the frequency control market. Some idea of the importance of quartz resonators can be judged from topics at the Annual Frequency Control Symposium, now in its 38th year. In this meeting, attended by some 700 timing specialists, quartz is the base material for more than 50% of the papers presented. Early devices used natural quartz from Brazil, but now the hydrothermally grown synthetic crystals are superior, and purified 'drifted' quartz can be obtained with guaranteed Q over 10⁸.

With the increasing sophistication of electronics emerging in the 50's and 60's, the needs for pre-tuned filter circuits which could avoid the complexities of multiple L.C.R. tuned filters lead to much exploratory work on compound resonators driven by piezoelectrics. At higher frequencies, needs for IF circuits for radio, TV and FM lead to the evolution of the trapped energy thickness mode resonators¹⁵ which are the basis for much of current filter designs.

Materials for Resonators and Filters

A significant problem with quartz resonators is the frequency shift induced by ionizing radiation, and there is much research in response to the military need for radiation-hard timing for navigation and control. In precise circuits, the only potential contender to quartz is the isomorphous berlinite (AlPO₄),¹⁶ an equally difficult crystal to grow, but with similar temperature compensating cuts, higher piezoelectric coupling and potential applications also in SAW systems.¹⁷

For inexpensive resonators, compound systems using magnetron sputtered ZnO films are finding increasing applications and there is interest in ZnO and AlN films on silicon for SAW devices.¹⁸ Lithium tetraborate (Li₂B₄O₇) has been shown to have higher coupling and temperature compensating SAW cuts.¹⁹

As an alternative to quartz in SAW devices needing broader bandwidth and higher coupling, ferroelectric LiNbO₃ is widely applied but the 60 ppm temperature coefficient of delay is undesirable for precise filter application.

Ferroelectric strontium barium niobate in the tetragonal tungsten bronze ferroelectric structure has been shown to have temperature compensating properties for SAW²⁰ but for a ferroelectric its coupling coefficient is disappointingly small. Lead potassium niobate in the same structure family has both high coupling and compensating cuts, but ferroelastic twinning makes it exceedingly difficult to grow and process for devices. Clearly other bronze structure crystals should be explored.

In trapped energy filters, PZT compositions are widely used because of the high coupling. Much work has been carried out in many companies in the US, Europe and Japan to incorporate modifier ions to control and reduce aging and temperature coefficients without drastic lowering of the piezoelectric coupling.

Basic Understanding

For the future, there are encouraging signs that the complexities of the ceramic piezoelectric can be deciphered with intrinsic and extrinsic contributions to piezoelectricity separated and the physics of systems more fully understood. In all current piezoceramics, the basic coupling between electric and elastic responses is the electrostriction of the paraelectric parent phase in the ferroelectric ceramic. There is now real progress towards a better theoretical and experimental description of electrostriction both in simple solids and in soft mode ferroelectrics.

Practically there is still need to improve and diversify the materials options for the design engineer. The composite structures provide some possibilities, but now with the improving sophistication in electroceramic processing, the possibility emerges to make very strongly grain oriented ceramics which can have intriguing tensor properties intermediate between those of the perfect single crystal and the randomly axed polycrystal. Such 'poor mans crystals' could permit the sophistication of composition manipulation which is the *signature* of the ceramic art in systems with more

sophisticated tensor properties than those of the simple poled ferroelectric ceramics.

Ferroelectrics

Both capacitors and transducer components frequently use ferroelectric materials in their construction and between them, these two applications represent the bulk of the market. There are, however, a number of more specialized and quite intriguing component applications which rely directly upon one or another of the properties of ferroelectrics which are coupled to the onset of electrical polarization.

In positive temperature coefficient resistors (PTCRs), the extremum of the dielectric permittivity at the ferroelectric Curie point T_c and the build up of polarization below T_c is manipulated to modify a potential barrier structure at the grain boundary and to control electrical current flow in a semiconducting ferroelectric.

For electro-optic applications, single crystals of ferroelectric ceramic compositions are frequently used, though there is now also the alternative family of hot pressed or hot forged transparent polycrystal forms. In both cases, the ionic motions in the crystal (or crystallites), which can be modulated by electric field, modify the electronic polarizability and thus control the refractive index of the material.

Both linear and quadratic electro-optic effects can be made large in different ferroelectric systems.

In suitably doped ferroelectric crystals, photon energy can be used to excite carriers which move in preferred directions relative to the ferroelectric polarization and become re-trapped in the insulator to generate very strong internal space charge fields. Such fields in turn modulate the refractive index, giving rise to a family of photo-ferroelectric effects which find application in hologram storage and in the exciting new field of four wave mixing.

Perhaps one of the simplest applications of ferroelectrics comes from the direct use of the temperature dependence of remanent polarization (P_r), the so called pyroelectric effect in crystals and ceramics. The charge-release on heating is such that properly interfaced with a low noise semiconductor F.E.T. a thin flake of ferroelectric can become an exceedingly sensitive broad band infrared detector. Vidicons using pyroelectric sensing have been developed of long wavelength IR imaging, and are becoming widely used in Europe to aid fire fighting by providing 'visibility' through heavy smoke.

The current thrust in the USA is towards large arrays of pyroelectric elements mated to charge coupled or other semiconductor interrogation to produce a high sensitivity focal plane array for infrared imaging at wavelengths where photon detectors must be cooled and thus become cumbersome and logistically awkward.

PTC Resistors

In PTC resistors, the objective of ceramic processing is to form a semiconducting grain structure interleaved with a very narrow barrier layer system at the grain boundary.²¹ The barrier height and thus the impedance to current flow through the ceramic depends upon the base permittivity of the barrier material, and it may be modified also by compensating polarization charge 'dumped' into the barrier structure by the onset of ferroelectric polarization in the grains.²² Thus at low temperatures in the ferroelectric phase where the barrier height is low, the resistivity is also low. Approaching T_c , P_r decays rapidly and above T_c the permittivity ϵ' also decreases, so that with increasing temperature resistivity climbs rapidly giving the PTC phenomenon.

In BaTiO₃, which is a component of all PTC resistor materials, the resistivity change occurs near the Curie temperature at 130°C and may encompass more than 3 orders change.²³ A typical PTC characteristic showing resistance as a function of temperature is shown in Fig. 2. To change the onset for the PTC effect requires a control of the ferroelectric Curie temperature in the ceramic and this is accomplished by forming solid solution with other perovskite phases. Unfortunately, only PbTiO₃ raises T_c and it is difficult to maintain resistivity step height in high-lead com-

positions due to the tendency for autocompensation by lead vacancies.

Control of a semiconductor process in a ceramic system is particularly difficult because of the tendency for impurities to accumulate in the grain boundaries, which in PTC are the regions requiring most careful control. However, with modern powders and refined process control, a good measure of reproducibility both in location on step height for the resistivity change has now been achieved.

Thermal applications for PTCR components cover a very wide range, from simple auto-stabilizing bed socks and rice warmers to more sophisticated temperature stable honeycomb heating elements¹¹ for hair dryers and in automatic warm up devices for automobiles. Electrical applications again cover a wide range of circuit functions from automatic overload protection to surge stabilization as in the degaussing girdles for color TV sets.

Single Crystals

It is perhaps a little premature to discuss single crystal optical components since much of the work is still at the research and very early development level, however, it is clear that with the wide adoption of optical fibers for shorter haul high density telephone circuits, and the rapidly upcoming transoceanic fiber cables, the needs for optical signal processing are expanding with phenomenal rapidity.

For hybrid systems, lithium niobate is clearly the single crystal ferroelectric of choice for current experimentation. Excellent indiffused surface guiding structures have been demonstrated using Ti diffusion into LiNbO₃,¹² and a number of modulator and switching circuits have been demonstrated in these guided structures.¹³

Damage thresholds have been a problem limiting power density in guides, but recently alternative doping and fabrication strategies appear to be alleviating these constraints.

The newer field of phase conjugate optics, image processing and dynamical holography are driving new needs for ferroelectric crystals with exceedingly high electro-optic coefficients. Old favorites like single domain KNbO₃, BaTiO₃, Ba_{1-x}Sr_xNb₂O₆ and Ba₂NaNb₅O₁₅ are in new demand, since for these applications the figure of merit contains the square of the linear E.O. coefficient (r_{33})¹⁴

At the research level, interesting questions begin to emerge as to the possibility of massive effective E.O. coefficients for mm wave applications in ferroelectrics and more work to establish loss levels and nonlinearity for frequencies close to the 'vort mode' resonance is urgently needed.

Polycrystal Materials

The lead lanthanum zirconate titanate (PLZT) family of hot pressed transparent ceramics is still the basis for most applications using polycrystal ceramics.¹⁵

Most practical work has been done using the 95:5:35 PLZT composition in the slim loop phase which has very high quadratic electro-optic response. The fast switching possible between birefringent (transmitting) and isotropic (non-transmitting) phase using surface or surface groove electrodes is exploited in current USAF flash protection goggles.¹⁶ New simple numeric and bar graph color displays have been based on the Newtonian subtraction color spectra available under high field in these ceramics,¹⁷ and it will be most interesting to observe their market penetration in competition with LCD display materials.

In more sophisticated research level efforts, there is continuing improvement in the scattering mode displays which use ion implanted photoconductive layers to index the switching regions. Resolution approaching 100 line pairs/mm has been reported in the image. A wide grey scale is possible and photon sensitivity comparable to bismuth silicon oxide SLM's has been achieved, but in systems which now have permanent memory.¹⁸

For all ferroelectric/electro-optic systems in the solid (rather than liquid crystal states), the high fields required for substantial optical change are rather penal in bulk devices. One cannot help feeling that thin film structures might be much more advantageous

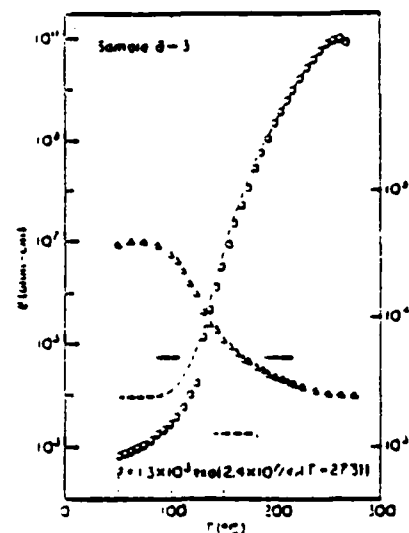


Fig. 2. PTCR effect in Sb₂O₃ doped BaTiO₃ (M. Kuwabara, *J. Amer. Ceram. Soc.* 64(11):639-644 (1981)).

for achieving very high fields at the low voltage drive levels compatible with silicon and GaAs circuitry.

Pyroelectrics

For most pyroelectric bolometric systems, the materials figure of merit lies between that for a vidicon material.

$$F = \frac{\rho}{KC'}$$

and that for a point detector of radiation

$$F = \frac{\rho}{C'(K \tan \delta)^{1/2}}$$

where ρ is the pyroelectric coefficient ($\rho = dP/dT$), C' is the thermal capacity (volume specific heat), K the relative dielectric permittivity and $\tan \delta$ the loss factor.

For ferroelectric with second order Curie points, ρ rises rapidly as T_c is approached from below, but K rises even faster — thus for a given capacitance input there is an optimum operating point below T_c which maximizes F .

In single crystal ceramics, Sr,Ba_{1-x}Nb₂O₆ is a preferred material both for high speed laser detectors, and for pyroelectric image planes.¹⁹

Poled polycrystal ceramic is also widely used, with compositions in the PZT family close to the single cell:multi cell ferroelectric/ferroelectric phase change in the rhombohedral compositions being preferred. In the ceramic, complex compositions are used to "smear" the abrupt phase change which is first order, and to control the resistivity of the ceramic so that in the following FET circuitry the expensive high gate drain resistor can be eliminated.²⁰

For focal plane arrays, the major problem is to provide electrical contact from each pixel element to the semiconductor interconnection array without thermally short circuiting the very low thermal capacity bolometer chip.

A number of new and innovative interconnect systems are under proprietary development, and it will be interesting to see how progress here influences the competition between pyroelectric bolometers and cooled photon detectors for practical imaging application.

References

1. L. H. Maxwell, D. M. Frenkel, and P. J. Franklin, "Layered High Dielectric Constant Capacitors," Symposium of Michigan Electrical Assn., pp. 73-82 (1981).
2. M. Herber and A. G. Martin, "The Application of Modern Materials to Electronic Components," *J. Brit. I.R.E.*, 11 (2) 107-115 (1961).
3. L. Hanks, "Theory of the Barrier Layer Effect in Semiconducting Barium Titanate," *Siemens Forsch. Ber.*, 3 (4) 209-13 (1979).
4. R. Wernicke, "Formation of Second-Phase Layers in SrTiO₃ Boundary Layer Capacitors," *Advances in Ceramics*, 1 (1) 251-71 (1981).
5. R. Wernicke, "Two Layer Model Explaining the Properties of SrTiO₃ Boundary Layer Capacitors," *Advances in Ceramics*, 1 (1) 272-81 (1981).
6. A. Yamaji and S. Waku, "Studies in SrTiO₃ Boundary Layer Dielectrics," *Rev. High Temp. Phys.*, 20 (17-4) 747-63 (1972).
7. K. O. Budd and D. A. Payne, "Internal Boundaries in Fine Grained WO₃ Doped SrTiO₃," *Bull. Amer. Ceram. Soc.*, 62 (3) 406 (1983).
8. H. Hagedorn, "Material and Technology Aspects of Ceramic Capacitors," *Bull. Amer. Ceram. Soc.*, 62 (3) 414 (1983).
9. J. Burn, "Flux Sintered BaTiO₃ Dielectrics," *J. Mat. Sci.*, 17 (3) 1398-1408 (1982).
10. R. B. Amis, H. U. Anderson, and C. E. Hoekings, U.S. Patent 4,082,906 (1978).
11. K. Wakino, K. Minai, and Y. Sakabe, "High Dielectric Constant Ceramics for Base Metal Multilayer Capacitors," U.S. Patent 4,115,493.
12. H. Takamizawa, K. Utsuno, M. Yonezawa, and T. Ohno, "Large Capacitance Ceramic Multilayer Ceramic Capacitors," *Proc. Jpn. Elect. Comp. Conf.*, 302-7 (1981).
13. G. Desgrain, H. Jali, and B. Ravent, "Ceramic PZT and PMN for Multilayer Capacitors Having a High Dielectric Constant," *Mat. Chem. and Phys.*, 8, 469-91 (1983).
14. G. B. Mahler, "Effects of Silver Doping on the Physical and Electrical Properties of PLZT Ceramics," *J. Amer. Ceram. Soc.*, 66 (6) 408-413 (1983).
15. G. Mahler, "A New PLZT Dielectric for Use in Characteristic XTR Multilayer Ceramic Capacitors," *Proc. 1981 Electron Comp. Conf.* (IEEE), 173-77 (1983).
16. K. Wakino and T. Sato, "Large Capacitance Multilayer Ceramic Capacitors with Base Metal Electrodes," *Proc. Jpn. Elect. Res. Res. Tech. Symp.*, CARTS 83, 104-72 (1983).
17. M. Yonezawa, K. Utsuno, and T. Ohno, "Properties of PbFe_{0.5}Nb_{0.5}O₃, PbFe_{0.5}Nb_{0.5}O₃ Ceramics," *Proc. Int. Mtg. on Ferroelectric Materials and Their Applications*, Kyoto Japan, pp. 297-301 (1977).
18. Mitsubishi Mining and Cement Co. Ltd., Multilayer Ceramic Capacitor Catalogue, Mitsubishi Int. Corp., Chemicals Dept., 320 Madison Ave., New York, NY 10022.
19. K. Hikos (private communication).
20. A. Chance, C. W. Ho, C. H. Bajorek, and M. Sampogna, *IEEE Trans. on CHMT*, 4, 1781 (1982).
21. C. W. Ho, O. A. Chance, C. H. Bajorek, and R. E. Acona, *IBM J. Res. Dev.*, 26, 266 (1982).
22. R. B. Gray, "Transducer and Method of Making the Same," U.S. Patent No. 2,486,560 (Nov. 1, 1949).
23. B. Jaffe, R. S. Rosh, and S. Marzullo, *J. Res. Nat. Bur. Stds.*, 58, 239-54 (1955).
24. B. Jaffe, W. R. Cuzko, Jr., and H. Jaffe, "Piezoelectric Ceramics," Academic Press, London/New York (1971).
25. Takamizawa and M. Takahashi, *Jpn. J. Appl. Phys.*, 11 (1) 31-5 (1972).
26. Landolt-Bornstein, "Tables on Elastic, Piezoelectric, Piezo-Optic and Electro-Optic Constants of Crystals," Vol. II 1, 1966, Vol. II, 2, 1969, Springer Verlag, Berlin.
27. R. E. Newnham, D. P. Skinner, and L. E. Cross, *Mat. Res. Bull.*, 13, 325 (1978).
28. R. E. Newnham, I. J. Bowen, K. Klinker, and L. E. Cross, "Composite Piezoelectric Transducers," *Materials Engineering*, 2, 93-9 (1980).
29. A. Safari, R. E. Newnham, L. E. Cross, and W. A. Schulze, "Perturbed PZT Polymer Composites for Piezoelectric Transducer Applications," *Ferroelectrics*, 41, 197-205 (1982).
30. H. Takemichi, S. Iwamura, E. Yamamoto, and Y. Ito, "Electromechanical Properties of (Pb,La)TiMnO₃ Ceramics (La-doped ferroelectric)," *J. Acoustic Soc. Amer.* 73 (4) 1114-20 (1982).
31. Y. Yamashita, S. Yoshida, and T. Takahashi, "Effects of Added Mn on the Piezoelectric Characteristics of (PbCa)TiO₃ Single Dielectric Ceramics," *Proc. Int. Mtg. on Ferroelectric Materials and Applications FMA-4*, Kyoto, Japan, p. 279 (1983).
32. H. Takemichi, S. Iwamura, Y. Ito, and K. Nagasawa, "Rare-Earth Substituted Piezoelectric PbTiO₃ Ceramics for Acoustic Wave Applications," *Ferroelectrics*, 31, 731 (1983).
33. L. E. Cross, S. J. Lang, R. E. Newnham, S. Nomura, and K. Uchino, "Large Electrostrictive Effects in Relaxor Ferroelectrics," *Ferroelectrics*, 23, 187-92 (1980).
34. K. Uchino, S. Nomura, L. E. Cross, R. E. Newnham, and S. J. Lang, "Electrostrictive Effect in Perovskites and Its Transducer Applications," *J. Mat. Sci.*, 16, 369-78 (1981).
35. W. G. Cady, U.S. Patent 1,491,246, Data presented to American Physical Society, February 26, 1921.
36. M. C. Hales and J. W. Burgess, "Design and Construction of Manganese Crystal Filters Using Lithium Tantalate," *Proc. IEEE*, 123 (7) 637-41 (1976).
37. G. R. Baruch and R. E. Newnham, "Piezoelectric Materials with Positive Elastic Constant Temperature Coefficients," *APCRU TR-73-163*, Final Report on Contract No. F19628-73-C-0118 (1975).
38. Z. P. Chang and G. R. Baruch, "New Temperature Compensating Materials with High Piezoelectric Coupling," *IEEE Trans.*, SU-23, 127 (1976).
39. K. Tsuyosuchi and M. Mikami, "Zero Temperature Coefficient SAW Delay Line on AlN Epitaxial Films," *Ultrasonics Symposium* '84 (1983).
40. M. M. Sharrocks, R. W. Whatmore, F. W. Ainger, and I. M. Young, "Lithium Tetroborate a New Temperature Compensating Substrate Material for SAW Devices," *Proc. 1981 Ultrasonics Symposium*, 337.
41. E. J. Stroh and R. R. Neureuther, "Ferroelectric/Piezoelectric SAW Transducers in Strontium Barium Niobate," *Proc. 1981 Ultrasonics Symposium*, 157.
42. L. Hanks, "Theory of the Barrier Effect in Semiconducting Barium Titanate," *Siemens Forsch. Ber.*, 3 (4) 209-13 (1979).
43. J. Daniels, K. H. Haerdtl, and R. Wernicke, "The PTC Effect in Barium Titanate," *Philos. Res. Rep.*, 38 (3) 77-82 (1979).
44. J. Daniels and R. Wernicke, "New Aspects of an Improved PTC Model," *Philos. Res. Rep.*, 38, 344-49 (1979).
45. S. Noda and N. Yamamoto, "Honeycomb Structured BaTiO₃ Ceramics for Heat-Work Applications," *VGX Techn. Rep.*, 8, 75-2 (1975).
46. R. C. Allfema, R. V. Schmitt, and E. H. Turner, "Characteristics of Ti-Diffused Lithium Niobate Directional Couplers," *Appl. Opt.*, 18 (23) 4012-25 (1979).
47. R. V. Schmitt and H. Kugelink, "Electro-Optically Switched Coupler with Stepped Q-B Reversal Using Ti-Diffused LiNbO₃ Waveguides," *Appl. Phys. Lett.*, 28 (9) 503-16 (1976).
48. G. Gumer, "New Applications of Ferroelectrics for Optical Devices," *Proc. European Meeting on Ferroelectrics EAF 3*, Ben Almadena, Spain, (1983), to be published in *Ferroelectrics*.
49. G. H. Haertling, "Improved Hix Pressed Ceramics with the (PbLa)(ZrTi) System," *J. Amer. Ceram. Soc.*, 54 (6) 303-19 (1971).
50. T. Culcher, "PLZT Thermal/Flexion Goggles: Concepts and Constraints," *Ferroelectrics*, 27, 173-78 (1981).
51. G. H. Haertling, "PLZT Reflective Displays," *Ferroelectrics*, 50, 189 (1981).
52. C. E. Land and P. S. Peercy, "Photo-Ferroelectric Sensitivity Enhancement in PLZT by Thermal Diffusion of Metals," *Ferroelectrics*, 59, 111 (1983).
53. T. Liu, "Critical Assessment in Pyroelectric Detectors," *Ferroelectrics*, 10, 53-9 (1976).
54. R. W. Whatmore, "High Performance Conducting Pyroelectric Ceramics," *Ferroelectrics*, 49, 201-10 (1983).

A PHENOMENOLOGICAL THEORY FOR PHASE TRANSITIONS IN
PEROVSKITE FERROELECTRICS WITH OXYGEN OCTAHEDRON TILTS

T.R. Halemane, M.J. Haun, L.E. Cross, and R.E. Newnham

A PHENOMENOLOGICAL THEORY FOR PHASE TRANSITIONS IN PEROVSKITE FERROELECTRICS WITH OXYGEN OCTAHEDRON TILTS

T. R. HALEMANE,† M. J. HAUN, L. E. CROSS and R. E. NEWNHAM

*Materials Research Laboratory, The Pennsylvania State University, University
Park, PA 16802 USA*

(Received December 15, 1984)

A phenomenological theory, based on the Landau-Ginsburg-Devonshire formalism is developed to explain phase transitions in perovskite ferroelectrics with oxygen octahedron tilts. In this approach, the Gibbs free energy function is expanded as a power series involving polarization and tilt angle as order parameters. After giving the general solutions, we apply the theory to the $\text{PbZr}_{0.9}\text{Ti}_{0.1}\text{O}_3$ system.

1. INTRODUCTION

Many ferroelectrics, especially those in the perovskite family, exhibit phase transitions involving tilts in the oxygen octahedral chains.¹ The solid solution $\text{PbZr}_{1-x}\text{Ti}_x\text{O}_3$ between the antiferroelectric PbZrO_3 and the ferroelectric PbTiO_3 , named PZT, has been used extensively in the electronics industry.² The difficulty in growing single crystals of PZT and the availability of a wide range of compositions to choose from make it desirable to have a workable theory for predicting dielectric, piezoelectric and other properties and phase transitions in PZT.

The PZT phase diagram¹ is shown in Figure 1. For mole fractions of PbTiO_3 in the range 0.06 to 0.37, a phase transition from a higher temperature rhombohedral ferroelectric phase $F_{R(HT)}$ to a lower temperature rhombohedral ferroelectric phase $F_{R(LT)}$ is observed. The lower temperature phase has the oxygen octahedral chain twisted, with neighboring corner-linked octahedra tilted in opposite directions. The tilts are about the [111] axis and are denoted by $a^-a^-a^-$ in the notation of Glazer.³ The space group for the $F_{R(HT)}$ phase is $R3m$ and that for the $F_{R(LT)}$ phase is $R3c$. PZT in the cubic paraelectric has the perovskite crystal structure ABO_3 , as shown in Figure 2.

In $\text{PbZr}_{0.9}\text{Ti}_{0.1}\text{O}_3$,⁴ for example, the transition from the cubic paraelectric state P_c to the rhombohedral ferroelectric state $F_{R(HT)}$ takes place at 250°C, and a further transition to the $F_{R(LT)}$ phase takes place at 100°C. The spontaneous polarization P_s is, in both the rhombohedral phases, along the [111] direction. The $F_{R(LT)}$ phase has, in addition, oxygen octahedron tilts around the [111] axis.

We present here a Gibbs free energy function capable of explaining such phase transitions with octahedral tilts. A similar thermodynamic phenomenological approach was used by Darlington⁵ for the $\text{NaNbO}_3\text{-KNbO}_3$ system. The thermody-

†Present Address: Physics Department, State University College, Fredonia, NY 14063.

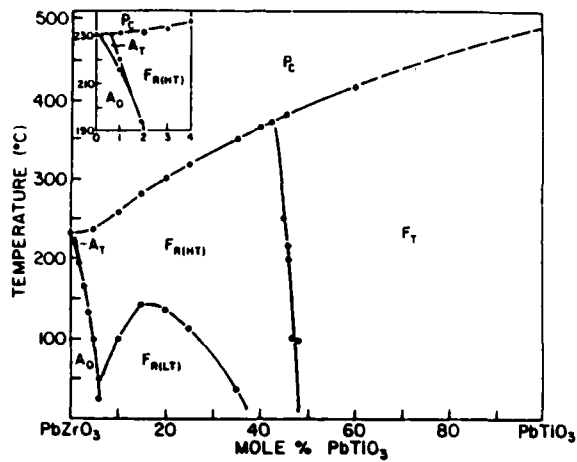


FIGURE 1 PbZrO_3 - PbTiO_3 phase diagram (see Reference 14).

dynamic theory of ferroelectricity based on Landau's treatment⁶ of phase transitions was originally developed by Devonshire.⁷ Recently, this treatment has been extended by Amin, Cross, and others⁸ to explain the existence of the morphotropic phase boundary (MPB) near $x = 0.5$ in $\text{PbZr}_{1-x}\text{Ti}_x\text{O}_3$ and also to predict its properties near the MPB. The region considered there does not have tilts of the oxygen octahedra.

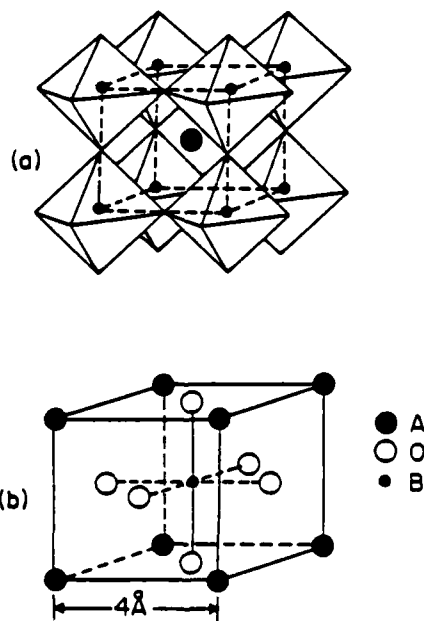


FIGURE 2 Two equivalent representations of the perovskite structure (see Reference 1).

In this paper, the focus is on developing a thermodynamic phenomenological theory which includes the transitions with tilts in the oxygen octahedra. This is carried out in Section 2 by considering both the polarization and tilt angle as order parameters, with the free energy function expanded as a power series. In Sections 3, and 4, we give the possible phase transitions and general solutions that result from the theory. In Section 5 and 6, we evaluate the constant coefficients and apply this model to PZT. Finally in Section 7, we discuss possible improvements and other applications.

2. PHENOMENOLOGICAL THEORY

Consider a single domain single crystal of $\text{PbZr}_{0.9}\text{Ti}_{0.1}\text{O}_3$ or any similar structures, in which the polarization (P) direction does not change during the phase transitions and in which the octahedral tilts can be described by an angle (θ) of rotation about a single axis.

From the first law of thermodynamics, for a polarizable, deformable solid subject to an electric field E , stress field X and a sublattice torque τ we can write assuming reversibility and extending Devonshire,⁷

$$dU = T dS + E dP + X dx + \tau d\theta. \quad (1)$$

Here U is the internal energy, T is the temperature, S is the entropy and x is the strain. The torque τ is responsible for the tilt $d\theta$. Since this tilt exists only in a portion of the crystal lattice, it cannot be considered a regular shear strain of the entire crystal. We can then write, for the elastic Gibbs energy $G = U - TS - xX$,

$$dG = -S dT + E dP - x dX + \tau d\theta \quad (2)$$

making it a function of T , P , X and θ .

At constant temperature T and zero stress ($X = 0$) conditions, we can expand G as a power series in θ and P . Assuming a centrosymmetric paraelectric state, the odd power terms in the expansion vanish yielding the following energy function:

$$G = G_0 = \frac{1}{2}g_2\theta^2 + \frac{1}{4}g_4\theta^4 + \frac{1}{6}g_6\theta^6 + \dots + \frac{1}{2}f_2P^2 + \frac{1}{4}f_4P^4 + \frac{1}{6}f_6P^6 + \dots + \frac{1}{2}d\theta^2P^2 + \dots \quad (3)$$

We neglect terms higher than the fourth powers resulting in

$$G = G_0 + \frac{1}{2}g_2\theta^2 + \frac{1}{4}g_4\theta^4 + \frac{1}{2}f_2P^2 + \frac{1}{4}f_4P^4 + \frac{1}{2}d\theta^2P^2. \quad (4)$$

Further, we assume

$$g_2 = \gamma_\theta(T - T_\theta).$$

and

$$f_2 = \gamma_p (T - T_p), \quad (5)$$

where γ_θ and γ_p are positive constants. T_θ and T_p will be related later to the transition temperatures between phases. We will assume $T_p \geq T_\theta$, but the case $T_p < T_\theta$ can be worked out in an analogous manner. We also required that $f_4 > 0$, and $g_4 > 0$ in Equation (4) to prevent G from becoming negative infinity. The phase transitions obtained will be of second-order.

For the equilibrium state, G should be a stable minimum with respect to P and θ . Therefore, we need

$$\frac{\partial G}{\partial \theta} = 0 \rightarrow \theta(g_2 + g_4\theta^2 + dP^2) = 0, \quad (6)$$

$$\frac{\partial G}{\partial P} = 0 \rightarrow P(f_2 + f_4P^2 + d\theta^2) = 0, \quad (7)$$

$$\frac{\partial^2 G}{\partial \theta^2} > 0 \rightarrow g_2 + 3g_4\theta^2 + dP^2 > 0, \quad (8)$$

$$\frac{\partial^2 G}{\partial P^2} > 0 \rightarrow f_2 + 3f_4P^2 + d\theta^2 > 0, \quad (9)$$

and

$$\begin{aligned} J(\theta, P) &\equiv \frac{\partial^2 G}{\partial \theta^2} \frac{\partial^2 G}{\partial P^2} - \left(\frac{\partial^2 G}{\partial \theta \partial P} \right)^2 > 0 \\ &\rightarrow (3g_4d)\theta^4 + (9g_4f_4 - 3d^2)\theta^2P^2 + (3f_4d)P^4 \\ &\quad + (3g_4f_2 + g_2d)\theta^2 + (3f_4g_2 + df_2)P^2 + g_2f_2 > 0. \end{aligned} \quad (10)$$

We now solve Equations (6) thru (10) simultaneously. If (8) and (10) are satisfied, (9) will be automatically satisfied. There are four possible solutions for the equilibrium values (θ_s, P_s) .

$$\begin{aligned} \text{Phase A:} \quad &\theta_s = 0, \quad P_s = 0, \\ &G = G_0, \quad f_2 > 0, \quad \text{and} \quad g_2 > 0. \end{aligned} \quad (11)$$

$$\begin{aligned} \text{Phase B:} \quad &\theta_s = 0, \quad P_s^2 = -\frac{f_2}{f_4}, \\ &G = G_0 + \frac{1}{4}f_2P_s^2, \quad f_2 < 0, \quad \text{and} \quad df_2 < g_2f_4. \end{aligned} \quad (12)$$

$$\text{Phase C: } \theta_s^2 = -\frac{g_2}{g_4}, \quad P_s = 0,$$

$$G = G_0 + \frac{1}{4}g_2\theta_s^2, \quad g_2 < 0, \quad \text{and} \quad dg_2 < f_2g_4. \quad (13)$$

$$\text{Phase D: } \theta_s^2 = \frac{df_2 - g_2f_4}{g_4f_4 - d^2}, \quad P_s^2 = \frac{dg_2 - g_4f_2}{g_4f_4 - d^2},$$

$$G = G_0 + \frac{1}{4}g_2\theta_s^2 + \frac{1}{4}f_2P_s^2,$$

$$df_2 > g_2f_4, \quad dg_2 > f_2g_4, \quad \text{and} \quad d^2 < g_4f_4. \quad (14)$$

The three inequalities in the Phase D solution, Equation (14), are not always independent. For example, when f_2, g_2, d, f_4, g_4 are all positive, the first two inequalities require $d^2 > f_4g_4$, and so all three of them cannot be satisfied simultaneously and phase D will not be available.

3. PHASE TRANSITIONS

We will now examine the consequences of the temperature dependences of g_2 and f_2 as given by Equation (5) as the crystal is cooled from high temperatures toward 0 K. We also have assumed $f_4 > 0, g_4 > 0, T_p > T_\theta$, and $d^2 < g_4f_4$. This last condition is necessary for phase D to be available.

At high temperatures ($T > T_p > T_\theta$), we have $f_2 > 0, g_2 > 0$ and phases B and C are not possible. Phase A is always possible for this region and phase D may exist under certain conditions but has higher free energy than phase A. All these conditions can be seen easily from the results given above for the four phases.

To investigate what happens when T is lowered, it is necessary to examine the four temperature-dependent inequalities $f_2 < 0, g_2 < 0, df_2 < g_2f_4$ and $dg_2 < f_2g_4$. For this purpose, it is convenient to define two additional temperature parameters T_r and T_s such that

$$df_2|_{T=T_r} = g_2f_4|_{T=T_r}, \quad (15)$$

and

$$dg_2|_{T=T_s} = f_2g_4|_{T=T_s}. \quad (16)$$

We then have

$$T_r = \frac{f_4\gamma_\theta T_\theta - d\gamma_p T_p}{f_4\gamma_\theta - d\gamma_p}. \quad (17)$$

TABLE I.

Phase transition sequences for different values of T_r, T_i in relation to T_θ, T_p , where^a $T_p > T_\theta$

No.	d	Temperature parameters values	Phase transition sequences
1	Negative	$T_\theta < T_r < T_i < T_p$	$A \xrightarrow{T_p} B \xrightarrow{T_r} D$
2		$T_\theta < T_i < T_r < T_p$	$A \xrightarrow{T_p} B \xrightarrow{T_r} \text{No Stable Phase} \xrightarrow{T_i} D$
3	Positive	$T_r < T_\theta < T_p < T_i$	$A \xrightarrow{T_p} B \xrightarrow{T_r} D$
4		$T_i < T_r < T_\theta < T_p$	$A \xrightarrow{T_p} B \xrightarrow{T_r} D \xrightarrow{T_i} C$
5		$T_r < T_i < T_\theta < T_p$	$A \xrightarrow{T_p} B \xrightarrow{T_i} (B, C) \xrightarrow{T_r} C$
6		$T_i < T_\theta < T_p < T_r$	$A \xrightarrow{T_p} B \xrightarrow{T_i} (B, C)$
7	Positive	$T_\theta < T_p < T_i < T_r$	$A \xrightarrow{T_p} B$
8		$T_\theta < T_p < T_r < T_i$	$A \xrightarrow{T_p} B$

^aTo generate phase transition sequences when $T_p < T_\theta$ replaces T_p by T_θ , T_θ by T_p , T_r by T_i , T_i by T_r , B by C and C by B in this table.

and

$$T_i = \frac{g_4 \gamma_p T_p - d \gamma_\theta T_\theta}{g_4 \gamma_p - d \gamma_\theta} \quad (18)$$

Several sequences of phase transitions are possible depending on the sign of d and the relative values of T_θ, T_p, T_r and T_i . These are listed in Table I.

For purposes of illustration, we discuss the case $T_r < T_\theta < T_p < T_i$ which occurs when d is positive and small. The analysis is made simpler by drawing a diagram as shown in Figure 3. In this diagram, $g_2 f_4, f_2 g_4, df_2$ and dg_2 are plotted as a function of temperature T . The intersection of lines df_2 and $g_2 f_4$ gives the temperature T_r , and the intersection of the dg_2 and $f_2 g_4$ lies gives T_i . For $T > T_i$, we see from the diagram that $dg_2 < f_2 g_4, df_2 < g_2 f_4, f_2 > 0$, and $g_2 > 0$, so that phase A is the only possibility. For $T_p < T < T_i$ also only phase A is possible. But when T decreases below T_p , then $f_2 < 0$, and $df_2 < g_2 f_4$. Now only phase B can exist until the temperature is lowered to T_r . Although g_2 becomes negative as T crosses T_θ , we do not stabilize phase C, because $dg_2 > f_2 g_4$ for $T < T_i$, and this non-availability of phase C, continues down to 0 K. But for $T < T_r$, we have $f_2 < 0, g_2 < 0, df_2 > g_2 f_4$, and $dg_2 > f_2 g_4$. These inequalities are consistent with $d^2 < f_4 g_4$ and phase D is the only equilibrium state in this region down to absolute zero temperature. Thus we have the phase transition sequence

$$A \xrightarrow{T_p} B \xrightarrow{T_r} D$$

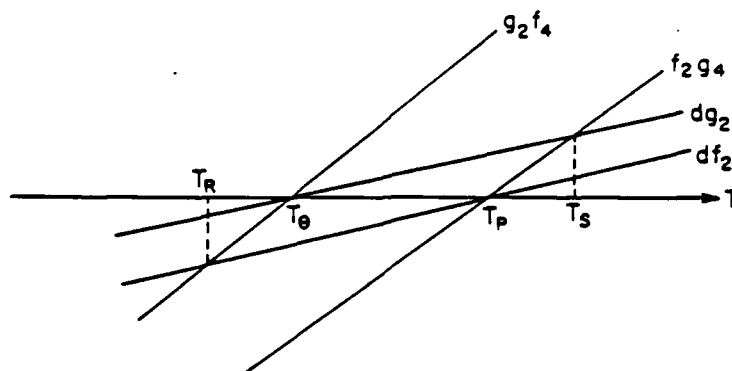


FIGURE 3 Diagram to aid understanding of the phase transition sequence for the case $T_r < T_\theta < T_p < T_s$.

for this case. If the numerical values are such that $T_r < 0$ K, then only the $A \xrightarrow{T_p} B$ transition will be observed.

The other transition sequences listed in Table I can be derived in a similar manner. It is found that in two of the cases, for certain temperatures, the phases B and C both correspond to energy minima. In such a case, one of the two phases will correspond to a metastable state.

The case for $T_p < T_\theta$ can be worked out similarly. It can, in fact, be deduced directly from Table I if we replace T_p by T_θ , T_θ by T_p , T_r by T_s , T_s by T_r , B by C and C by B in Table. We will then have the transitions $A \xrightarrow{T_\theta} C \xrightarrow{T_p} D$.

↑
I

4. GENERAL SOLUTIONS

In this section we derive general expressions for the physical properties of the polarization, dielectric constant, tilt angle and torsion constant for octahedral tilts. These results are applied to PZT in the next section.

A. Polarization

Phase A: $P_s = 0.$

Phase B:
$$P_s^2 = -\frac{\gamma_p}{f_4}(T - T_p)$$

$$= \alpha(T_p - T). \quad (19)$$

where

$$\alpha = \gamma_p / f_4. \quad (20)$$

Phase C:

$$P_s = 0.$$

Phase D:

$$\begin{aligned} P_s^2 &= \frac{dg_2 - g_4 f_2}{g_4 f_4 - d^2} \\ &= \beta(T_s - T), \end{aligned} \quad (21)$$

where

$$\beta = \frac{g_4 \gamma_p - d \gamma_\theta}{g_4 f_4 - d^2}. \quad (22)$$

It is easy to show by definitions of α , β , T_r , and T_s , that

$$\alpha(T_p - T_r) = \beta(T_s - T_r). \quad (23)$$

This implies polarization is continuous during the $B \xrightarrow{T_r} D$ transition.

B. Dielectric Constant

The dielectric constant ϵ_R is defined in terms of the inverse susceptibility χ by

$$\chi = \frac{1}{\epsilon_0(\epsilon_R - 1)}, \quad (24)$$

where we have

$$\chi = \frac{\partial^2 G}{\partial P^2} = f_2 + 3f_4 P^2 + d\theta^2. \quad (25)$$

We can then show for the different phases,

Phase A:

$$\begin{aligned} \chi &= f_2 \\ &= \gamma_p(T - T_p). \end{aligned} \quad (26)$$

Phase B:

$$\begin{aligned} \chi &= f_2 + 3f_4 P_s^2 \\ &= 2\gamma_p(T_p - T). \end{aligned} \quad (27)$$

$$\begin{aligned}
\text{Phase C:} \quad \chi &= f_2 + d\theta_s^2 \\
&= \frac{g_4\gamma_p - d\gamma_\theta}{g_4}(T - T_s),
\end{aligned} \tag{28}$$

where T_s is defined by Equation (18).

$$\begin{aligned}
\text{Phase D:} \quad \chi &= f_2 + 3f_4P_s^2 + d\theta_s^2 \\
&= 2f_4P_s^2 \\
&= 2f_4\beta(T_s - T),
\end{aligned} \tag{29}$$

where β is given by Equation (22) and f_4 by Equation (20).

C. Octahedral Tilt Angle

We get the following results:

$$\begin{aligned}
\text{Phase A:} \quad \theta_s &= 0. \\
\text{Phase B:} \quad \theta_s &= 0. \\
\text{Phase C:} \quad \theta_s^2 &= -g_2/g_4 \\
&= \frac{\gamma_\theta}{g_4}(T_\theta - T).
\end{aligned} \tag{30}$$

$$\begin{aligned}
\text{Phase D:} \quad \theta_s^2 &= \frac{df_2 - g_2f_4}{g_4f_4 - d^2} \\
&= \lambda(T_r - T),
\end{aligned} \tag{31}$$

where

$$\lambda = \frac{f_4\gamma_\theta - d\gamma_p}{g_4f_4 - d^2}. \tag{32}$$

It can be shown by definitions of λ , T_r , and T_s , that

$$\gamma_\theta(T_\theta - T_s) = \lambda g_4(T_r - T_s). \tag{33}$$

This implies continuity of the tilt angle in a $D \xrightarrow{T_s} C$ transition.

D. Torsion Constant for Octahedron Tilts

The torque τ acting on the oxygen octahedral sublattice is from Equation (2) given by,

$$\tau = \frac{\partial G}{\partial \theta} = g_2 \theta + g_4 \theta^3 + d\theta P^2. \quad (34)$$

The torsion constant of the octahedron is then given by

$$k = \frac{\partial \tau}{\partial \theta} = g_2 + 3g_4 \theta^2 + dP^2. \quad (35)$$

The frequency ω of the rotational phonon soft-mode is given by $\sqrt{k/I}$, with the proportionality constant I giving a measure of the inertia of the octahedra for rotational motion. We can, therefore, obtain the following results for k and ω in the different phases.

Phase A:

$$k = g_2 = \gamma_\theta (T - T_\theta),$$

$$\omega = \sqrt{\mu (T - T_\theta)}, \quad (36)$$

where

$$\mu = \gamma_\theta / I. \quad (37)$$

Phase B:

$$k = g_2 + dP_s^2$$

$$= \frac{\gamma_\theta f_4 - d\gamma_p}{f_4} (T - T_r),$$

$$\omega = \sqrt{\nu (T - T_r)}, \quad (38)$$

where

$$\nu = \frac{\gamma_\theta f_4 - d\gamma_p}{f_4 I}. \quad (39)$$

Phase C:

$$k = 2\gamma_\theta (T_\theta - T),$$

$$\omega = \sqrt{2\mu (T_\theta - T)}. \quad (40)$$

Phase D:

$$k = g_2 + 3g_4 \theta_s^2 + dP_s^2$$

$$= 2g_4 \theta_s^2$$

$$= 2g_4 \lambda (T_r - T),$$

$$\omega = \sqrt{\delta (T_r - T)}, \quad (41)$$

where

$$\delta = \frac{2g_4\lambda}{I}. \quad (42)$$

We see here that the phonon soft-mode frequency varies as $|T - T_\theta|^{0.5}$ in phases A and C, and as $|T - T_r|^{0.5}$ in phases B and D. Looking back at Table I, the $A \xrightarrow{T_r} C$ transition is not possible since $T_p > T_\theta$, but the $B \xrightarrow{T_r} D$ transition is possible, and we see here that it involves the condensation of a soft-mode.

5. EVALUATION OF THE CONSTANT COEFFICIENTS

In order to compare theory and experiment, it is necessary to evaluate the various constant coefficients. The Gibbs free energy function of Equation (4) has seven independent constant parameters γ_p , T_p , f_4 , γ_θ , T_θ , g_4 and d . All the other adjustable parameters such as T_r , T_s , α , β , and λ that we have defined for convenience are functions of these seven independent constants. However, one has to proceed with caution in using experimental data to evaluate these constants. For example, one can use experimental values of polarization and tilt-angle at different temperatures to obtain constants like α , T_s , and γ , but it will not be proper to get the Gibbs energy coefficients directly from them. The latter are deduced from the experimentally determined constants. We show here how this can be done.

The experimental data that are normally available are the polarization, dielectric constant, tilt-angle, and soft-mode phonon frequencies measured as functions of temperature. In order to be self-consistent, it is important that the relationships between the different parameters are established fully and only seven independent parameters determined by comparison with experiment, with the others being derived from this independent set. For example, we can consider T_p , T_θ , T_r , T_s , γ_p , α , and λ as an independent set, whose values can be conveniently determined from the experimental data of the polarization, dielectric constant, tilt angle and rotational soft-mode frequency. To derive the other constants from these, we make use of equations (17), (18), (20), (23) and the relation

$$\gamma_p - \beta f_4 = \lambda d, \quad (43)$$

which follows easily by definition of λ and β . There is another similar relation

$$\gamma_\theta - \lambda g_4 = \beta d, \quad (44)$$

but it is not independent of the others used here.

We can then show that

$$f_4 = \gamma_p/a. \quad (45)$$

$$\begin{aligned} d &= \frac{\gamma_p \beta f_4}{\lambda} \\ &= \frac{\gamma_p}{\lambda} \frac{T_s - T_p}{T_s - T_r}. \end{aligned} \quad (46)$$

$$\begin{aligned} \gamma_\theta &= \frac{d \gamma_p (T_r - T_p)}{f_4 (T_r - T_\theta)} \\ &= \frac{\gamma_p \alpha}{\lambda} \frac{(T_s - T_p)(T_r - T_p)}{(T_s - T_r)(T_r - T_\theta)}. \end{aligned} \quad (47)$$

and

$$\begin{aligned} g_4 &= \frac{d \gamma_\theta (T_s - T_\theta)}{\gamma_p (T_s - T_p)} \\ &= \frac{\gamma_p \alpha}{\lambda^2} \frac{(T_s - T_p)(T_r - T_p)(T_s - T_\theta)}{(T_s - T_r)^2 (T_r - T_\theta)}. \end{aligned} \quad (48)$$

Now, using the above results we can further show that

$$\frac{\mu}{\nu} = \frac{\gamma_\theta f_4}{\lambda (g_4 f_4 - d^2)} = \frac{T_p - T_r}{T_p - T_\theta}, \quad (49)$$

and

$$\frac{\mu}{\delta} = \frac{\gamma_\theta}{2 g_4 \lambda} = \frac{(T_s - T_r)}{2(T_s - T_\theta)}. \quad (50)$$

Sets other than the one we have used here (for example T_p , T_θ , T_r , T_s , γ_p , γ_θ , and β) can also be used.

The results presented in this section are applicable to all the cases listed in Table 1.

6. APPLICATION TO PZT

We now apply the phenomenological theory and the results derived in the previous sections to the case of $\text{PbZr}_{0.9}\text{Ti}_{0.1}\text{O}_3$. The experimental single crystal data of Glazer, Mabud and Clarke⁴ are used to calculate the values of the frequency parameters to provide comparison of theory with experiment. The treatment given here is only

preliminary, because higher order terms in the Gibbs free energy expansion are needed for greater accuracy, especially if these phase transitions are of first order, as some authors assert.¹⁰

The transition sequence in $\text{PbZr}_{0.9}\text{Ti}_{0.1}\text{O}_3$ is $A \rightarrow B \rightarrow D$. The $A \rightarrow B$ transition is at 250°C and the $B \rightarrow D$ transition takes place at 100°C . By reference to Table I, we identify $T_p = 250^\circ\text{C}$ and $T_s = 100^\circ\text{C}$. It can be shown easily that our model requires both transitions to be second-order i.e. $P_s|_{T_s, D} = P_s|_{T_s, B}$. Using data from reference 4, at 100°C ,

$$\alpha(250 - 100) = (0.38)^2, \quad (51)$$

and

$$\beta(T_s - 100) = (0.38)^2. \quad (52)$$

Also, at 20°C , $P_s = 0.45 \text{ C m}^{-2}$ from Reference 4, so that

$$\beta(T_s - 20) = (0.45)^2. \quad (53)$$

Solving Equations (51), (52) and (53) we get

$$\alpha = 9.62 \times 10^{-4} \text{ C}^2 \text{ m}^{-4}/^\circ\text{C}, \quad (54)$$

$$\beta = 7.262 \times 10^{-4} \text{ C}^2 \text{ m}^{-4}/^\circ\text{C}, \quad (55)$$

and

$$T_s = 298.8^\circ\text{C}. \quad (56)$$

Thus,

$$P_s = \begin{cases} 0 & \text{for } T \geq 250^\circ\text{C} \\ \sqrt{9.626 \times 10^{-4}(250 - T)} \text{ C m}^{-2} & \text{for } 100^\circ\text{C} \leq T \leq 250^\circ\text{C} \\ \sqrt{7.262 \times 10^{-4}(298.8 - T)} \text{ C m}^{-2} & \text{for } T \leq 100^\circ\text{C}. \end{cases} \quad (57)$$

The polarization P_s is plotted versus temperature in Figure 4. The general behavior is well described by our model, but there is not good quantitative agreement. As a further comparison, our model predicts in phase B,

$$\frac{P_s^2|_{T_p + \Delta T}}{P_s^2|_{T_p + 2\Delta T}} = 0.5, \quad (58)$$

whereas experimentally this ratio is approximately 0.7. The dielectric constant for

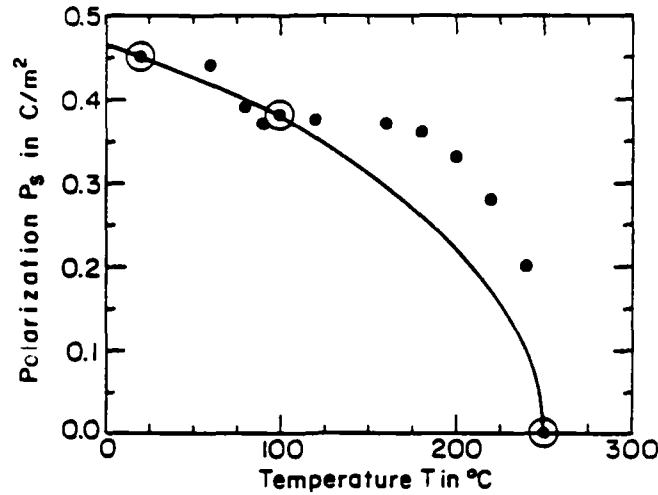


FIGURE 4 The polarization P_s plotted versus temperature. The solid curves were determined from the theory presented in this paper. The experimental data points are from Reference 4. The circles indicate the data points that were used for the evaluation of the constant parameters.

$\text{PbZr}_{0.9}\text{Ti}_{0.1}\text{O}_3$ at different temperatures has the form

$$\epsilon_R = \begin{cases} 1 + \frac{1}{\epsilon_0 \gamma_p (T - 250)} & \text{for } T > 250^\circ\text{C}, \\ 1 + \frac{1}{2\epsilon_0 \gamma_p (250 - T)} & \text{for } 100^\circ\text{C} < T < 250^\circ\text{C}, \text{ and} \\ 1 + \frac{1}{2\epsilon_0 f_4 \beta (298.8 - T)} & \text{for } T < 100^\circ\text{C}. \end{cases} \quad (59)$$

Using the data from Reference 4 that $\epsilon_R = 5000$ at 300°C , we give

$$\gamma_p = \frac{4 \times 10^{-6}/^\circ\text{C}}{\epsilon_0}. \quad (60)$$

Also

$$f_4 = \frac{\gamma_p}{\alpha} = \frac{4.1554 \times 10^{-3}}{\epsilon_0}. \quad (61)$$

The ϵ_R given by Equation (59) is plotted in Figure 5 as a function of temperature, along with the experimental curve from Reference 4. Again, the overall pattern as predicted by our model agrees with experiment, but the numerical values differ. As a

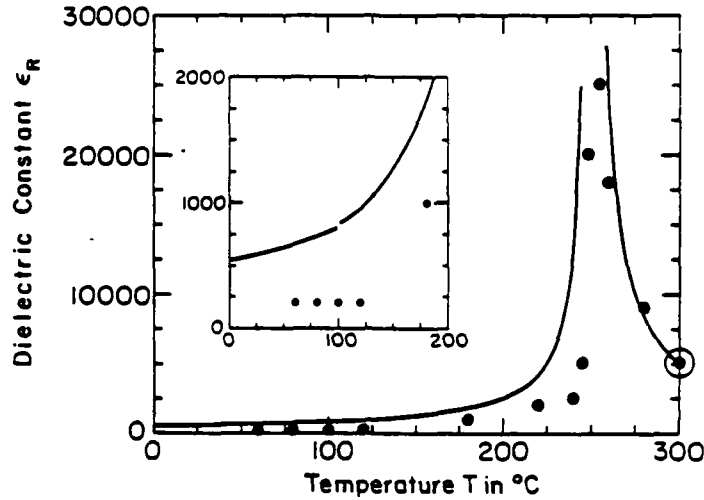


FIGURE 5 The dielectric constant ϵ_R plotted versus temperature. The solid curves were determined from the theory presented in this paper. The experimental data points are from Reference 4. The circle indicates a data point that was used for the evaluation of a constant parameter.

further comparison, our model predicts.

$$\frac{(\epsilon_R|_{T_p-\Delta T} - 1)}{(\epsilon_R|_{T_p+\Delta T} - 1)} = 2, \quad (62)$$

but experimentally this ratio is about 5.

Using $\theta_s = 4.83^\circ$ at 60°C as given in Reference 4, we calculate

$$\lambda = 1.776 \times 10^{-4} \text{ rad}^2/\text{C}, \quad (63)$$

so that the temperature dependence of θ_s is given by

$$\theta_s = \begin{cases} 0 & \text{for } T \geq 100^\circ\text{C.} \text{ and} \\ \sqrt{1.776 \times 10^{-4}(100 - T)} \text{ radian} & \text{for } T \leq 100^\circ\text{C.} \end{cases} \quad (64)$$

The tilt angle θ_s is plotted versus temperature in Figure 6. Experimentally only one other value of θ_s , 5.42° at 25°C , is known from Reference 4. However, Michel *et al.*¹¹ give 7.5° as the room temperature value. More experimental data are needed for a better comparison.

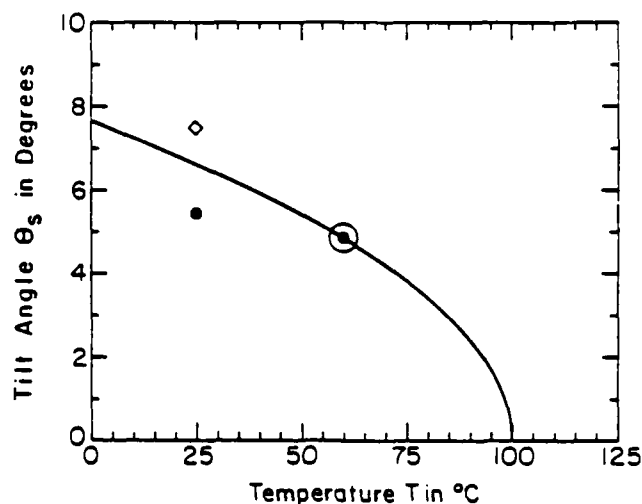


FIGURE 6 The tilt angle θ_s plotted versus temperature. The solid curve was determined from the theory presented in this paper. The experimental data points are from References 4 and 11. The circle indicates a data point that was used for the evaluation of a constant parameter.

For the phonon frequency ω associated with the rotational soft-mode, we have

$$\omega = \begin{cases} \sqrt{\mu(T - T_\theta)} & \text{for } T > 250^\circ\text{C}, \\ \sqrt{\nu(T - 100)} & \text{for } 100^\circ\text{C} < T < 250^\circ\text{C}, \text{ and} \\ \sqrt{\delta(100 - T)} & \text{for } T < 100^\circ\text{C}. \end{cases} \quad (65)$$

The constants μ , ν , δ , and T_θ , which are related by Equations (49) and (50) can be determined by comparison with the observations of Raman or other spectra suitable to the present case. The temperature dependence predicted by Equation (65) can then be verified. Experimental data for such comparisons are not yet available.

Looking at Table I, with $T_r = 100^\circ\text{C}$, $T_p = 250^\circ\text{C}$, and $T_s = 299^\circ\text{C}$ (we could not evaluate T_θ due to lack of experimental data) we conclude that the present example corresponds to the $T_r < T_\theta < T_p < T_s$ case for which d is positive and small. This leads to the $A \rightarrow B \rightarrow D$ transition sequence, as expected.

7. DISCUSSION

Considering the tilt angle and polarization as order parameters, we have succeeded in developing in LDG type phenomenological theory for phase transitions in ferroelectrics involving tilts of sublattices like the oxygen octahedral chain in perovskites. By restricting the power series expansion for the free energy to fourth order terms, we ended up with second order transitions ($f_4 > 0$, and $g_4 > 0$). For

better accuracy higher order terms will be needed. Also to treat first-order transitions, it would be necessary to make $f_4 < 0$, and $g_4 < 0$, and therefore to include terms of at least up to sixth powers.

In this paper we have restricted discussion to cases where the polarization direction and the direction of tilt axis do not change during the transitions. This was done to keep the treatment simple for a first application. But extensions to relax these restrictions are straightforward and would include terms involving polarization components P_x, P_y, P_z and rotation components $\theta_x, \theta_y, \theta_z$. A further extension can be made to allow for tilts where successive octahedra *along* an axis can have either the same or opposite sense of tilt. [If we choose any particular axis, then in a direction *perpendicular* to it, successive octahedra are constrained to have opposite tilts about that axis—see Glazer.³] This can be done by using two interpenetrating sublattices a and b with rotation angles θ_a and θ_b about a given axis for the two sublattices. When $\theta_a = \theta_b$, the tilts are of the same sense and if $\theta_a = -\theta_b$, the tilts are of the opposite sense. This technique is similar to that used for anti-ferroelectricity by Kittel¹² and Cross.¹³ Extensions along these lines to PZT and other tilted systems will be made in the future.

REFERENCES

1. "Crystal Structures: A Working Approach," by Helen D. Megaw, W. B. Saunders Company (1973).
2. L. E. Cross, *Ceramic Bulletin*, **63**, 586 (1984).
3. A. M. Glazer, *Acta Cryst.*, **B28**, 3384 (1972).
4. A. M. Glazer, S. A. Mabud and R. M. Clarke, *Acta Cryst.*, **B34**, 1060 (1978).
5. C. N. W. Darlington, *Philosophical Magazine*, **31**, 1159 (1975).
6. See, for example, "Thermal Physics," by Charles Kittel and Herbert Kinemen, W. H. Freeman and Company (1980).
7. A. F. Devonshire, *Advances in Physics*, **3**, 85 (1954).
8. A. Amin, R. E. Newnham, L. E. Cross and D. E. Cox, *Journal of Solid State Chemistry*, **37**, 248 (1981).
9. J. D. Axe in "Physics of Electronic Ceramics," Part B, edited by L. L. Hench and D. B. Dove, Marcel Dekker, Inc., NY, pp. 749–773 (1972).
10. R. Clarke, A. M. Glazer, F. W. Ainger, D. Appleby, N. J. Poole, and S. G. Porter, *Ferroelectrics*, **11**, 359 (1976).
11. C. Michel, J. M. Moreau, G. D. Achenbach, R. Gerson and W. J. James, *Solid State Commun.*, **1**, 865 (1969).
12. C. Kittel, *Phys. Rev.*, **82**, 729 (1951).
13. L. E. Cross, *Journal of the Physical Society of Japan*, **23**, 77 (1967).
14. See, for example, "Piezoelectric Ceramics" by B. Jaffe, W. R. Cook and H. Jaffe, Academic Press (1971).

A PHENOMENOLOGICAL GIBBS FUNCTION FOR THE SINGLE CELL
REGION OF THE $\text{PbZrO}_3\text{:PbTiO}_3$ SOLID SOLUTION SYSTEM

A. Amin, M.J. Haun, B. Badger, H. McKinstry, and L.E. Cross

A PHENOMENOLOGICAL GIBBS FUNCTION FOR THE SINGLE CELL REGION OF THE $\text{PbZrO}_3\text{:PbTiO}_3$ SOLID SOLUTION SYSTEM

A. AMIN, M.J. HAUN, B. BADGER, H. MCKINSTRY AND L.E. CROSS
Materials Research Laboratory, The Pennsylvania State
University, University Park, PA 16802

ABSTRACT--The ADAGE computer graphics system has been used to develop a modified Devonshire form for the elastic Gibbs function to describe the simple proper ferroelectric phases in the $\text{PbZrO}_3\text{:PbTiO}_3$ family of crystalline solid solutions. The unusual morphotropic phase boundary between tetragonal and rhombohedral forms has been used to help delineate the coefficients in the function at that composition. For the Devonshire formulation, spontaneous strain in the ferroelectric phases is assumed to be electrostrictive in origin and an x-ray determination of the strains as function of composition and temperature has been used to derive the composition and temperature dependence of the high order stiffness coefficients. The Gibbs function which has been derived permits for the first time the calculation of the full family of thermal, elastic, dielectric, and piezoelectric parameters for the ferroelectric single domain states and an evaluation of the manner in which these parameters change under different elastic and electric boundary conditions.

1.0 INTRODUCTION

In many ferroelectric crystals, it has often proven useful to correlate the dielectric, piezoelectric, and elastic properties of paraelectric and ferroelectric phases by phenomenological thermodynamic theory. The change in the thermodynamic potential associated with the onset of the ferroelectric phase is described through a Taylor series expansion in powers of the order parameter (e.g., of the dielectric polarization in the simple proper ferroelectric) and of the coupling parameters to other interesting thermodynamic variables.

The permitted terms and coupling parameters are limited by the crystal symmetry of the prototypic paraelectric structure, and the coefficients of these terms are assumed to be continuous through any of the phase transitions into and between ferroelectric phases.

For many crystals this Landau:Ginsburg:Devonshire formalism gives an excellent semiquantitative description of the dielectric, elastic, piezoelectric, and electrothermal properties when only the lowest order terms are linearly temperature dependent, higher order terms temperature independent and often for a very truncated series expansion⁽¹⁻³⁾. For a more accurate description over a wider temperature range, additional higher order terms, and/or temperature dependent higher order coefficients can be included^(4,5).

A valid general criticism of the application of the LDG formalism to the description of the elasto-dielectric properties of a general non-linear solid is that in using the simple infinitesimal strain formulation and the simple conventional definition of polarization, the electrostriction tensor coefficients resulting are not strictly invariant under rotation of axes. The proper variables as discussed by Toupin⁽⁶⁾ are the Legrangian strain and the material measure of polarization (MMP). Unfortunately, however, in this more rigorous formulation, much of the simplicity and transparency of the original simple thermodynamic argument is lost.

For the special case of the simple proper ferroelectric materials in which the dielectric stiffness is anomalously small while the elastic compliance is almost normal, it has been shown⁽⁷⁾ that the correction terms to the simply formulated electrostriction constants are quite small. In application of the phenomenology to a ceramic system, in which most of the material parameters are not known to better than $\pm 10\%$, the application of the simpler thermodynamic method is probably justified, and is used in this paper.

In ferroelectric polycrystalline ceramics, a complete Gibbs function is particularly valuable since often the mechanical and electric boundary conditions upon the individual crystallites are uncertain, and it is frequently not clear whether 'abnormal' properties are intrinsic and to be associated with these boundary conditions, or are extrinsic and associated with such phenomena as domain and phase boundary motion. The situation can become particularly interesting when the ferroelectric is at a composition or temperature close to a ferroelectric:ferroelectric phase boundary where quite minor changes in the boundary stresses can give rise to major changes in the property tensor^(8,9).

For materials where good single domain single crystals are available, the individual components of the property tensors can be measured over a wide temperature range, and the development of a suitable energy function is quite straightforward. In systems where only ceramic samples are available and good single crystals are unobtainable, the procedure is more complicated and must necessarily be indirect.

The lead zirconate:lead titanate (PZT) crystalline solution system is an excellent example where good single domain single crystal data are unavailable even for the ferroelectric end member (PbTiO_3). It is a system where the technological materials of most interest are grouped about a ferroelectric:ferroelectric

transition (the so-called morphotropic phase boundary) and for which a representative Gibbs function could be of considerable use.

In the approach described in this paper, an ADAGE graphics computer and an IBM 370 computer have been programmed to solve the polynomial equations of the LGD treatment. The coefficients of the energy function and their linear temperature derivatives are under dial control in the analogue section of the ADAGE, with the output presented graphically as a $\Delta G:T$ diagram. The highly unusual feature of morphotropy (degeneracy between tetragonal and rhombohedral solutions of the function) has been used to distinguish the very limited set of coefficients which will produce this phenomenon.

Experimental data least likely to be strongly influenced by the ceramic character of the PZTs have been used to characterize the composition dependence of the ΔG function, and to permit a machine plotting of the full phase diagram for the single cell PZT compositions and of the dielectric, piezoelectric, and electrothermal characteristics of compositions in this phase region.

2.0 PHENOMENOLOGICAL ENERGY FUNCTION

The elastic Gibbs free energy for a simple proper ferroelectric derived from a prototypic phase of $m3m$ symmetry under isothermal conditions may be expressed in the form⁽³⁾:

$$\begin{aligned}
 \Delta G = & \alpha_1^X (P_1^2 + P_2^2 + P_3^2) + \alpha_{11}^X (P_1^4 + P_2^4 + P_3^4) + \alpha_{12}^X (P_1^2 P_2^2 + P_2^2 P_3^2 + P_3^2 P_1^2) \\
 & + \alpha_{111}^X (P_1^6 + P_2^6 + P_3^6) + \alpha_{112}^X (P_1^4 (P_2^2 + P_3^2) + P_2^4 (P_1^2 + P_3^2) + P_3^4 (P_1^2 + P_2^2)) \\
 & + \alpha_{123}^X P_1^2 P_2^2 P_3^2 - 1/2 s_{11}^P (X_1^2 + X_2^2 + X_3^2) - s_{12}^P (X_1 X_2 + X_2 X_3 + X_3 X_1) \\
 & - 1/2 s_{44}^P (X_4^2 + X_5^2 + X_6^2) - Q_{11} (X_1 P_1^2 + X_2 P_2^2 + X_3 P_3^2) \\
 & - Q_{12} (X_1 (P_2^2 + P_3^2) + X_2 (P_3^2 + P_1^2) + X_3 (P_1^2 + P_2^2)) \\
 & - Q_{44} (X_4 P_2 P_3 + X_5 P_1 P_3 + X_6 P_1 P_2)
 \end{aligned} \tag{1}$$

where the α_i^X , α_{ijk}^X , and α_{ijkl}^X are the dielectric stiffness and higher order stiffness coefficients at constant stress, the s_{ij}^P are the elastic compliance coefficients measured at constant polarization, and the Q_{ij} are the cubic electrostriction constants in polarization notation. The expression is complete up to all sixth power terms in polarization, but contains only fourth order terms in electrostrictive and elastic behavior.

The first partial derivatives of the energy with respect to the components of P , X , and T give the conjugate parameters: the electric field E_i , the negative of the strain $-x_{ij}$, and the entropy change $-S$, respectively.

$$\frac{\partial \Delta G}{\partial P_i} = E_i \text{ (a), } \frac{\partial \Delta G}{\partial X_{ij}} = -x_{ij} \text{ (b), } \frac{\partial \Delta G}{\partial T} = -S \text{ (c)} \quad (2)$$

Appropriate second partial derivatives give the dielectric stiffnesses, elastic compliances and piezoelectric constants:

$$\frac{\partial^2 \Delta G}{\partial P_i \partial P_j} = \chi_{ij} \text{ (a), } \frac{\partial^2 \Delta G}{\partial X_i \partial X_j} = -s_{ij} \text{ (b), } \frac{\partial^2 \Delta G}{\partial P_i \partial X_j} = -b_{ij} \text{ (c)} \quad (3)$$

Equation (2a) with $E_i = 0$, and the condition that equations (3a), (3b), and (3c) must have positive values, give the conditions for stability of the spontaneously polarized states. The four solutions of equation (1) which are of interest for the PZT family dielectrics are:

Cubic

$$P_1^2 = P_2^2 = P_3^2 = 0 \text{ (a), } \Delta G = 0 \text{ (b)} \quad (4)$$

Tetragonal

$$P_3^2 = \frac{-a_{11}^X + [(a_{11}^X)^2 - 3a_{11}^X a_{111}^X]^{1/2}}{3a_{111}^X}, \quad P_1^2 = P_2^2 = 0 \text{ (a)}$$

$$\Delta G = a_{11}^X P_3^2 + a_{11}^X P_3^4 + a_{111}^X P_3^6 \text{ (b)} \quad (5)$$

Orthorhombic

$$P_1^2 = P_2^2 = \frac{-(2a_{11}^X + a_{12}^X) \pm [(2a_{11}^X + a_{12}^X)^2 - 12a_{11}^X (a_{111}^X + a_{112}^X)]^{1/2}}{6(a_{111}^X + a_{112}^X)}, \quad P_3^2 = 0 \text{ (a)}$$

$$\Delta G = 2a_{11}^X P_1^2 + 2(a_{11}^X + a_{12}^X) P_1^4 + 2(a_{111}^X + a_{112}^X) P_1^6 \text{ (b)} \quad (6)$$

Rhombohedral

$$P_1^2 = P_2^2 = P_3^2 = \frac{-(a_{11}^X + a_{12}^X) \pm [(a_{11}^X + a_{12}^X)^2 - a_{11}^X (3a_{111}^X + 6a_{112}^X + a_{123}^X)]^{1/2}}{3a_{111}^X + 6a_{112}^X + a_{123}^X} \text{ (a)}$$

$$\Delta G = 3a_{11}^X P_3^2 + 3(a_{11}^X + a_{12}^X) P_3^4 + (3a_{111}^X + 6a_{112}^X + a_{123}^X) P_3^6 \text{ (b)} \quad (7)$$

The a coefficients are continuous functions of composition and/or temperature.

The spontaneous elastic strains in the ferroelectric single domain states, under the conditions $X_i = 0$, may be deduced from equation (2b) which leads to the following relations:

Cubic

$$x_1 = x_2 = x_3 = x_4 = x_5 = x_6 = 0 \quad (8)$$

Tetragonal

$$x_3 = Q_{11}P_3^2, \quad x_1 = x_2 = Q_{12}P_3^2, \quad x_4 = x_5 = x_6 = 0 \quad (9)$$

Orthorhombic

$$\begin{aligned} x_1 = x_2 &= (Q_{11} + Q_{12})P_1^2 \\ x_3 &= 2Q_{12}P_1^2, \quad x_4 = x_5 = 0, \quad x_6 = Q_{44}P_1^2 \end{aligned} \quad (10)$$

Rhombohedral

$$\begin{aligned} x_1 = x_2 = x_3 &= (Q_{11} + 2Q_{12})P_3^2 \\ x_4 = x_5 = x_6 &= Q_{44}P_3^2 \end{aligned} \quad (11)$$

It may be noted that in equation (10) the strain system appears monoclinic as it is expressed with respect to the original cubic axes (1,2,3), and that the strain tensor may be diagonalized by a 45° rotation in the 1,2 plane corresponding to the proper choice of orthorhombic axes.

The relative dielectric stiffnesses (X_{ij}) were derived from equation (3a) resulting in:

Cubic

$$X_{11} = X_{22} = X_{33} = 2a_1^X \epsilon_0, \quad X_{12} = X_{23} = X_{31} = 0 \quad (12)$$

Tetragonal

$$\begin{aligned} X_{33} &= (2a_1^X + 12a_{11}^X P_3^2 + 30a_{111}^X P_3^4) \epsilon_0 \\ X_{11} = X_{22} &= (2a_1^X + 2a_{12}^X P_3^2 + 2a_{112}^X P_3^4) \epsilon_0, \quad X_{12} = X_{23} = X_{31} = 0 \end{aligned} \quad (13)$$

Orthorhombic

$$\begin{aligned} X_{11} = X_{22} &= (2a_1^X + (12a_{11}^X + 2a_{12}^X)P_1^2 + (30a_{111}^X + 14a_{112}^X)P_1^4) \epsilon_0 \\ X_{33} &= (2a_1^X + 4a_{12}^X P_1^2 + (4a_{112}^X + 2a_{123}^X)P_1^4) \epsilon_0, \quad X_{12} = (4a_{12}^X P_1^2 + 16a_{112}^X P_1^4) \epsilon_0 \\ X_{23} = X_{31} &= 0 \end{aligned} \quad (14)$$

Rhombohedral

$$\begin{aligned} X_{11} = X_{22} = X_{33} &= (2a_1^X + (12a_{11}^X + 4a_{12}^X)P_3^2 + (30a_{111}^X + 28a_{112}^X + 2a_{123}^X)P_3^4) \epsilon_0 \\ X_{12} = X_{23} = X_{31} &= (4a_{12}^X P_3^2 + (16a_{112}^X + 4a_{123}^X)P_3^4) \epsilon_0 \end{aligned} \quad (15)$$

To yield units of energy for the free energy functions, the a coefficients were divided by the permittivity of free space (ϵ_0), as shown in Section IV. Thus, the multiplication by ϵ_0 was required in Equations (12) through (15) to give relative dielectric stiffnesses.

In the rhombohedral state, the polarization can be along any of the $\langle 111 \rangle$ directions of the original cubic axes. By rotating these axes so that the new x_3 axis is along the $[111]$ direction, the new dielectric stiffness coefficients (indicated by a prime) can be related to the old coefficients (defined by equation 15) with the following equations:

$$\begin{aligned} \chi'_{11} &= \chi'_{22} = \chi_{11} - \chi_{12}, \quad \chi'_{33} = \chi_{11} + 2\chi_{12} \\ \chi'_{12} &= \chi'_{23} = \chi'_{31} = 0 \end{aligned} \quad (16)$$

The dielectric susceptibility coefficients (η_{ij}) can be determined from the reciprocal of the dielectric stiffness matrices. For a diagonalized stiffness matrix, such as the matrices defined by equations (13) and (16) for the tetragonal and rhombohedral states, the diagonal susceptibility coefficients (η_{11} , η_{22} and η_{33}) are simply the reciprocal of the corresponding stiffness coefficients, and the off-diagonal susceptibilities (η_{12} , η_{23} and η_{31}) are zero. The susceptibility coefficients for the non-diagonalized stiffness matrix defined by equation (15) for the rhombohedral state can be determined from the following relations:

$$\begin{aligned} \eta_{11} = \eta_{22} = \eta_{33} &= \frac{\chi_{11}^2 - \chi_{12}^2}{\chi_{11}^3 - 3\chi_{11}\chi_{12}^2 - 2\chi_{12}^3} \\ \eta_{12} = \eta_{23} = \eta_{31} &= \frac{\chi_{12}^2 - \chi_{11}\chi_{12}}{\chi_{11}^3 - 3\chi_{11}\chi_{12}^2 + 2\chi_{12}^3} \end{aligned} \quad (17)$$

Equation (17) gives the dielectric susceptibility coefficients for the rhombohedral state based on the original cubic axes.

The piezoelectric polarization related b_{ij} coefficients can be derived from equation (3c) as shown below:

Cubic

$$b_{ij} = 0 \quad (18)$$

Tetragonal

$$\begin{aligned} b_{33} &= 2Q_{11}P_3 \\ b_{31} &= b_{32} = 2Q_{12}P_3 \\ b_{15} &= b_{24} = Q_{44}P_3 \end{aligned} \quad (19)$$

Orthorhombic

$$\begin{aligned} b_{11} &= b_{22} = 2Q_{11}P_1 \\ b_{12} &= b_{13} = b_{21} = b_{23} = 2Q_{12}P_1 \\ b_{16} &= b_{26} = b_{34} = b_{35} = Q_{44}P_1 \end{aligned} \quad (20)$$

Rhombohedral

$$\begin{aligned} b_{11} &= b_{22} = b_{33} = 2Q_{11}P_3 \\ b_{12} &= b_{13} = b_{23} = b_{21} = b_{31} = b_{32} = 2Q_{12}P_3 \\ b_{15} &= b_{16} = b_{26} = b_{24} = b_{35} = b_{34} = Q_{44}P_3 \end{aligned} \quad (21)$$

The piezoelectric strain coefficients d_{ij} for the tetragonal or rhombohedral states can be related to the b_{ij} coefficients by:

$$\begin{aligned} d_{33} &= \eta_{33}\epsilon_0 b_{33} = 2\eta_{33}\epsilon_0 Q_{11}P_3 \\ d_{31} &= \eta_{33}\epsilon_0 b_{31} = 2\eta_{33}\epsilon_0 Q_{12}P_3 \\ d_{15} &= \eta_{11}\epsilon_0 b_{15} = \eta_{11}\epsilon_0 Q_{44}P_3 \end{aligned} \quad (22)$$

The dielectric susceptibilities η_{11} and η_{33} in equation (22) are based on the original cubic axis, and thus for the rhombohedral state should be determined from equation (17).

The piezoelectric voltage coefficients g_{ij} are related to the b_{ij} coefficients by a factor of $(k-1)/k$, where k is the dielectric constant. PZT compositions have a $k \gg 1$, thus the g_{ij} coefficients are approximately equal to the b_{ij} coefficients. Hence, for the tetragonal or rhombohedral states, the g_{ij} coefficients are:

$$\begin{aligned} g_{33} &\approx b_{33} = 2Q_{11}P_3 \\ g_{31} &\approx b_{31} = 2Q_{12}P_3 \\ g_{15} &\approx b_{15} = Q_{44}P_3 \end{aligned} \quad (23)$$

If the temperature and composition dependence of the dielectric stiffness, higher order stiffness, and electrostriction constants are known, then the full family of spontaneous strains and polarizations, and dielectric and piezoelectric properties can be determined. In the next section values of these constants will be found that reproduce the morphotropic boundary between the tetragonal and rhombohedral phases. Then experimental data will be used to scale and refine these constants to give quantitative agreement with the properties of PZT.

3.0 COMPUTATION PROCEDURE

To give the observed Curie Weiss behavior of the dielectric permittivity in the paraelectric phase, it is evident from equation (12) that the coefficient α_1^X must be a linearly increasing function of temperature passing through zero at the Curie Weiss temperature θ , where α_1^X changes from negative to positive values. The temperature θ must be below the ferroelectric transition temperature (T_c). The dielectric stiffness and higher order stiffness coefficients may be functions of both temperature and composition, but in any crystalline solution system, it is expected that the variation be smooth and continuous across the whole phase diagram.

Initial studies have suggested that even if the parameters α_1^X , α_{11}^X , α_{12}^X , and α_{111}^X are given linear temperature dependence, a proper tetragonal: rhombohedral morphotropy cannot be developed from the simple Devonshire function ($\alpha_{112}^X = \alpha_{123}^X = 0$). However, by adding a positive α_{112}^X parameter to destabilize the orthorhombic phase and a negative α_{123}^X parameter to restabilize the rhombohedral phase, tetragonal and rhombohedral phases can be made coincident over a wide temperature range without any interleaving of the orthorhombic region.

To permit ready visualization of the influence of the α parameters on the resulting phase stabilities, the ADAGE was programmed to operate in a split screen mode. The right-hand half of the screen plots ΔG_1 vs T for all possible stable phases. ΔG_1 was derived from a computer solution of the equations (5) and (7) which yield the appropriate values of P_i at each temperature. On the ADAGE, the α coefficients were under dial control and linear temperature coefficients could be added to either the parameters α_{11}^X or α_{123}^X . Markers were inserted at each of the intersections of the different phase stabilities, marking the equilibrium transition temperatures. This information on phase stabilities was then transferred to the left portion of the screen. The α parameters were then incremented to new values under machine control, and the process was repeated. In this manner, a hypothetical phase diagram can be rapidly built up for any given initial choice of parameters and any chosen scheme of parameter increments. Since the starting values and progression increments are under analog control on the ADAGE system, new combinations can be 'dialed' in at the start of each run and a wide range of parameter combinations can be tested in quite a short period.

Experience using this plotting program has confirmed our earlier expectations in that:

1. We cannot reproduce morphotropy with the simple Devonshire function.

2. In the Devonshire formalism, as expected, the parameter $\phi = \alpha_{12}^X / \alpha_{11}^X$ controls the relative stability of tetragonal to orthorhombic and rhombohedral phases. However, the orthorhombic phase always interleaves or is degenerate with the rhombohedral.

3. To generate a near vertical tetragonal-rhombohedral boundary requires a positive value of Q_{112} and a negative value of Q_{123} .

4. For all parameter combinations which generate a near vertical morphotropic phase boundary (at Zr:Ti ratio ~1:1) the orthorhombic phase is always very close to (but metastable with respect to) the overlapping tetragonal and rhombohedral stability curves.

Having developed a small family of dimensionless parameters which generate a sharp morphotropic change between rhombohedral and tetragonal phases, the task is to scale and refine the fitting so that it describes quantitatively the properties of real PZT compositions. For this purpose, it is clearly necessary to draw upon additional experimental data. It is desirable that in choosing the appropriate results care be taken in selecting those parameters and measurements which are least likely to be perturbed by the ceramic boundary conditions.

In this fitting we chose:

1. The composition dependence of the ferroelectric phase transition temperature (T_c).

2. The temperature dependence of the spontaneous polarization P_s for a series of carefully characterized compositions across the tetragonal and the single cell rhombohedral compositions in the phase diagram.

There appears to be rather general agreement as to the nature of (1) with good accord between several sets of measurements by independent observers. For (2) it is not possible to measure P_s directly in these ceramic solid solutions. However, making use of equations (9) and (11) we may relate the spontaneous strains x_1 , x_2 , and x_4 to the appropriate calculated values of P_3^2 .

The strains x_1 , x_2 , and x_4 were determined by high temperature x-ray powder diffraction for well characterized powder samples of $PbTiO_3$ and several PZT compositions⁽¹⁰⁾. The experimental data for compositions with tetragonal room temperature symmetry are shown in Figure 1 and for rhombohedral compositions in Figure 2. Using equations (9) and (11), P_3^2 was derived from the experimental data, and calculated and measured P values were fitted using Q_{11} , Q_{12} , Q_{44} , θ , and $P_S(T_c)$ (the spontaneous polarization P_3 of the tetragonal state at T_c) as fitting parameters. Values of these parameters were determined at each of the compositions where the spontaneous strains were measured, and are plotted versus composition in Figure 3 for Q_{11} , Q_{12} , and Q_{44} , and in Figure 4 for θ and $P_S(T_c)$.

Even given complete lack of constraint, the required Q values do not change markedly with composition, and a good fitting of observed and calculated strains can be obtained with composition independent Q parameters. Thus composition and temperature independent Q values were used for the theoretical calculations, with $Q_{11} = 6.6 \times 10^{-2} \text{ m}^4/\text{C}^2$, $Q_{12} = -3.2 \times 10^{-2} \text{ m}^4/\text{C}^2$, and $Q_{44} = 1.5 \times 10^{-2} \text{ m}^4/\text{C}^2$, as shown by the solid lines in Figure 3.

To obtain the composition dependence of the θ and $P_S(T_c)$ parameters, the values were fit with polynomial equations, as

shown by the solid curves in Figure 4. The experimental values of the transition temperature T_c from the PZT phase diagram were also fitted with a polynomial equation. These equations were then used to calculate values of θ , $P_S(T_c)$, and T_c for the theoretical calculations, and are:

$$\begin{aligned} T_c &= (211.8 + 486.0x - 280.0x^2 + 74.42x^3)^\circ\text{C} \\ \theta &= (208.2 + 489.6x - 322.8x^2 + 164.7x^3 - 63.81x^4)^\circ\text{C} \\ P_S(T_c) &= (0.1194 + 0.2001x - 0.04854x^2 - 0.002914x^3) \text{ C/m}^2 \end{aligned} \quad (24)$$

x is the mole fraction of PbTiO_3 in PZT.

After adjusting the Q_{11} , Q_{12} , Q_{44} , θ , and $P_S(T_c)$ parameters, recalculation of the phase diagram confirmed that minor changes had not significantly degraded the initial fitting of morphotropy, and a final trimming of the equations lead to the following parameter scheme:

$$a_{11}^X = \chi_0(T - \theta), \quad \chi_0 = \frac{1}{2\varepsilon_0 C}, \quad \text{where } C \text{ is the Curie constant.}$$

$$a_{11}^X = -\frac{2a_{11}^X(T_c)}{P_S^2(T_c)}$$

$$a_{12}^X = \phi a_{11}^X, \quad \text{where } \phi = 9.8 \text{ in } \text{PbZrO}_3 \text{ changing linearly with composition to } -12.0 \text{ in } \text{PbTiO}_3$$

$$a_{111}^X = \frac{a_{11}^X(T_c)}{P_S^4(T_c)}$$

$$a_{112}^X = 8000/\varepsilon_0 C$$

$$a_{123}^X = [-45,000(1-x) - 20,000x]/\varepsilon_0 C, \quad \text{where } x \text{ is the mole fraction of } \text{PbTiO}_3 \text{ in } \text{PbZrO}_3:\text{PbTiO}_3$$

The temperature independent relation given above for a_{11}^X and a_{111}^X were required to cause the free energies (ΔG) of the cubic and tetragonal states to be equal at the transition temperature T_c .

To quantify the Gibbs function, it is necessary to select the scaling parameter χ_0 . In materials with lower T_c values, this is readily accomplished by a direct measurement of the dielectric permittivity as a function of T above T_c in the paraelectric phase and a fitting to the Curie Weiss law.

For the PZTs, the high Curie temperatures lead to considerable difficulty, and values of the Curie constant have been reported ranging from 1.5 to $15 \times 10^5 \text{ }^\circ\text{C}^{-1}$. An indirect method has been used to determine the compositional dependence of the Curie constant (C) from a combination of calorimetric and phenomenological data⁽¹¹⁾, as shown by the data points in Figure 5. The solid curve is a Gaussian distribution used to fit the experimental data, and is of the following form:

$$C = ae^{b(x-d)^2} + e, \quad (26)$$

where $a = 6.2 \times 10^5$, $b = -37.2$, $d = 0.5$, $e = 1.5 \times 10^5$, and x is the mole fraction of PbTiO_3 in PZT. Using this equation to determine the Curie constant as a function of composition, the values of T_c , θ , $P_s(T_c)$, ϕ , and the α stiffness coefficients were determined at various compositions across the PZT phase diagram, as shown in Table 1.

4.0 COMPARISON OF EXPERIMENTAL AND CALCULATED PARAMETERS FOR PZT

4.1 Phase Diagram

The experimental phase diagram for the PZT solid solution system is shown in Figure 6⁽¹²⁾. The region of interest which is accessible to the simple phenomenology involves the single cell compositions in the regions marked P_c , F_T , and $F_{R(HT)}$. Antiferroelectric orthorhombic and multicell rhombohedral $F_{R(LT)}$ phases have not been accounted for.

A first trial at the phenomenological fitting using a linear T_c vs composition to explore the possibilities of morphotropy is shown in Figure 7. The final fitting using the parameters listed in the previous section is shown in Figure 8, plotted over the experimental data for comparison.

For the region between 0.25 and 1.0 mole fraction PbTiO_3 , the free energy as a function of composition is shown in Figure 9 for temperatures of 25°C , 125°C , and 300°C . The dashed curve labeled MPB is the crossover corresponding to the morphotropic phase boundary between the tetragonal and rhombohedral phases.

4.2 Spontaneous Polarization

Data are not available in the literature for P_s in any of the PZT compositions of interest. There are some single crystal values for pure lead titanate, and one set of measurements of P_s vs T ⁽¹³⁾ is summarized in Figure 10. The agreement between the experimental measurements and phenomenological calculation is fairly good considering that the higher order dielectric stiffness constants were independent of temperature. The theoretical temperature dependence of P_s originated from the dielectric stiffness coefficient α_1 , which was given a temperature dependence based on the Curie-Weiss law.

The calculated temperature dependence of the spontaneous polarization for several PZT compositions in the tetragonal phase field are shown in Figure 11. From these curves the trend of P_S at 25°C as a function of composition across the phase diagram is depicted in Figure 12.

4.3 Dielectric and Piezoelectric Single Domain Properties

The calculated single domain dielectric susceptibility coefficients for $PbTiO_3$ (Fig. 13), PZT 50:50 (Fig. 14), and PZT 60:40 (Fig. 15) have been derived. It should be noted that in these figures the susceptibility η is almost identical to the normal dielectric permittivity, and that the scales for values above and below T_c are different. The change in the room temperature components of η calculated as a function of composition are shown in Figure 16. The susceptibility coefficients for the cubic (η_p) and tetragonal (η_{11} and η_{33}) state were calculated from the reciprocal of the stiffness matrices defined by equations (12) and (13), respectively. The susceptibility coefficients (η_{11} and η_{33}) for the rhombohedral state were based on the principal axes of the rhombohedral unit cell with the spontaneous polarization along the x_3 -axis. Thus the reciprocal of the stiffness matrix defined by equation (16) was used for the calculation of the susceptibilities for the rhombohedral state.

The piezoelectric constants d_{33} , d_{31} , and d_{15} were calculated as a function of temperature for $PbTiO_3$ and PZT 50:50 as shown in Figures 17 and 18, respectively. The corresponding temperature dependent g values g_{33} , g_{31} , and g_{15} are given in Figures 19 and 20. Modifications of the room temperature d values as a function of composition at room temperature are depicted in Figure 21, with the related g values in Figure 22.

5.0 DISCUSSION

The agreement between experimental and phenomenological descriptions of morphotropy exhibited in Figure 8 is obviously very good and has been achieved without any abrupt changes in the energy parameters. The Gibbs free energy difference between stable and metastable phases at the $PbTiO_3$ composition agrees well with that proposed by Henning and Hardtl⁽¹⁴⁾ on empirical grounds, though from our calculations the free energies themselves are not linear functions of the composition.

For the parameters chosen, the calculated polarizations agree quite well with those derived from spontaneous strain measurements though there is some evidence from the more rapid rise near T_c in the calculated data that the series expansion is too rapidly truncated, or correspondingly that temperature coefficients on the highest order terms are needed. The electrostriction constants derived in this analysis are comparable with the measured constants for $PbTiO_3$ and as expected do not change significantly with composition across the whole phase diagram.

With the constant χ_0 chosen to provide a good fitting with the available thermal data, the calculated permittivity temperature curves are not unreasonable, with values of the Curie Weiss slope being as expected towards the lowest values measured in PZTs. At the lead titanate end of the composition system, the high stability of the tetragonal phase is exhibited in the lower values of transverse susceptibility (η_{11}). However, on approaching the morphotropic phase boundary α_{11} begins to increase markedly. Calculated values for η are, however, still only about half the room temperature values usually measured even in hard PZTs.

A probable explanation for the observed discrepancy between theory and experiments at room temperature is that a major part of the dielectric polarizability in the ceramic is extrinsic arising from the motion of polar domain or phase boundaries. Some support for this hypothesis can be derived from recent measurements of permittivity and piezoelectric response of PZT ceramics down to 4.2°K⁽¹⁵⁾. At this very low temperature, extrinsic effects should be frozen out, and indeed both donor and acceptor doped PZTs of a common Zr:Ti ratio do come to the same value of permittivity ϵ_{33} and to very similar values of d_{33} and d_{31} . These lower temperature data are in excellent accord with low temperature projections from the present thermodynamic theory, suggesting that it does in fact model the intrinsic response rather effectively.

A startling feature of the response of the doped PZTs is the manner in which dielectric and piezoelectric response scale together.

It would appear that the domain or phase boundary motion driven by the weak E field must be shape changing, i.e. that 180° wall processes are not strongly involved, but that the active domains must be of ferroelastic type.

A more detailed discussion of the fitting to the low temperature data, and of the influences of elastic and dielectric boundary conditions on the phase stability will be presented in a later paper.

The behavior of the piezoelectric d and g coefficients again appears to reflect the significantly lower dielectric polarizability of the single domain state - the calculated g coefficients being on the whole slightly larger than the measured values and the calculated d coefficients being small even for very hard PZTs.

References

1. H. Muller, Phys. Rev. 47, 175 (1935); 57, 829 (1940); 58, 563 (1940); 58, 805 (1940).
2. V. Ginsburg, J. Exp. Theor. Phys. SSSR 15, 739 (1945).
3. A.F. Devonshire, Phil. Mag. 40, 1040 (1949).
4. W.R. Buessem, L.E. Cross, and A.K. Goswami, J. Amer. Ceram. Soc. 49, 33 (1966).
5. A.K. Goswami and L.E. Cross, Phys. Rev. 171, 549 (1968).

6. R.A. Toupin, *J. Rat. Mech. Anal.* 5, 849 (1956); *Int. J. of Eng. Sci.* 1, 101 (1963).
7. G.R. Barsch, B.N.N. Achar, and L.E. Cross, *Ferroelectrics* 35, 187 (1981).
8. L.E. Cross, *Phil. Mag.* 7, 44 (1953).
9. W.R. Buessem, L.E. Cross, and A.K. Goswami, *J. Amer. Ceram. Soc.* 49, 36 (1966).
10. A. Amin, Phenomenological and Structural Studies of Lead Zirconate-Lead Titanate Piezoceramics, Ph.D. Thesis, The Pennsylvania State University (1979).
11. A. Amin, L.E. Cross, and R.E. Newnham, *Ferroelectrics* 37, 647 (1981).
12. B. Jaffe, W.J. Cook, and H. Jaffe, Piezoelectric Ceramics, Academic Press, London, p. 136 (1971).
13. V.G. Gavril'yachenko, I.R. Spinko, and F. Martynenko, *Soviet Physics Solid State* 12, 1203 (1970).
14. D. Henning and H.K. Hardtl, Proc. Intl. Conf. Science of Ceramics, Baden, Baden, West Germany (1971).
15. X.L. Zhang, Z.X. Chen, L.E. Cross, and W.A. Schulze, *J. Mat. Sci.* 18, 968 (1983).

FIGURE CAPTIONS

- Fig. 1. Spontaneous strain data plotted versus temperature measured by high temperature x-ray powder diffraction for PZT samples in the tetragonal phase field. The scattering of the data points is $\pm 0.2 \times 10^{-3}$ for x_1 , and $\pm 0.1 \times 10^{-3}$ for x_2 .
- Fig. 2. Spontaneous strain data plotted versus temperature measured by high temperature x-ray powder diffraction for PZT samples in the rhombohedral phase field. The scattering of the data points is $\pm 0.8 \times 10^{-4}$ for x_4 .
- Fig. 3. Values of the polarization related electrostriction constants Q_{11} , Q_{12} , and Q_{44} required to fit calculated and experimental spontaneous strain data.
- Fig. 4. Values of the Curie-Weiss temperature θ and the spontaneous polarization of the tetragonal state at T_c required to fit the experimental and phenomenological spontaneous strain data. The solid curves are polynomial fits of the data (see equation 24).
- Fig. 5. The Curie constant plotted versus composition. The data points are from reference 9, and the solid curve is Gaussian distribution used to fit the data (see equation 26).
- Fig. 6. The phase diagram for the $\text{PbZrO}_3\text{:PbTiO}_3$ solid solution system (from reference 12).
- Fig. 7. The initial fitting to generate a morphotropic boundary between the tetragonal (F_T) and rhombohedral ($F_{R(HT)}$) phases using a linear T_c vs composition.
- Fig. 8. Superposition of experimental and phenomenological PZT phase diagrams. The T_c curve is a polynomial fit of the experimental data (see equation 24). The curve between the F_R and F_T phase was determined from the cross-over of the tetragonal and rhombohedral free energies (see Fig. 9).
- Fig. 9. The elastic Gibbs free energy for the tetragonal, rhombohedral, and orthorhombic states plotted versus composition across the single cell region of the PZT phase diagram of 25, 125, and 300°C.
- Fig. 10. The spontaneous polarization P_s plotted versus temperature for PbTiO_3 . The data points and solid curve represent experimental single-crystal measurements from reference 13. The dashed curve is the phenomenological calculation using equation (5a).
- Fig. 11. The spontaneous polarization plotted versus temperature for several PZT compositions in the tetragonal phase field. Equation (5a) was used for these calculations.
- Fig. 12. The spontaneous polarization plotted versus composition at 25°C. Equations (5a) and (7a) were used for the tetragonal and rhombohedral phase fields, respectively.
- Fig. 13. The calculated dielectric susceptibility plotted versus temperature for PbTiO_3 .
- Fig. 14. The calculated dielectric susceptibility plotted versus temperature for a 50:50 PZT composition.
- Fig. 15. The calculated dielectric susceptibility plotted versus temperature for a 60:40 PZT composition.

- Fig. 16. The dielectric susceptibility plotted versus composition at 25°C.
- Fig. 17. The calculated piezoelectric strain coefficients d_{ij} plotted versus temperature for PbTiO_3 .
- Fig. 18. The calculated piezoelectric strain coefficients d_{ij} plotted versus temperature for a 50:50 PZT composition (the tetragonal state was assumed).
- Fig. 19. The calculated piezoelectric voltage coefficient g_{ij} plotted versus temperature for PbTiO_3 .
- Fig. 20. The calculated piezoelectric voltage coefficients g_{ij} plotted versus temperature for a 50:50 PZT composition (the tetragonal state was assumed).
- Fig. 21. The calculated piezoelectric strain coefficients d_{ij} plotted versus composition at 25°C.
- Fig. 22. The calculated piezoelectric voltage coefficients g_{ij} plotted versus composition at 25°C.

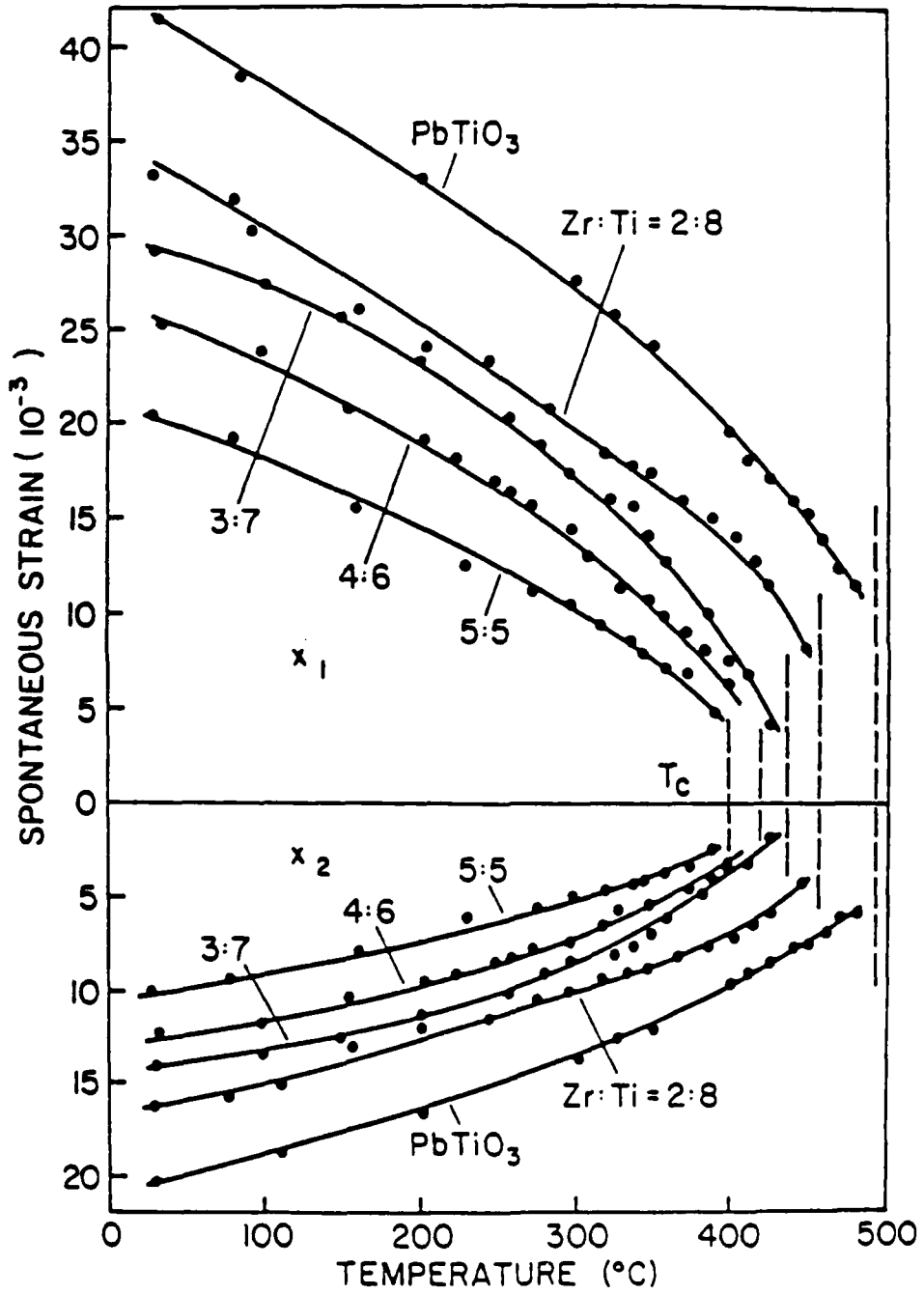


Fig. 1.

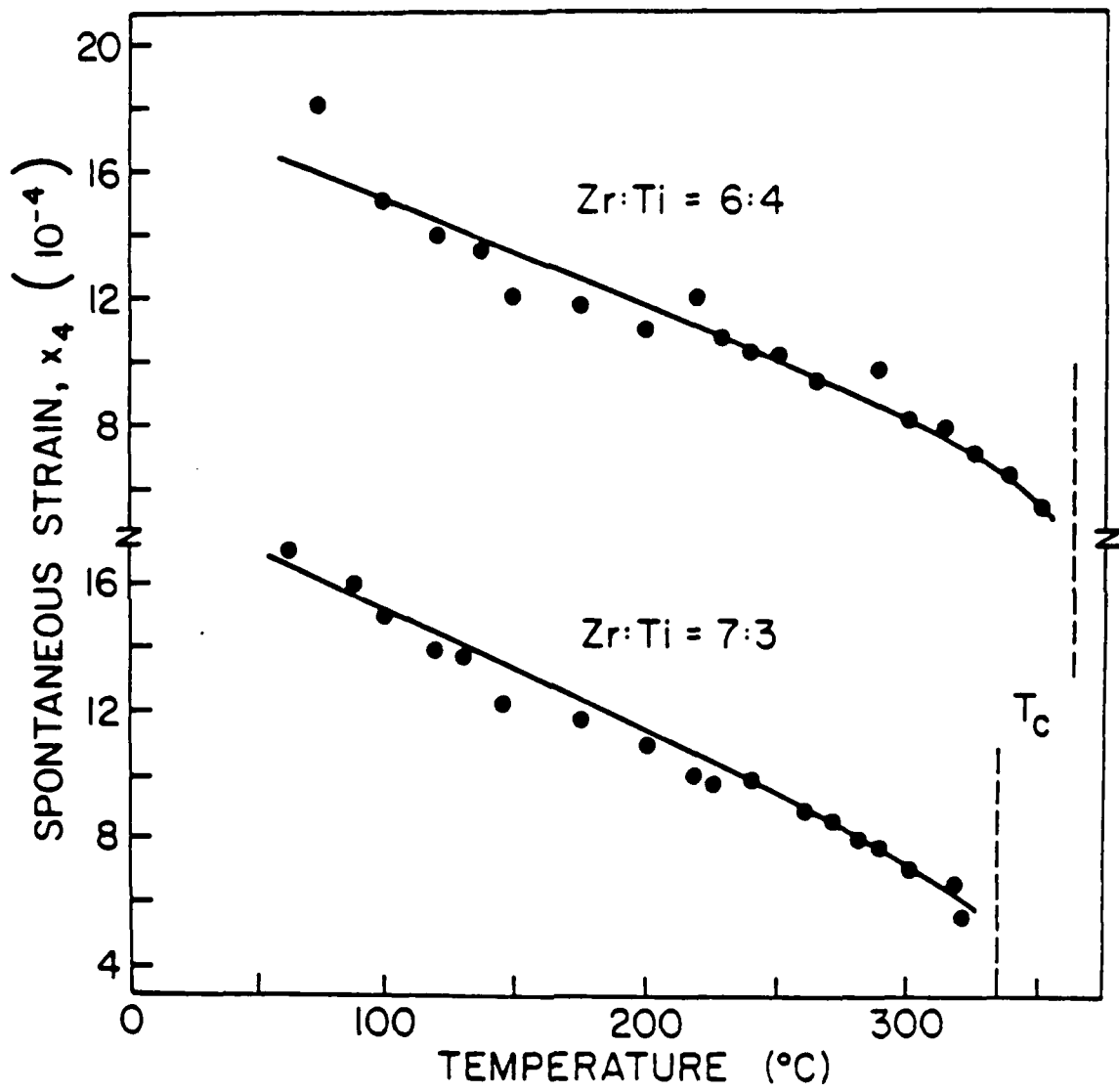


Fig. 2.

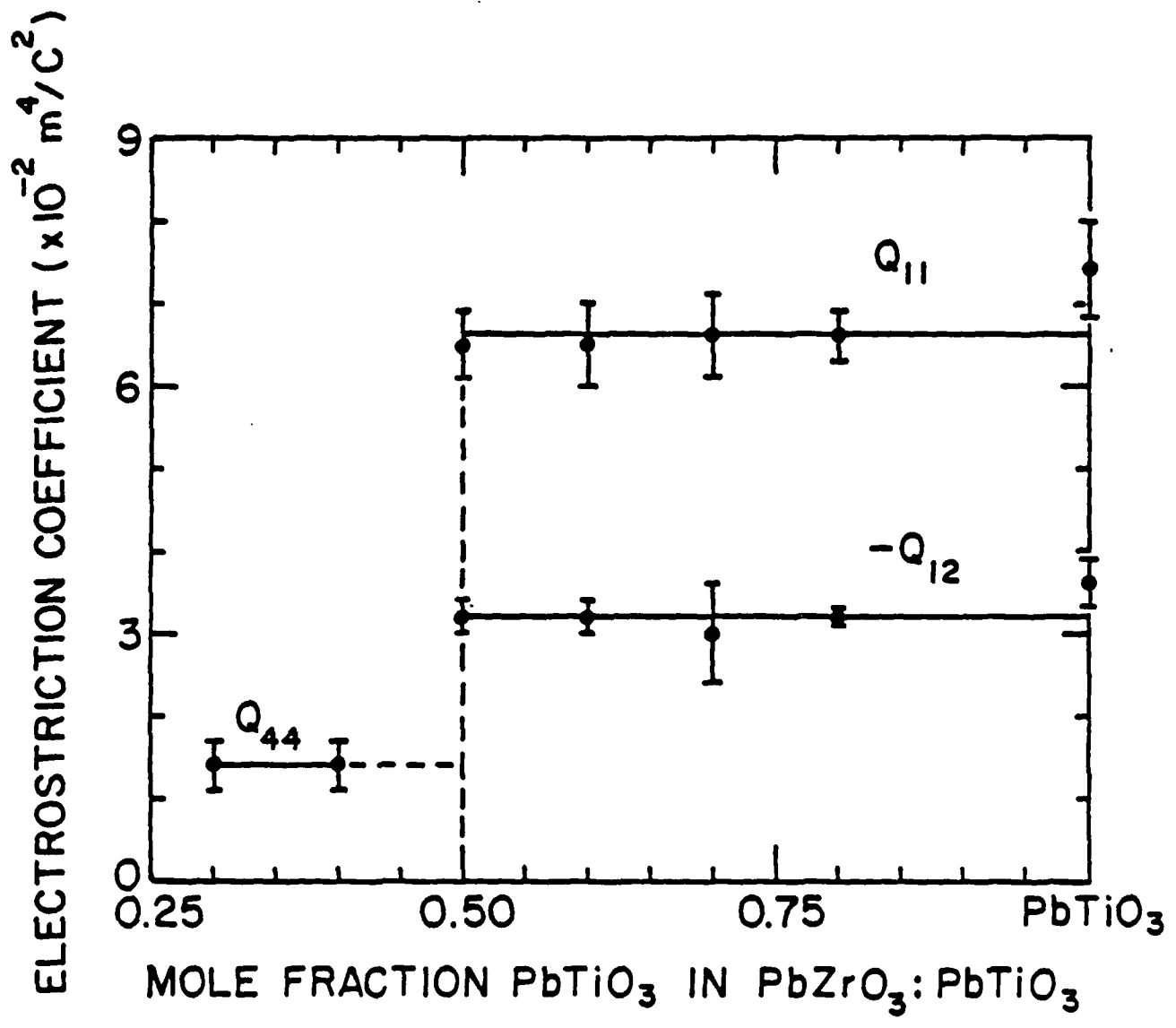


Fig. 3.

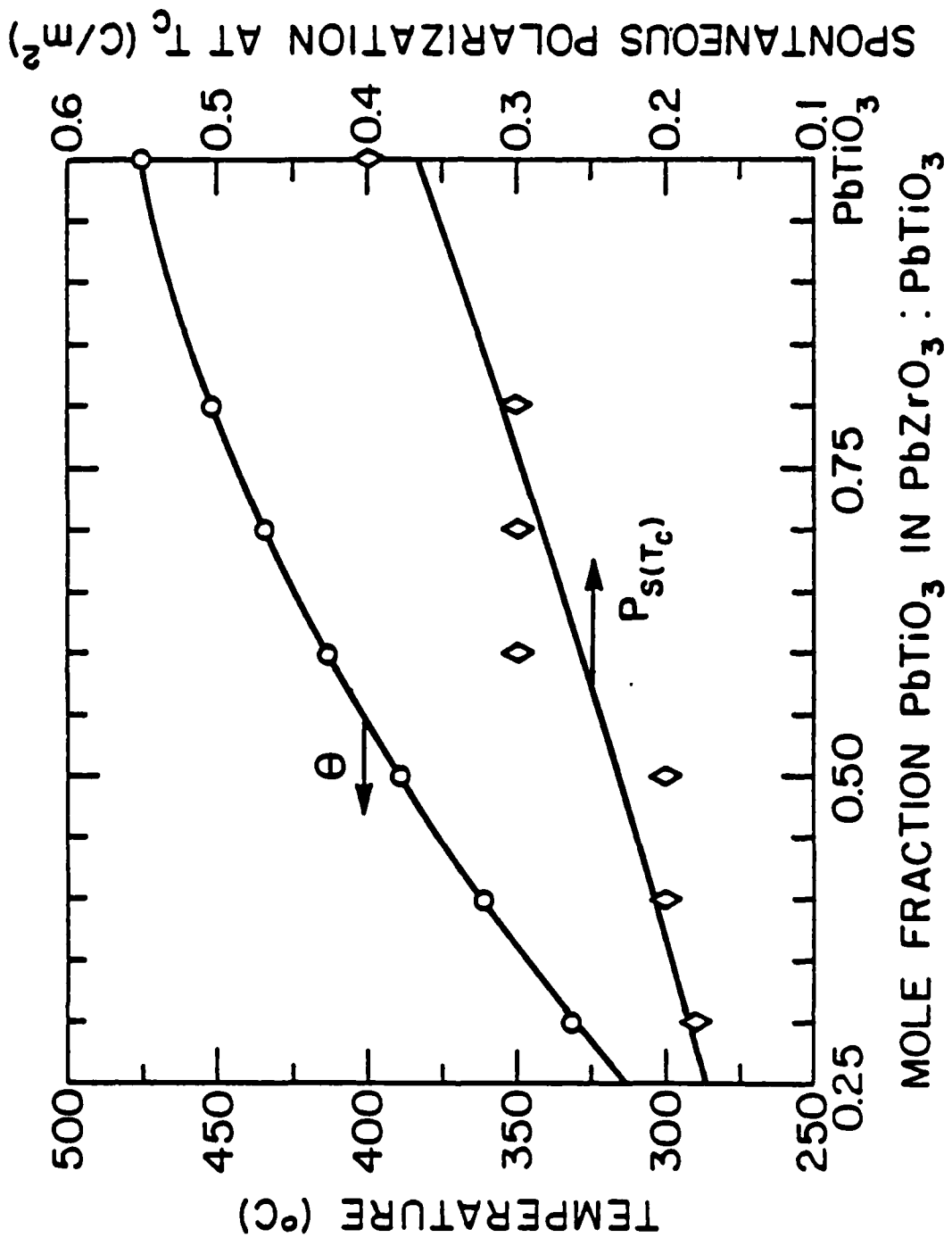


Fig. 4.

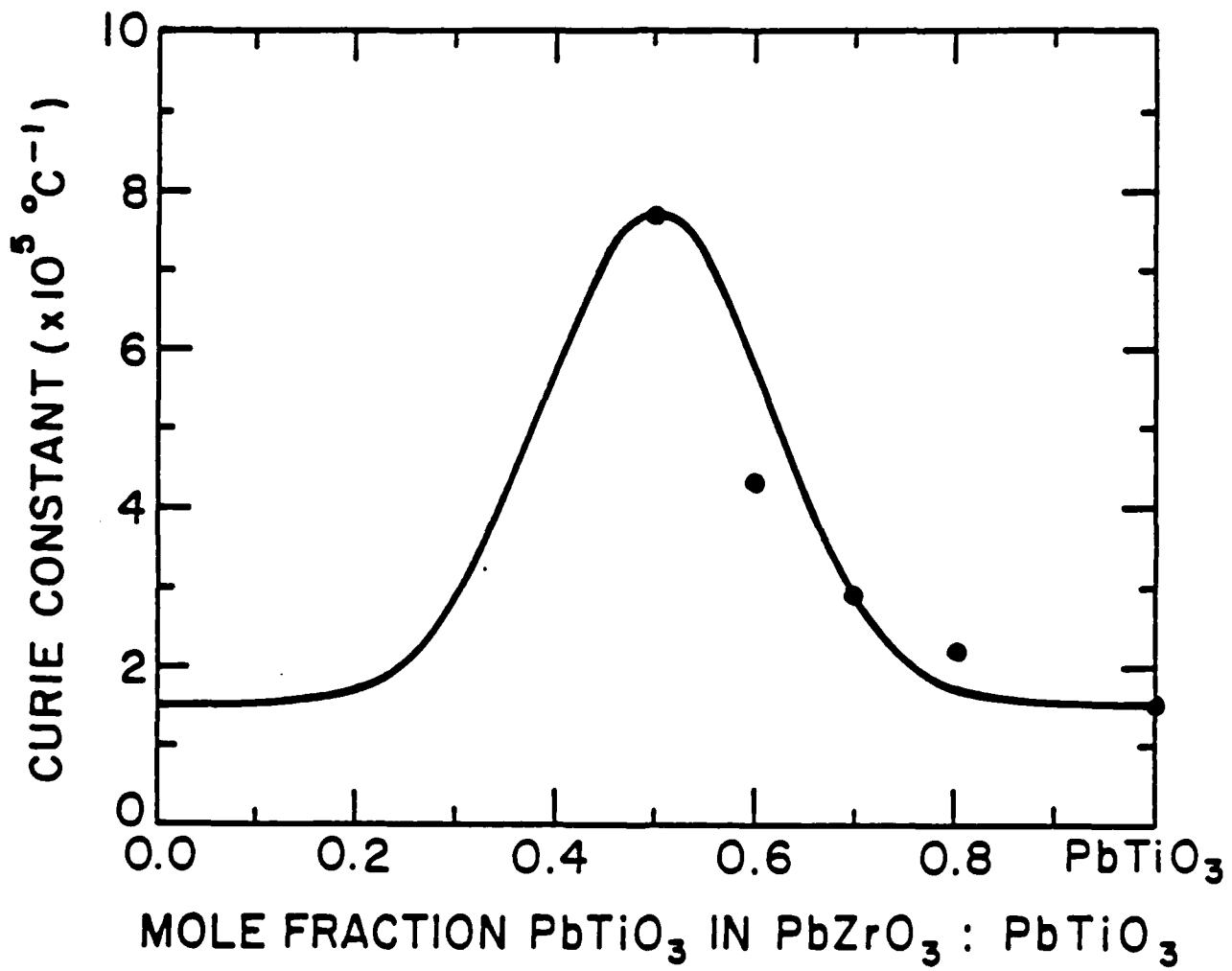


Fig. 5.

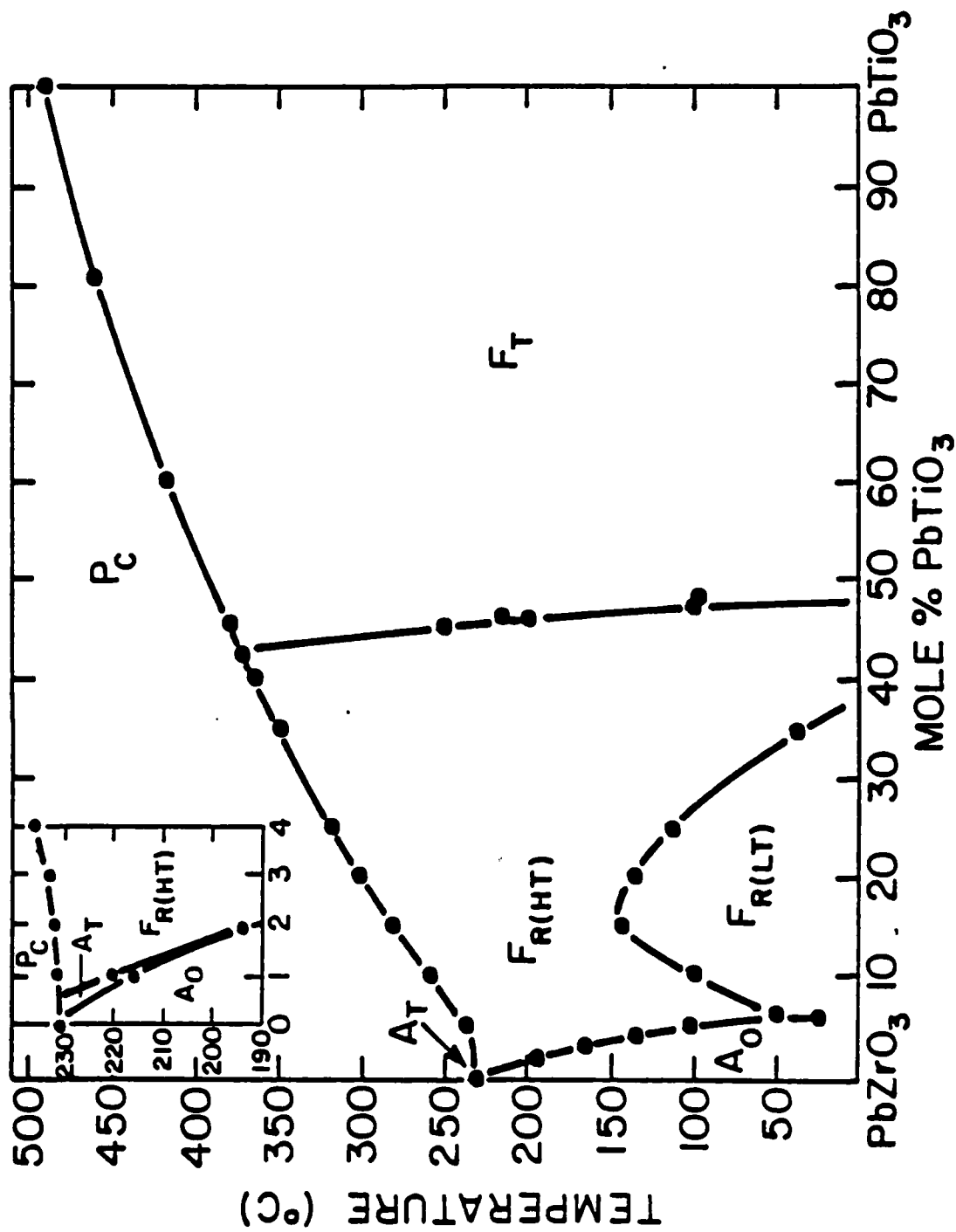


Fig. 6.

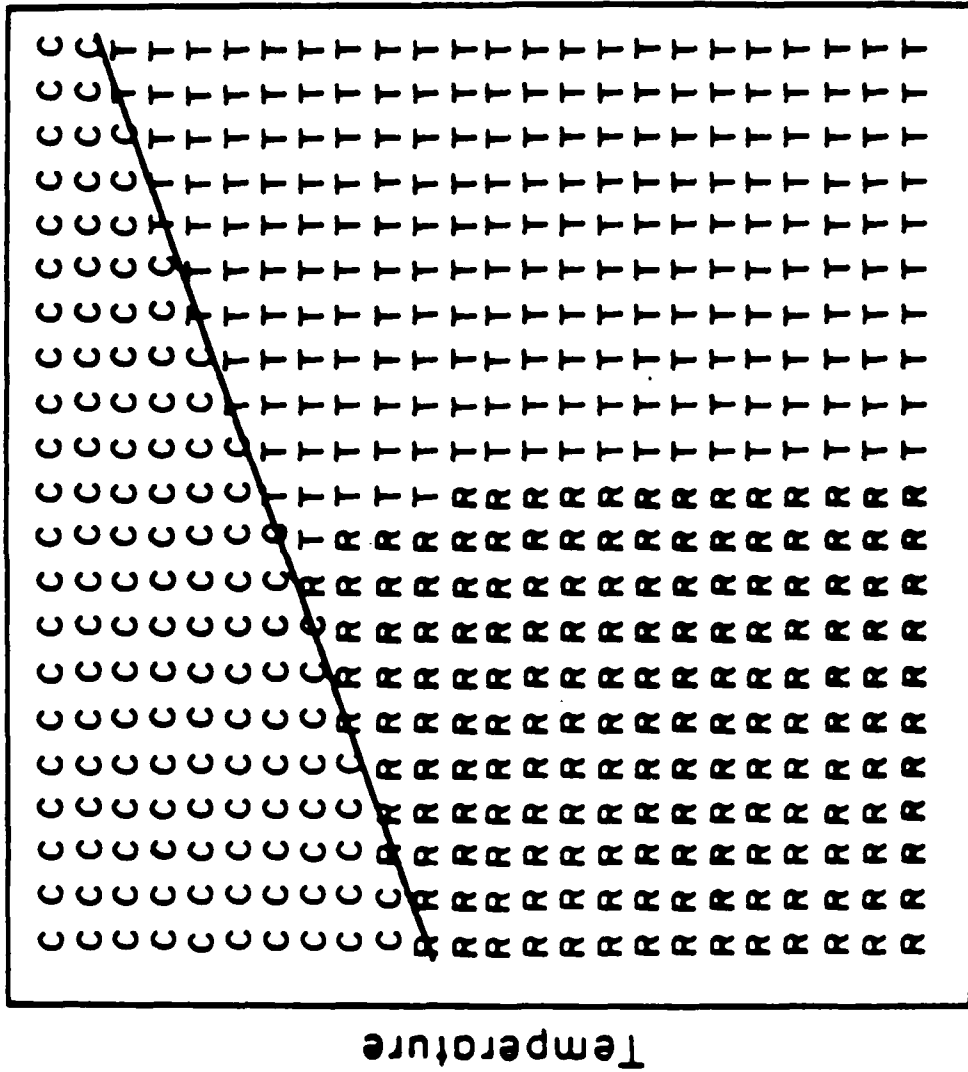


Fig. 7.

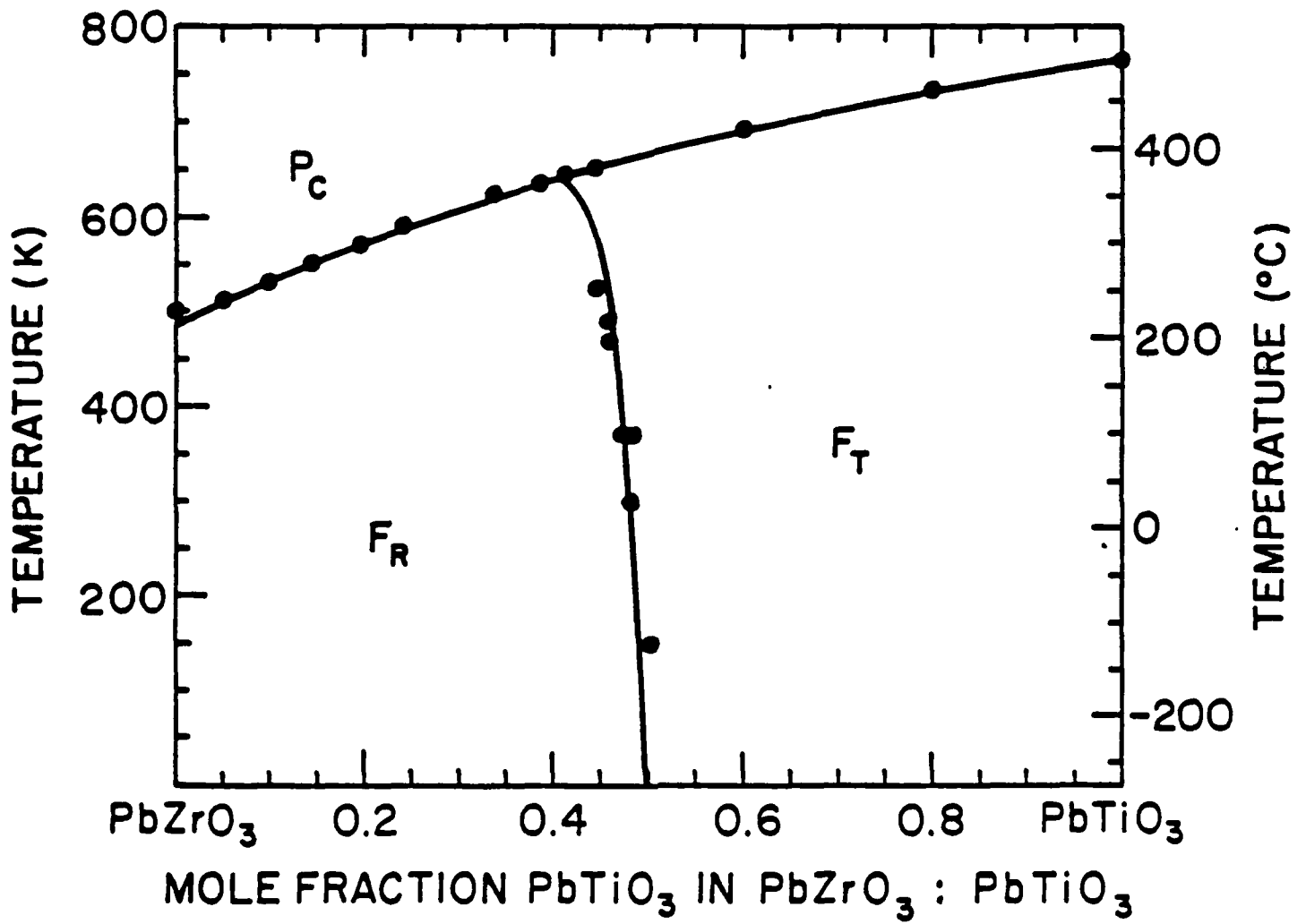


Fig. 8.

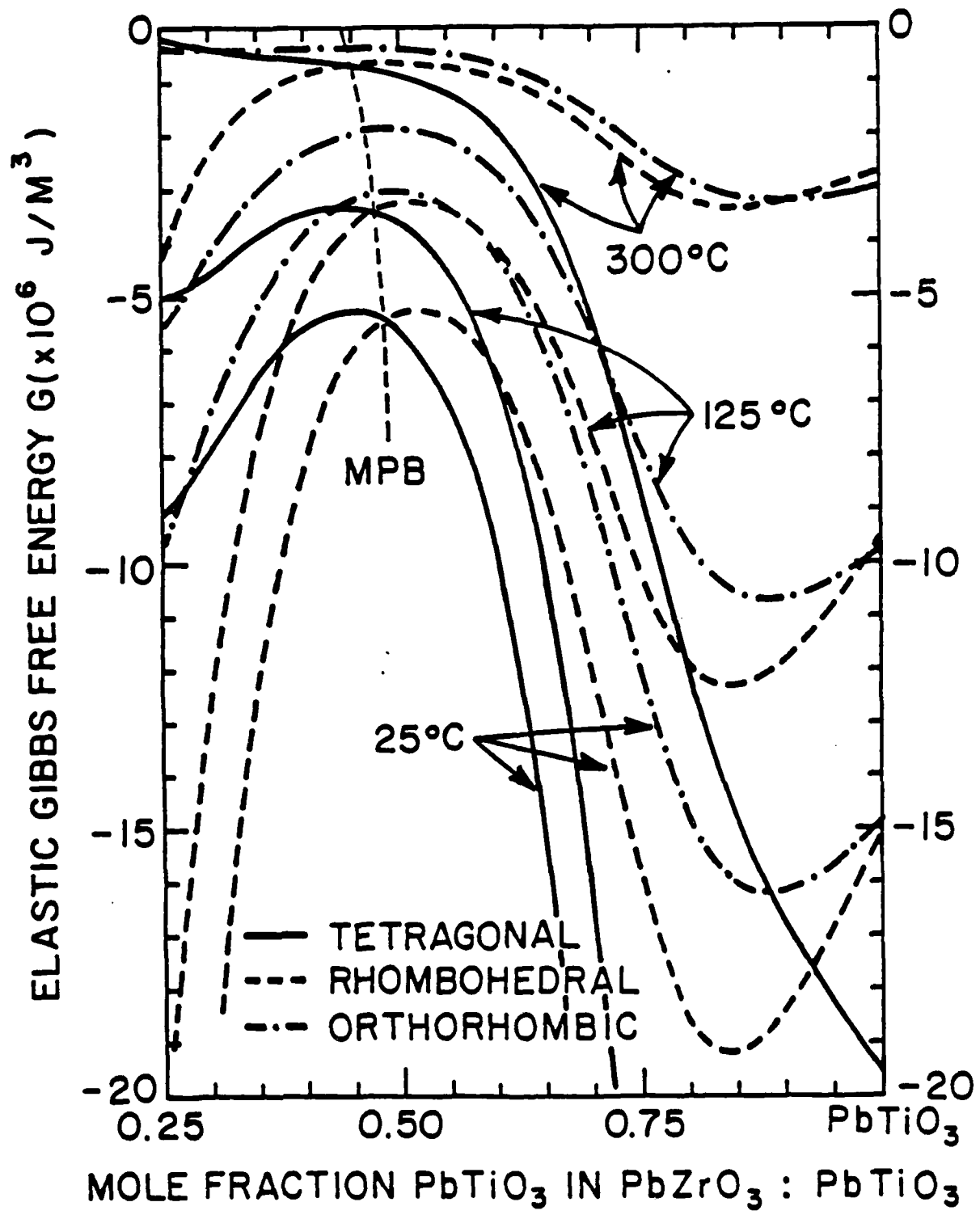


Fig. 9.

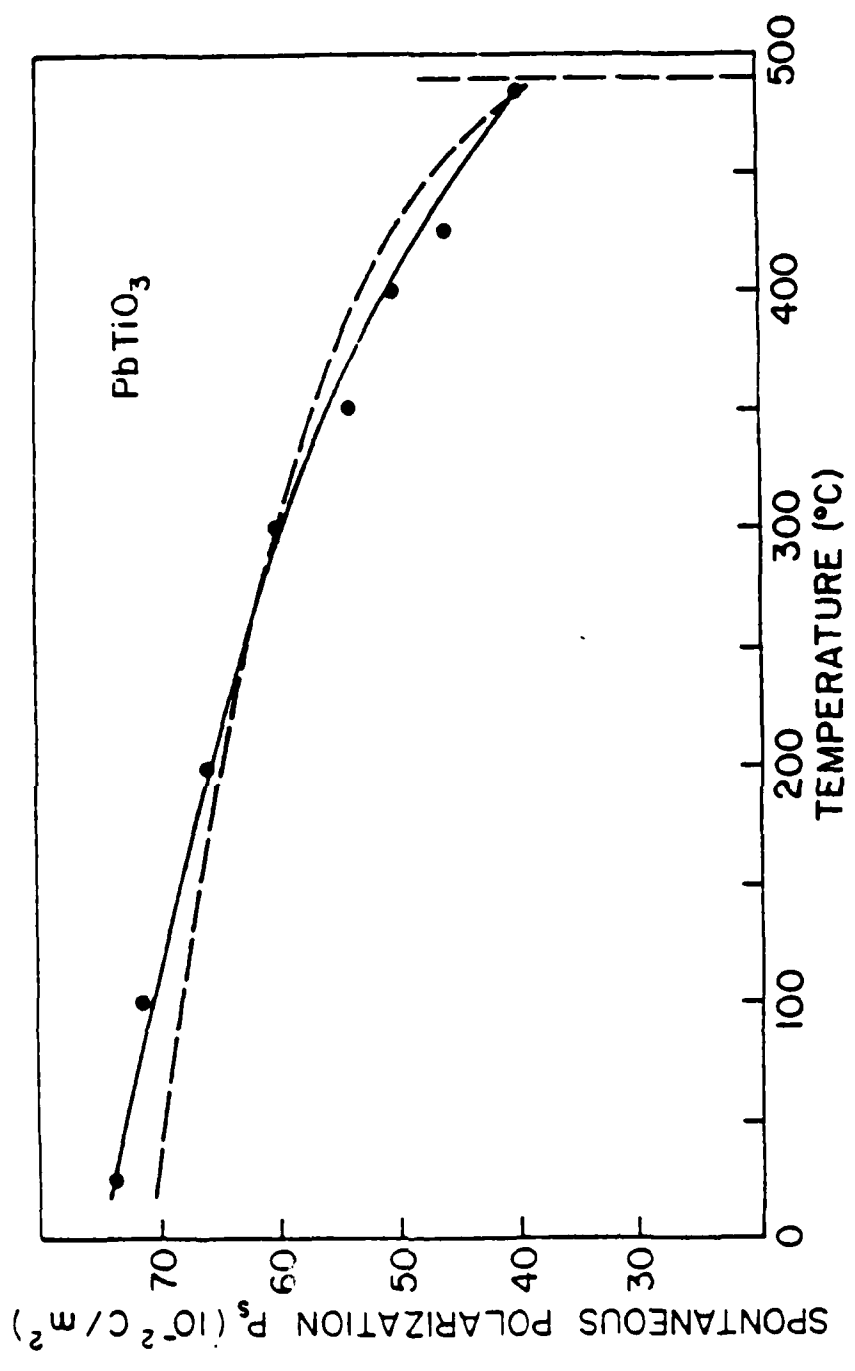


Fig. 10.

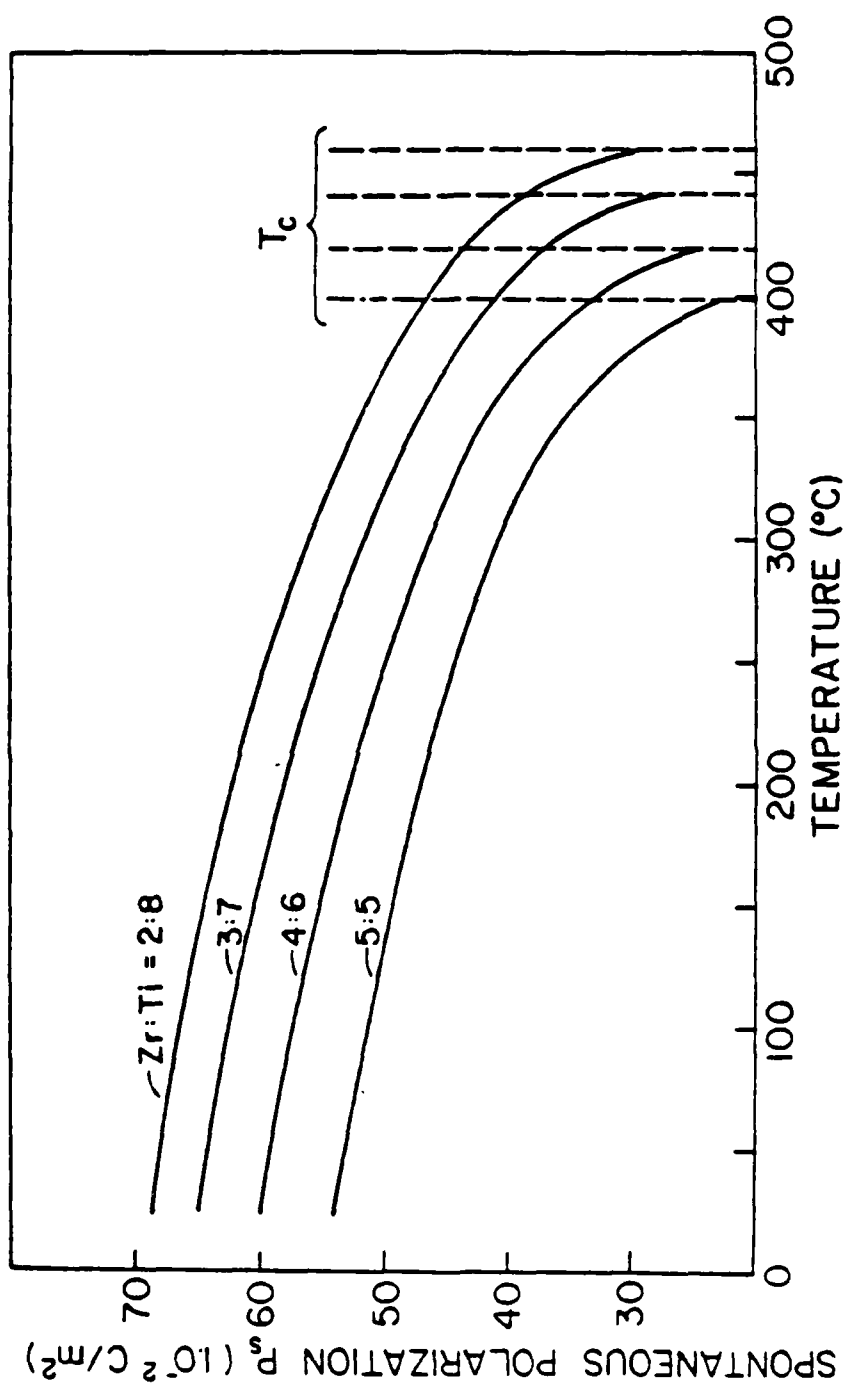


Fig. 11.

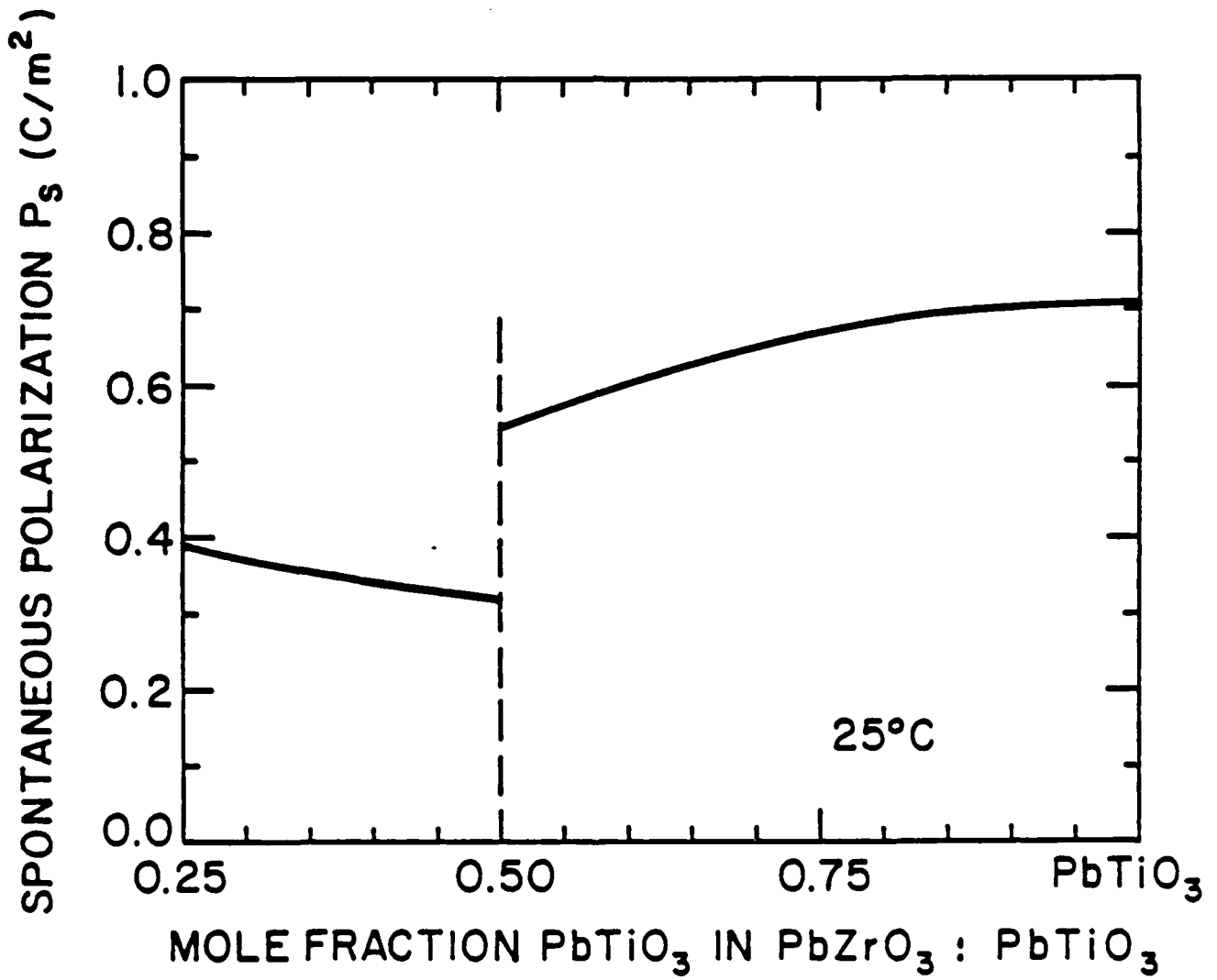


Fig. 12.

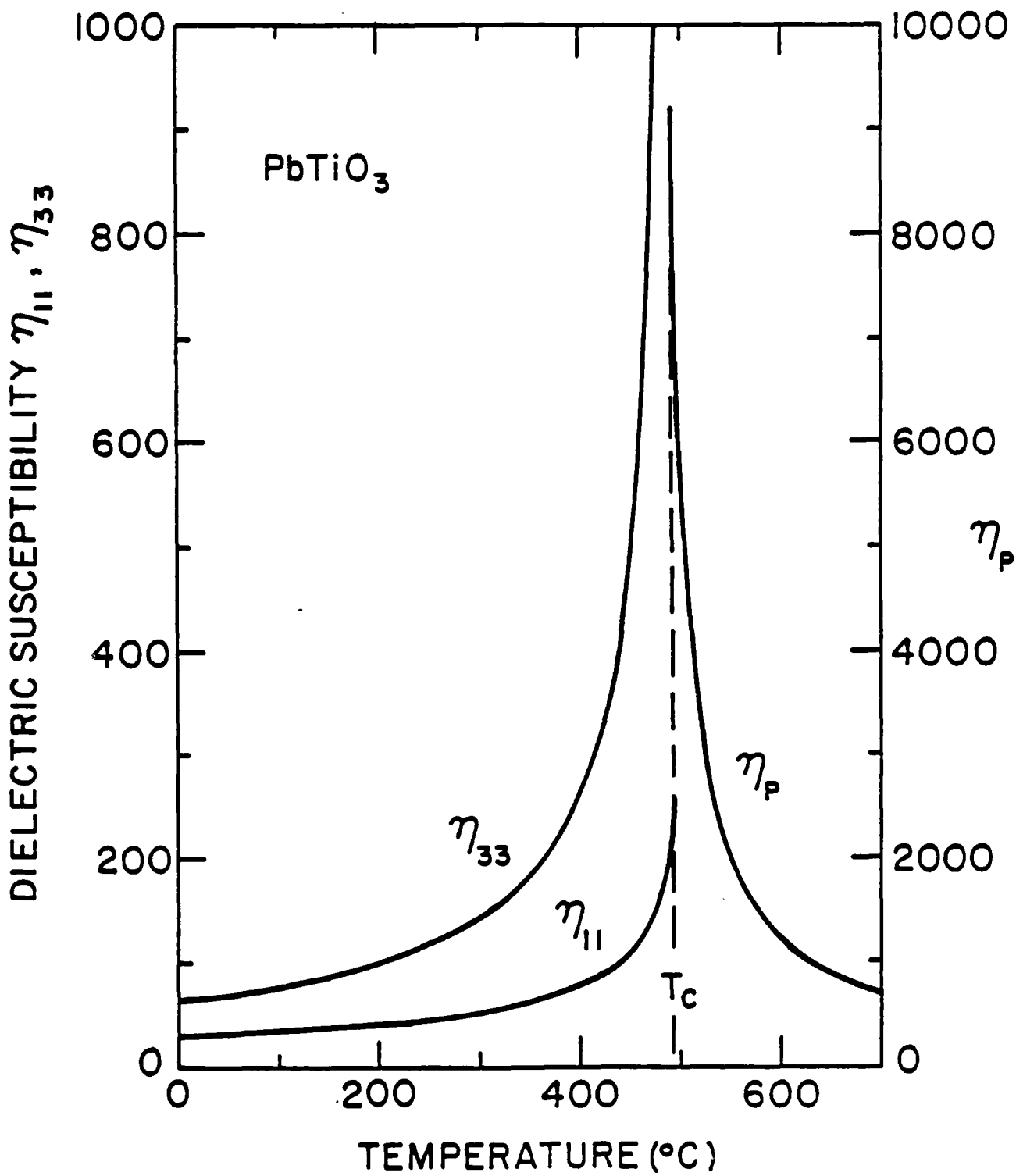


Fig. 13.

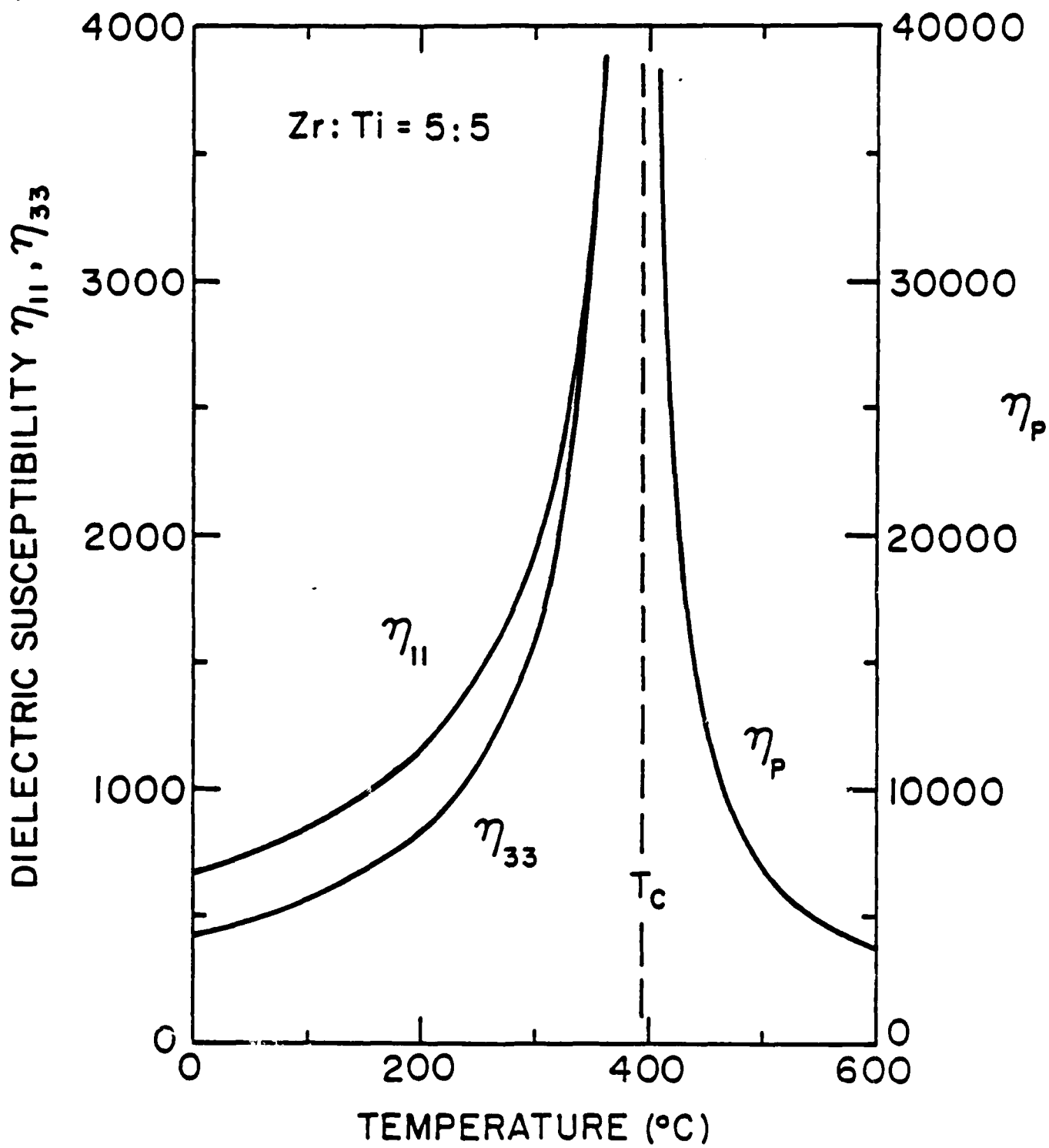


Fig. 14.

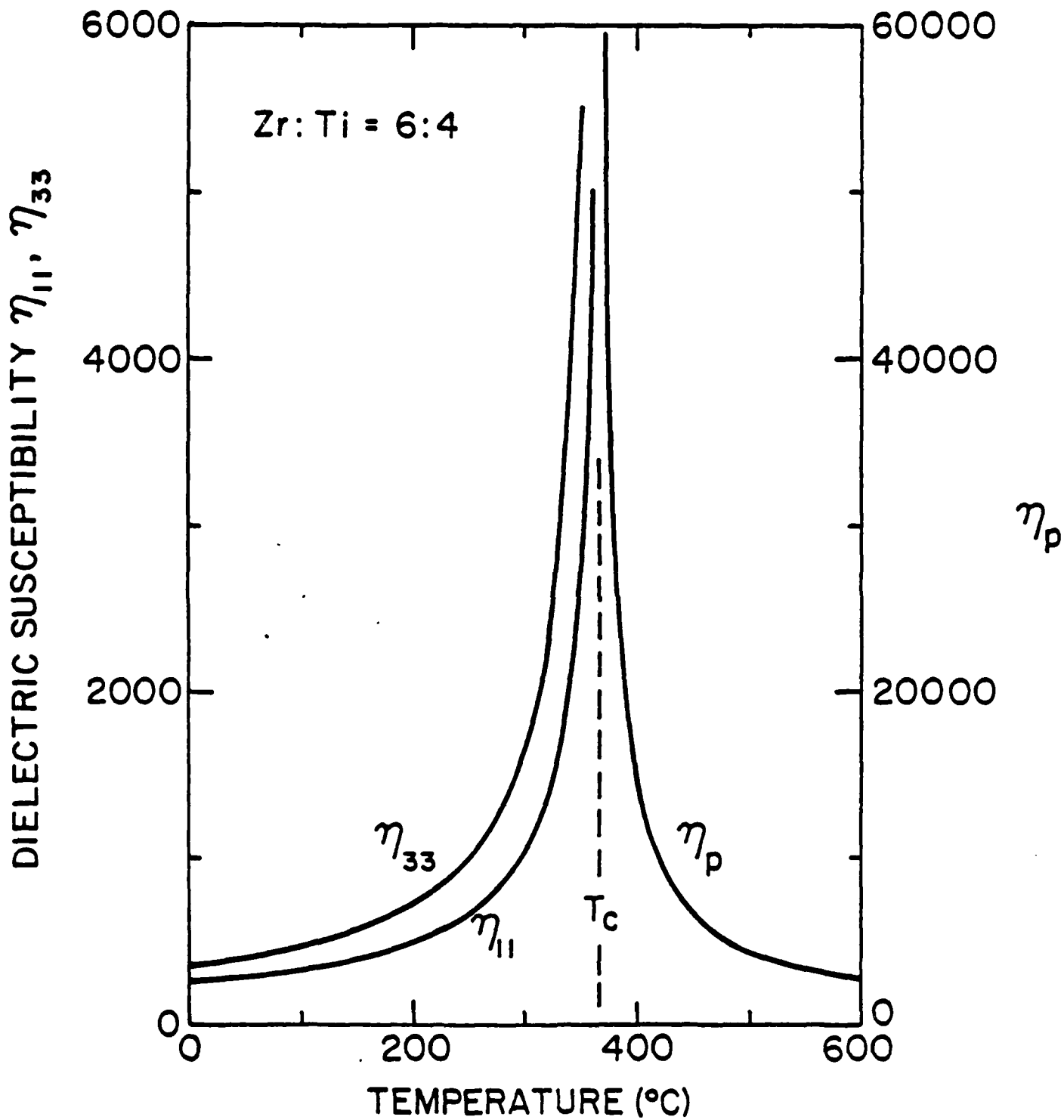


Fig. 15.

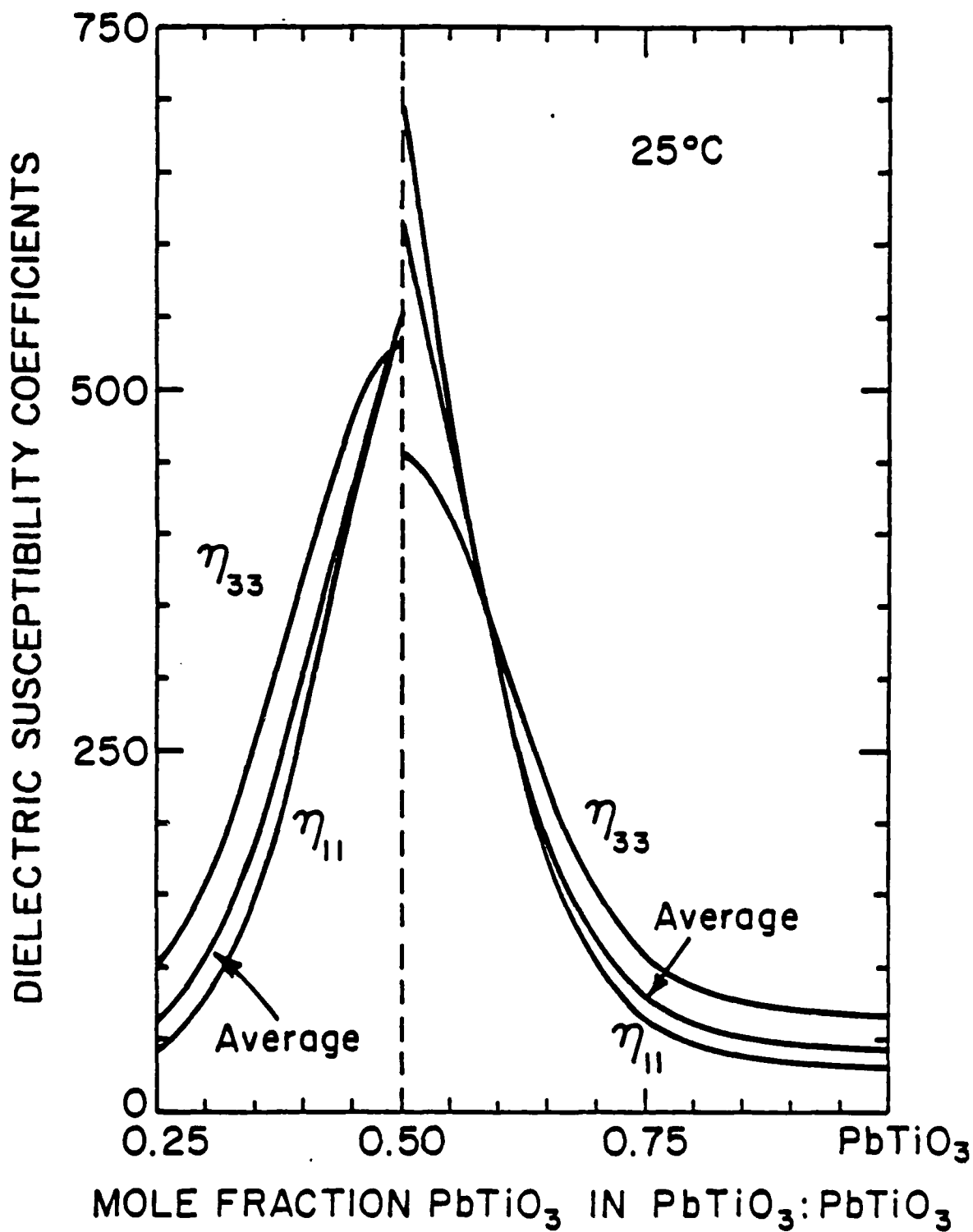


Fig. 16.

PIEZOELECTRIC COEFFICIENT $d_{33}, -d_{31}$ ($\times 10^{-12}$ C/N)

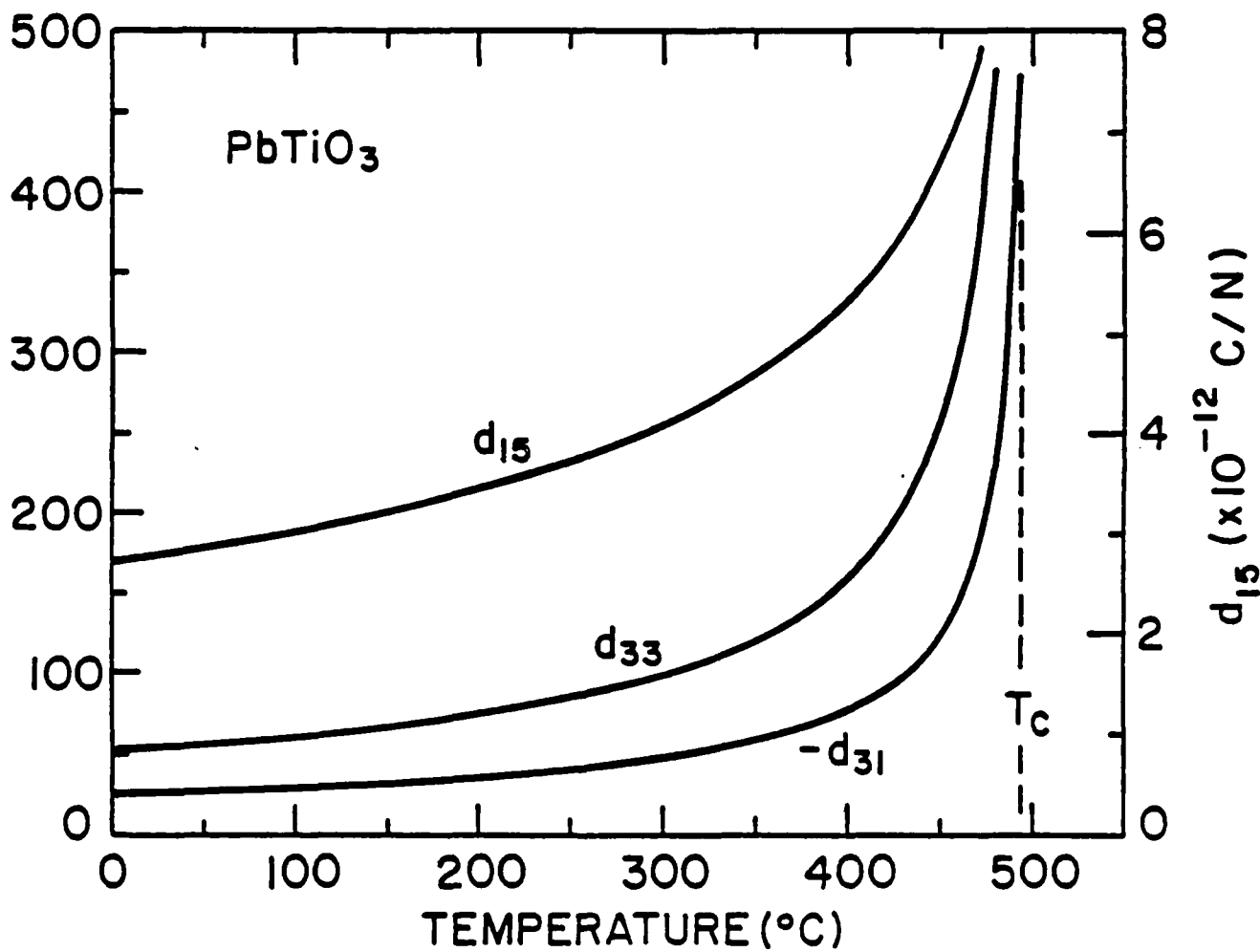


Fig. 17.

PIEZOELECTRIC COEFFICIENT $d_{33}, -d_{31}$ ($\times 10^{-12}$ C/N)

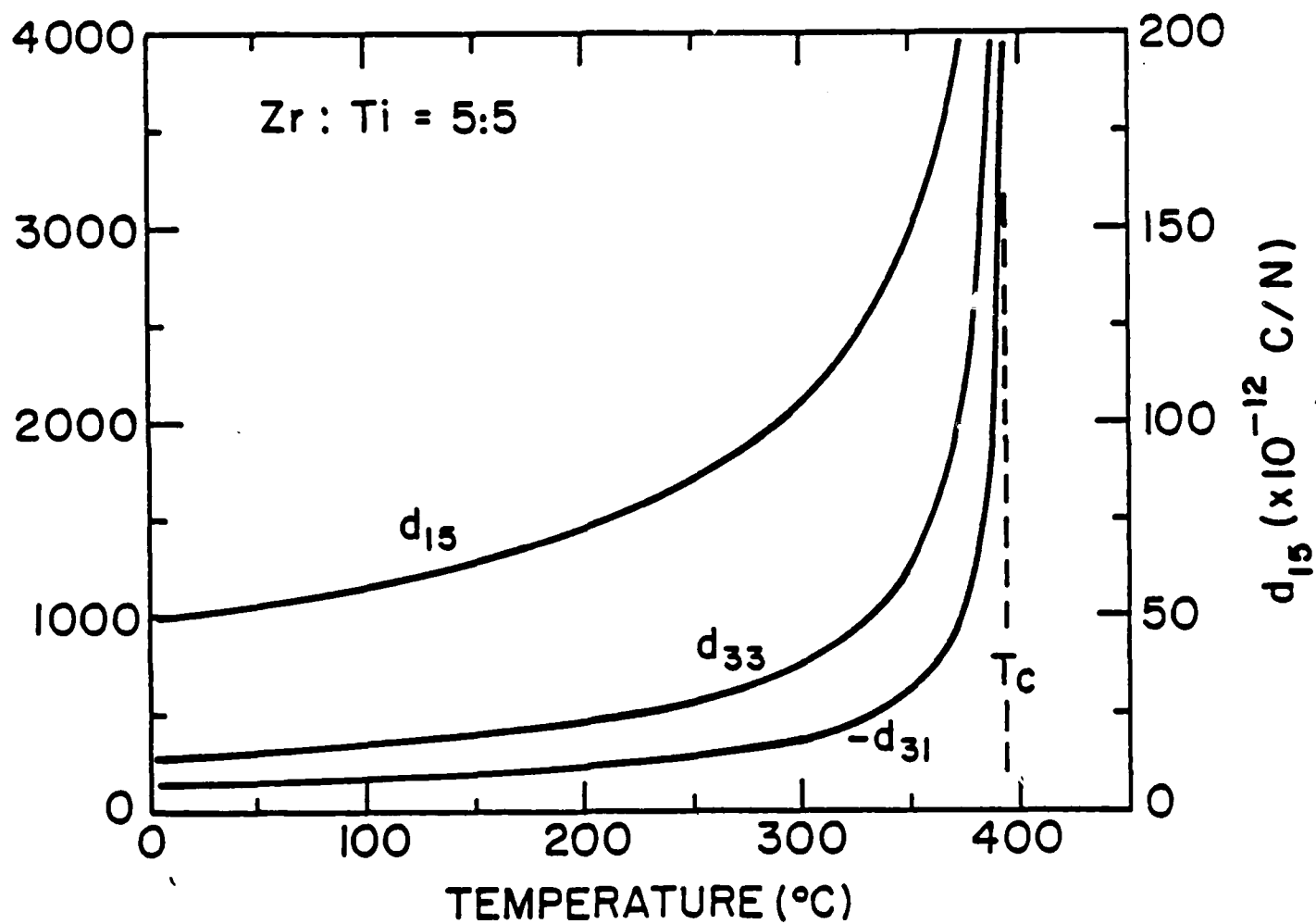


Fig. 18.

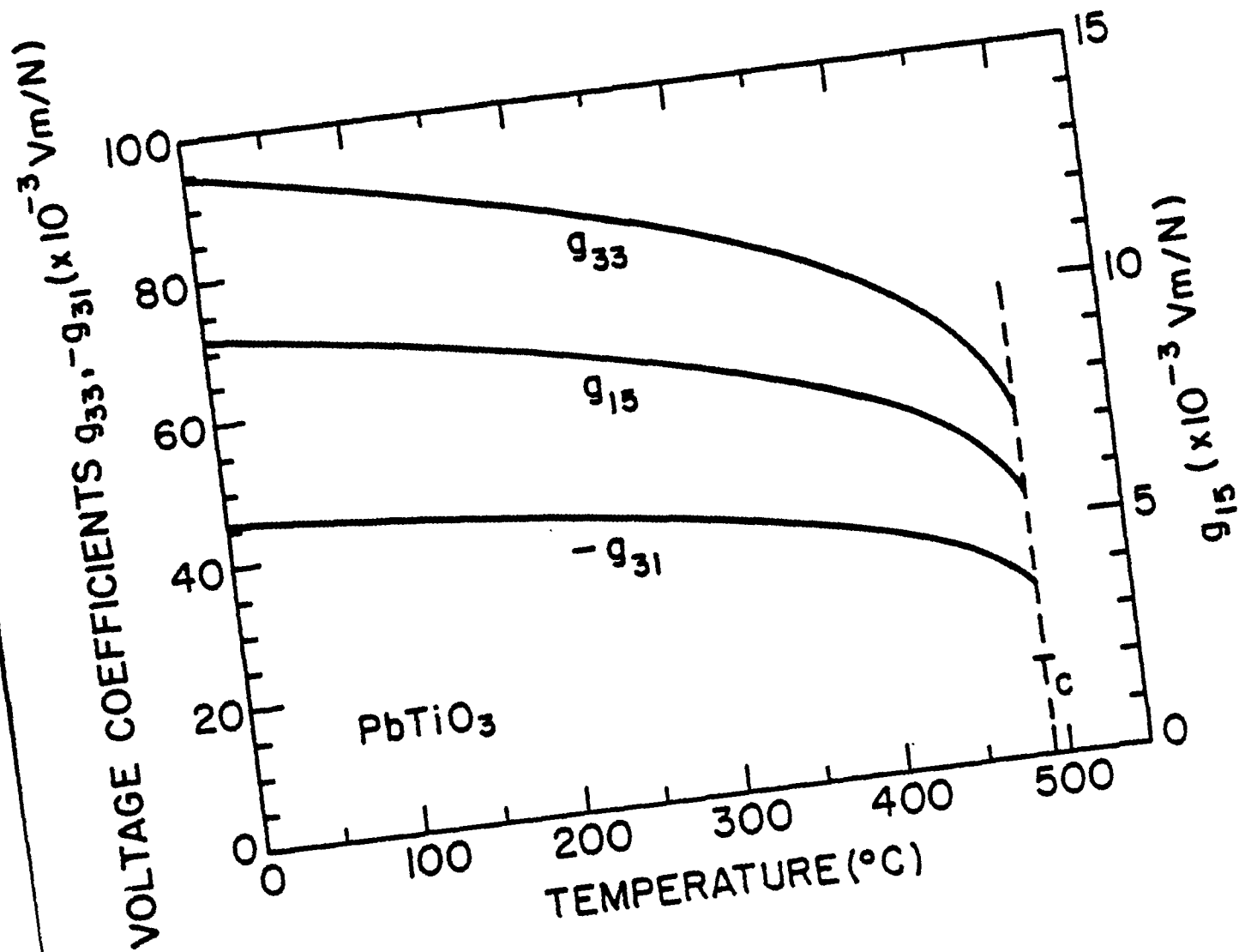


Fig. 19.

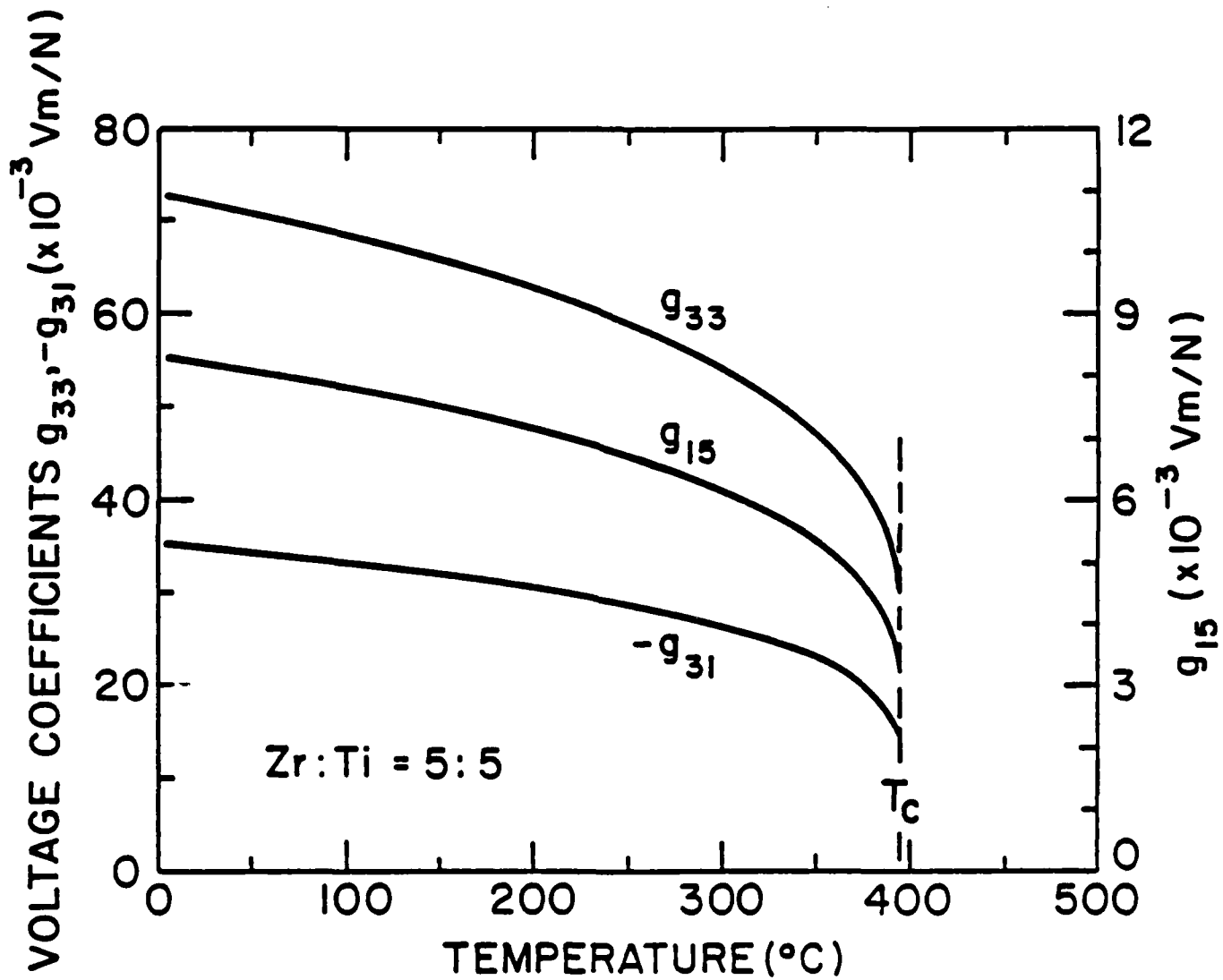


Fig. 20.

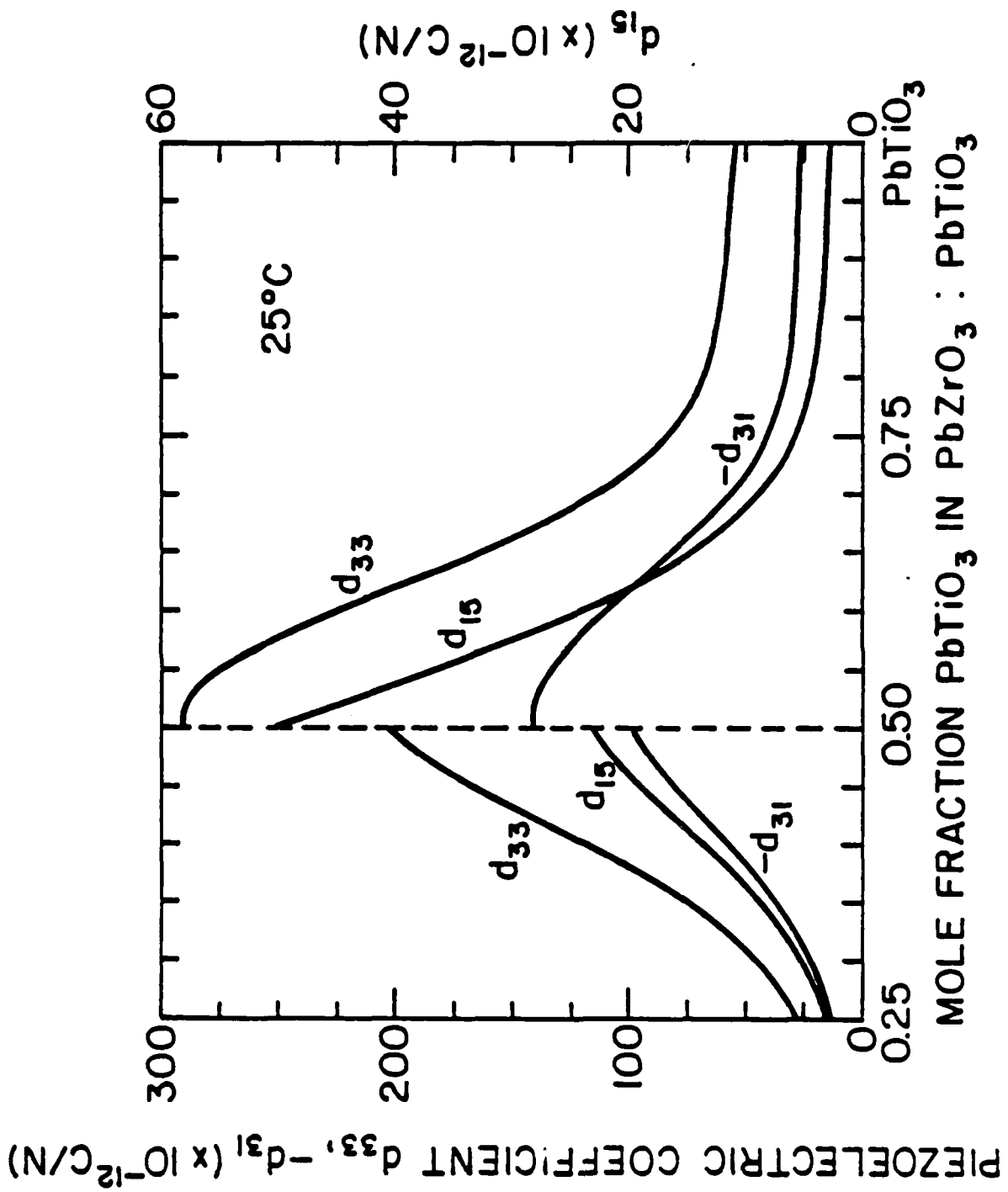


Fig. 21.

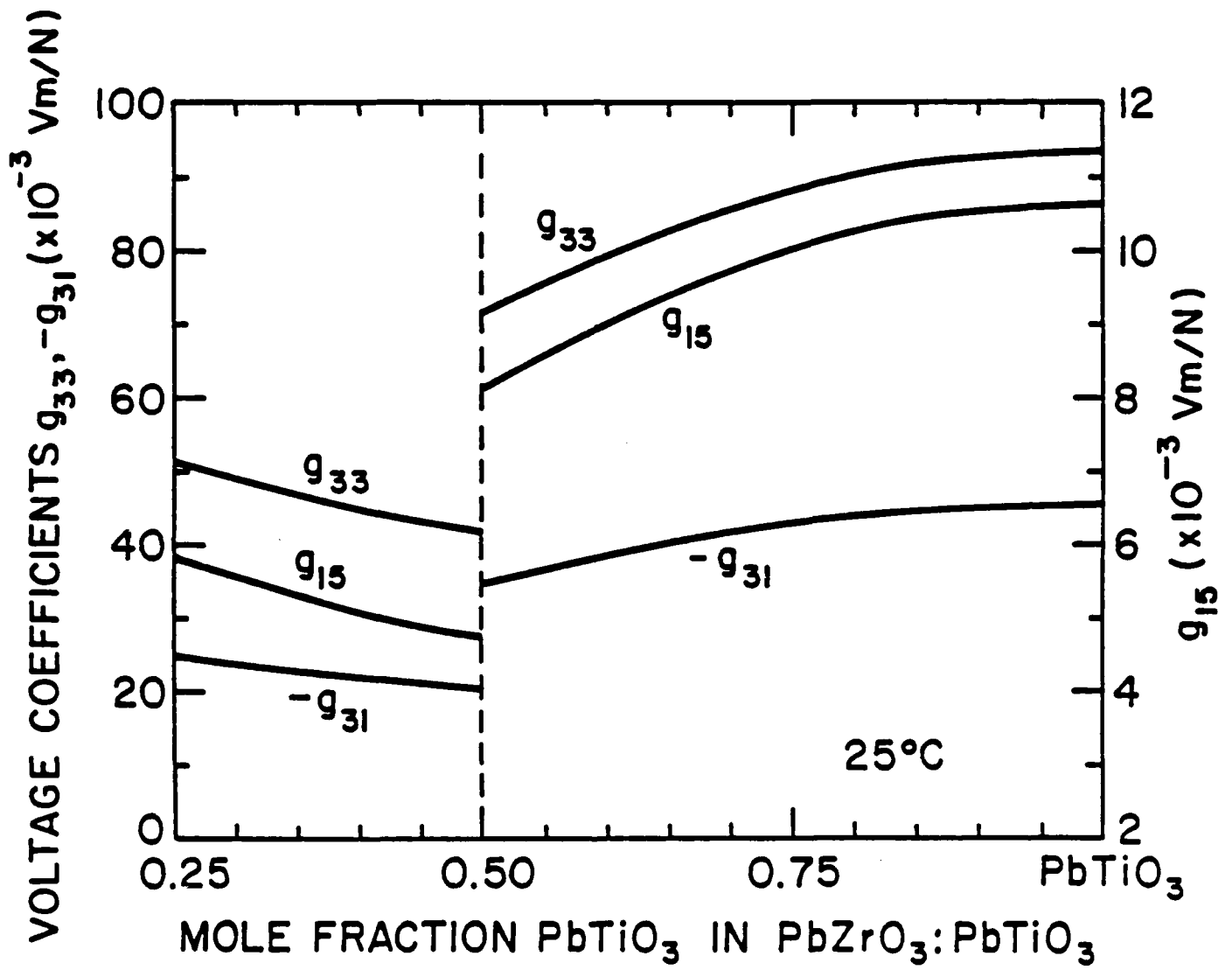


Fig. 22.

Table I. Calculated Values of T_0 , θ , Φ (TC), ϕ , and the α Stiffness Coefficients.

	Mole Fraction $PbTiO_3$ in $PbZr_{0.5}PbTi_{0.5}O_3$										
	0	.1	.2	.3	.4	.5	.6	.7	.8	.9	1
T_0 (°C)	211.8	257.7	298.4	334.4	366.1	394.1	418.7	440.3	459.5	476.7	492.2
θ (°C)	208.2	254.1	294.4	330.0	361.3	388.9	413.1	433.9	451.5	465.6	475.9
$\Phi_S(T_0)$ (C/m ²)	0.119	0.140	0.161	0.183	0.207	0.231	0.256	0.282	0.309	0.336	0.365
α_{11}^I ($\times 10^5$ m/F) at T_0	13.55	13.45	13.07	8.650	4.695	3.814	5.519	12.43	26.37	41.45	61.38
α_{11}^I ($\times 10^7$ m/F) at 25°C	-6.894	-8.533	-8.857	-5.938	-3.289	-2.669	-3.795	-7.963	-14.02	-16.41	-16.97
α_{11}^I ($\times 10^7$ m ³ /C ² F)	-19.10	-13.70	-10.07	-5.153	-2.226	-1.431	-1.677	-3.139	-5.535	-7.294	-9.235
ϕ	9.80	7.62	5.44	3.26	1.08	-1.10	-3.28	-5.46	-7.64	-9.82	-12.0
α_{12}^I ($\times 10^7$ m ³ /C ² F)	-187.2	-104.4	-54.78	-16.80	-2.404	1.574	5.500	17.14	42.28	71.63	110.8
α_{111}^I ($\times 10^8$ m ³ /C ⁴ F)	67.33	35.16	19.41	7.658	2.605	1.342	1.279	1.974	2.903	3.223	3.469
α_{112}^I ($\times 10^9$ m ³ /C ⁴ F)	6.021	5.960	5.260	3.116	1.565	1.173	1.565	3.116	5.260	5.960	6.021
α_{123}^I ($\times 10^9$ m ³ /C ⁴ F)	-33.87	-31.66	-26.30	-14.60	-6.846	-4.767	-5.868	-10.71	-16.44	-16.76	-15.05

PIEZOELECTRIC COMPOSITE MATERIALS FOR ULTRASONIC TRANSDUCER APPLICATIONS
PART 1. RESONANT MODES OF VIBRATION OF PZT ROD-POLYMER COMPOSITES

T.R. Gururaja, W.A. Schulze, L.E. Cross, and R.E. Newnham

Piezoelectric Composite Materials for Ultrasonic Transducer Applications

Part I. Resonant Modes of Vibration of PZT Rod-Polymer Composites

T.R. Gururaja, W.A. Schulze*, L.E. Cross and E.E. Newnham

Materials Research Laboratory
The Pennsylvania State University
University Park, PA 16802

B.A. Auld and J. Wang

Ginzton Laboratory
Stanford University
Stanford, CA 94305

Abstract

The objective of the present work was to gain a deeper understanding of the behavior of PZT-polymer composites for applications such as ultrasonic medical diagnosis in the MHz frequency range. These composites were originally developed for low frequency hydrophone applications. PZT rod-polymer composites have been prepared with 5 to 30 volume percent PZT using 0.28 mm and 0.45 mm rods. In a disc of PZT rod-polymer composite material, there are three principal types of resonance: the planar mode, the thickness mode, and various lateral modes caused by the regular periodicity of the PZT rod in the composite. These resonance modes have been studied by the following techniques: 1. Electrical impedance measurement as a function of frequency. 2. Laser probe dilatometry of the dynamic displacement as a function of frequency and position in the composite lattice. The observed resonance behavior is found to be a result of lateral interactions in the composite through the epoxy medium. The effect of temperature on the electromechanical properties of the composite has also been investigated. Implications of these results for design optimization of ultrasonic transducer are discussed.

*Present Address: New York State College of Ceramics at Alfred University, Alfred, NY 14802.

I. Introduction

The design and fabrication of composite materials optimized for a special application has been the subject of extensive research recently. The applications range from mechanical structures to electronic devices. In designing composite materials, primary importance is given to the proper choice of component phases and the way in which they are interconnected to maximize a predefined figure of merit for the application envisaged. An important class of these new materials is the family of piezoelectric ceramic-polymer composite transducers. To date, most of the work on piezoelectric ceramic-polymer composite materials has been focused on hydrophone applications in the low frequency (<40 KHz) range, where the dimensions of the transducer are much smaller than the acoustic wavelength [1-8]. Heretofore, there have been no studies to investigate the usefulness of these composites at higher frequencies (1-10 MHz) for medical diagnostic and nondestructive testing applications. At these frequencies, the acoustic wavelength is comparable to the scale of the composite microstructure. The acoustic impedance, bandwidth, and radiation patterns of the composite transducer can be controlled in such a sophisticated manner which is impossible in single phase materials. The results of a systematic investigation of the composite materials made from piezoelectric lead zirconate titanate (PZT) ceramics and piezoelectrically inactive polymer are reported here. The study was described in the present ^{paper work} _^ focused on understanding electromechanical properties of the composite materials in resonant configurations. The knowledge of the high frequency dynamic behavior of the composite was then used to evaluate the composite materials for ultrasonic transducer applications with an emphasis on medical diagnostic applications. The results are discussed in the accompanying paper (Part II).

In Section II, the requirements of a piezoelectric transducer for ultrasonic imaging applications and the limitations of the existing single phase transducer materials are described. In Section III, a brief review of the earlier works on piezoelectric ceramic-polymer composites of relevance to the present work is given. Advantages of the use of composites for ultrasonic applications are pointed out. The criteria used to select an appropriate composite structure for a detailed investigation for high frequency transducer applications are also described. Bulk mechanical properties of the polymer phase that strongly influence ultrasonic properties of the composite are summarized in Section IV. The characterization of all the different resonance modes in the composite are discussed in Section V. Laser probe measurements are presented in Section VI. The effect of temperature on the resonance modes in the composite are dealt with in Section VII. Finally, the implication of the results on the high frequency vibration behavior of the composites in air for the ultrasonic imaging applications are summarized in Section VIII.

II. Piezoelectric Transducer Material Parameters

The basic requirements of a piezoelectric transducer for ultrasonic diagnostic imaging are an ability to generate short acoustic pulses and receive them with high sensitivity in the frequency range of 1-10 MHz. The transducer should also exhibit good axial and lateral resolution to visualize structures with dimensions of the order of a millimeter or less [9]. In terms of the material parameters, these requirements can be summarized as follows:

1. The piezoelectric material should have a high electromechanical coupling coefficient for high sensitivity.
2. The acoustic impedance of the transducer should be well matched to that of the load to minimize reflection losses at the interface. The acoustic impedance matching at the interface determines the Q (broadband nature) of the transducer.

AD-A168 465

PIEZOELECTRIC AND ELECTROSTRICTIVE MATERIALS FOR
TRANSDUCER APPLICATIONS(U) PENNSYLVANIA STATE UNIV
UNIVERSITY PARK MATERIALS RESEARCH LAB

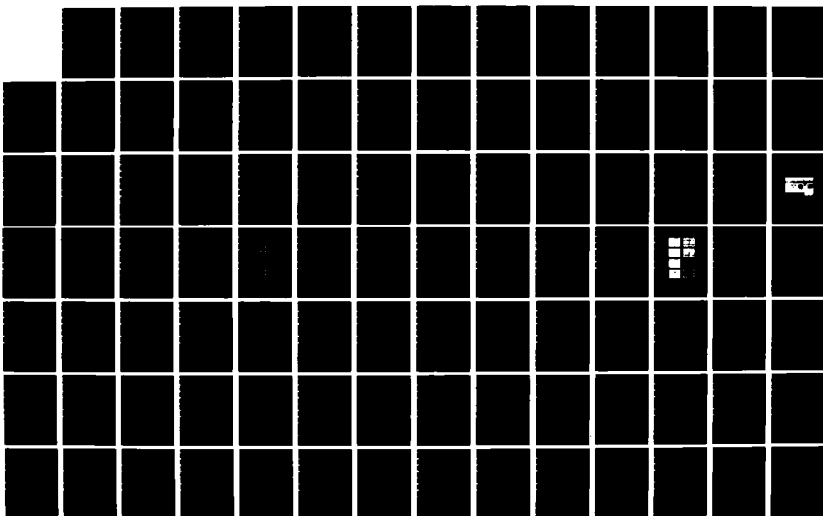
3/4

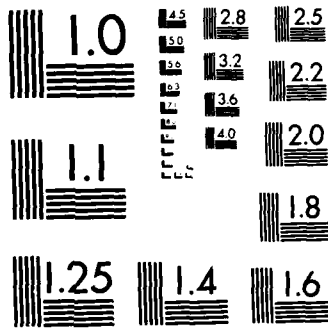
UNCLASSIFIED

L E CROSS ET AL MAY 85 N00014-82-K-0339

F/G 9/1

NL





MICROCOPY RESOLUTION TEST CHART
NATIONAL BUREAU OF STANDARDS-1963-A

It is well known that the piezoelectric ceramic materials such as PZT with high electromechanical coupling suffer from a severe disadvantage when operated with a low impedance load like that of the human body. The acoustic impedance of PZT is around $30 \times 10^6 \text{ kg/m}^2\text{-sec}$ while the tissues have acoustic impedance near that of water, $1.5 \text{ kg/m}^2\text{-sec}$. (Henceforth all acoustic impedances will be given in units of $10^6 \text{ kg/m}^2\text{-sec}$ called M rayl.) As a result of the acoustic impedance mismatch, the coupling of the acoustic energy at the transducer-load interface is very poor. The resonance behavior is thus high Q (narrow bandwidth). The consequence of a high Q in a transducer is a slow pulse-rise time and a prolonged ring down with a detrimental effect on range resolution.

In practice, two methods are used to increase the transducer bandwidth. In the first method, the resonance of the piezoelectric element is mechanically damped with a well matched backing medium [10]. As a result a large portion of the available energy is transmitted into the backing material resulting in a lower sensitivity. In the second method, the frequency bandwidth of a transducer is increased by the use of an impedance matching layer of quarter wavelength in thickness and characteristic impedance equal to the geometric mean of those of the transducer and load [10]. More recently, Goll and Auld [11], Desilets et al. [12], and Souquet et al. [13] have made complete theoretical and experimental analyses for obtaining optimum acoustic matching. Depending on the specific requirements of sensitivity, bandwidth, and impulse response, the optimum acoustic impedance of the matching layer for a PZT ceramic disc operating into a water equivalent load varies from 4 to 7. Since no readily available material has its acoustic impedance near this value, a matching layer must be prepared synthetically, which is not always easy. However, in practice, such material is prepared by mixing suitable metallic powder such as aluminum with some epoxy resin [10,13,14]. The

composite matching layer configurations have relatively large attenuation coefficient and add to further loss of acoustic energy.

Desilets et al. [12] and Goll [15] have further improved the bandwidth and the sensitivity of their disc transducers using multiple layer impedance matching schemes. Although two layer matching schemes work very well with readily available materials, the transducer fabrication is quite involved. As the frequency of operation is increased, the thickness of the matching layer decreases which makes the fabrication more difficult.

The recent development of piezoelectric polymer materials such as polyvinylidene fluoride (PVF_2) has opened up new possibilities for transducers operating with low acoustic impedance media [16]. PVF_2 has a low acoustic impedance, reasonable piezoelectric coupling, high g_{33} coefficient and offers wide bandwidth frequency response which are excellent properties for acoustic imaging in low impedance load. Several intrinsic limitations of PVF_2 transducers, as discussed in detail by Collerame et al. [17] and Hunt et al. [18], restrain their extensive use in ultrasonic imaging applications. Major limitations are mentioned below. First of all it is very difficult to produce samples with resonance near the typical operating frequency in medical ultrasound; although recently some researchers have been successful in producing 1-2 mm thick polarized PVF_2 films [19]. The d_{33} coefficient of PVF_2 is only 10 pC/N, and hence PVF_2 is a poor ultrasonic transmitter. In addition PVF_2 has a dielectric constant of only 11 at 1 KHz which decreases at higher frequencies. Thus, the electrical impedance of PVF_2 transducers is high and is in general more difficult to match than the piezoelectric ceramics. The dielectric loss tangent in PVF_2 is 0.25 at 2.5 MHz and acts as a major source of absorption of electrical energy applied to the transducer. In the receiver mode, the dielectric loss is found to diminish the signal to noise ratio.

As discussed above, single phase piezoelectric materials (ceramic or polymer) are far from being optimized for ultrasonic imaging applications. Thus, a composite material combining the desirable properties of two different phases might be superior. This concept has proven to be highly successful in designing composite materials consisting of PZT and piezoelectrically inactive polymer. The hydrostatic piezoelectric coefficients of these composites were 2 to 3 orders higher than that of the piezoelectric phase used in the composite. Although the design and fabrication of different types of piezoelectric composite materials for hydrophone applications at low frequencies (<40 KHz) has been reported in several papers [1-8], for completeness a brief summary is presented here in the next section.

III. Composite Piezoelectric Transducers

PZT ceramics, which is commonly used as a piezoelectric transducer material, suffers from several disadvantages when used as a hydrostatic pressure sensor. The hydrostatic piezoelectric coefficient $d_h (=d_{33}+2d_{31})$ of PZT is low due to opposite signs of piezoelectric strain coefficients d_{33} and d_{31} , even though the magnitudes of both d_{33} and d_{31} are large. The hydrostatic voltage coefficient $g_h (d_h/\epsilon_0 k)$ is also small because of its high relative permittivity k . ϵ_0 is the permittivity of free space.

To improve the magnitude of d_h and g_h , a number of different diphasic composites using PZT and passive polymers have been fabricated. It was shown that the phase connectivity, defined as the manner in which the individual phases are interconnected, is the key feature in designing the composite materials. The electrical flux pattern and mechanical stress distribution together with the resulting physical and piezoelectric properties depend strongly on the phase connectivity. In a diphasic composite, there are ten possible connectivity patterns designated as 0-0, 1-0, 2-0, 3-0, 1-1, 2-1, 3-

1, 2-2, 3-2, and 3-3. A 1-3 connectivity pattern, for example, consists of parallel PZT rods embedded in a three dimensionally continuous polymer matrix [3]. In the notation used here, the piezoelectric phase appears first.

Dielectric and piezoelectric properties of different types of PZT-polymer composite materials designed for the hydrophone applications are summarized in Table 1. Hydrostatic d and g coefficients were measured by a substitution method [7]. As listed in the table, a 3-3 composite comprises of PZT and polymer phases continuously self-connected in three dimensions to give two interlocking skeletons in intimate contact with one another [1,6]. A 1-3-0 composite is a 1-3 PZT rod-polymer composite with a third phase such as hollow glass spheres or pores not in contact with each other [20]. In composite with 0-3 connectivity, piezoelectric ceramic particles (PZT, pure and modified lead titanate) 1 to 10 μ in size are loaded in a polymer matrix [8]. Composites of PZT and polymer with 3-1 and 3-2 connectivity patterns have been fabricated by drilling holes in sintered PZT blocks and filling the holes with epoxy [7]. In designing all these composite material, the primary goal was to decouple the transverse d_{31} coefficient and lower the dielectric permittivity to augment the hydrostatic d and g coefficients. The product of d_h and g_h listed in Table 1 was used as the figure of merit for the hydrophone applications.

From Table 1, it is evident that the hydrostatic pressure sensitivity of some of the composites was orders of magnitude larger than the corresponding values of the piezoelectric phase used in the composites. The density of the composite could be adjusted between the densities of the component phases. Composites with porous polyurethane phase were prepared to have positive buoyancy in water. By choosing soft polymers such as silicone rubber and polyurethane, composites were made flexible.

PZT polymer composites have several advantages over conventional piezoceramic materials for ultrasonic applications. In composites most of the

PZT (70-95%) is replaced by a low density polymer, and hence results in a better acoustic impedance matching to the human body. The composites also have a relatively low mechanical Q (3-10) [21]. These properties of the composites appear well suited for the broad bandwidth applications. Although PZT has a high d_{33} coefficient, the voltage coefficient g_{33} is low because of the high dielectric constant. Thus, PZT is a poor receiver of ultrasound. The concept of composite transducer allows designing a composite structure to enhance the g_{33} coefficient and improve the sensitivity in the receiving mode. If the receiving voltage sensitivity of the transducer is enhanced, the human body can be interrogated at lower ultrasonic energy and the biological effects of ultrasound, if any, can be minimized.

The following criteria were used here to select composite material of an appropriate connectivity for a systematic investigation intended towards ultrasonic transducers. Transducers for ultrasonic imaging applications are operated in a half wavelength thickness mode for maximum sensitivity. Thus, the major requirement of a composite was to have a well defined thickness resonance with a reasonably good piezoelectric coupling coefficient and a low Q. Pulse-echo amplitude and bandwidth of air backed composite transducers operating with water load in the low megahertz frequency range determined by the tone-burst pulse-echo method [22] were used as additional parameters.

Among all the different composites, only those with PZT rods embedded in Spurr's epoxy* matrix with regular periodicity (1-3 connectivity) appeared to be very promising for the ultrasonic transducer application [21]. The thickness coupling coefficient for these composites was determined to be about 60-70%. This value compares favorably with the thickness coupling coefficient

*Polysciences, Warrington, PA.

of 49% for PZT-5 disc used in commercial transducers. Mechanical Q of the composites was low (3-10) compared to that of PZT-5 (80). The pulse-echo amplitude of these composite transducers was large (2-3 V to 10 V input signal) and comparable to ^{those} of commercially available transducers. 1-3 composites had additional advantages. There are many variables including PZT rod diameter, volume percent of the PZT and polymer phases, which can be varied relatively easily to optimize the properties for particular application. The continuous poling technique [23] can be used to polarize long PZT rods, which can then be arranged in a polymer matrix in such a way to obtain a desired radiation pattern. Since the composite structure resembles a transducer array, the knowledge of the high frequency dynamic behavior of these composites might be helpful in resolving some of the problems encountered in array applications, such as minimizing the acoustic cross talk between the adjacent elements. Because of the above advantages, 1-3 composites were chosen for an extensive investigation aimed at high frequency transducer applications.

A detailed procedure for fabricating composites with 1-3 connectivity has been reported by Klicker and co-workers [3]. In brief PZT-501A* rods were extruded using an organic binder and then fired at 1285°C for one-half hour. Fired rods were aligned using an array of appropriately spaced holes drilled in a pair of brass discs bolted parallel to each other. The array of PZT rods was then cast in Spurr's epoxy matrix. The composite so formed was cut perpendicular to the length of the rod and lapped to the required thickness. The composite was then electroded with silver paint on the major surfaces and poled conventionally by applying an electric field of 20 kV/cm for five minutes in a heated oil bath at 80°C. Different composites were prepared with

*Ultrasonic Powders, Inc., South Plainfield, NJ.

approximately 5, 10, 20, and 30 volume percent PZT using 0.45 mm rods, and with 10 and 20 volume percent PZT using 0.28 mm rods. Table 2 gives the periodicity (distance between the centers of neighboring PZT rods) of PZT rods in each of the above composites. The composite samples were shaped as circular discs of diameter 19 mm and varying thickness from 0.5 mm to 5 mm. A picture of typical composite samples is given in Figure 1.

Results on the average properties including density, piezoelectric d_{33} coefficient, and dielectric permittivity of PZT rod-polymer composites have been reported earlier by Klicker et al. [3]. Data for the composite samples used in the present work are listed in Table 2 along with the properties of single phase PZT-501A for comparison.

IV. Bulk Mechanical Properties of Spurr's Epoxy

Spurr's epoxy is the piezoelectrically inactive phase in the composite material considered here. However, its function in the composite transducer is quite critical. When the composite is used as an ultrasonic transmitter, the epoxy has to effectively couple the ultrasonic energy from a high acoustic impedance PZT to a low acoustic impedance load. Similarly in the receiving mode, the ultrasonic energy incident on the composite should be transferred effectively to the piezoelectrically active PZT. The important parameters of the polymer which influence the performance of the composite as an ultrasonic transducer are its acoustic impedance, longitudinal and shear wave velocities and attenuation coefficients and their dependence on frequency. These properties of the polymer determine the interaction among the neighboring PZT rods, and hence the high frequency dynamic behavior of the composite. Measurement techniques used to determine these parameters in Spurr's epoxy are described elsewhere [24]. Only the results which are useful for analysis of the vibration behavior of the composites are presented here.

The longitudinal and transverse wave velocities in Spurr's epoxy were determined to be 2060 m/sec and 1150 m/sec, respectively. The acoustic impedance of the Spurr's epoxy was calculated to be 2.27×10^6 kg/m²-sec. The attenuation of the transverse wave in Spurr's epoxy was measured to be 6 dB/cm at 0.5 MHz. The attenuation coefficient was found to increase with the square of the frequency. The glass transition temperature T_g is another characteristic parameter for polymeric material. The glass transition temperature is defined as the temperature below which the material behaves like a glass and above which the material is rubberlike and soft [25]. In the present work, T_g and its dependence on frequency was determined by measuring dielectric loss tangent of Spurr's epoxy as a function of temperature and frequency. At the glass transition temperature, the loss tangent goes through a peak and can be easily identified. For Spurr's epoxy, T_g was found to be a function of frequency varying from 70°C at 100 Hz to 121°C at 1 MHz with a shift of 12-15°C per decade of frequency.

V. Resonance Modes

Resonance modes in composite materials, as in single phase materials, are defined by the geometry and dimension of the specimen. In a circularly shaped 1-3 composite material, the resonance modes observed are the planar mode, the thickness mode, and a number of lateral modes related to the regular periodicity of the PZT rods in the composite. Characterization of the different resonance modes in 1-3 PZT rod-polymer composite will be described in the following subsections. Knowledge of the resonant vibration behavior of the composites in air is important and helpful in the evaluation of the composites as an ultrasonic transducer operating into water equivalent load.

a. Planar Mode Resonance

The planar (also called radial) mode vibration in thin disc, as illustrated in Figure 2a, involves simultaneous mechanical motion in the 1 and 2 directions driven by the electric field in the 3 direction (poling direction). Since the diameter was the largest dimension (19 mm) in all the composite samples, the planar mode was the lowest frequency resonance mode.

The IRE Standard on piezoelectric measurements [26] was used to determine the electromechanical coefficients and elastic constants. The most important parameters for calculating these constants are the series and parallel resonance frequencies f_s and f_p , the geometric capacitance C_0 , and the impedance minimum $|Z_m|$ at resonance. A spectrum analyzer (HP 3585A) which provides a circuit similar to the transmission network recommended by the IRE Standard was used in measuring frequencies f_m and f_n corresponding to minimum and maximum impedance. In the presence of high mechanical losses, f_m and f_n are quite different from f_s and f_p . The IRE Standard recommends the following approximation to calculate $\Delta f = f_p - f_s$ from the measured value of f_m and f_n [26]

$$\Delta f = (f_p - f_s) \sim \frac{f_n - f_m}{\left(1 + \frac{4}{M^2}\right)^{1/2}} \quad (1)$$

where the figure of merit M is given by

$$M = \frac{1}{2\pi f_s R_1 C_0} = \frac{1}{2\pi f_m (C_0 + C_1) |Z_m|} \quad (2)$$

where C_0 , C_1 are the capacitance of the parallel and series branch and R_1 the resistance of the series branch of the equivalent circuit of the piezoelectric material near resonance. The sum $(C_0 + C_1)$ is the static capacitance which was

measured at a frequency well below fundamental resonance, for instance at 1 KHz. These approximations are valid for resonances with $M > 3$.

The planar coupling coefficient k_p was calculated from the expression given by [27]

$$k_p^2 = \frac{\Delta f}{f_s} \left[\frac{R_1^2 - (1 - \sigma^2)}{1 + \sigma} \right] \quad (3)$$

where σ is the Poisson's ratio of the material. Since the Poisson's ratio of both PZT and epoxy are approximately 0.3, the Poisson's ratio of the composite was assumed to be 0.3. The value of $R_1 = 2.05$ for $\sigma = 0.3$. f_s was approximated to f_m .

The mechanical quality factor Q can be evaluated from the relation [26]

$$\frac{1}{Q} = 2\pi f_s |Z_m| (C_0 + C_1) \left(\frac{f_p^2 - f_s^2}{f_p^2} \right) \quad (4)$$

For $M > 3$, the above expression was simplified to

$$\frac{1}{Q} \approx 4\pi \Delta f |Z_m| (C_0 + C_1) \quad (5)$$

The calculated values of k_p and Q from Equations (3) and (5) for several composites are summarized in Table 3. The frequency constant N_p for the planar mode (product of resonance frequency and the diameter) is also listed in the table. The data are divided into two groups depending on the thickness of the sample. The first group investigated consisted of thin samples with a thickness of about 0.6 mm. The second group comprised of all samples thicker than 3 mm and were classified as thick samples. The properties remained virtually constant in the two extreme limits. The data listed in the table are an average of the measurements of at least five samples.

As it emerges from Table 3, the figure of merit M for the radial mode resonance of all the composites was between 1 and 2. As mentioned before, Equations (3) and (5) used for calculating k_p and Q are not fully valid for values of $M < 3$. Subsequently, the values of k_p and Q listed in Table 3 are far from being exact. However, since the value of M is approximately the same for all the samples, the uncertainty in assessing k_p and Q is of the same order. Hence the results can be used for a relative comparison of samples having different volume fraction PZT.

Table 3 indicates that the planar coupling coefficient k_p of the composites increases with increase in the volume fraction of PZT. Thick composites have a higher k_p compared to thin composites of the same volume fraction. Lower values of k_p in thin samples indicate that the mechanical energy is not efficiently coupled from the PZT rods to the polymer and from the polymer back to the PZT rods. The coupling becomes more efficient for thicker samples indicating a greater homogeneity. A similar explanation can be given for the difference in the frequency constant between the thick and thin samples.

In the last column of Table 3, the longitudinal velocity C_t perpendicular to the length of the rod is listed. The value of C_t was calculated using the relation [27]

$$f_s = \frac{2.05}{2\pi a} [(E_t/\rho(1-\sigma^2))]^{1/2} \quad (6)$$

where f_s is the series resonance frequency of the planar resonance. E_t is the elastic modulus of the composite perpendicular to the PZT rod axis, ρ is the density, and a is the radius. In the above expression, $(E_t/\rho)^{1/2}$ corresponds to the longitudinal velocity C_t perpendicular to the rod axis. In calculating

C_t from Equation (6), f_s was measured and σ was assumed to be 0.3 as already mentioned.

An attempt was made to theoretically estimate the longitudinal velocity C_t by obtaining an expression for the elastic modulus E_t perpendicular to the rod axis as a function of volume fraction of PZT. Knowing E_t and the density $\bar{\rho}$ of the composite (Table 2), C_t was calculated from the expression $C_t = (E_t/\bar{\rho})^{1/2}$.

The effective modulus E_t in the transverse direction can be calculated by the Reuss constant stress model [14] which assumes that the two phases experience equal stress. This assumption seems appropriate for a combination of hard filler in a soft matrix, because the matrix should deform more than the filler and the stress in such a solid should be fairly constant. The effective modulus by the Reuss model is given by

$$\frac{1}{E_t} = \frac{v_1}{E_1} + \frac{v_2}{E_2} \quad (7)$$

where v_1 and v_2 are the volume fractions and E_1 and E_2 are the elastic moduli of the two phases. Elastic modulus for the PZT phase perpendicular to the length of the rod is given by $E = C_{11}^E = 12.1 \times 10^{10} \text{ N/m}^2$ (elastic stiffness under constant electric field) [28]. Elastic modulus of epoxy was calculated from the longitudinal velocity (2060 m/sec) and density (1.1 gm/cc) to be $4.7 \times 10^9 \text{ N/m}^2$. The experimental and calculated values of C_t are plotted in Figure 3.

As it can be seen from Figure 3, there is a large discrepancy between the experimental and the measured velocities at low volume percent PZT. At high volume fractions, the measured velocity approaches the calculated value. However, a good agreement was observed between the theoretical and experimental value of C_t in composites of steel filament in an epoxy matrix of

similar structure as the PZT rod-polymer composites [29]. The above explained discrepancy in the present work is probably because of the velocity calculations using Equation 6. Equation 6 was derived for a single phase ceramic material and is probably not completely valid for the composite materials considered here.

The figure of merit M for radial mode resonance of the composite samples was less than two [Table 3]; hence, the approximations suggested by the IRE Standard are not applicable. Therefore, the exact coefficients were determined by using the vector impedance method [30]. An LCR bridge (HP 4192A) was interfaced with a computer (HP 9825A) to measure the complex impedance as a function of frequency around the resonance frequency of the sample. A computer program was designed to measure the impedance at very small frequency intervals (~ 10 Hz) of frequency close to the series and parallel resonance frequencies for the exact determination of these two frequencies.

The results of the above experiment for selected samples with 20% PZT of thicknesses varying from 0.6 mm to 5.15 mm are given in Table 4 and are compared with the results from the IRE Standard method. A comparison of k_p and Q determined by the two methods shows clearly the limitations of the IRE method for resonances with low M . From the vector impedance method, it is observed that k_p is large for thick samples and decreases gradually as the sample thickness is reduced. Q increases as the thickness decreases, approaching the Q of single phase PZT-501A (80) [28].

The planar mode resonance was studied as a function of temperature up to 100°C . It was observed that the planar coupling coefficient remained virtually constant with increase in temperature. However, the amplitude of the resonance spectrum decreased gradually with temperature and was suppressed below 0.1 dB at 100°C . Measurements could not be made on the radial mode

resonance above 100°C. It is interesting to note that this temperature corresponds to the glass transition temperature of Spurr's epoxy (Section IV) at the resonance frequency f_r (50 KHz). It is conceivable that the suppression of the radial mode above 100°C is due to the very lossy nature of the Spurr's epoxy around the glass transition temperature.

Figure 4 shows a plot of frequency constant of the radial mode resonance as a function of temperature up to 100°C. Since the elastic stiffness is directly proportional to the square of the frequency constant (Equation 6), the plot is a measure of softening of the epoxy at higher temperatures. A reduction of 40% seen in the frequency constant from 0 to 100° corresponds to softening of the epoxy by about 65%.

Thus, in general, the planar coupling coefficient of the composites increased with the volume percent PZT. For a given volume percent, thick samples had higher coupling coefficients than thin samples (28% and 13% respectively for 20 percent PZT composite). The planar mode resonance was defined mainly by the elastic modulus of the Spurr's epoxy modified to some extent by the mass loading of PZT rods.

b. Thickness Mode Resonance

The thickness mode resonance of the composite samples (Figure 2b) is of greatest importance in this study as it is utilized for transmitting and receiving longitudinal ultrasonic waves. In this mode, PZT rods vibrate in the fundamental length longitudinal 33 mode and the unclamped piezoelectric coupling coefficient k_{33} is applicable for this mode [28]. But if the PZT rods are considered as being an integral part of the composite, this mode corresponds rather to the laterally clamped thickness mode with coupling coefficient k_t . The planar mode resonance, discussed in the preceding sections, occurs at a considerably lower frequency and is the fundamental

resonance mode. Since the composite is treated as a monolithic transducer material, the resonance of the composite corresponding to the 33 mode of the PZT rods will be referred to as thickness mode resonance.

The thickness mode coupling coefficient k_t , mechanical quality factor Q , and the frequency constant N_t^D (at constant D) were evaluated from the following equations [26]

$$k_t^2 = \frac{\pi}{2} \frac{f_s}{f_p} \tan \left(\frac{\pi}{2} \frac{\Delta f}{f_p} \right) \quad (8)$$

$$Q = 4\pi\Delta f |Z_m| (C_0 + C_1) \quad (9)$$

and

$$N_t^D = f_p t \quad (10)$$

where t is the thickness and meaning of the other terms in the above equation are described in Section Va. The IRE Standard method was used to calculate these properties of the composite corresponding to the thickness mode resonance.

The experimental results are summarized in Table 5. The data are again divided into two groups: thin samples with thickness around 0.6 mm and thick samples with thickness above 3 mm. As it can be seen in the table, with the exception of the 5% PZT composites, the figure of merit M for the thickness mode resonance of all other samples was above three. Hence, the approximations recommended by the IRE Standard to calculate k_t and Q are valid. Indeed the values of the k_t and Q determined by the vector impedance method on a selected number of samples were within 2% of the values calculated by the IRE Standard method.

Data listed in Table 5 indicate that for the thickness mode resonance of thin samples ($t \approx 0.6$ mm), k_t was 60-70% and Q was 3 to 10. For thick samples

($t > 3$ mm), k_t was approximately 50% and Q was 20 to 30. In general, thin composites had higher coupling coefficient k_t and frequency constant N_t^D compared to thick samples while the mechanical Q showed the reverse trend. The coupling coefficient and the frequency constant of thin samples were close to that of single phase PZT-501A ($k_{33} = 70\%$ and $N_t^D = 3700$ Hzm for PZT 501A) and were independent of the volume percent of PZT. In thick samples, both k_t and N_t^D were proportional to the volume percent of PZT.

The observed behavior of the composites in the thickness mode resonance can be explained as follows. At the resonance frequency, PZT rods vibrate with a large amplitude. The vibrating rods act as a source of complex transverse waves in the epoxy propagating in a direction perpendicular to the axis of PZT rods. These transverse waves generated in the epoxy interact with the array of PZT rods. In the first approximation the interaction is assumed to involve only nearest neighbors. Effectiveness of the interaction depends on the amplitude and phase of the transverse wave relative to that of the PZT rods. For thin samples resonating around 2.25 MHz, the wavelength of the transverse wave is approximately 0.5 mm (taking the transverse wave velocity to be 1150 m/sec from Section IV). It is also known that the Spurr's epoxy is extremely lossy for transverse waves at this frequency. This results in only a weak interaction between the vibration of neighboring PZT rods. The relatively low Q of thin samples indicates that the rod vibrations are partly damped by the surrounding polymer.

The thick sample resonate around 0.5 MHz and the wavelength of transverse waves in the epoxy is approximately 2.3 mm. The wavelength is 1.5 to 3 times larger than the separation distance between the PZT rods in the composites of different volume percent PZT. Since the attenuation of the transverse waves in the epoxy is relatively low at 0.5 MHz (~ 6 dB/cm), the amplitude of the

transverse wave must be significant to cause a strong interaction between the rods through the epoxy medium. The low coupling coefficient in thick samples is probably a result of the phase cancellation effect between the vibrating rods (due to the electrical excitation) and the mechanical interaction between the rods through the epoxy. The low mechanical loss in the epoxy is reflected in the high Q of the composite.

The longitudinal velocity C_ℓ along the length of the rod can be theoretically estimated by calculating the elastic modulus E_ℓ of the composite parallel to the PZT rods. At frequencies where the transverse wavelength is much larger than the separation distance between the rods, the Voigt constant strain model [14] can be applied. The composite modulus using the Voigt average is written as

$$E_\ell = v_1 E_1 + v_2 E_2 \quad (11)$$

where E_1 and E_2 are the moduli and v_1 and v_2 are the volume fractions of the two phases (PZT and epoxy). For PZT rods with diameter small compared to length, the modulus along the length is given by $E = 1/S_{33}^D = 10.5 \times 10^{10} \text{ N/m}^2$ (the Young's modulus of the rod at constant electric displacement). The longitudinal velocity C_ℓ was calculated from the relation $C_\ell = (E_\ell/\bar{\rho})^{1/2}$.

The experimentally determined longitudinal velocity C_ℓ expressed as twice the frequency constant N_t^D , is given in the last column of Table 5. This velocity is compared with the calculated values in Figure 5. The excellent agreement between the experimental and theoretical values further supports the equal strain model for calculating the effective modulus of the composite along the rod axis.

c. Lateral Mode Resonances

In addition to the radial mode and thickness mode resonances and their overtones, other resonances were observed in the frequency range 0 to 2 MHz. The frequencies of these resonances were independent of sample thickness, but were related to the lateral periodicity of the PZT rods in the composite. Absolute value of electrical admittance was measured on samples as a function of frequency in the ambience of air and water using a spectrum analyzer (HP 3585A). Here samples of different thickness and volume fraction were examined to identify the different resonances observed in the 0 to 2 MHz frequency range. The three major resonances of interest are designated as f_{ℓ} , f_{t1} , and f_{t2} as categorized in Table 6.

The resonance corresponding to f_{ℓ} was inversely proportional to the thickness of the sample. This resonance was heavily damped when the resonator was immersed in water. Such behavior suggests that resonance at f_{ℓ} is the longitudinal thickness vibration. The longitudinal velocity of sound, calculated using the formula $C_{\ell} = 2tf_{\ell}$ agrees very well with the theoretically estimated value for the composites of different volume fractions, as discussed in detail in the previous section.

The resonances at f_{t1} and f_{t2} were very similar in nature. For a certain volume fraction, these resonances always occurred at specified frequencies regardless of the thickness of the sample. As can be seen in Table 6, increase in the volume fraction results in closer spacings of rods (reduction of the unit cell) and the resonances f_{t1} and f_{t2} move to higher frequencies.

The behavior of the composites could be explained by simple averaging schemes such as the constant strain model and the constant stress model for wavelengths large or small compared to the lattice periodicity (section Va and Vb). In the vicinity of the resonances of f_{t1} and f_{t2} , the wavelength of the transverse shear wave is comparable to the unit cell dimensions of the array

and the analysis is more complicated. A Brillouin theory of elastic wave propagation in a two dimensionally periodic lattice corresponding to the PZT rod-polymer composite was developed by Auld et al. [31]. For laterally propagating shear waves with polarization along the rods, the lowest stopband frequencies were calculated. The existence of stopbands was related to Bragg scattering from planes of rods having various orientations in the square lattice. The essential phenomena can be explained by reference to Figure 6. Suppose in Figure 6a that a z-polarized, x-propagating shear wave is incident on the grating. At a frequency for which the rod spacing d is one-half the shear wavelength (λ_s), constructive reflection (Bragg scattering) occurs from vertical planes of rods, and resonance occurs between adjacent vertical planes. The x-propagating wave is also scattered from planes of rods at 45 degrees to the x and y axes; but in this case, Bragg conditions are not satisfied and resonance does not occur. A stopband exists at $d = \lambda_s/2$ for an x-propagating wave, but there is no resonant scattering into y-propagating waves. At the stopband edge, the solution is a standing wave along x. From the square symmetry of the lattice, a similar standing wave solution along y also exists. This behavior corresponds to the first stopband of the lattice.

When the rod spacing d is one shear wavelength, a completely different standing wave pattern results, as illustrated in Figure 6a. In this case a z-polarized, x-propagating wave is again Bragg scattered with a phase shift of 2π from one vertical plane of rods to an adjacent plane. However, it is easily verified that the wave is also Bragg scattered at the same frequency by the 45° planes of rods, so that resonant scattering of the x-propagating wave into a y-propagating wave occurs. These y-propagating waves also experience resonance scattering of the same type. As a result, the solution is a two dimensional resonant standing wave pattern as shown in Figure 6a. Here the

rods all vibrate in phase and correspond to the second stopband of the square lattice.

For a z-polarized, z-propagating wave incident on the lattice, no Bragg scattering can occur because the structure is uniform along z. However, a spatial modulation of the phase fronts is produced by the difference in the properties of the rods and matrix. Consequently, space harmonics are generated but none are resonant. Similar conclusions are obtained for z-propagating waves of other polarizations.

In the following section, detailed laser probe measurements of the actual displacement on the composite to analyze the nature of vibration at these frequencies are reported.

VI. Laser Probe Measurements

The measurements of actual displacement on the composite samples were performed using the laser heterodyne technique [31]. The samples were fine polished ($\pm 1 \mu\text{m}$) and electroded with highly reflecting gold electrodes for the laser probe measurements. Relative amplitude and phase of the ultrasonic displacement was measured along two scan paths: along a row of PZT rods and on the epoxy surface in between two adjacent rows of PZT rods as shown in Figure 6. Figure 7 gives electrical input impedance data taken on one of these samples (Sample #101 in Table 6) showing the existence of three strong resonances. Figures 8, 9, and 10 show laser scan plots of vibration amplitude and phase taken at frequencies f_{t1} , f_{t2} , and f_{λ} , respectively for this sample.

a. Vibration Pattern at Frequency f_{t1}

The plot in Figure 8 shows the complex vibration pattern at frequency f_{t1} corresponding to the second stopband along the unit cell, (Figure 6a), where the rods all vibrate in phase. (Vibrations at the first stopband discussed earlier have a 180° phase shift from one plane of the rods to the next and

cannot be excited electrically in a uniformly electroded sample.) Superposition of the x and y standing waves illustrated shows that the z-displacement has a positive maximum at a, negative maximum at b, and zero at c. Because of symmetry, these statements apply at all equivalent points in the lattice. In the scans of Figure 8, the maxima of the standing wave pattern at a and b are 180° out of phase, as predicted. The predicted zeros at c in Figure 8a and at the equivalent point in Figure 8b are less satisfactorily reproduced, possibly due to imperfections in the lattice and inaccuracy in alignment of the scan. The velocity of the transverse waves, $C_s = df_{t1}$ is tabulated in Table 6.

b. Vibration Pattern at Frequency f_{t2}

The plot in Figure 9 shows the complex vibration pattern at frequency f_{t2} corresponding to the stopband in Figure 6b. This is another of the higher stopbands for which the rods vibrate in phase and can be excited by uniform electrodes. At f_{t2} , standing transverse waves along the unit cell diagonals are superposed to give maximum displacements 180° out of phase at a and c, and maximum in phase displacements at a and b. These features are clearly observable in the scans of Figure 9, except that the maximum at a is smaller than that predicted from the assumed standing wave pattern. This is attributed to the presence of higher space harmonics such that the standing wave patterns are not simple sinusoids. It can also be seen from Figure 6b that the displacement at point d, midway between a and b, is predicted to be zero; and this has been verified experimentally. The velocity C_s of transverse waves, as tabulated in the last two columns of Table 6 is lower than the measured velocity of 1150 m/sec (Section V). This is possibly due to the mass loading by the PZT rods.

c. Vibration Pattern at Frequency f_2

Figure 10 shows plots of complex vibration pattern at the frequency f_2 , which corresponds to the simple longitudinal thickness resonance of the homogeneous plate along z. It was noted earlier that no resonant space harmonic exist in this case, so that weaker standing wave patterns are to be expected in the xy plane. This is clearly visible in the figure. The small phase variations are attributed to the damping in the composite which was not considered in the theory outlined above [31].

As is clearly seen in Figure 10, the amplitude of vibration on the epoxy at f_2 is about 5 to 8 dB larger than on the PZT rods indicating an effective coupling of the ultrasonic energy from PZT to epoxy. The PZT rods vibrating due to electrical excitation act as the source of transverse waves in the epoxy travelling in a direction perpendicular to the axis of the PZT rods. The transverse waves produced interact with neighboring rods to produce the resultant vibration pattern. The vibration pattern depends very much on the wavelength of the transverse waves in relation to the periodicity of the lattice. As the wavelength of the transverse waves becomes larger compared to the lattice periodicity, ultrasonic displacement on the composite is expected to be more uniform.

Figures 10, 11, and 12 compare the ultrasonic displacements on the surface of composites 101, 102, and 103 (Cf., Table 6) resonating in the longitudinal thickness vibration at frequencies 620, 414 and 270 KHz, respectively. All the samples have 10 volume percent PZT with a periodicity of the lattice equal to 1.27 mm. The only variable in the samples are the wavelengths transverse wave at the thickness resonance frequency, which are respectively 1.9, 2.7 and 4.3 mm for the above three samples (calculated using the transverse wave velocity in Spurr's epoxy of 1150 m/sec). The difference in amplitude of vibration between the PZT and epoxy observed in sample 101 is

greatly reduced in sample 102. This is directly attributed to the longer wavelength of transverse waves in sample 102. For sample 103, the transverse wavelength is more than three times the periodicity and there is no noticeable difference in amplitude between the PZT and epoxy. The composite vibrates uniformly across the surface with almost equal strain on the PZT and epoxy. Small phase variations seen across sample 101 are not measurable for sample 103. This is probably because of the reduced attenuation in the epoxy at lower frequencies (Section IV). The vibration pattern observed in sample 103 is in accordance with the assumption in Section Vb of the constant strain model used to calculate the effective modulus along the fiber axis, when transverse wavelengths are large compared to periodicity. This uniform ultrasonic displacement observed on the surface of the composite is a clear indication of efficient coupling of the mechanical energy from PZT to the epoxy. Since the acoustic impedance of the epoxy is relatively close to that of the human body, an effective coupling of acoustic energy from the composite transducer to the human body is ensured.

VII. Effect of Temperature on the Resonance Modes

In this section, the effect of temperature on the electromechanical properties of the composite is discussed. It is clear from the preceding sections that the high frequency dynamic behavior of 1-3 composite is strongly dependent on the mechanical properties such as the velocity and attenuation of ultrasonic waves in the Spurrs epoxy. These properties of Spurrs epoxy are very sensitive to temperature. The Spurrs epoxy is glassy at room temperature and goes through the glass transition temperature to a rubber like material in a temperature interval of only about 100°C. In the glassy state, it was also shown (Section Va) that the compliance of the epoxy increased by approximately 65% in the temperature range of 0 to 100°C. Thus, a study of the temperature

dependence of the resonance modes will help in understanding the electromechanical properties of composites with different polymer matrices, having a wide range of elastic properties.

In the experiment, the resonance behavior of composites freely suspended in air was studied as a function of temperature from 0 to 150°C. Thickness mode coupling coefficient k_t , mechanical Q and the frequency constant N_t^D of the composite were determined at 2°C intervals both in heating and cooling cycles. The heating and cooling rates were maintained at approximately 2°C minute.

Figure 13 shows plots of absolute value of admittance as a function of frequency from 0.1 to 1.1 MHz for sample 103 (10% PZT composite with 0.45 mm rods, thickness 5.15 mm) at different temperatures up to 170°C. The behavior is typical of all thick (thickness > 3 mm) composites. According to the analyses given in the previous section, the three major resonances observed at room temperature (Figure 13a) were identified as follows.

1. Resonance at 0.262 MHz was identified as a half wave resonance along the thickness of the composite and is denoted by f_ℓ .

2. Resonance at 0.644 MHz was identified as the standing wave pattern in the epoxy arising from lateral periodicity of the PZT rods. This resonance is denoted by f_{t1} .

3. Resonance at 1.030 MHz was identified as the third overtone of the thickness mode.

Weak secondary resonances below the thickness mode resonance frequency were ascribed to the overtones of the planar mode resonance of the composite disc.

The effect of temperature on the above resonance modes (Figure 13) is explained below. As the temperature was increased from 25°C, the epoxy is

expected to mechanically soften at a faster rate than PZT. Therefore, the resonance frequency f_{t1} , which is mainly determined by the elastic modulus of the polymer, decreased at a faster rate than the resonance frequency f_{ℓ} which is defined by the composite modulus E_{ℓ} . As seen in Figures 13 b to d, at higher temperatures f_{t1} gradually approaches f_{ℓ} and finally merges with f_{ℓ} at approximately 110°C. In the temperature range from 10 to 130°C, the two modes interfere with each other. At temperatures above 130°C, f_{t1} passes through f_{ℓ} and eventually disappears at a temperature around 135°C. This disappearance can be attributed to the fact that above the glass-transition temperature the epoxy is less viscous and cannot support a standing wave pattern of the transverse wave (glass transition temperature of Spurr's epoxy is around 110°C at 200 KHz, from Section IV). It is worthwhile to note that above 130°C, the amplitude of thickness mode was increased (Figure 13 e to h). The secondary low frequency resonances clearly seen at 25°C disappear at approximately 100°C. This disappearance is again ascribed to the lossy nature of the epoxy around the glass transition temperature.

The coupling coefficient k_t and Q of the thickness mode resonance for sample 130 are plotted as a function of temperature in Figures 14 and 15, respectively. The value of k_t (0.48) determined at room temperature (25°C) did not change substantially up to approximately 110°C. In the temperature range from 100 to 130°C, k_t exhibited a minimum. Above 130°C, after the transverse mode had disappeared, k_t increased significantly to about 60%. As shown in Figure 15, the mechanical Q at 25°C was about 20. The Q remained constant to approximately 100°C and decreased to a value of 5 at temperatures above 130°C.

The observed coupling coefficient k_t and Q in a thick sample at room temperature were attributed to the strong mechanical interaction among PZT rods through the epoxy matrix. At temperatures above the glass transition

temperature $T_g \approx 110^\circ\text{C}$), the epoxy is rubber like and soft. As a result, the mechanical interaction among PZT rods becomes weaker as also indicated by an increase in the amplitude of the resonance spectrum (Figure 13 e-h). In effect, k_t of the composite approaches k_{33} of a freely suspended PZT rod (70%) and Q decreases because of the damping provided by the lossy polymer. It may be recalled here that for a thin (thickness ≈ 0.6 mm) composite sample, k_t was 60-70% and Q was 3-10 (Table 5). These values are very close to those measured for thick composites above the temperature T_g . It appears that the nature of vibration of a thick composite above T_g resembles that of a thin composite at room temperature.

In thin samples, since the coupling among the PZT rods is very weak at room temperature, the increase of temperature above T_g is unlikely to affect the resonance behavior. This seems to be confirmed by the plot of k_t versus temperature for a typical thin composite sample with thickness mode frequency at 2.25 MHz (Figure 16). No significant variation of k_t was seen over the entire temperature range of 0 to 150°C . Thus, the temperature dependence of the electromechanical properties of composites further supports the proposed model describing the nature of vibration for different resonance modes of 1-3 composites.

VIII. Conclusions

The resonance modes in circular shaped 1-3 PZT rod-polymer composites were fully characterized. In general, the planar coupling coefficient increased with increase in volume percent PZT. For a given volume percent PZT, thick samples had better planar coupling coefficient than the thin samples.

For thickness mode resonance of thin samples, $k_t = 60-70\%$ and $Q = 3-10$. For thick samples, $k_t = 50\%$ and $Q = 20-30$. The difference in the observed

behavior was explained by considering the strength of the interaction among the PZT rods through the epoxy. At the thickness mode resonance, the coupling of acoustic energy from PZT to epoxy was found to be most efficient, when the transverse wavelength in epoxy at the resonance frequency was much larger than the periodicity of the lattice. When this condition is satisfied, the composite vibrates like a homogeneous body and it will be shown in the following paper [part II] that the composite materials exhibit excellent sensitivity operating into water load. From the effect of temperature on resonance behavior, it is clear that the interaction among the PZT rods through the epoxy matrix can either be enhanced or suppressed depending upon the properties of the polymer phase. Composites with low transverse coupling could be utilized for linear and phased array systems.

In addition to the above two modes of resonances, additional modes were observed because of the regular lateral periodicity in the structure. The results showed that these resonances arose from the superposition of the standing wave pattern of the transverse waves in the epoxy. The experimental results were in excellent agreement with the theory of wave propagation in two dimensionally periodic solids.

Acknowledgements

The authors are grateful to Dr. W.A. Smith and Dr. A. Shaulov of North American Philips Laboratories and Dr. P.A. Levin of Drexel University (Dept. of Electrical and Computer Engineering and Biomedical Engineering and Science Institute) for their comments and discussions, Mrs. Linda Webster for preparing samples, and Mr. P. Moses for writing software for computer interfacing. Financial support was provided by the North American Philips Laboratories.

REFERENCES

1. Newnham, R.E., D.P. Skinner, and L.E. Cross, 'Connectivity and Piezoelectric-Pyroelectric Composites,' *Mat. Res. Bull.* 13, 525-536 (1978).
2. Skinner, D.P., R.E. Newnham, and L.E. Cross, 'Flexible Composite Transducers,' *Mat. Res. Bull.* 13, 599-607 (1978).
3. Klicker, K.A., J.V. Biggers, and R.E. Newnham, 'Composites of PZT and Epoxy for Hydrostatic Transducer Applications,' *J. Amer. Ceram. Soc.* 64, 5-8 (1981).
4. Klicker, K.A., W.A. Schulze, and J.V. Biggers, 'Piezoelectric Composites with 3-1 Connectivity and a Foamed Polyurethane Matrix,' *J. Amer. Ceram. Soc.* 65, C208-C210 (1982).
5. Newnham, R.E., L.J. Bowen, K.A. Klicker, and L.E. Cross, 'Composite Piezoelectric Transducers,' *Materials in Engineering* 2, 93-106 (1980).
6. Rittenmyer, K., T.R. ShROUT, W.A. Schulze, and R.E. Newnham, 'Piezoelectric 3-3 Composites,' *Ferroelectrics* 41, 189-195 (1982).
7. Safari, A., R.E. Newnham, L.E. Cross, and W.A. Schulze, 'Perforated PZT-Polymer Composites for Piezoelectric Transducer Applications,' *Ferroelectrics* 41, 197-205 (1982).
8. Banno, H. and S. Saito, 'Piezoelectric Properties of Composites of Synthetic Rubber and $PbTiO_3$ and PZT,' *US-Japan Study Seminar on Dielectric and Piezoelectric Ceramics*, M-4 (1982).
9. Wells, P.N.T. 'Biomedical Ultrasonics,' Academic Press, London (1977).
10. Kosoff, G., 'The Effects of Backings and Matchings on the Performance of Piezoelectric Ceramic Transducers,' *IEEE Trans. on Sonics and Ultrasonics*, SU-13, 20-30 (1966).

11. Goll, J.H. and B.A. Auld, 'Multilayer Impedance Matching Schemes for Broadbanding of Water Loaded Piezoelectric Transducers and High Q Electrical Resonators,' IEEE Trans. Sonics and Ultrasonics, SU-22, 52-53 (1975).
12. Desilets, C.S., J.D. Fraser, and G.S. Kino, 'The Design of Efficient Broadband Piezoelectric Transducers,' IEEE Trans. on Sonics and Ultrasonics, SU-25, 115-125 (1978).
13. Soquet, J., P. Defranould, and J. Desbois, 'Design of Low-Loss Wide-Band Ultrasonic Transducers for Noninvasive Medical Application,' IEEE Trans. Son. Ultrason., SU-26, 75-81 (1979).
14. Lees, S. and C.L. Davidson, 'Ultrasonic Measurement of Some Mineral Filled Plastics,' IEEE Trans. on Sonics and Ultrasonics, SU-24, 222-225 (1977).
15. Goll, J.H., 'The Design of Broad-Band Fluid-Loaded Ultrasonic Transducers,' IEEE Trans. on Sonics and Ultrasonics, SU-26, 385-393 (1979).
16. Sessler, G.M., 'Piezoelectricity in Polyvinylidene Fluoride,' J. Acoust. Soc. Amer. 70, 1596-1608 (1981).
17. Callerame, J., R.H. Tancrell, and W.T. Wilson, 'Transmitter and Receiver for Medical Ultrasonics,' IEEE Ultrasonic Symposium Proceedings, 407-411 (1979).
18. Hunt, J.W., M. Arditi, and F.S. Foster, 'Ultrasound Transducers for Pulse-Echo Medical Imaging,' IEEE Trans. on Biomedical Engineering, BME-30, 453-481 (1983).
19. McGrath, J.C., L. Holt, D.M. Jones, and I.M. Ward, 'Recent Measurements on Improved Thick Film Piezoelectric PVDF Polymer Materials for Hydrophone Applications,' Ferroelectrics 50, 13-20 (1983).

20. Lynn, S.Y., R.E. Newnham, K.A. Klicker, K. Rittenmyer, A. Safari, and W.A. Schulze, 'Ferroelectric Composites for Hydrophones,' *Ferroelectrics* 38, 955-958 (1981).
21. Gururaja, T.R., W.A. Schulze, T.R. Shrout, A. Safari, L. Webster, and L.E. Cross, 'High Frequency Applications of PZT/Polymer Composite Materials,' *Ferroelectrics* 39, 1245-1248 (1981).
22. Erikson, K.R. 'Tone-Burst Testing of Pulse-Echo Transducer,' *IEEE Trans. Sonics and Ultrasonics*, SU-26, 7-14 (1979).
23. Gururaja, T.R., D. Christopher, R.E. Newnham, and W.A. Schulze, 'Continuous Poling of PZT Fibers and Ribbons and its Application to New Devices,' *Ferroelectrics* 47, 193-200 (1983).
24. Gururaja, T.R., W.A. Schulze, and L.E. Cross, 'Bulk Mechanical Properties of the Spurr's Epoxy and Eccogel Polymers,' (to be published in *J. Polymer Sci.*).
25. Ferry, J.D., 'Viscoelastic Properties of Polymers,' Wiley, NY (1980).
26. IRE Standards on Piezoelectric Crystals: Measurements of Piezoelectric Ceramics, 1961,' *Proc. IRE*, 49, 1161-1169 (1961).
27. Mason, W.P. 'Electrostrictive Effect in Barium Titanate Ceramics,' *Physical Review* 74, 1134-1147 (1948).
28. Berlincourt, D.A., D.R. Curran, and H. Jaffe, 'Piezoelectric and Piezomagnetic Materials and Their Function in Transducers,' *Physical Acoustics*, Vol. 1, Part A, Chap. 3, Ed. by W.P. Mason, Academic Press, Ny (1964).
29. Ross, C.A., 'Stress Wave Propagation in Composite Materials,' *Dynamic Response of Composite Materials*, Fall Meeting of the Society for Experimental Stress Analysis, 1-19 (1980).

30. Holland, R. and E.P. EerNisse, 'Accurate Measurement of Coefficients in a Ferroelectric Ceramic,' IEEE Trans. on Sonics and Ultrasonics, SU-16, 173-181 (1969).
31. Auld, B.A., H.A. Kunkel, Y.A. Shui, and Y. Wang, 'Dynamic Behavior of Periodic Piezoelectric Composites,' Proc. 1983 IEEE Ultrasonics Symposium, 554-558 (1984).

FIGURE CAPTIONS

- Figure 1 Typical 3-1 composites with PZT rods embedded in Spurr's epoxy.
- Figure 2 Resonance modes in a disc-shaped piezoelectric material.
- Figure 3 Longitudinal velocity perpendicular to the PZT rod axis as a function of volume percent PZT in composites.
- Figure 4 Effect of temperature on the Frequency constant of radial mode resonance of 1-3 composites.
- Figure 5 Longitudinal velocity along the PZT rod axis as a function of volume percent PZT in composites.
- Figure 6 Unit cell geometries and laser scan paths. (a) Standing waves at the second stopband, along the unit cell edge. (b) Standing waves at the second stopband, along the unit cell diagonals.
- Figure 7 Measured electrical input impedance of composite transducer #101 (10% PZT in Spurr's epoxy, PZT rod diameters - 0.45 mm, period = 1.27 mm, thickness = 1.93 mm. Transducer diameter = 19.0 mm.
- Figure 8 Laser scan measurement of relative amplitude and phase of the acoustic vibration at $f_{t1} = 801.9$ KHz (sample #101). (a) Scan along rods. (b) Scan between rods.
- Figure 9 Laser scan measurements of relative amplitude and phase of the acoustic vibration at $f_{t2} = 801.9$ KHz (sample #101). (a) Scan along rods. (b) Scan between rods.
- Figure 10 Laser scan measurements of relative amplitude and phase of the acoustic vibration at $f_{\ell} = 620.7$ KHz (sample #101). (a) Scan along rods. (b) Scan between rods.
- Figure 11 Laser scan measurements of relative amplitude and phase of the acoustic vibration at $f_{\ell} = 414$ KHz of sample #102. (a) Scan along rods. (b) Scan between rods.

Figure 12 Laser scan measurements of relative amplitude and phase of the acoustic vibration at $f_2 = 270$ KHz of sample #103. (a) Scan on rods. (b) Scan in between rods.

Figure 13 Temperature dependence of various resonances in a composite samples (sample #103).

y-axis - frequency 0.1 to 1.1 MHz

y-axis - relative admittance (50 dB).

Figure 14 Typical effect of temperature on the thickness coupling coefficient of a thick composite sample (sample #103).

Figure 15 Typical effect of temperature on the Q of thick composite sample (sample #103).

Figure 16 Typical effect of temperature on the thickness coupling coefficient of a thin composite sample (sample #201).

Table 1. Dielectric and Piezoelectric Properties of PZT-Polymer Composites.

Description of Composite	Density (gm/cc)	Dielectric Constant, K	$g_h (10^{-3} \text{VmN}^{-1})$	$d_h (\text{pCN}^{-1})$	$d_h g_h (10^{-15} \text{m}^2 \text{N}^{-1})$	Reference
Single Phase PZT	7.6	1800	2.5	40	100	3
Coral Replamine, PZT Composite	3.3	50	140	36	5040	2
3-3 PZT-Spurrs Epoxy (BURPS)	4.5	620	20	110	2200	6
PZT-Silicone Rubber (BURPS)	4.0	450	45	180	8100	6
1-3 PZT Rods - Spurr's Epoxy	1.4	54	56	27	1536	3
PZT Rods - Polyurethane	1.4	40	56	20	1100	4
1-3-0 PZT Rods - Spurr's Epoxy + Glass Spheres	1.3	78	60	41	2460	20
PZT Rods - Foamed Polyurethane	0.9	41	210	73	14600	4
0-3 PbTiO_3 - Chloroprene Rubber	--	40	100	35	3500	8
Bi_2O_3 Modified PbTiO_3 - Chloroprene Rubber	--	40	28	10	280	8
3-1 Perforated 3-1 Composite	2.6	650	30	170	5100	7
3-2 Perforated 3-2 Composite	2.5	375	60	200	12000	7

Table 2. Physical, Dielectric, and Piezoelectric Properties of PZT Rod-Polymer Composites.

Volume % PZT	Rod Diameter (mm)	Periodicity d (mm)	Density ρ (gm/cc)	Dielectric Permittivity, ϵ	d_{33} Coefficient (pC/N)
5	0.45	1.78	1.41	79	155
10	0.45	1.26	1.64	109	194
20	0.45	0.90	2.29	238	320
30	0.45	0.73	3.08	380	375
10	0.28	0.78	1.62	94	183
20	0.28	0.55	2.36	217	339
Single Phases PZT	--	--	7.6	1400	400

Table 3. Electromechanical Properties of Composites from the Radial Mode Resonance.

Volume % PZT (rod diameter)	Thickness	M	k _p (%)	Q	N(Hz·m) (Frequency Constants)	C _t Longitudinal Velocity (m/sec)
5% (0.45 mm)	Thin (0.6mm)	0.97	17.0	40	1064	1483
	Thick (>3mm)	~1.4	21.7	36	1120	1561
10% (0.45 mm)	Thin	1.1	16.6	42	1011	1409
	Thick	1.5 to 2.0	23.0	34	1080	1506
20% (0.45 mm)	Thin	1.2	21.0	23	955	1331
	Thick	1.5 to 2.3	26.5	34	1043	1454
30% (0.45 mm)	Thin	1.1	20.0	32	950	1324
	Thick	2.0	26.7	36	1046	1458
10% (0.28 mm)	Thin	1.1	18.8	36	1032	1439
	Thick	1.5	23.1	35	1097	1529
20% (0.28 mm)	Thin	1.1	22.0	32	970	1352
	Thick	1.7	25.5	35	1057	1474

Table 4.

Comparison of IRE Standard Method and Vector Impedance Method for Calculating Electromechanical Coupling Coefficients.
(20% PZT composite, rod diameter = 0.45 mm)

Sample No.	Thickness in mm	IRE Standard Method					Vector Impedance Method		
		f_p^m (KHz)	M	$\Delta f \approx f_p^m - f_s$ (KHz)	k_p (%)	Q	$f_p - f_s$	k_p (%)	Q
200	0.66	2.320	1.0	1.041	22.6	24	0.350	12.9	72
201	2.54	1.820	1.7	1.168	22.8	39	0.929	20.3	48
202	3.05	1.998	1.9	1.364	24.7	37	1.184	22.9	43
203	3.95	2.225	2.0	1.585	26.4	35	1.480	25.6	39
204	4.60	2.386	2.2	1.760	27.8	35	1.717	27.7	37
205	5.15	2.842	2.4	2.172	30.8	30	1.792	27.8	37

Table 5.

Thickness Mode Resonance in Composites.

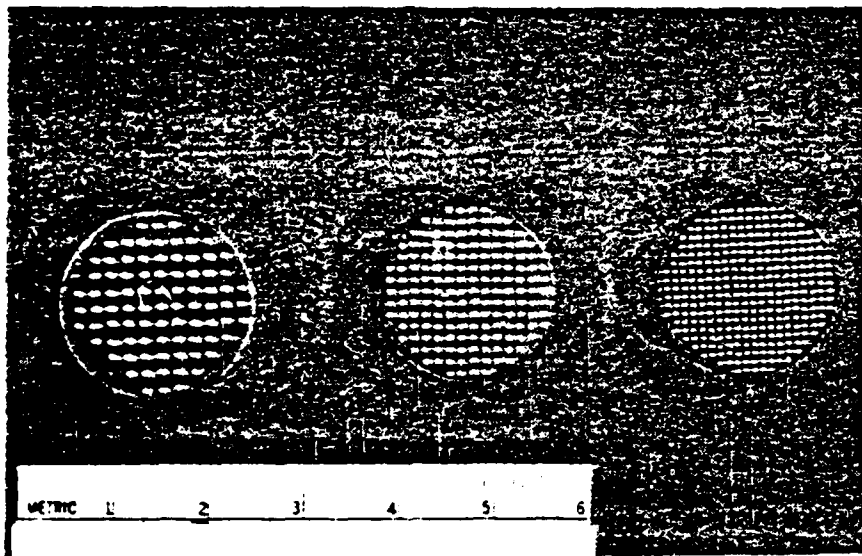
Volume % PZT (Rod Diameter (mm))	Thickness (mm)	Figure of Merit, M	k_t (%)	Q	Frequency Constant N_t^D (Hz m)	Longitudinal Velocity (m/sec) $C_\ell = 2N_t^D$
5 (0.45)	0.6	2.2	57.1	5	1834	3668
	4 to 6	2.4	27.5	31	1327	2654
10 (0.45)	0.6	4 to 6	68.0	7	1820	3640
	3.6	4 to 6	40.0	23	1492	2984
20 (0.45)	0.6	5 to 7	68.9	9	1853	3706
	3 to 5	5 to 7	55.1	18	1603	3203
30 (0.45)	2.4	12	61.1	26	1687	3374
	0.6	3 to 5	62.6	4	1956	2912
10 (0.28)	1.9	3.6	40.6	22	1403	2806
20 (0.28)	0.6	5 to 7	72.0	8	1874	3748
	2.9 to 3.4	5 to 7	50.0	25	1555	3110

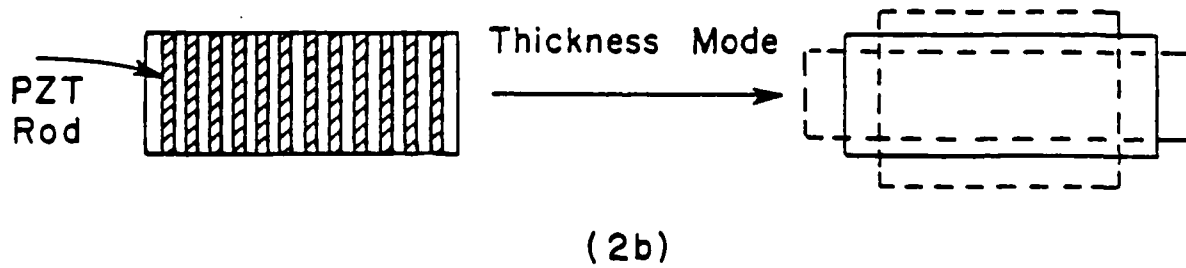
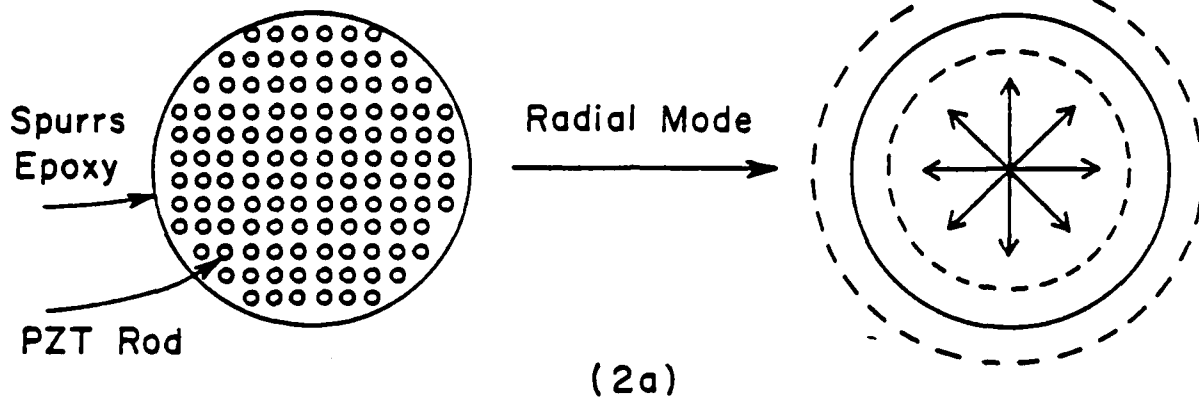
Table 6.

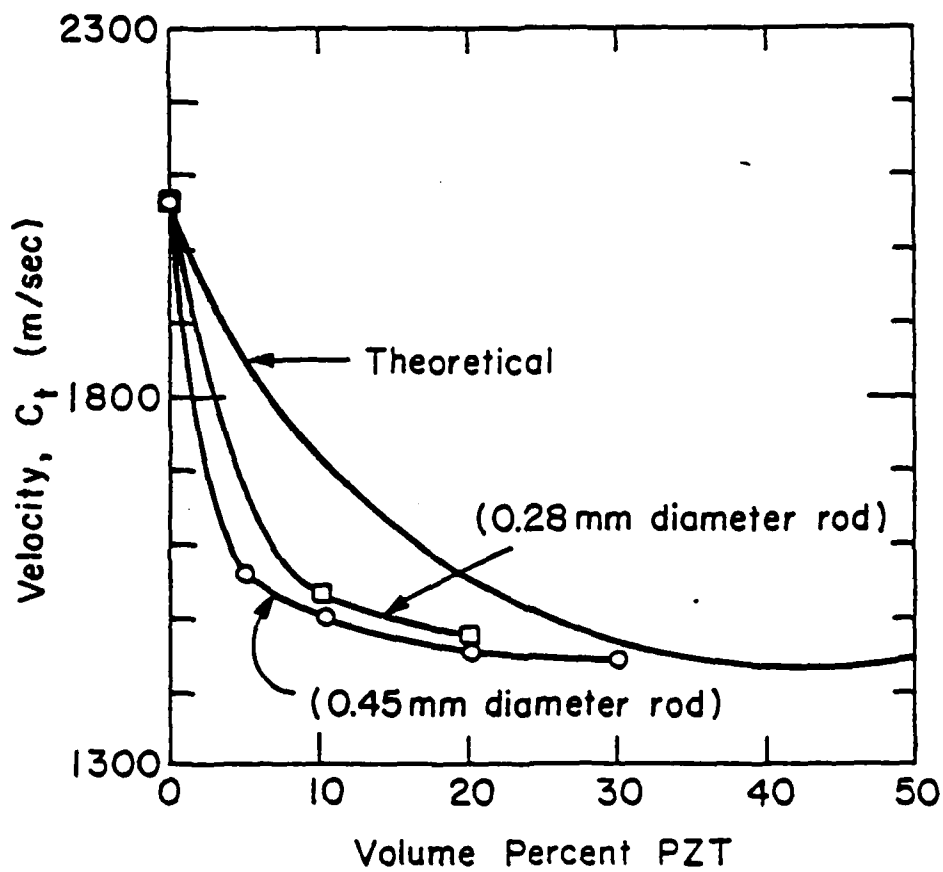
Resonant Modes in Composite Materials.

Volume % P/T	Sample No.	Rod Diameter	Thickness t (mm)	Periodicity in mm	Resonance Frequency in KHz				$C_s = \frac{d}{\sqrt{2}} f_{12}$ m/sec	
					f_{ℓ}	f_{11}	f_{12}	$C_{\ell} = 21f_{\ell}$ m/sec		
5	51	0.45	2.59	1.58	450	604	786	2330	954	878
	52	0.45	4.00	1.76	312	483	691	2496	853	859
	53	0.45	4.80	1.76	262	449	--	2514	790	--
	54	0.45	5.90	1.76	222	437	730	2618	769	908
10	101	0.45	1.93	1.27	604	804	1096	2294	1021	984
	102	0.45	3.64	1.27	410	662	1006	2984	840	903
	103	0.45	5.15	1.27	262	644	--	2698	721	--
20	201	0.45	2.54	0.90	540	894	--	2742	804	--
	202	0.45	3.05	0.90	455	830	--	2774	747	--
	203	0.45	3.95	0.90	348	828	--	2748	745	--
	204	0.45	4.60	0.90	296	886	--	2722	792	--
	205	0.45	5.15	0.90	270	825	--	2780	742	--
30	301	0.45	2.44	0.73	569.5	1125	--	2778	821	--
	302	0.45	5.15	0.73	276.5	1188	--	2848	867	--

500002







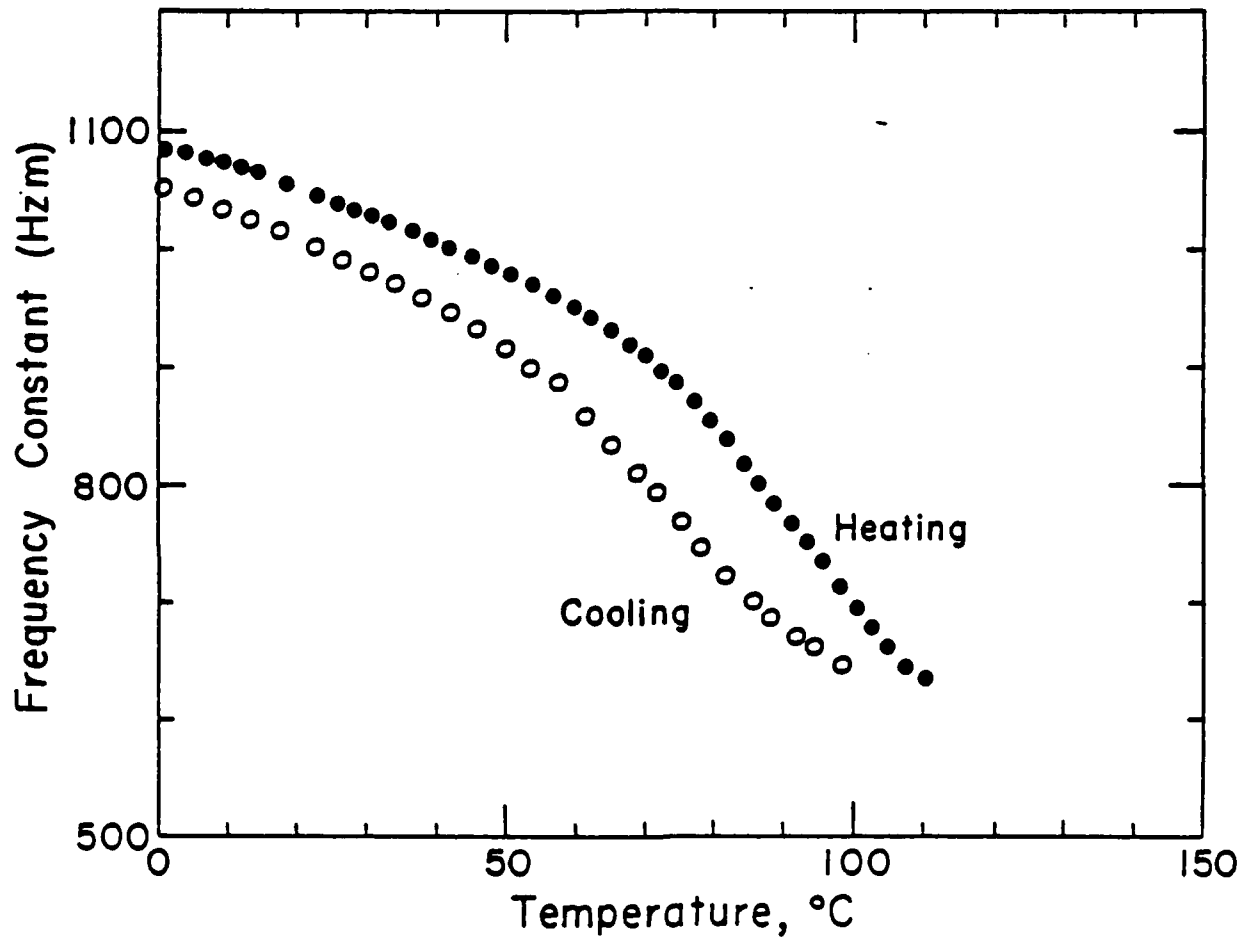
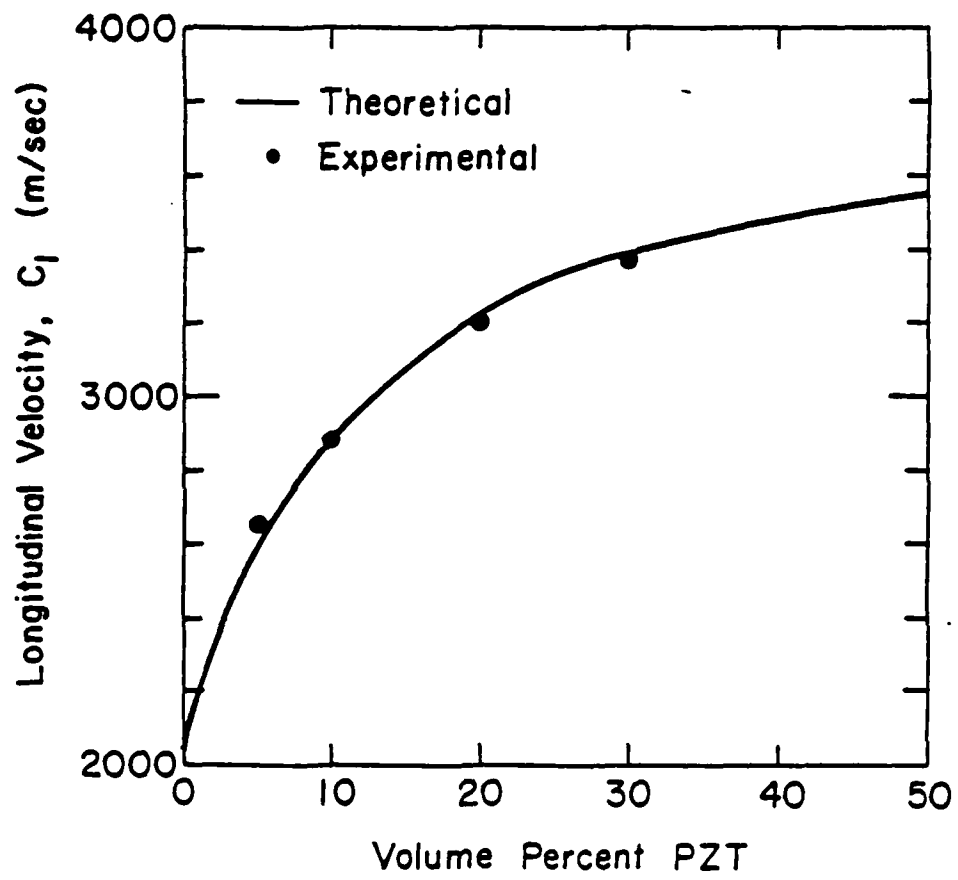
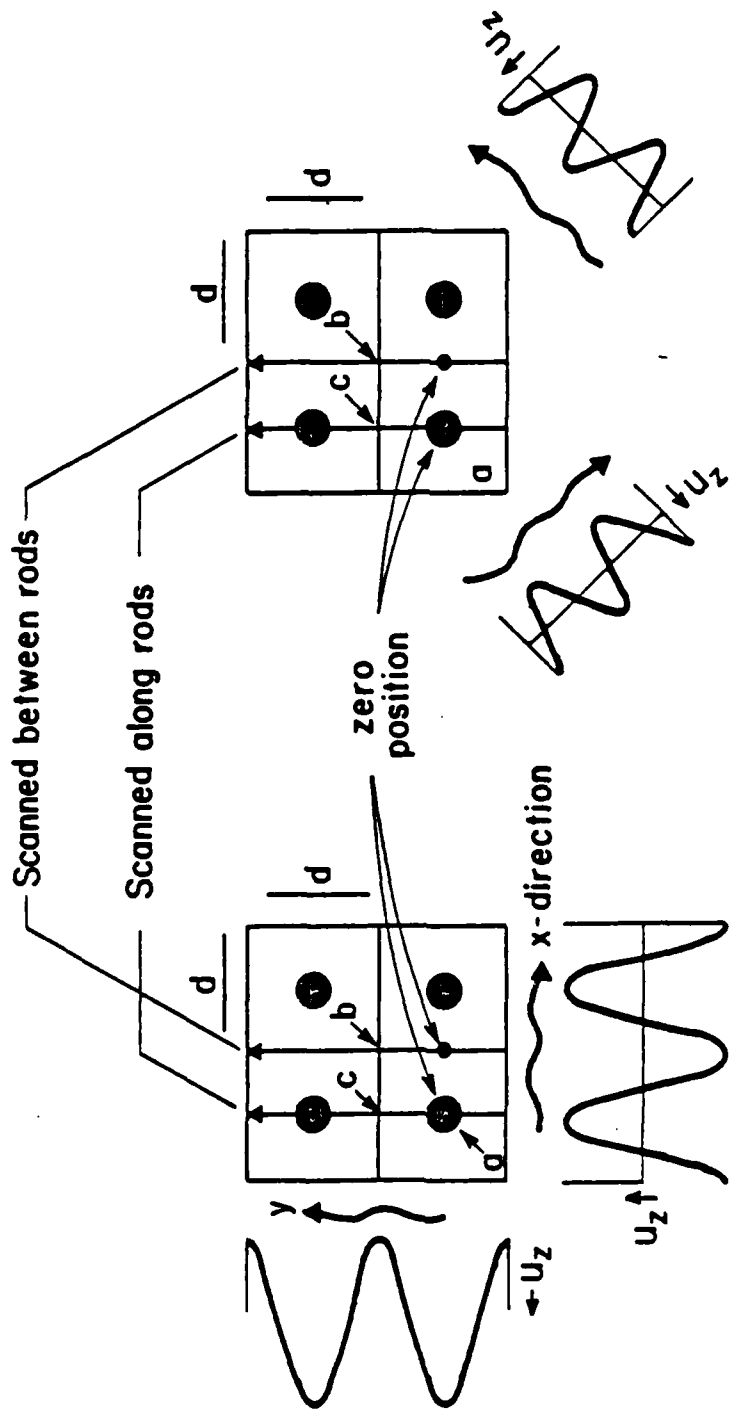
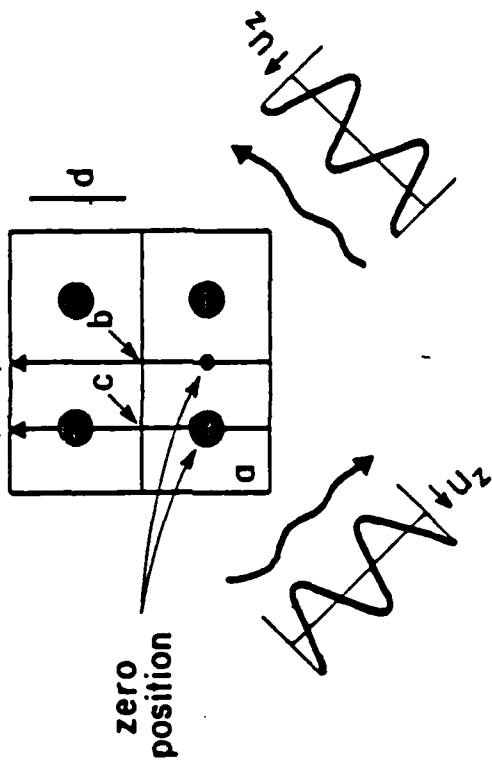


Fig 4

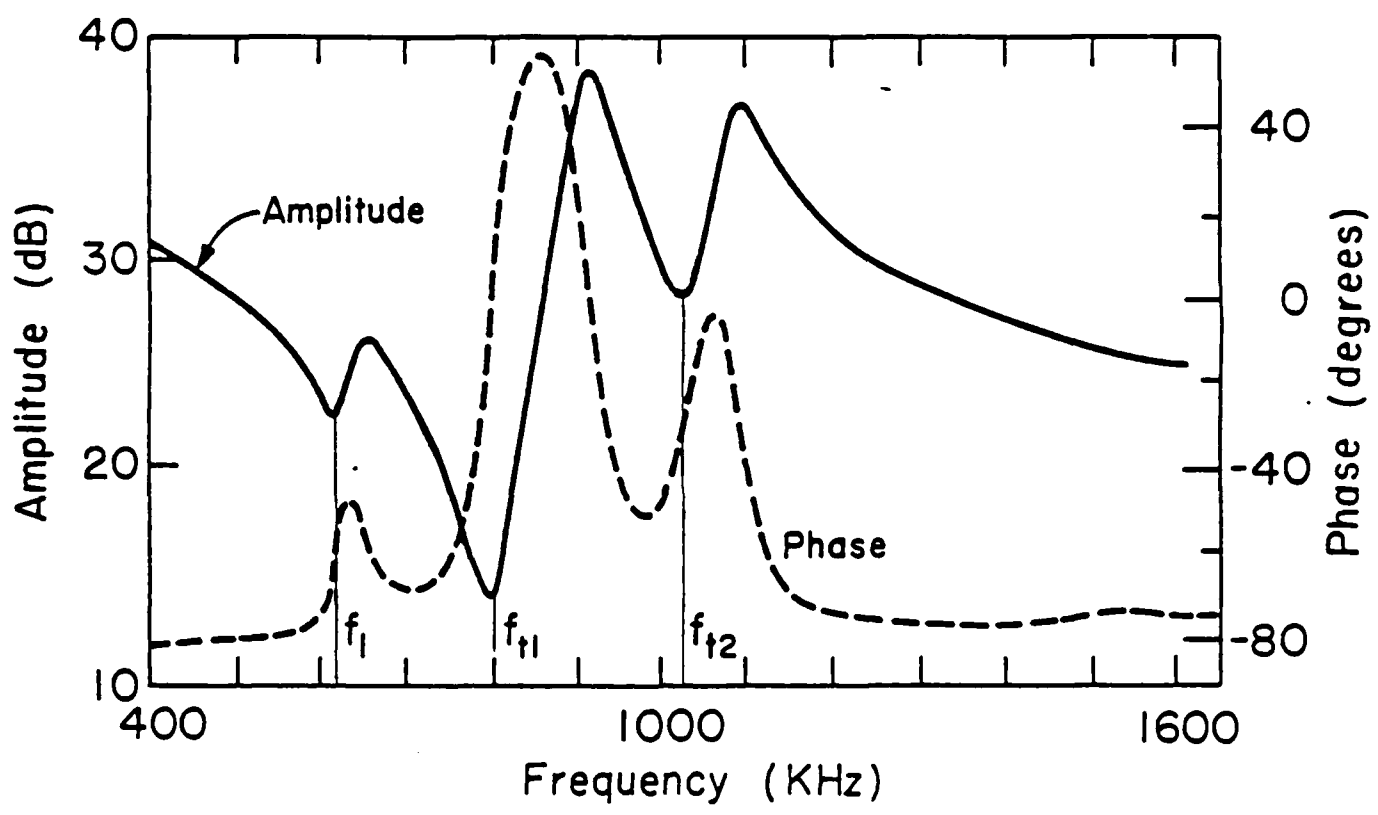


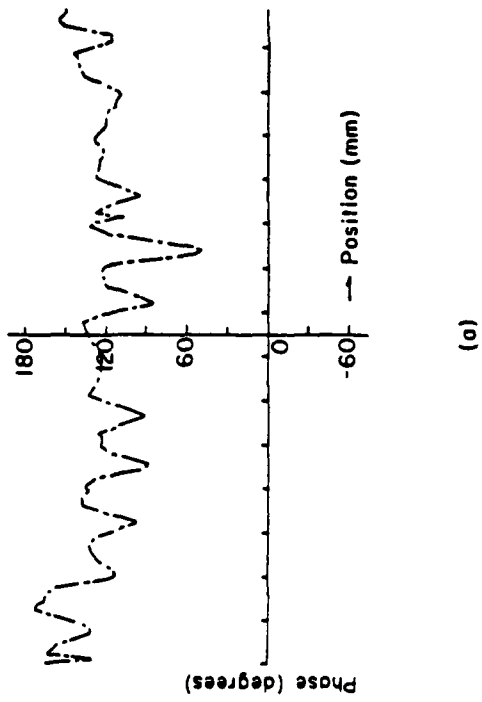
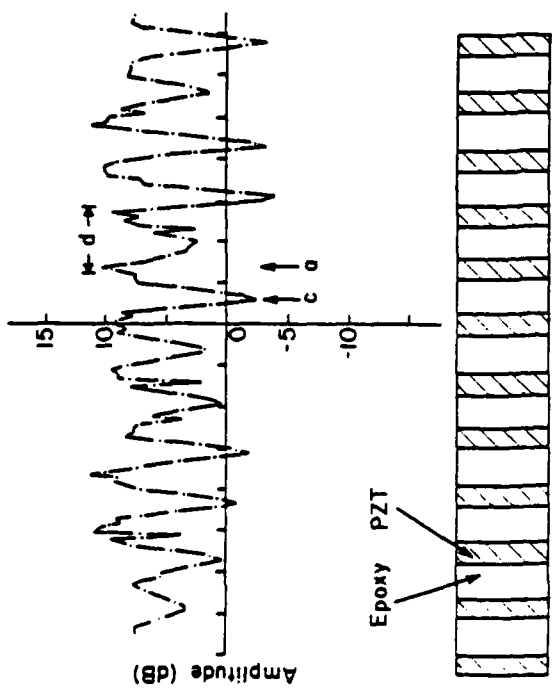
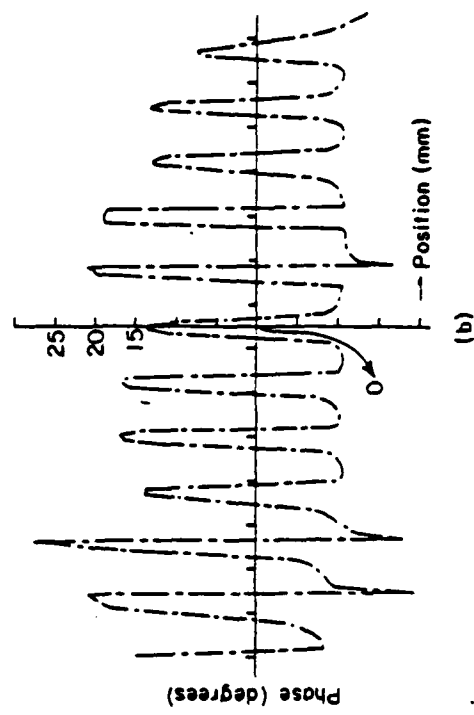
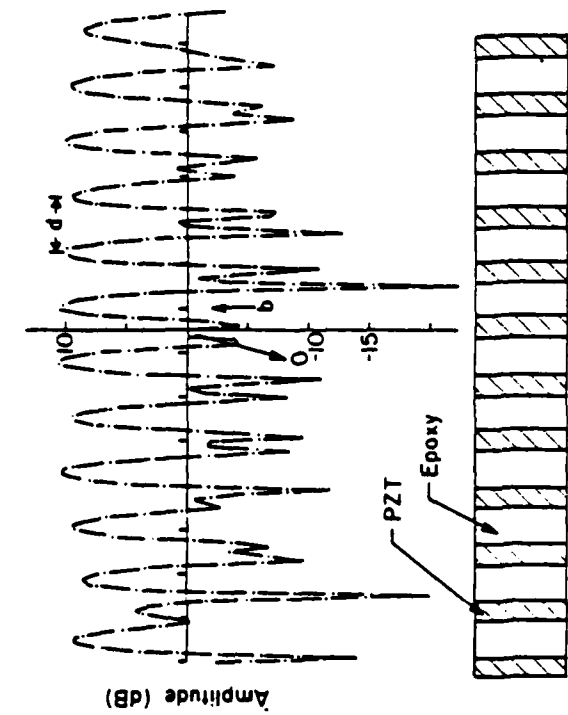


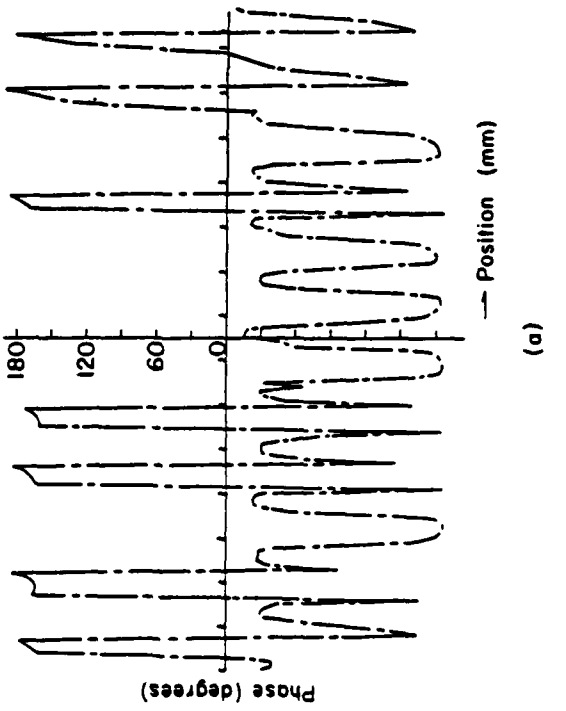
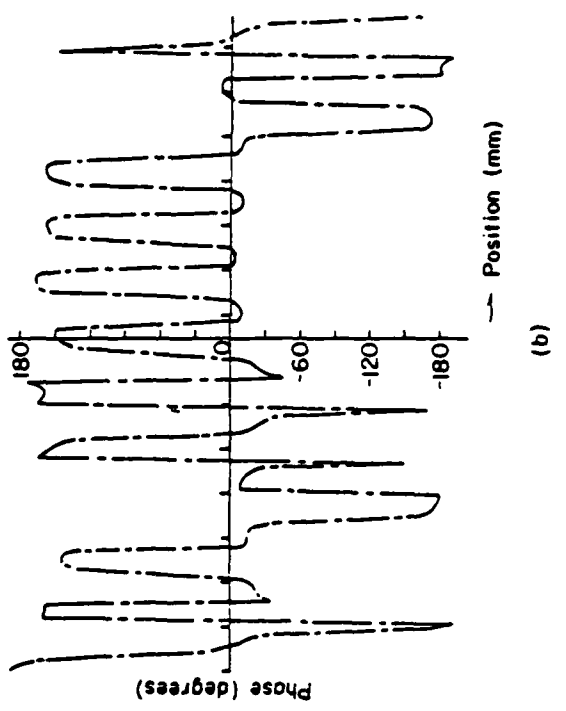
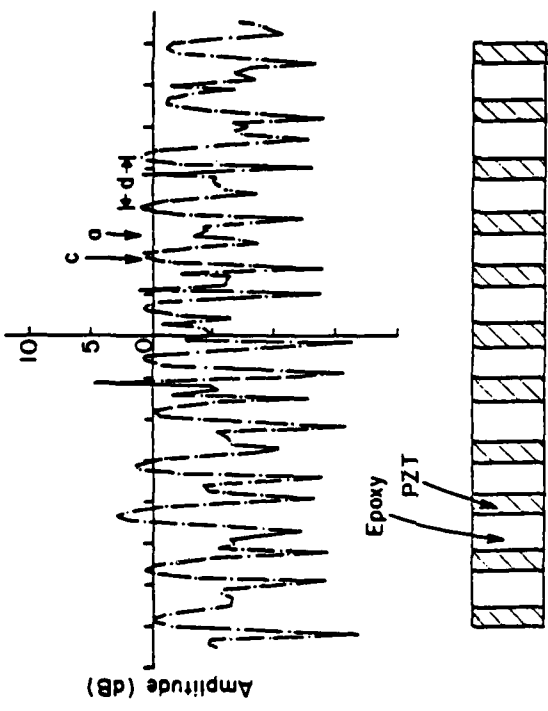
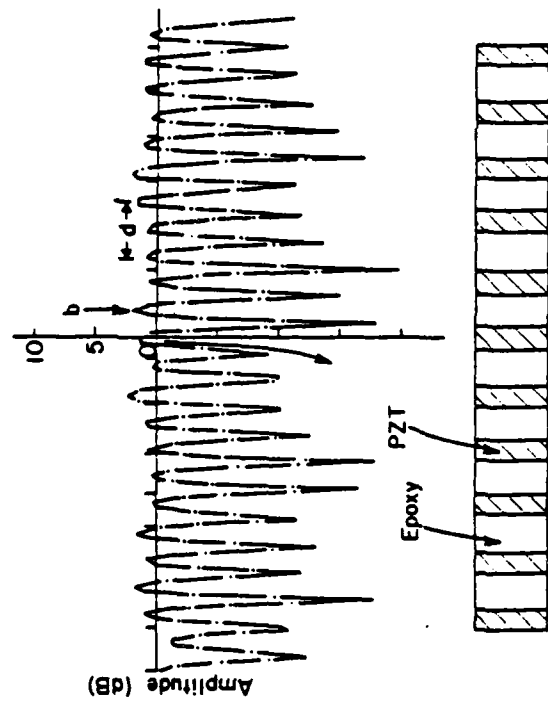
(a)



(b)

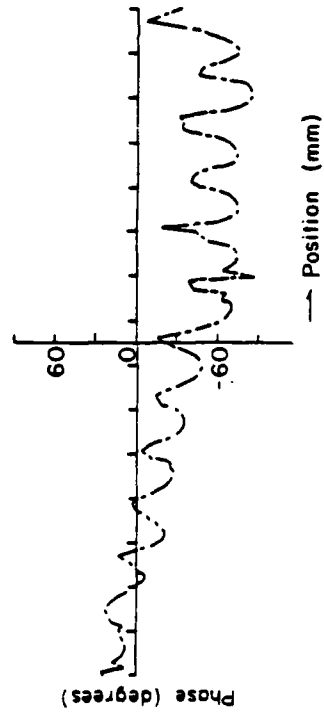
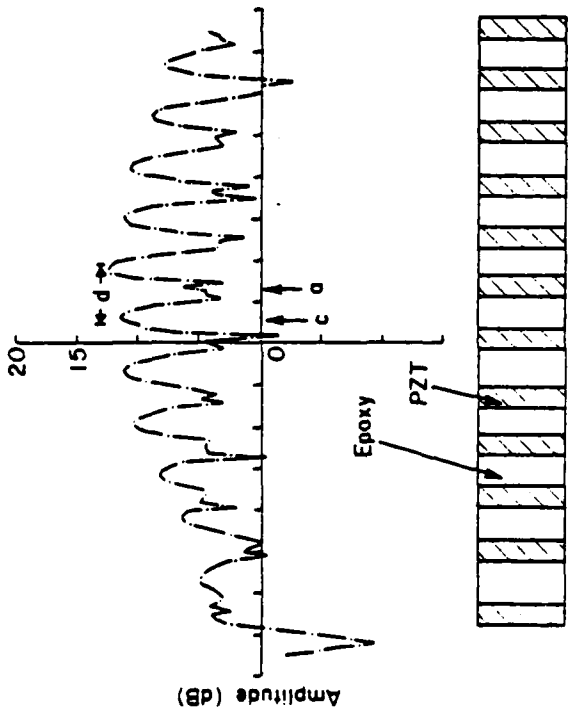
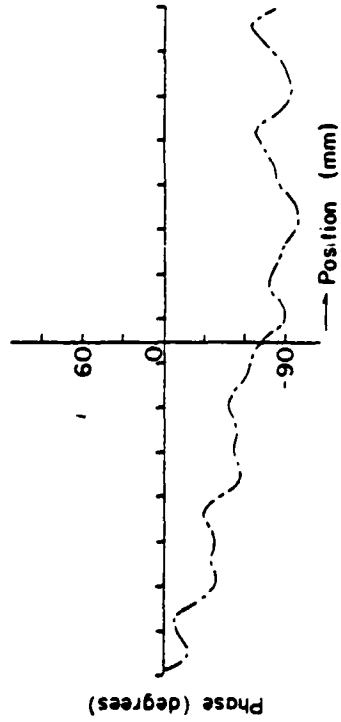
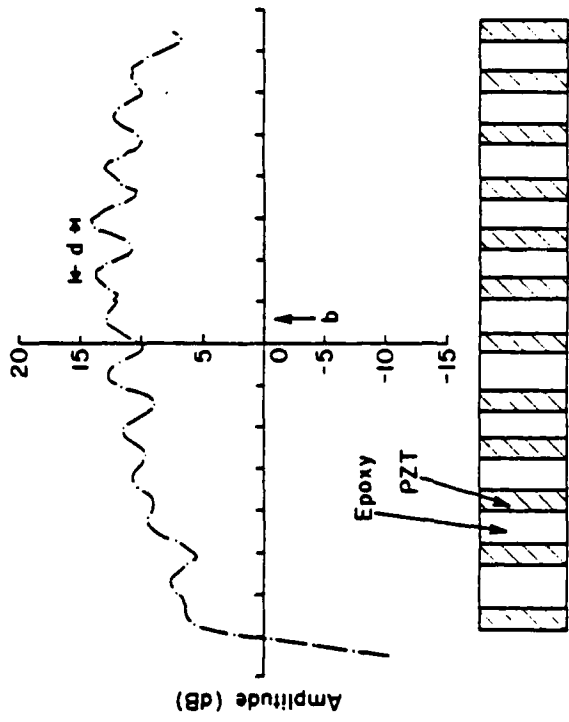






(b)

(a)



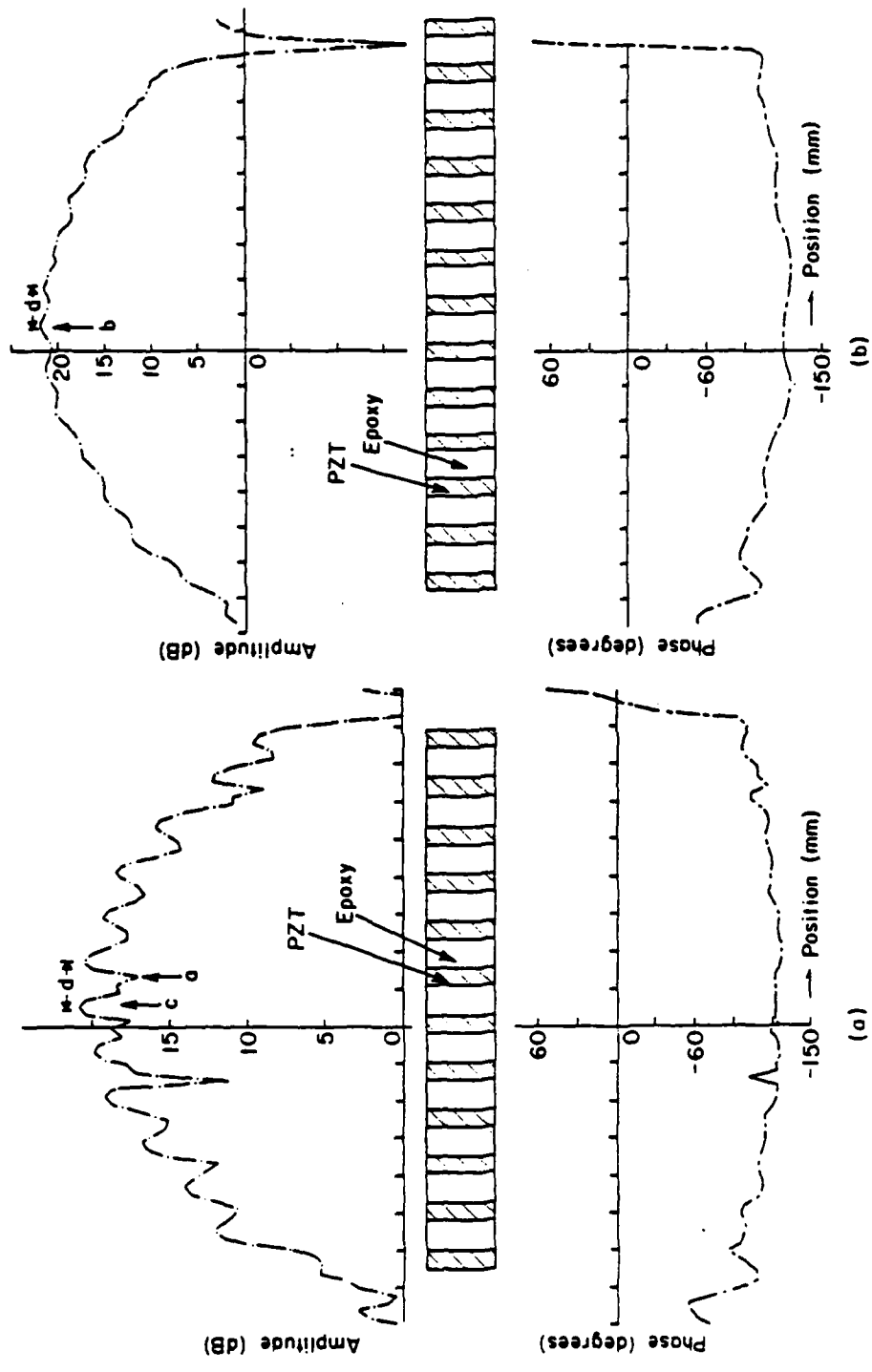


Fig 11

2000

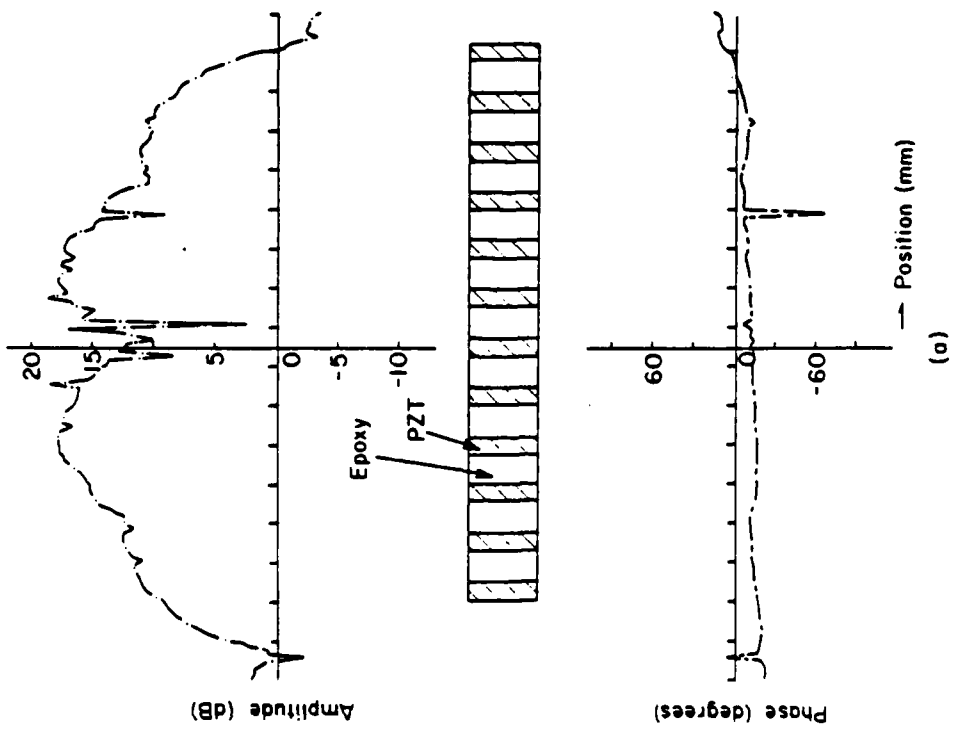
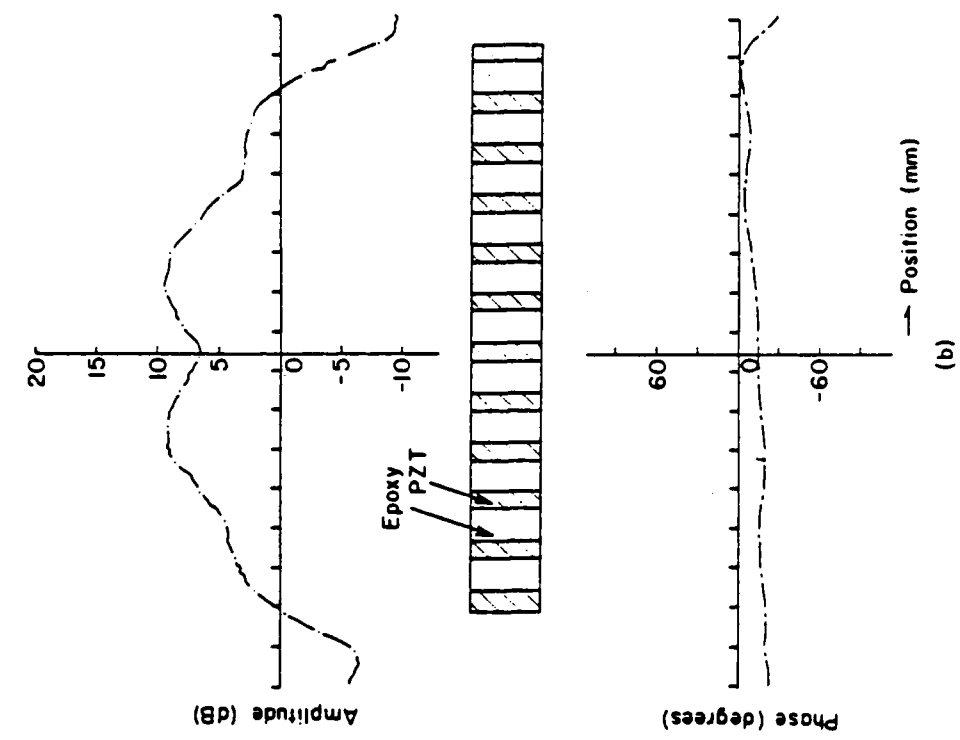
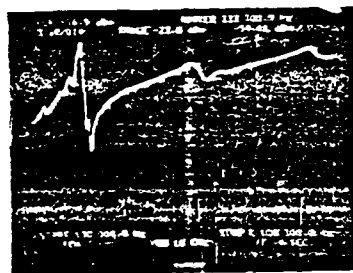


Fig 12



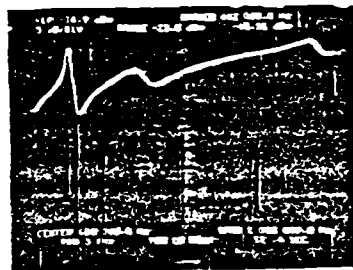
25°C

(a)



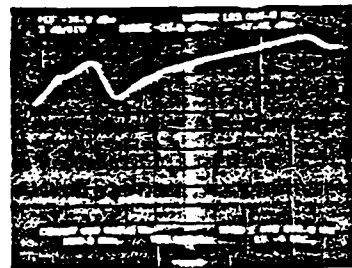
125°C

(e)



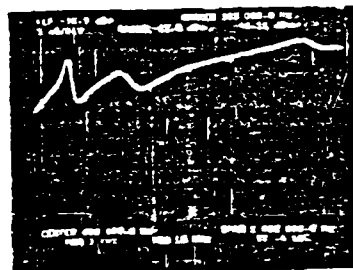
100°C

(b)



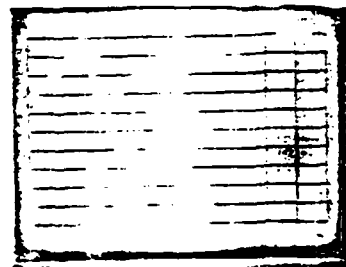
139°C

(f)



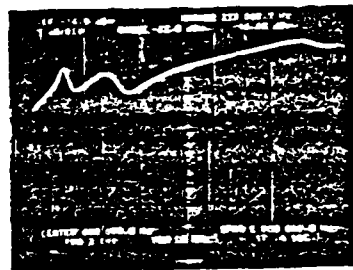
165°C

(c)



150°C

(g)



115°C

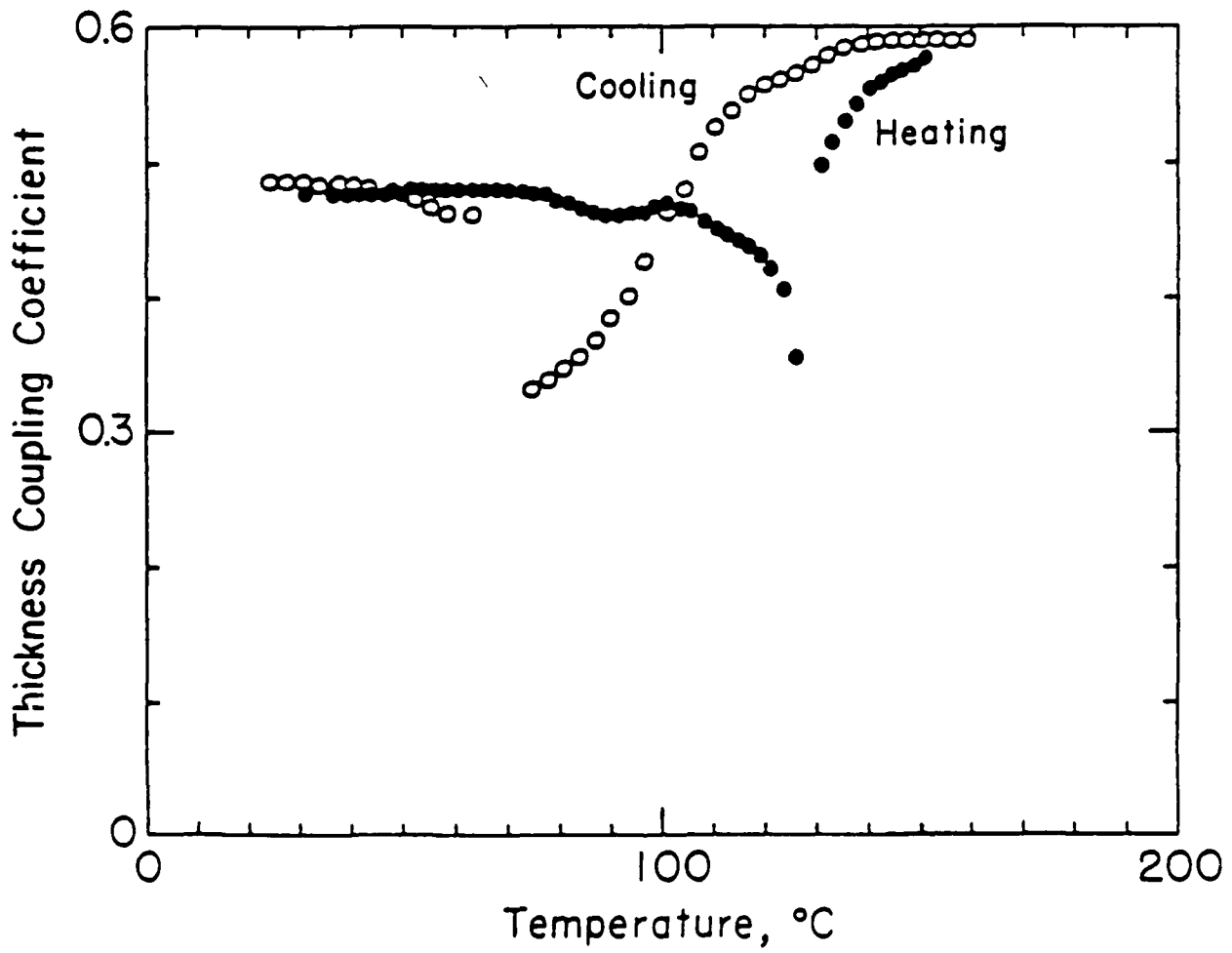
(d)

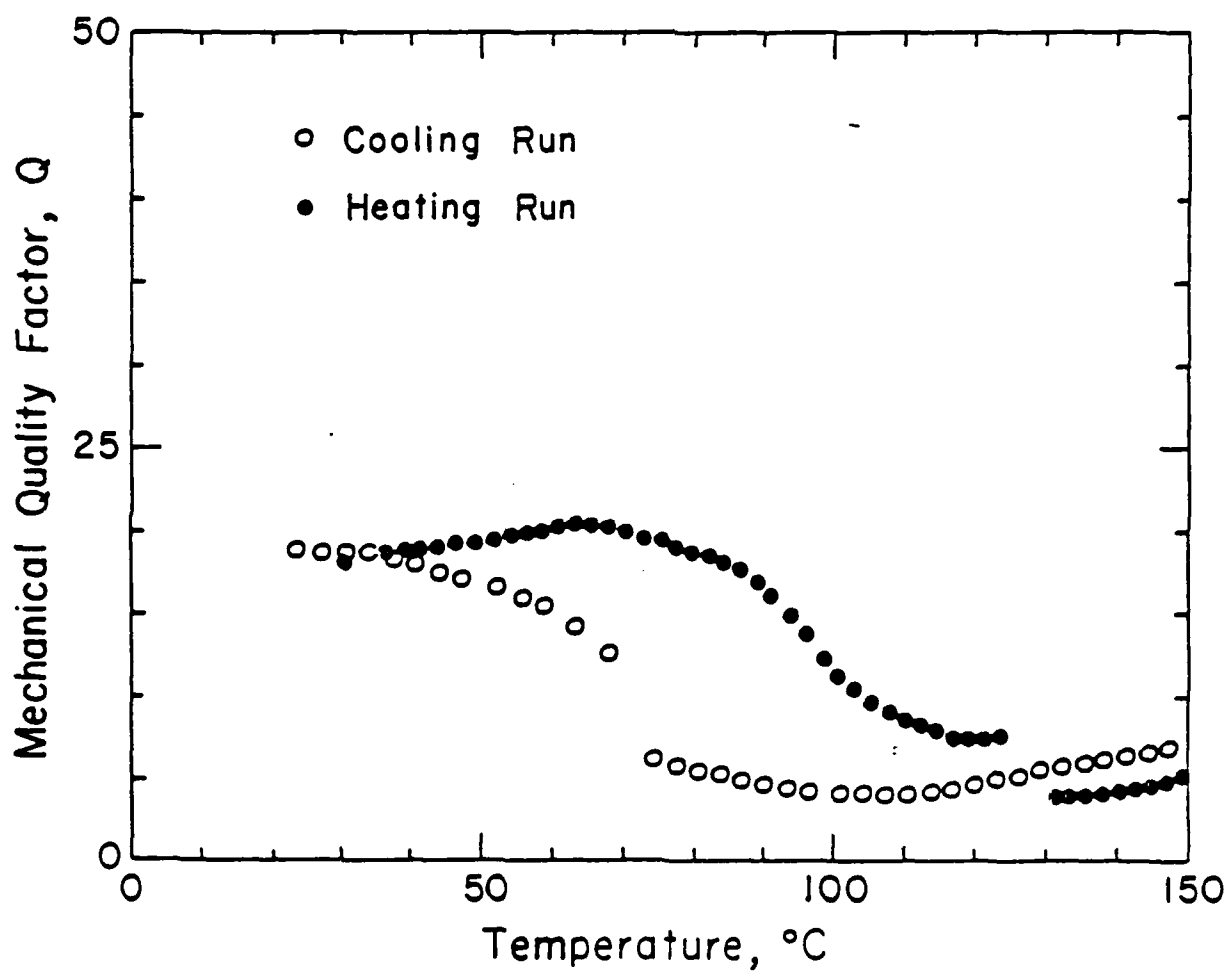


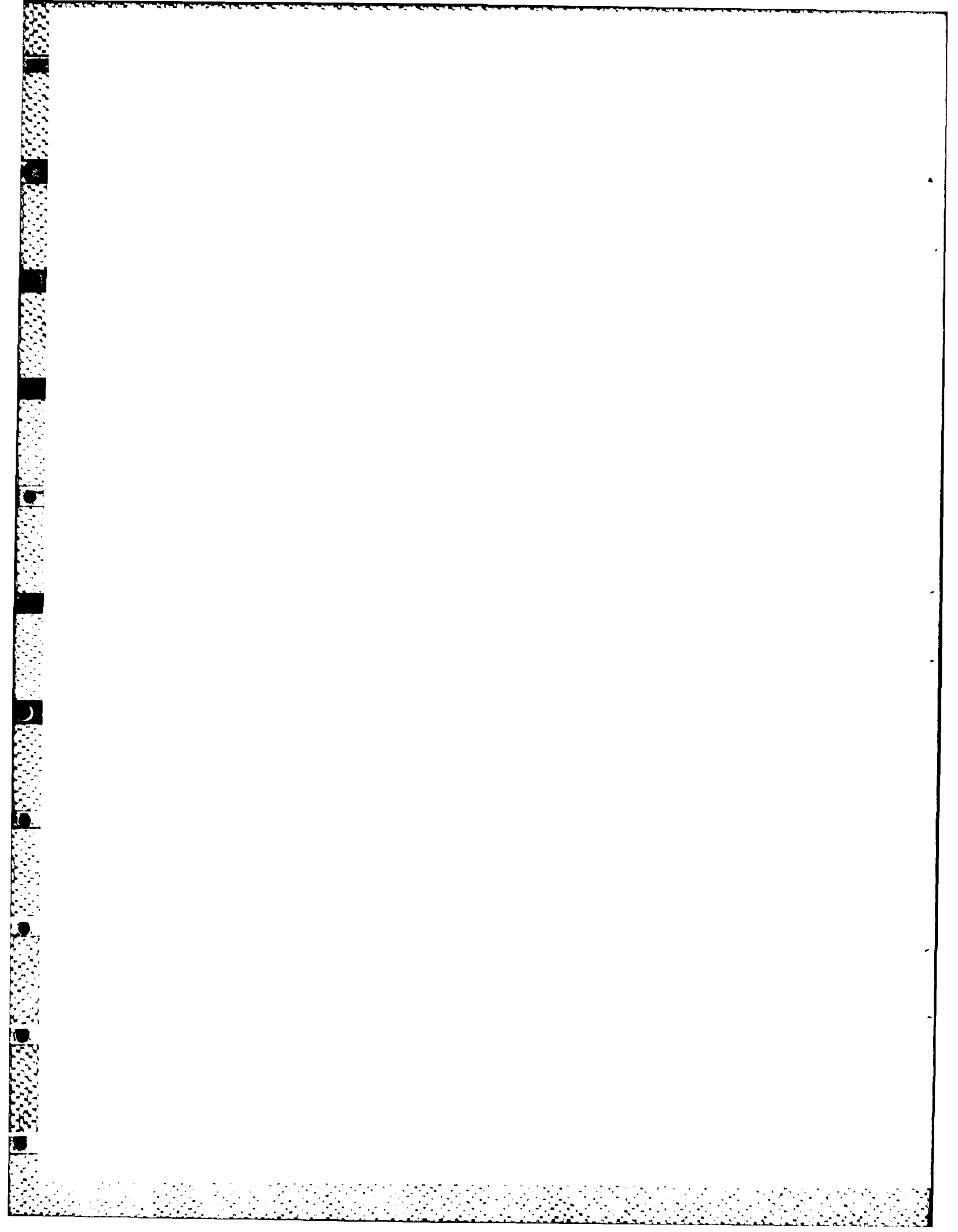
170°C

(h)

Temperature Dependence of Various Resonances in a Composite Sample.
 x-axis - frequency 0.1 to 1.1 MHz
 y-axis - relative admittance (50 dB).







PIEZOELECTRIC COMPOSITE MATERIAL FOR ULTRASONIC TRANSDUCER APPLICATIONS:
PART II. EVALUATION FOR ULTRASONIC MEDICAL APPLICATIONS

T.R. Gururaja, W.A. Schulze, L.E. Cross, and R.E. Newnham

Piezoelectric Composite Materials for Ultrasonic Transducer Applications:

Part II. Evaluation for Ultrasonic Medical Applications

T.R. Gururaja, W.A. Schulze*, L.E. Cross, and R.E. Newnham

Materials Research Laboratory
The Pennsylvania State University
University Park, PA 16802

Abstract

The electro-acoustic properties of PZT rod-polymer composites relevant for ultrasonic transducer applications are reported. Acoustic impedance of the composite materials was measured by three different techniques in the frequency range from 0.3 to 3.5 MHz. Dependence of the acoustic impedance as a function of volume fraction of PZT and frequency was also modeled theoretically. Time delay spectrometry was employed to calibrate the free-field transmitting and receiving voltage responses of the composite materials. The acoustic impedance of the composite materials were in the range of 3 to 10 M rayl. The figure of merit in the receiving mode of composite materials was three times that of PZT. The figure of merit of 20 percent PZT composite ($Z = 7.3$ M rayl) was further enhanced by fifty percent using a single layer impedance transformer of lucite ($Z = 3.3$ M rayl). These composite materials were molded into curved shapes by simple thermal process to fabricate focused transducers. The axial and lateral beam profiles of focused composite transducers are presented.

I. Introduction

A detailed study on the resonant modes of vibration of PZT rod-polymer composites was already reported in Part I [1]. The results showed that

*Present Address: New York State College of Ceramics at Alfred University, Alfred, NY 14802.

although the polymer is piezoelectrically inactive, it plays a substantial role in the composite from the acoustic point of view. Moreover, it was shown that the mechanical properties of the Spurr's epoxy markedly influence the piezoelectric response of the composite. Larger ultrasonic displacement amplitude of the epoxy, as compared to that of the PZT at the thickness mode resonance, was evidence of the efficient coupling of the acoustic energy from PZT to the epoxy. Since the acoustic impedance of the epoxy is relatively close to that of the human body, an effective coupling of acoustic energy from the transducer to the human body is ensured. The present paper deals with the evaluation of PZT rod-polymer composites with 1-3 connectivity as an ultrasonic transducer for medical diagnostic applications. Since the acoustic impedance of the human body is very close to that of water, the transducer evaluation was carried out with water as the loading medium.

Initially, the composite transducers were tested in the pulse-echo mode (Section II). In general, understanding the behavior of a transducer solely from the pulse-echo measurements is extremely difficult, because those measurements combine both transmitting and receiving characteristics of the transducer. The results are also modified by the characteristic impedance of the transducer as a function of frequency. Therefore, these parameters are measured individually. Section III describes the experimental results and theoretical modeling of the acoustic impedance of the composites as a function of frequency and volume percent PZT. The transmitting and receiving voltage response of the composite transducers are dealt with in Section IV and V, respectively. These results together with a knowledge of the piezoelectric response of the composite from the previous paper (Part I) will be used to account for the performance of the composite as an ultrasonic transducer. The effect of a single quarter wavelength matching layer on the performance of the

composite transducer is considered in Section VI. It will be shown that these composite materials can be molded into curved shapes by simple thermal process to fabricate focused transducer. The axial and lateral beam profile of thus focused composite transducers are presented in Section VII, and a concluding discussion is given in Section VIII.

II. Pulse-Echo Measurements

The pulse-echo response of the airbacked composite transducers were determined by the tone-burst pulse-echo method described by Erikson [2]. A schematic diagram of the experimental set up is shown in Figure 1. The composite transducer was mounted in a water tank at the end of a stainless steel tube using silicone rubber as glue. The transducer mounting had independent angular adjustment in two orthogonal phases. The tone-burst signal of an appropriate frequency from a function generator (Interstate-F74) was fed into a power amplifier (ENI-411A). The amplified tone-burst (10 V peak) of 15 to 20 cycles with a repetition rate of approximately 1 KHz was used to excite the transducer. A fine polished ($\pm 1 \mu\text{m}$) steel block (10 cm x 10 cm x 2.5 cm) was used as a reflector. The steel reflector was placed at the a^2/λ distance from the transducer, where a is the radius of the transducer and λ is the wavelength of the center frequency of the transducer. The distance a^2/λ corresponds to the transition from near field to far field. At this distance, the transducer beam is a collimated plane wave with a smoothly varying amplitude and phase profile [2].

The amplitude of the echo signal for a constant 10 V peak input was measured as a function of frequency around the peak response. The following parameters were determined: 1. Frequency of the maximum pulse-echo amplitude (f_0) (also referred to here as center frequency) together with the corresponding value of peak amplitude. 2. Frequencies (f_1 and f_2) at which

the pulse-echo amplitude is one-half (-6 dB) of the maximum pulse-echo response. The product of the maximum pulse-echo amplitude and the 6 dB bandwidth ($f_2 - f_1$) was used as the principal figure of merit for assessing the performance of the composite transducer. The quality factor Q defined as ($f_0 / f_2 - f_1$) was used to characterize the broadband nature of the transducer.

The electric impedance of some composite transducers at resonance was relatively high ($>100 \Omega$) compared to the 50Ω internal impedance of the amplifier which is in parallel with the transducer. Therefore, the received echo signal was loaded by the lower impedance of the amplifier. Since the electrical impedance of the composite depends on the volume percent PZT and thickness, the echo signals were loaded to different extents. Thus a comparison of the pulse-echo response of different composite transducers was difficult. The electrical loading effects were corrected by using back-to-back zener diodes, inserted between the amplifier and the transducer. The diodes allow voltage to be applied to the transducer during excitation while acting as a high impedance during reception. The excitation and the reflected signals were detected using a 10X oscilloscope probe. The total capacitance of the probe, cables, and diodes was about 15 Pf.

The composite transducers described in this paper were fabricated to operate in thickness mode resonance at a frequency of 2.25 MHz. This frequency, often used in ultrasonic imaging systems, was originally chosen for demonstrating the performance of the composite transducers.

The data presented in Table 1 refer to composites of thickness 0.6 mm with a center frequency around 2.25 MHz. With 50Ω termination, the highest echo signal amplitude (2.4 V) was received from the composites with 20 and 30 volume percent PZT rods of diameter 0.45 mm. These samples had comparable voltage-bandwidth product. The highest pulse-echo amplitude (3.25 V) with the

back-to-back zener diode termination came from the composite sample with 20% PZT rods of diameter 0.45 mm.

Both types of 10% composites had higher electrical impedances and were severely loaded by the 50 Ω termination. The high impedance termination using the zener diodes increased the pulse-echo voltage amplitude by a factor of two. However, this was significantly below the values recorded for 20 and 30% PZT as shown in Table 1.

The pulse-echo responses of composites were compared with a commercial transducer (Rohe #5601, transducer diameter = 13 mm). This transducer was supposedly provided with backing and matching layers for the optimum performance. The composite transducers with 20 and 30% PZT compared favorably with that of the commercial transducer. However, the bandwidth of the composite transducer was narrower (Table 1). It is interesting to note that the pulse-echo figure of merit of several composite transducers is comparable to that of an optimized commercial piezoelectric transducer.

As it emerges from the study of the thickness mode resonance of the composites samples [1], thin composites resonating at approximately 2.25 MHz do not vibrate as a collective unit. The PZT rods vibrate quite freely with only a light damping from the epoxy matrix. The composite transducer can be pictured as acting similar to a PZT disc with a light backing material. As the frequency of the thickness mode resonance is decreased by increasing the thickness of the sample, the lateral interaction between the rods through the epoxy becomes stronger and the composite acts more like a homogeneous material. The strong lateral interaction in thick samples was found to be a result of the long wavelength of the transverse wave compared to the periodicity of the lattice. This was clearly seen from the observation of vibration pattern of the composite sample resonating in thickness mode at 270 KHz [1]. Since the stress transfer between the PZT and polymer is better when

the above requirement is satisfied, an improvement was expected in the pulse-echo figure of merit in composites operating at lower frequencies.

To experimentally verify the above proposition, composites with a range of thicknesses from 0.6 to 5.15 mm were fabricated to study their performance as a function of frequency at peak response. The results indicated some improvement in the pulse-echo response compared to measurements at 2.25 MHz. For example, a relatively thick composite (thickness = 3.17 mm) with thickness mode resonance at 450 KHz displayed a loop gain of 1.0 (echo amplitude of 10 V for 10 V excitation) and Q of 3.5.

However, it should be noted here that the evaluation of thick composites resonating in the range of a few hundred KHz by the tone-burst pulse-echo method was complex due to the following reasons: 1. The electrical impedance at resonance frequency of the composite samples increased linearly with increase in thickness. A 20% PZT composite with a thickness of 4 mm resonating at 350 KHz had a minimum impedance of about 400 Ω . At this relatively high impedance level, even the diode isolation cannot provide the necessary decoupling from the 50 Ω termination. The transducer in the receiving mode appears more like a current source than a voltage source. The problem is even more serious for composites with 5 and 10% PZT because the value of the impedance minimum at resonance frequency increases as the volume percent PZT is decreased. 2. As the testing frequency decreases, the sound wavelength increases; hence, the a^2/λ axial distance at which the steel reflector is positioned becomes closer. For a transducer of diameter 1.9 cm resonating at 350 KHz, the a^2/λ distance is approximately 2.1 cm (assuming $C = 1480$ cm/sec in water at 20°C). The travelling time for sound in water from the transducer to the reflector and back for this distance is approximately 28 μ sec. To establish a steady state condition, transducer was excited for a

minimum of 15 cycles. At 350 KHz, this corresponds to 43 μ sec, which is larger than the pulse-echo round trip time. This means that the echoes begin returning before the electrical excitation has stopped. This also poses a serious problem.

A possible solution was to use the spectrum analyzer method [2]. The transducer was excited by an electrical impulse (250 V peak) of duration less than 100 nanoseconds supplied by an ultrasonic transducer analyzer (UTA-3, KB-Aerotech). A time delayed gate is triggered with this excitation pulse and is adjusted in time delay and gate length to pass only the reflected echo. The processed signal from the analyzer was displayed on a high frequency oscilloscope (Gould - OS3300) to determine ringdown time of the transducer. The signal from the UTA-3 was displayed on a spectrum analyzer (HP 3585A) to obtain a plot of amplitude versus frequency of the reflected echo. Since the excitation pulse was very narrow, the problem of interference of the echo signal with the excitation pulse encountered in the tone-burst method was partly solved, however, the method was not free of other limitations. Since the transducer is not matched electrically to the pulse, not all the pulse energy is delivered to the transducer. The receiver has terminating impedance of 50 Ω , thus, it has the serious loading effect on the received signal.

As explained above, it was very difficult to evaluate composite transducers and realize their advantages solely by pulse-echo measurements. Therefore, the composite materials ^{were} characterized separately for their acoustic impedance, transmitting and receiving voltage responses, which are reported in subsequent sections.

III. Characteristic Acoustic Impedance

The characteristic acoustic impedance (Z) (referred to as acoustic impedance from here on) of the transducer is an important property which

determines the effectiveness of the coupling of ultrasonic energy from the transducer to the load. The acoustic impedance is the product of density ρ and velocity of sound C in the material. In a single phase material, measurement of these properties is relatively easy and well described [3]. However, it is not so for composite materials. Composites usually exhibit anisotropic behavior. The properties of the constituent phases must be averaged properly. In the PZT rod-polymer composites considered here, the interaction between polymer and PZT, and among neighboring PZT rods is a function of frequency. Therefore, dependence of acoustic impedance on frequency also needs to be considered. Three techniques, namely reflection, transmission, and resonance, were used to determine the acoustic impedance and its frequency dependence. The results are reported in the following subsections. The acoustic impedance of the composites were also theoretically modeled and compared with the experimental data.

a. Reflection Technique

In the reflection technique, the acoustic impedance of a composite was determined by comparing the amplitude of reflection of a plane acoustic wave from the sample with that from a standard material, e.g. stainless steel, of known acoustic impedance. The experimental set-up was the same as that used for the tone-burst pulse-echo technique (Figure 1). The reflector was placed at the a^2/λ distance. A commercial ultrasonic transducer was used to measure the pulse-echo signal from both the sample and the standard reflector. The transmitting voltage response and receiving voltage sensitivity of the transducer need not be taken into account as the same transducer is used for measuring reflections from both the standard material and the specimen.

The tone-burst pulse-echo experiment was carried out as a function of frequency with a stainless steel block (10 cm x 10 cm x 2.54) reflector. The

driving voltage of the transducer was kept constant at 10 V. It can be shown [4] that the pulse-echo amplitude X is proportional to the reflection coefficient at the water:reflector interface. That is [4]

$$X \propto \frac{Z_1 - Z_2}{Z_1 + Z_2} \quad (1)$$

where Z_1 and Z_2 are the acoustic impedances of the steel reflector and water, respectively.

The stainless steel block was then replaced by a composite sample and the pulse-echo amplitude Y was noted. If Z'_1 is the acoustic impedance of the composite sample,

$$Y \propto \frac{Z'_1 - Z_2}{Z'_1 + Z_2} \quad (2)$$

From Equations (1) and (2), the acoustic impedance of the composite sample (Z'_1) can be expressed in terms of X , Y , Z_1 , and Z_2 . Since it is known that $Z_1 = 45.4 \times 10^6$ rayl and $Z_2 = 1.5 \times 10^6$ rayl [5], the expression for the acoustic impedance of the composite sample is given by

$$Z'_1 = 1.5 \left(\frac{46.9X + 43.9Y}{46.9X - 43.9Y} \right) \times 10^6 \text{ rayl} \quad (3)$$

By substituting the values of X and Y at a specified frequency, the acoustic impedance can be calculated from Equation (3).

The validity of the technique was tested by determining the acoustic impedance of a few standard materials such as lucite, fused silica and aluminum with known acoustic impedance of 3.1, 13 and 17 M rayl, respectively. The measured values of Z for these materials were 3.2, 12.6 and 17.1 M rayl which are in excellent agreement. The experiments were also conducted with transducers of different type (focused, nonfocused) and with the reflector

placed at different distances (at a^2/λ distance, at the focal length of the transducer, etc.). No substantial difference in the measured impedances was observed.

Composite samples of thickness 2-3 cm with 5, 10, 20 and 30 volume percent PZT rods of diameter 0.45 mm were fabricated. The samples were not poled because such thick samples require excessively large poling voltages (40-60 kV). Figure 2a shows a plot of the acoustic impedance of several different composites in the frequency range from 0.3 to 1.3 MHz, and Figure 2b extends the plot from 1 to 3.5 MHz. Low frequency data were obtained using a lead metaniobate transducer (Ultran Lab, Inc., diameter = 2.5 cms) with a center frequency of 0.7 MHz and a very broad bandwidth ($Q \approx 1$). The distance between the transducer and the reflector was 7.5 cm corresponding to the a^2/λ distance at 0.7 MHz. Measurements in the frequency range from 1 to 3.5 MHz were carried out using a focused transducer (Rohe 5616, diameter = 1.9 cm, focal length = 9 cm) with a center frequency of 2.25 MHz. The separation between the transducer and reflector in this case was 9 cm, the focal length of the transducer.

The following observations were made by inspecting the acoustic impedance plots of Figure 2. As expected, the acoustic impedance increased with increase in the volume percent PZT. Moreover, the acoustic impedance was strongly frequency dependent. The composite samples showed a series of minima in Z at low frequency. Above 2.5 MHz, the variations are minimized and the value of Z reached a saturation. The position of the first minimum in Z occurred at a higher frequency for larger volume percent PZT. The acoustic impedance increased steadily at frequencies below the first minimum. The acoustic impedance of single phase epoxy, measured by the same procedure, is also shown in Figure 2 for comparison. There was no variation of Z of epoxy

in the frequency range considered in this work. The results were analyzed carefully to find an explanation for the observed dispersion in Z .

The minima for 5, 10, 20 and 30% PZT composites occur at 0.45, 0.625, 0.825 and 1.125 MHz, respectively. The frequencies have an inverse relationship with the lateral periodicity of the corresponding composite. The product of the frequency at the acoustic impedance minima and the lateral periodicity of the composite was found to be a constant of value 800 m/sec. It is interesting to note that the frequency corresponding to the minima in Z in each composite matches with the resonance frequency f_{t1} [1]. The resonance frequency f_{t1} corresponds to the standing wave pattern of the transverse waves with the wavelength equal to the lateral periodicity of the lattice. It should be pointed out here that the value of the acoustic impedance at the minima was approximately the same for all volume percent PZT (1.6 M rayl), which is surprisingly lower than that of the epoxy (2.3 M rayl).

There is a small discrepancy in the values of acoustic impedance around 1 MHz measured using the two different transducers. This is possibly because the transducers were operating far away from their center frequencies, and hence were not very sensitive. Thus the measurements performed in the transition region from one transducer to the other are not very precise.

All the above observed phenomena may be explained as follows. The acoustic wave incident on the composite sets it into vibration. Due to the difference in compliance between the two component phases, viz PZT and Spurr's epoxy, a transverse wave originating at the interface and propagating in a direction perpendicular to the rod axis is launched in the epoxy matrix. At the frequency where the transverse wavelength is equal to the periodicity, resonant scattering of waves by the vertical planes of the PZT rods results in a two dimensional standing wave pattern as described in Part I [1]. Measurements of the surface displacements of the composite at this frequency

showed that the epoxy at the center of the unit cell of the periodic lattice vibrates 180° out of phase with PZT and with a much larger amplitude. This standing wave pattern is most likely established after a few cycles of the incident wave. The acoustic impedance minima at this frequency are caused by the cancellation effects between the incident wave and the large amplitude vibration of the epoxy with a phase difference of 180° .

Support for the above explanation is provided in Figure 3 where tone-burst pulse-echo signals reflected from a composite sample are shown. Figure 3a depicts a typical signal measured at frequencies far away from the minima in the acoustic impedance. The signal builds up to a saturation value in 1 or 2 cycles depending on the Q of the transducer and remains constant. The amplitude is affected only by the reflections from the rear surface of the composite sample as indicated by an increase in amplitude in the last few cycles. The reflected signal from a composite at the acoustic impedance minima is shown in Figure 3b. The amplitude approaches a saturation value, but the signal declines after the first two cycles and reaches a minimum value. Interference of the signal with the reflected signal from the rear surface of the composite sample makes it difficult to analyze the wave pattern after a few cycles. Figure 3c presents similar data with an expanded abscissa. Thus, the acoustic impedance minima observed arises from the destructive interference between the incident signal and the reflections from the composite sample. Therefore, the minima in acoustic impedance are only an apparent phenomena because of the complex resonance in the composites.

Resonance experiments [1] indicated another strong lateral resonance mode, referred to as f_{t2} . This resonance was associated with standing waves along the unit cell diagonal. For a 5% sample, f_{t2} was approximately 0.7 MHz and a corresponding minimum was seen in the acoustic impedance plot as

expected (Figure 2a). Acoustic impedance for the 10% sample is also seen to approach a minimum around 1.00 MHz (Figure 2a), which corresponds to f_{t2} for the 10% composite. In addition to the acoustic impedance minima just described additional minima were observed up to about 2 MHz possibly due to more complex lateral modes.

b. Modeling of Acoustic Impedance

The acoustic impedance of the composites was modeled to explain the observed frequency dependence discussed in the previous section.

Above 2 MHz, the acoustic impedance was found to be relatively independent of frequency. At this frequency, experimental evidence showed that the PZT rods were vibrating without an appreciable lateral interaction. Therefore, this situation can be modeled using Reuss averaging [6] which assumes that the constituent phases experience the same stress. According to the Reuss averaging scheme, the modulus of elasticity parallel to the length of the rod E_{ℓ} is given by

$$\frac{1}{E_{\ell}} = \frac{v_1}{E_1} + \frac{v_2}{E_2} \quad (4)$$

where v_1 and v_2 are volume fractions and E_1 and E_2 are the appropriate elastic moduli of the constituent phases. For unpoled PZT rods, the elastic modulus is $E = 1/s_{11}^E = 6.098 \times 10^{10} \text{ N/m}^2$ [7]. For the epoxy, the elastic modulus was found to be $E = 4.7 \times 10^9 \text{ N/m}^2$ [1]. From the calculated values of E_{ℓ} using Equation 4 and the mean density $\bar{\rho}$ listed in Table 2 of Part I [1], the acoustic impedance of the composites was evaluated from the expression $Z = (\bar{\rho} E_{\ell})^{1/2}$. Both the measured and calculated values are compared in Table 2. The frequency range above 2 MHz, where the wavelength of the transverse waves is much smaller than the periodicity of the lattice, is called region 1 for discussion purposes. There is a good agreement between the theory and the

experiment supporting the explanation of the mode of vibration outlined above for frequencies above 2 MHz.

At frequencies below the minima in Z corresponding to f_{t1} , the lateral interaction increases gradually and the two phases vibrate in a cooperative mode. The displacements of PZT and epoxy were found not only to be in phase but also with almost equal amplitude [1]. Thus, the Voigt averaging scheme [6], which assumes constant strain on the constituent phases can be used to estimate the effective longitudinal modulus E_2 of the composite. The composite modulus according to the Voigt model is given by

$$E_2 = v_1 E_1 + v_2 E_2 \quad (5)$$

Using the values of the elastic moduli for the PZT and epoxy given above, the effective modulus and acoustic impedance of the composites were calculated, and are compared with the measured values of Z at 0.3 MHz in Table 2. This frequency range, where wavelength of transverse waves is larger than the periodicity, is called region 3 in this paper. The theoretically predicted increase in the acoustic impedance at frequencies below the first acoustic impedance minima was seen in all the composites. However, the measured values were on the average 20% lower than the estimated value. The discrepancy between the experiment and theory is possibly due to the diffraction losses. Because of the relatively small size of the composite sample (diameter = 1.9 cm) compared to the size of the steel reflector (10 cm x 10 cm), it is conceivable that not all of the acoustic energy was reflected back from the composite sample to the transducer.

A correction to account for the diffraction losses in the acoustic impedance measurements was applied experimentally by using the standard reflector of exactly the same dimension as the composite sample. Then the

experimental setup for the two reflections to be compared becomes identical, and hence the uncertainty in the measurement because of the diffraction losses is minimized. Figure 4 compares the earlier data with the new data corrected for diffraction losses for a 10% composite sample. As can be seen, the corrected value of the acoustic impedance approaches 4.1 M rayl at 0.3 MHz, which is in excellent agreement with the predicted values based on the constant strain model (Table 2). Based on the experimental and theoretical results, the acoustic impedance as a function of frequency can be classified into three regions.

In region 1, corresponding to frequencies above 2 MHz, the transverse wavelength is much smaller than the rod spacing d and the two phases appear to be decoupled. There is not much influence of epoxy on the vibration of the PZT rods. A significant improvement in the pulse-echo response in terms of the figure of merit cannot be expected in this region, if the composite is used as a single element transducer. On the other hand, the situation is desirable for a linear or phased array transducer construction, where the acoustical cross coupling between elements should be as low as possible.

In region 3, corresponding to the frequency far below the first minimum in the acoustic impedance, the composite acts as a homogeneous material. Maximum stress is transferred from PZT to polymer and vice versa. The composite is expected to perform better as a single element transducer with an improved pulse-echo figure of merit.

In region 2, the periodicity of the lattice and the wavelength of the transverse waves are comparable. This region is helpful in understanding the complex vibrational modes in two dimensionally periodic structures. In this region, the composite can possibly be used as a resonant sound absorber.

c. Transmission Technique

The acoustic impedance of the composites was also determined by measuring the velocity of longitudinal waves along the PZT rod axis. The method chosen for measuring the longitudinal velocity was similar to the standing wave method described by McSkimin (8). An acoustic wave of a particular frequency is made to impinge on the sample. The wave transmitted to the specimen is reflected back and forth giving rise to a series of transmitted pulses. At discrete frequencies, the emerging wave trains will be in phase leading to a constructive interference. The constructive interference occurs at a frequency for which the path length (twice the specimen thickness) is equal to an integral number of wavelengths in the specimen at that frequency. The principle of the method is to determine the value of the integer at one of the discrete frequencies when the in-phase condition is satisfied. The experiment is described in detail elsewhere (9).

The longitudinal velocity was determined for 20 and 30% PZT composites around 0.5 MHz, which is below the frequency corresponding to the acoustic impedance minima (Figure 2a). The velocity values were multiplied by the average density to obtain the acoustic impedance. The resulting data shown in Table 3 are in excellent agreement with the values estimated theoretically for region 3.

d. Resonance Technique

The velocity of longitudinal waves determined by the resonance technique described in part I [1] was also used to determine the acoustic impedance of composite samples. The velocities for different composites are listed in the last column of Table 5 of Part I [1]. Values of the acoustic impedance evaluated from the measured velocity and density of composites are listed in Table 4. Theoretically calculated acoustic impedance are also tabulated for

comparison. In the piezoelectric resonance experiments, PZT rods in the composite are electrically poled. Hence, for calculating the elastic modulus of the composite, the modulus of the PZT rods $E = 1/s_{33}^D = 10.5 \times 10^{10} \text{ N/m}^2$ (7) was used.

As it emerges from Table 4, in region 1 (>2 MHz), a poor agreement between the estimated and measured acoustic impedance was found. This was anticipated because the rods are vibrating relatively freely and the resonance technique measured the velocity of PZT phase only. Hence the product of this velocity with the average density of the sample gives a much higher estimate of the acoustic impedance.

In region 3 (<0.5 MHz), the agreement between the theory and the experiment is excellent (Table 4). It is interesting to note that the three completely independent techniques give extremely consistent data on the acoustic impedance in region 3.

IV. Calibration of Composite Transducer as a Receiver of Ultrasonic Waves

This section deals with the evaluation of composite transducers as an ultrasonic receiver. The receiving sensitivity is considered to be of greater importance than the transmitting response, especially in biomedical-diagnostic applications, because only a limited acoustic energy level can be applied to the human body. This limit has to be sufficiently low so bioeffects of ultrasound, if any, are minimized. Hence if the receiving sensitivity is augmented, the body can be interrogated at lower ultrasonic levels. Therefore, initially attention was focused on the receiving properties of the composite transducers.

The receiving characteristics of a transducer were assessed by its free-field voltage sensitivity (M_0). The free field sensitivity is the ratio of the output open circuit voltage to the free-field sound pressure in the

undisturbed plane progressive wave [11]. For an ultrasonic transducer, in addition to a highest possible voltage sensitivity, a fast pulse-echo time and low ringing are required in order to achieve good axial resolution. In an air backed transducer, these parameters are mainly determined by the piezoelectric coupling coefficient k_t and acoustic impedance Z of the transducer relative to that of the human body. In composite material since both k_t and Z are dependent on frequency, the reception characteristics are also expected to be a function of frequency.

The time delay spectrometry (TDS) technique [12], which allows the determination of the free-field voltage sensitivity as a continuous function of frequency, was used for calibrating the composite transducers. The TDS concept is based on converting a propagation time from transmitter to receiver into a certain frequency shift by keeping a constant frequency sweep rate so the time and frequency are linked together. Consequently, selectivity in time is proportional to selectivity in frequency with the sweep rate as conversion factor (e.g., 0-20 MHz sweep in one second corresponds to 20 Hz per microsecond). Only one direct signal will be detected, if a band pass filter receiving the electrical signal from the ultrasonic hydrophone is swept with a suitable delay in relation to the transmitter driving signal and has an appropriate (narrow) bandwidth. Hence, the TDS technique virtually eliminates the effects of multiple transmission paths, standing waves, and other interference caused by reflected signals.

The experimental arrangement employed for calibration (Figure 5) utilized a spectrum analyzer (HP 3585A) with a built-in frequency offset unit. The sine swept signal from the tracking generator drives a specially designed transducer (transmitter) via a power amplifier (ENI 411A). The ultrasonic signal in the far field was detected with a needle-like 1 mm diameter

calibrated PVF₂ polymer probe [13] and fed into the spectrum analyzer input (1 MΩ termination). The detected signal was compared with the calibration curve of the probe (Figure 6) to determine the absolute pressure at the probe as a function of frequency. The unknown receiver (composite) was then positioned exactly in the probe location and its voltage response was recorded on the spectrum analyzer. Ratio of the voltage response of the composite transducer to the sound pressure as determined by the polymer probe gives the free-field voltage sensitivity M_o of the receiver. The result is expressed in volts per micropascal or in decibels [dB = 20 log(M_o volt/μPa)].

In the above experiment, the spectrum analyzer was interfaced with a computer (HP 9825A) to record the data at each step and calculate the free-field voltage sensitivity as a function of frequency. The result was transferred back and displayed on the spectrum analyzer in dB relative to 1 V/μPa.

The calibration uncertainty of the polymer probe (Figure 6) in frequency range from 1 to 10 MHz is reportedly ±1.5 dB and ±2 dB from 0.1 to 1 MHz [14]. The probe exhibited good frequency characteristics up to 10 MHz with relatively high sensitivity and gave highly reproducible calibration of the composite transducers.

A number of commercial and custom made transducers were used as transmitters for calibrating the composites as receivers. The center frequency of the transducers varied from 0.3 to 3.5 MHz. The diameter of the transducers ranged from 0.5 to 2.5 cm. Such a wide variety of transmitters were used to make sure that the receiver was always in the far-field of the transmitter. The distance between the transmitter and receiver was maintained at 22 cms; the transmitter chosen in a particular case was such that this distance was greater than $\pi(a_1^2 + a_2^2)/\lambda$, where a₁ and a₂ are the radii of the transmitter and receiver, respectively and λ is the wavelength. Under such a

condition, it was estimated from Sabin's calculations [15] that the error introduced due to marginal test distance is less than 1 dB.

Using Mason's model [16], Shaulov and Smith [17] have derived an expression for the maximum open-circuit voltage response ($|V|_{\max}$) and the 3 dB bandwidth ($\Delta f_{3\text{dB}}$) of a homogeneous transducer without breaking or matching layers.

The expressions are given by

$$|V|_{\max} = \frac{4g_{33}Pt}{\pi} \left(\frac{Z_2}{Z_1}\right) \quad (6)$$

and

$$\Delta f_{3\text{dB}} = \frac{C}{\pi t} \left(\frac{Z_1}{Z_2}\right) \quad (7)$$

In these expressions, g_{33} is the piezoelectric voltage coefficient, P is the incident pressure, t is the thickness of the transducer, C is the velocity of sound in the piezoelectric medium, and Z_1 and Z_2 are the acoustic impedance of the loading medium and the transducer respectively.

The gain bandwidth product G , given by the product of the maximum voltage sensitivity and the 3 dB bandwidth is

$$G = \left(\frac{|V|_{\max}}{p}\right) (\Delta f_{3\text{dB}}) = \frac{4g_{33}C}{\pi^2} \quad (8)$$

For PZT 501A, $g_{33} = 26 \times 10^{-3}$ Vm/N, $C = 3800$ m/sec, and $G = 40$ Volt Hz/Pa.

The gain bandwidth product G was used in this work as the figure of merit in analyzing the receiving response of the composite transducers. The experimentally determined value of G for the composites was compared with the calculated value of G for PZT. Any improvement in the gain bandwidth product was consequently attributed to a more effective coupling of the ultrasonic energy due to the epoxy phase.

Composite samples with 10, 20, and 30 volume percent PZT and thickness ranging from 0.6 to 5.15 mm were calibrated for their receiving voltage response, and the results are summarized in Table 5. The maximum voltage sensitivity and the 3 dB bandwidth were the two main parameters measured in each case. From these measurements, the gain bandwidth product G was calculated.

The measurements on each sample were carried out at least twice to check the reproducibility. Most of the composites were calibrated using more than one transmitter. The reproducibility in the voltage sensitivity was always within 0.5 dB. From the consistency in the measurements performed, a maximum error in the figure of merit was estimated to be 10%.

From the velocity of the transverse waves in the Spurr's epoxy (1150 m/sec), the transverse wavelength was calculated at the frequency of the maximum reception sensitivity. As discussed earlier, the interaction between the PZT and the epoxy increases when the wavelength of the transverse wave becomes large compared to the periodicity. Thus the data were analyzed with respect to the ratio γ of the wavelength of the transverse waves to the periodicity of the lattice. An improvement in the figure of merit was expected as this ratio increased.

A typical plot of the receiving voltage sensitivity as a function of frequency for a composite with center frequency $f_0 \approx 2.25$ MHz is shown in Figure 7. It is very interesting to note that the minima seen in the receiving voltage sensitivities at frequencies below 2.5 MHz correspond to frequencies of lateral resonant modes f_{t1} , f_{t2} , etc. At these frequencies, the acoustic energy is dissipated in setting up complex lateral resonances in the composite.

As shown in Table 5, the figure of merit G for both 10 and 20% PZT composite with $f_0 \approx 2.25$ MHz appears to be independent of the volume fraction of PZT and is very close to that of the calculated value of 40 (VHz/Pa) for single phase PZT. The resonance data and the acoustic impedance results both indicated that the PZT rods in the composite at $f_0 = 2.25$ MHz vibrate relatively freely. The figure of merit G of the composite, being close to that of free PZT rods, is a further confirmation of the inferred vibration pattern in the composite when the periodicity is larger than the transverse wavelength. As the wavelength approaches the periodicity, laterally resonant modes are set up and the interference between the two modes results in a reduced figure of merit (sample 101). The figure of merit G gradually increases for larger ratio $\gamma = \lambda_s/d$, as expected. The figure of merit for $\gamma \approx 4$ is increased three folds over that of PZT. Samples 102, 201 and 301 are made of 10, 20, and 30 volume % PZT and have approximately the same value of the ratio γ (≈ 2). It is interesting to note that the figure of merit of these samples is close to 80 (VHz/Pa). Similar agreement can be found between samples 103 and 203 with $\gamma \approx 3$.

The observed behavior indicated that the performance of a composite is directly related to the ratio between the wavelength of transverse waves and the periodicity of the lattice regardless of volume percent of PZT. The above experimental observation suggests that one of the ways of increasing the efficiency of the composite for operation at high frequency (2 to 5 MHz) is to scale down the composite structure.

V. Calibration of Composite Transducers as a Transmitter of Ultrasonic Waves

The transmitting characteristics of a transducer for medical imaging can be characterized by its transmitting voltage response (S_0) and Q . The transmitting voltage response is the ratio of the sound pressure apparent at a

distance of one meter in a specified direction from the effective acoustic center of the transducer to the voltage applied across the electrical input terminals [11]. In this study, the transmitting voltage response of the composite transducers was determined at the near-field far-field transition region (a^2/λ distance) along the axis of the circular transducer. The Q of the transducer is the ratio of frequency at peak response to 3 dB bandwidth.

The same experimental set up shown in Figure 5 was used for the calibration of the composites as a transmitter. The composite transducer to be calibrated is excited by the tracking generator of the spectrum analyzer via the power amplifier. The ultrasonic signal at the a^2/λ distance detected by the calibrated needle-like polymer probe [13] was fed into the spectrum analyzer input (1 M Ω). The detected signal was adjusted for the calibration of the probe to calculate the pressure at a^2/λ distance. The excitation voltage as a function of frequency was also measured by feeding the output of the power amplifier to the input (1 M Ω) of the spectrum analyzer. Quotient of the detected pressure to the excitation voltage gives the transmitting voltage response. In this experiment also, the spectrum analyzer was interfaced with a computer (HP 9285A) to record the data at each step to calculate S_0 in dB re. 1 μ Pa/V. The test distance between the two transducers being only a^2/λ , an error is introduced in the measurement [15]. Since the radii of the composite transmitter and the probe were kept constant, and all the measurements were performed at a^2/λ distance from the projector the correction factor is a constant. The correction factor was estimated to be approximately equal to 3.5 dB, which should be added to the measured S_0 in all the experiments.

Composites of different thickness and volume fraction were calibrated for their transmitting voltage response at their thickness mode resonance frequency. The results are summarized in Table 6. Figure 8 shows a typical

plot of transmitting voltage sensitivity of a composite transducer with $f_0 \approx 2.25$ MHz.

It was observed that for transducers operating around 2.25 MHz, the transmitting voltage response (S_0) depends on the volume percent PZT. There was a 6 dB reduction in S_0 observed going from the 20% PZT composite to the 10% PZT composite. A further reduction of 8-10 dB was observed for the 5% PZT composite. The observation suggests that the transmitting response of a composite transducer is proportional to the volume fraction of the piezoelectrically active material present in the composite. If this hypothesis is correct, it plausibly explains why the 20% composites gave about twice the pulse-echo signal of the 10% composite (Table 1).

The composite transducers resonating below 1 MHz were calibrated to examine the effect of the cooperative interaction between PZT and epoxy on the transmitting voltage response. However, a frequency independent figure of merit could not be defined to ascertain the frequency dependence of the transmitting voltage response because of the following reasons: 1. At low frequencies where the dimensions of the projector are small in comparison with the wavelength in water, the transmitting characteristics are well described [11]. The piezoelectric material being stiffness controlled, a constant voltage applied to the transducer results in a constant displacement. Furthermore, since acoustic pressure generated by the transmitter is proportional to the acceleration, the transmitting voltage response increases at a rate of 12 dB/octave [$S_0 \propto (\text{frequency})^2$]. At high frequencies, where the transducer dimensions are comparable to the wavelength, the simple source concept cannot be applied because of resonance effects. 2. The transmitting voltage response also depends on the directivity pattern of the transducer [18]. When the circumference of the circular transducer is less than one-half

wavelength, that is $ka = 2\pi a/\lambda < 0.5$, the piston behaves like a point source, and when ka exceeds 3 the piston is more directional.

In the present study, the following assumptions were made to evaluate the frequency dependence of the transmitting voltage response of the composite. Since all the composites are operated at half wavelength thickness resonance, the thickness t of the sample bears a constant relation with wavelength at the operating frequency. Furthermore, since the amplitude of excitation signal is kept constant, a constant displacement can still be assumed in comparing the transmitting voltage response at different frequencies. Under this assumption, the transmitting voltage response is expected to increase at a rate of 12 dB/octave as the frequency is increased [11]. Because the radius of the transducer is kept constant, an increase in the operating frequency makes the ultrasonic beam from the transducer less divergent, resulting in an increased pressure along the axis [18]. From the above argument, it appears that the frequency dependence of the transmitting voltage response should be greater than 12 dB/octave.

Figure 9 shows the plot of maximum transmitting voltage response as a function of frequency. The transmitting voltage responses for 10 and 20 percent PZT composites were 195.8 and 201.9 dB (re. 1 μ Pa/V) respectively. With the previously stated assumptions, a reduction of 24 dB in the transmitting voltage response was expected for the measurements performed at 0.5 MHz. However, a reduction of only 10 dB was actually measured. Also it is observed from Figure 9 that at low frequencies (around 0.5 MHz), the rate of increase of S_0 with frequency fits a straight line of slope 8-10 dB/octave.

These results confirm that the transmitting voltage response of composite transducers is, as anticipated, a function of frequency. At frequencies where the transverse wavelength is large compared to the periodicity, there appears to be an increase (~ 14 dB) in the transmitting voltage response. The

enhancement can be attributed to the improved interaction between PZT and epoxy at lower frequencies (<0.5 MHz). The improved performance should, however, be extended to higher frequency range (2-5 MHz) typical for ultrasonic diagnostic applications. This will require having a large ratio of the transverse wavelength to the periodicity at the operating frequency.

The Q of the composite transducers operating at different frequencies are compared in the last column of Table 6. For composites resonant around 2.25 MHz, Q is approximately 6 and is comparable to the values of Q measured by the resonance technique in air [1]. Coupling the transducer to water load has not altered the bandwidth characteristics, which is an indication of poor coupling of ultrasonic energy into water. Composites resonant around 0.5 MHz had relatively large Q in air (20-30), but by water loading, the Q was reduced to about 4. This is most likely due to a better matching of ultrasonic energy between the composite and water.

The acoustic impedance at 2.25 MHz for a given volume percent PZT composite is much lower than the value at about 0.5 MHz. The acoustic impedance data suggest that the transfer of acoustic energy from water to the composite or vice versa should be better at higher frequencies. The results on the transmitting and receiving voltage responses indicate that at higher frequency, the energy is not being properly coupled to the piezoelectric phase although the transfer of energy between the two media may be more effective. The observed behavior is again an indication of poor acoustic coupling between PZT and polymer at frequencies (2.25 MHz) where the transverse wavelength is much smaller than the periodicity. Thus, if the composites prepared in the study are operated around 0.5 MHz, there appears to be efficient transfer of acoustic energy from PZT to water via the epoxy phase. As a result,

substantial improvement in the receiving and transmitting voltage responses was observed.

VI. Effect of the Matching Layer on the Performance of Composite Transducers

The composite transducers showed a substantial improvement in receiving and transmitting voltage responses, when operated at resonance in the low frequency range where the transverse wavelength is large compared to the periodicity. The Q of the composite transducer was reduced from about 25 to about 4 when coupled with water load. The measured value of Q is relatively large for medical diagnostic applications where a Q of 2 to 2.5 is usually recommended [19] for a good axial resolution. Larger Q in the composite transducers was also apparent from the slow pulse-rise time and prolonged ringing in the pulse-echo response.

Relatively large Q values observed in the composite transducers was attributed to the acoustic impedance mismatch between the transducer and the load. The acoustic impedance of a 20% PZT composite in the low frequency range is 7.3 M rayl (Table 4) which results in a pressure reflectivity of 65% with water load. To improve the impedance matching, a matching layer between the transducer and the load was considered. For optimum transmission, the matching layer has to be a quarter wavelength in thickness and of characteristic impedance equal to the geometric mean of those of the transducer and of the loading medium [20]. In the present situation, Z of the matching layer was calculated to be 3.3 M rayl. Several polymer systems have acoustic impedance in this range.

A 20% PZT composite of thickness 3.07 mm was chosen to study the effect of a quarter wave matching layer. Since lucite ($Z = 3.2$ M rayls) was readily available and had an acoustic impedance very close to the required value, a quarter wave matching layer of lucite material was pressure bonded to the

transducer using an epoxy (Tracon 2115). The thickness of the bonding layer was less than 25 μm . The frequency (f_0) at maximum pulse-echo response was 0.54 MHz. This composite with the matching layer was characterized for its receiving and transmitting voltage response.

The gain bandwidth product (G) in the receiving mode of the matched transducer was 180 (V \cdot Hz/Pa) which is 4.5 times higher than that of a corresponding PZT rod. The transducer had a very broad band response with Q of 1.8. The transmitting voltage sensitivity was 186.5 dB re 1 $\mu\text{Pa/V}$ and Q in the transmission mode was also about 1.8. Comparing the results of the matched transducer with those of unmatched 20% PZT composites such as 201, 202, 251 (Tables 5 and 6) operating around 0.5 MHz, it can be seen that major contributions for the enhanced response come from the broadening of the bandwidth. This is quite evident from the pulse-echo response of the matched transducer shown in Figure 10. The pulse-rise time is very fast and the ringing is low (Figure 10a), as exemplified in the broad nature of the frequency spectrum (Figure 10b). These experiments demonstrate that composite transducers with a single matching layer can have excellent performance in medical diagnostic applications.

As mentioned previously, the improved performance should, however, be extended to the higher frequency range (2 to 5 MHz) typical for ultrasonic diagnostic applications. From the experimental results, the substantial improvement can clearly be attributed to the strong interaction between the PZT and epoxy where the transverse wavelength was large compared to the periodicity. This observation suggests that one of the ways of increasing the efficiency of the composite for operation at high frequency is to scale down the composite structure. This means that the rod diameter and the periodicity of the lattice in the composite structure should be scaled down by at least a factor of five to operate at approximately 2 MHz.

VII. Focused Composite Transducer

This section deals with shaping a composite transducer to focus sonic beam to a narrow beam width. Composite materials can be molded into curved shapes by simple thermal process as explained below.

Thin composites (~ 0.6 mm) of 10 and 20% PZT were prepared in a flat shape by the usual procedure. A spherical mold with a curvature of 9.5 cm was heated in a small oven to 80°C which is just above the glass transition temperature of the Spurr's epoxy ($T_g \approx 70^\circ\text{C}$ at 100-Hz). At this temperature epoxy was quite soft and flexible. The composite sample was placed on the mold and allowed to reach thermal equilibrium. A slight deformation under gravity was noticed. The backing mold was placed on top to force the composite to conform to the spherical curvature of the mold. The mold set was kept at 80°C for an hour or so and cooled slowly ($\sim 1/2^\circ$ per minute) to room temperature.

To measure the axial beam profile, the focused composite transducer was driven by continuous wave excitation at the frequency of maximum response. The calibrated miniature hydrophone probe (Section IV) [13] was used to measure the transmitting voltage response along the axis of the transducer. Figure 11 shows the axial beam profile of a 20% PZT composite transducer ($f_0 = 2.25$ MHz) before and after focusing. The peak response for nonfocused transducer was 200 dB re 1 $\mu\text{Pa}/\text{V}$ at 12.1 cm which corresponds to the expected a^2/λ distance. After focusing, the response peaked at an axial distance of 7.6 cm with a gain of 8.5 dB in the transmitting voltage response. Table 7 summarizes the results of the focusing studies on both 10 and 20% PZT composite transducers. The maximum response in all the cases occurred at a distance slightly farther than the expected 6 cm based on the theoretical calculations by O'Neil [21]. This discrepancy is probably due to the fact

that the theory was developed for a single phase material and may not be fully valid for the composite transducer.

Lateral beam profile at the distance of maximum response was measured using the polymer probe. An x-y-z micromanipulator was used to move the hydrophone probe away from the axis of the transducer in steps of 0.63 mm. The lateral beam width was calculated from the points where the effective relative pressure was $1/e = 0.368$ of the peak [22]. The lateral beam widths at the peak response are listed in Table 7. There was nominally a 30 to 40% reduction in the beam width after focusing. The beam widths are slightly larger than the theoretically calculated value of 4.6 mm [22].

The tone-burst pulse-echo response with the stainless steel reflector at the distance corresponding to the peak response was measured for both the nonfocused and focused transducers (Table 7). Since the transmitting voltage response was increased by a factor of 2 (6 dB) on focusing, a considerable improvement in the pulse-echo amplitude was also expected. Surprisingly, it was noticed that in most cases there was actually a small decrease in the pulse-echo amplitude. It was suggested that the spherical curvature on the transducer affects the receiving voltage sensitivity and is the cause for the decreased pulse-echo signal. A further support for this is presented in the following paragraph.

The degree of the concavity h of the transducer is comparable to the wavelength λ in water at 2.25 MHz ($h/\lambda = 0.7$), and hence modifies substantially the phase profile of the reflected beam at the transducer face. Since the receiving voltage sensitivity is dependent on the phase profile of the pressure at the transducer face [15], focusing was expected to affect the receiving sensitivity. As anticipated, the average gain bandwidth product of

a focused transducer operating at 2.25 MHz was 26 Hz V/pa compared to the measured value of 36 Hz V/pa for a flat transducer (Table 5).

VIII. Conclusions

The composite transducers were initially characterized by the pulse-echo method. To evaluate the composites thoroughly, the acoustic impedance, and the transmitting and receiving voltage responses were measured separately as a function of frequency. Frequency dependence of the acoustic impedance were modeled by calculating the average elastic modulus at two extreme conditions. The acoustic impedance modeled using the Voigt constant strain model showed excellent agreement with the measured values at 0.3 MHz. Measured values of acoustic impedance at 3.5 MHz were in excellent agreement with the values modeled by the constant stress model.

The figure of merit in the receiving mode for a composite with $f_0 = 2.25$ MHz was close to the calculated value for a single phase PZT. This result indicated virtually no contribution from the epoxy phase because of the weak interaction between PZT and epoxy. As the operating frequency was reduced below 0.5 MHz, the figure of merit G was increased by a factor of 3. The substantial improvement in G provided additional evidence for the strong interaction between PZT and epoxy at low frequencies. A similar improvement was observed in the transmitting voltage response for composites operated around 0.5 MHz.

The performance of the composite transducer was further improved by the use of a quarter wavelength matching layer of lucite material between the transducer and load. The figure of merit G in the receiving mode of the composite transducer was increased by about 50 percent when the matching layer was used. The Q of the matched transducer was less than 2, which is advantageous in achieving good axial resolution.

The results show that the 1-3 composite materials are excellent candidates for medical diagnostic transducer applications. However, it should be noted that the improved performance of the composite transducer should be extended to higher frequencies (2 to 5 MHz) typical for the ultrasonic diagnostic applications. It was demonstrated that the composite transducers can be focused by a relatively simple technique. As a result of focusing, it was possible to generate a concentrated sonic beam with narrower beam width.

Acknowledgements

The authors are grateful to Dr. W.A. Smith and Dr. A. Shaulov of North American Philips Laboratories and Dr. P.A. Lewin of Drexel University (Dept. of Electrical and Communication Engineering and Biomedical Engineering and Science Institute) for their comments and discussions, Mrs. Linda Webster for preparing samples and Mr. P. Moses for writing software for computer interfacing. Financial support was provided by the North American Philips Laboratories.

REFERENCES

1. Gururaja, T.R., W.A. Schulze, L.E. Cross, R.E. Newnham, B.A. Auld and J. Wang, 'Piezoelectric Composite Materials for Ultrasonic Transducer Applications. Part I. Resonant Modes of PZT Rod-Polymer Composites,' IEEE Trans. on Sonics and Ultrasonics (previous paper in this volume).
2. Erikson, K.R., 'Tone-Burst Testing of Pulse-Echo Transducer,' IEEE Trans. Sonics and Ultrasonics, SU-26, 7-14 (1979).
3. McSkimin, H.J., 'Ultrasonic Methods for Measuring the Mechanical Properties of Liquids and Solids,' Physical Acoustics, Vol. 1, Part A, Chapt. 4, Ed. by W.P. Mason, Academic Press, NY (1964).
4. Kinsler, L.E. and A.R. Frey, Fundamentals of Acoustics, 2nd Edition, Wiley, NY (1962).
5. Rose, J.L. and B.B. Goldberg, Basic Physics in Diagnostic Ultrasound, Wiley, NY (1979).
6. Lees, S. and C.L. Davidson, 'Ultrasonic Measurement of Some Mineral Filled Plastics,' IEEE Trans. on Sonics and Ultrasonics, SU-24, 222-225 (1977).
7. Berlincourt, D.A., D.R. Curran, and E. Jaffe, 'Piezoelectric and Piezomagnetic Materials and Their Function in Transducers,' Physical Acoustics, Vol. 1, Part A, Chapt. 3, Ed. by W.P. Mason, Academic Press, NY (1964).
8. McSkimin, H.J. 'Measurements of Elastic Constants at Low Temperatures by Means of Ultrasonic Waves - Data for Silicon and Germanium Single Crystals and for Fused Silica,' J. Appl. Phys. 24, 988-997 (1953).
9. Gururaja, T.R., W.A. Schulze, and L.E. Cross, 'Bulk Mechanical Properties of the Spurr's Epoxy and Eccogel Polymers,' (to be published in J. Polym. Sci.).

10. O'Brien, W.D., Jr., 'Safety of Ultrasound,' Handbook of Clinical Ultrasound, Wiley, NY (1978).
11. Bobber, R.J., Underwater Electroacoustic Measurements, Naval Research Laboratory Publication, Washington, DC (1970).
12. Lewin, P.A., 'Calibration and Performance of Evaluation of Miniature Ultrasonic Hydrophones Using Time Delay Spectrometry,' IEEE Ultrasonic Symposium Proceedings, 660-664 (1981).
13. Lewin, P.A., 'Miniature Piezoelectric Polymer Ultrasonic Hydrophone Probes, Ultrasonics,' 213-216 (1981).
14. Lewin, P.A. (private communication).
15. Sabin, G.A., 'Calibration of Piston Transducers at Marginal Test Distances,' J. Acoust. Soc. Amer. 36, 168-173 (1964).
16. Mason, W.P., Electromechanical Transducer and Wave Filters, Von Nostrand, Princeton, NJ (1942).
17. Shaulov, A. and W.A. Smith (to be published).
18. Beranek, L.L., Acoustics, McGraw-Hill, NY (1954).
19. Benjavic, R.A. and J.A. Zagzebski, 'Ultrasonic Pulse-Echo Beam Width and Axial Response: Approximations for Clinical Broadband Focused Transducer,' Ultrasound in Med. and Biol. 7, 63-71 (1981).
20. Goll, J.H., 'The Design and Broad-Band Fluid-Loaded Ultrasonic Transducers,' IEEE Trans. on Sonics and Ultrasonics, SU-26, 385-393 (1979).
21. O'Neil, H.T., 'Theory of Focusing Radiators,' J. Acous. Soc. Amer. 21, 516-526 (1949).
22. Lees, S., 'Useful Criteria in Describing the Field Pattern of Focusing Transducers,' Ultrasonics 16, 229-232 (1978).

FIGURE CAPTIONS

- Figure 1 Block diagram of tone-burst pulse-echo method.
- Figure 2a Acoustic impedance of composites as a function of frequency (0 to 1.5 MHz).
- Figure 2b Acoustic impedance of composites as a function of frequency (1 to 3.5 MHz).
- Figure 3 Echo signal from composite samples
- (a) At a frequency far away from the minima in Z .
 - (b) At a frequency corresponding to minima in Z .
 - (c) At a frequency corresponding to minima in Z (expanded time scale).
- Figure 4 Correction on the value of acoustic impedance due to diffraction losses.
- Figure 5 Experimental set up for calibration of ultrasonic transducers.
- Figure 6 Calibration chart of PVDF ultrasonic probe.
- Figure 7 Receiving voltage sensitivity of a composite transducer ($f_0 \approx 2.25$ MHz).
- Figure 8 Transmitting voltage response of a composite transducer ($f_0 \approx 2.25$ MHz).
- Figure 9 Plot of maximum transmitting voltage response (S_0) as a function of frequency at maximum S_0 .
- Figure 10 Pulse-echo response of a composite transducer with a single matching layer (spectrum analyzer method). (a) Wave form of the echo signal. (b) Frequency content of the echo signal.
- Figure 11 Axial beam profile of a non-focused and focused composite transducer.

Table 1.
 Pulse-Echo Response of Composite Transducers.
 Center Frequency $f_0 \approx 2.25$ MHz.

V lume % PZT	PZT Rod Diameter (mm)	Echo Signal (50Ω Load) V_{50} (volt)	6 dB Bandwidth BW (MHz)	Q	Figure of Merit $V_{50}BW$	Echo Signal (Diode Isolation) V_D (volt)	6 dB Bandwidth BW (MHz)	Figure of Merit $V_D BW$
10	0.45	0.8	0.4	5.6	0.32	1.5	0.50	0.75
20	0.45	2.4	0.45	5	1.08	3.25	0.45	1.46
30	0.45	2.4	0.5	4.5	1.20	--	--	--
10	0.28	0.35	0.7	3.2	0.25	1.0	0.85	0.85
20	0.28	1.25	0.45	5	0.56	2.1	0.45	0.95
Commercial Transducer (Rohe # 5601)	--	1.2	1.0	2.25	1.2	3.0	1.3	3.9

Table 2. Acoustic Impedance (Z) of Composites.

Volume % PZT	Region 1 (Frequency > 2 MHz)		Region 3 (Frequency < 0.4 MHz)	
	Calculated (Z)	Measured (Z) at 3.5 MHz	Calculated (Z)	Measured (Z) at 0.3 MHz
5	2.6	--	3.3	2.3
10	2.9	2.8	4.1	3.5
20	3.6	3.0	6.0	4.9
30	4.5	3.7	8.2	6.5

Table 3. Acoustic Impedance by Transmission Technique.

Volume % PZT	Measured Longitudinal Velocity (m/sec)	Measured Z 10^6 Rayl (at 0.5 MHz)	Calculated Z 10^6 Rayl (from Table 2)
20	2682 \pm 8	6.1	6.0
30	2780 \pm 14	8.5	8.2

Table 4. Acoustic Impedance Values as Determined by Resonance Technique.

Volume % PZT	Region 1 (>2 MHz)		Region 3 (~0.4 MHz)	
	Wavelength << Periodicity		Wavelength >> Periodicity	
	Calculated Z	Measured Z	Calculated Z	Measured Z
5	2.6	5.1	3.7	3.7
10	2.9	5.9	4.9	4.9
20	3.6	8.4	7.5	7.3
30	4.5	--	10.3	10.3

Table 5.
Receiving Voltage Response (M_0) of Composite Transducers.

Sample No	Volume % PZT	Rod Diameter mm	Thickness t (mm)	Periodicity (d) mm	Frequency at Max Response (MHz)	Transverse Wavelength at Max Sensitivity (mm)	$\gamma = \frac{\lambda_s}{d}$	Max Sensitivity M_0 ($\mu\text{V}/\text{Pa}$)	3 dB Bandwidth $\Delta f_{3\text{dB}}$ (kHz)	Figure of Merit $M_0 \Delta f_{3\text{dB}}$ ($\frac{\mu\text{V}}{\text{Pa}}$)
100	10	0.45	0.66	1.27	2.25	0.50	0.39	130	288	37.4
101	10	0.45	1.93	1.27	0.88	1.29	1.01	200	105	21.0
102	10	0.45	3.64	1.27	0.44	2.60	2.04	496	168	83.2
103	10	0.45	5.15	1.27	0.30	3.83	3.01	955	120	114.6
200	20	0.45	0.66	0.9	2.25	0.50	0.55	144	252	36.2
201	20	0.45	2.54	0.9	0.625	1.84	2.04	531	154	81.8
202	20	0.45	3.05	0.9	0.525	2.21	2.45	750	133	99.8
203	20	0.45	3.95	0.9	0.400	2.86	3.17	933	115	107.3
205	20	0.45	4.60	0.9	0.352	3.26	3.62	1047	109	114.1
205	20	0.45	5.15	0.9	0.300	3.83	4.25	1128	110	124.1
301	20	0.78	2.60	0.6	0.625	1.84	3.06	684	133	90.9
301	30	0.45	2.44	0.73	0.7	1.64	2.74	575	140	80.5

AD-A160 465

PIEZOELECTRIC AND ELECTROSTRICTIVE MATERIALS FOR
TRANSDUCER APPLICATIONS(U) PENNSYLVANIA STATE UNIV
UNIVERSITY PARK MATERIALS RESEARCH LAB

4/4

UNCLASSIFIED

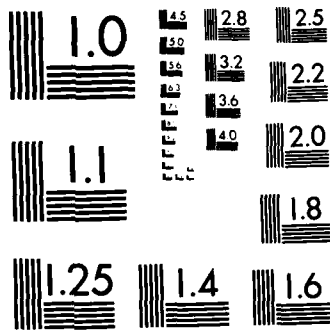
L E CROSS ET AL

MAY 85 N00014-82-K-0339

F/G 9/1

NL

							END						
+													
													END FILED D12



MICROCOPY RESOLUTION TEST CHART
NATIONAL BUREAU OF STANDARDS-1963-A

Table 6.
Transmitting Voltage Response (S_0) of Composite Transducers.

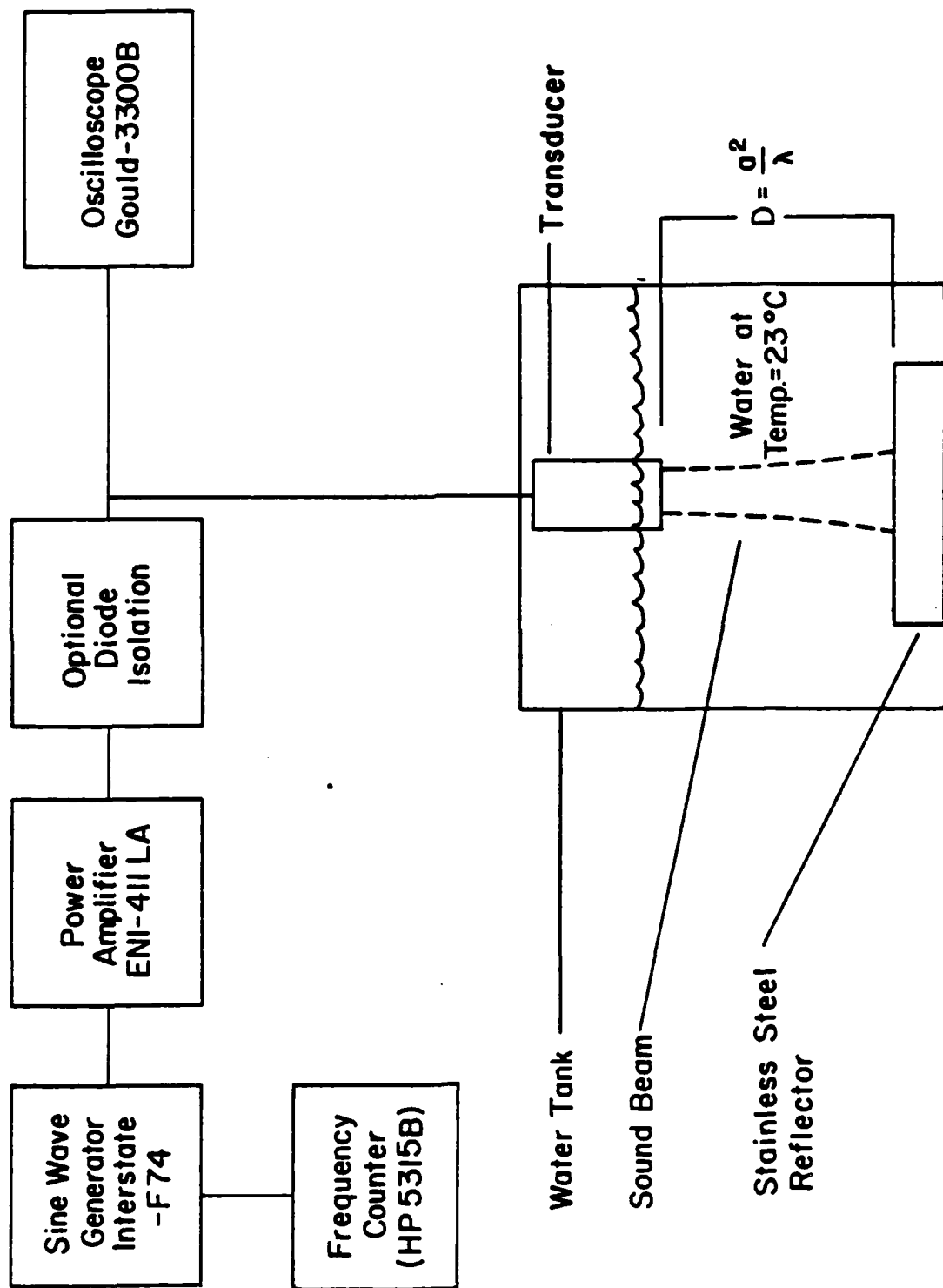
Sample No.	Volume % PZT	Thickness (mm)	Frequency at max Response (f_0)	Transverse Wavelength at Max Response (λ_s , mm)	λ_s periodicity d	S_0 in dB re 1 $\mu\text{Pa}/\text{V}$	$Q = \frac{f_0}{\Delta f_{3\text{dB}}}$
100	10	0.66	2.25	0.50	0.39	195.8	5 to 6
102	10	3.64	0.425	2.70	2.13	185.0	---
103	10	5.15	0.287	4.00	3.15	181.5	3.8
200	20	0.66	2.25	0.50	0.55	201.9	6.7
201	20	2.54	0.540	2.13	2.36	194.0	4.8
202	20	3.05	0.480	2.39	2.66	191.5	5.1
203	20	3.95	0.370	3.11	3.45	188.7	4.3
204	20	4.60	0.312	3.68	4.09	186.6	4.8
301	30	2.44	0.597	1.93	2.63	196.4	5.0

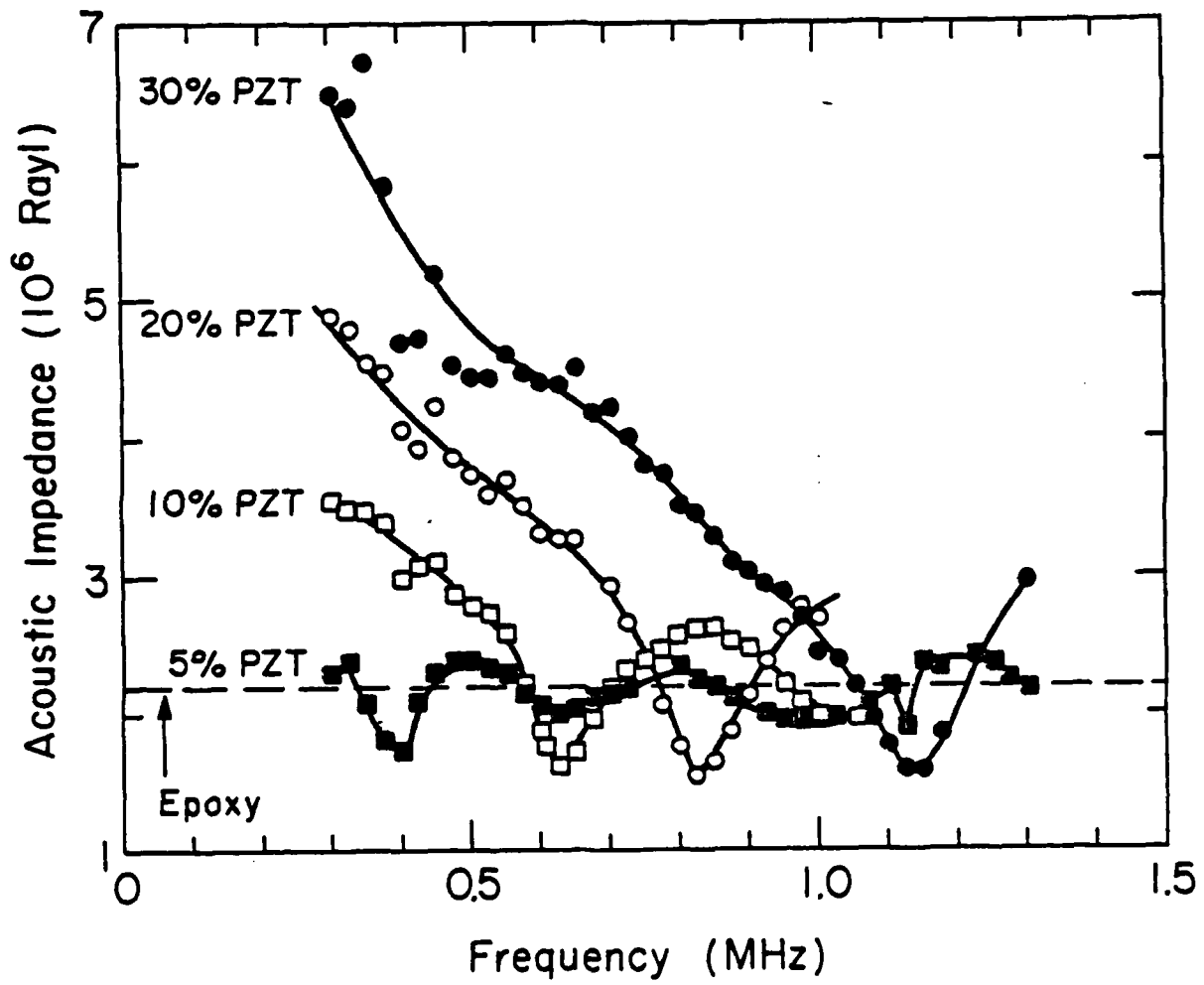
Table 7.

Beam Width, Transmitting Voltage Response (S_0) and Pulse-Echo Response of Focused Composite Transducers. (Radius of Curvature = 9.5 cm).

Volume % PZT	Sample No.	Frequency at Max S_0 (MHz)	Focused?	$D = a^2/\lambda$ (cm)	Distance, T at Peak S_0	Max S_0 in $\frac{1 \mu Pa}{V}$ dB re $\frac{1 \mu Pa}{V}$	Beam Width* 1/e criteria (cm)	Pulse- Echo Voltage, V at T
10	100a	2.05	No	12.3	11	196.8	0.82	1.5
			Yes	---	6.6	201.8	0.51	1.1
10	100b	2.02	No	12.1	11.6	194.9	1.00	1.3
			Yes	---	7.1	201.2	0.63	1.1
20	200a	2.01	No	12.1	12.1	200	0.83	1.9
			Yes	---	7.6	208.5	0.58	2.4
20	200b	2.01	No	12.1	12.1	201.9	1.00	2.6
			Yes	---	7.6	206.6	0.66	2.2

*Beam width measured at a pressure level 1/e = 0.368 of the peak.





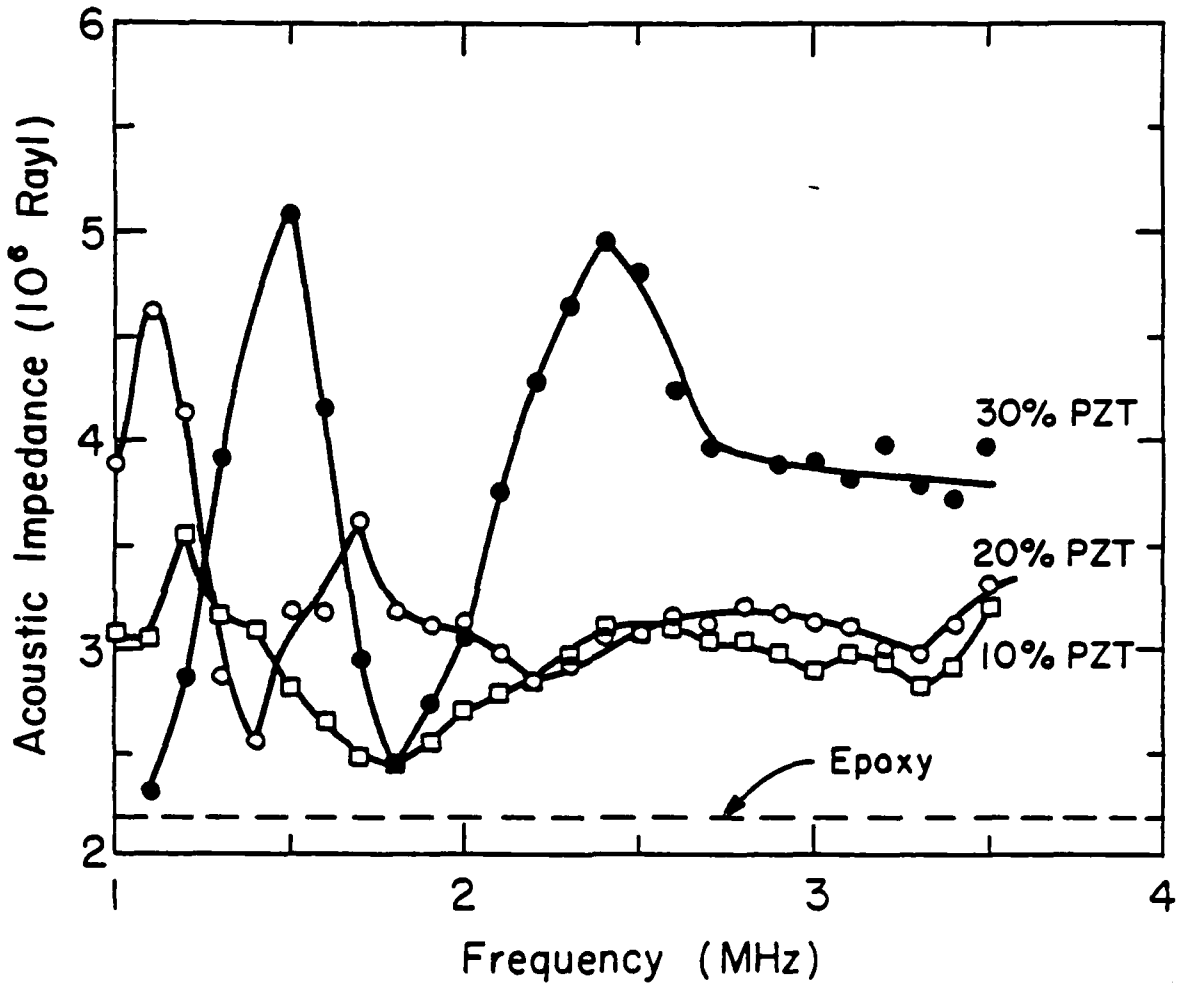
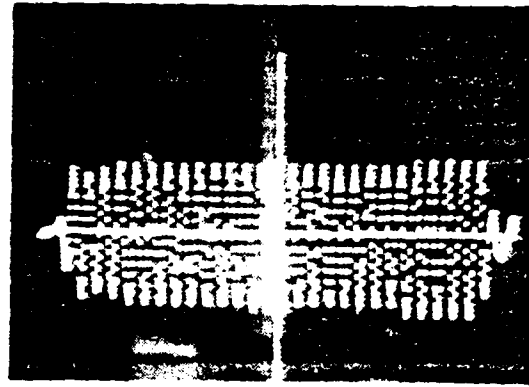
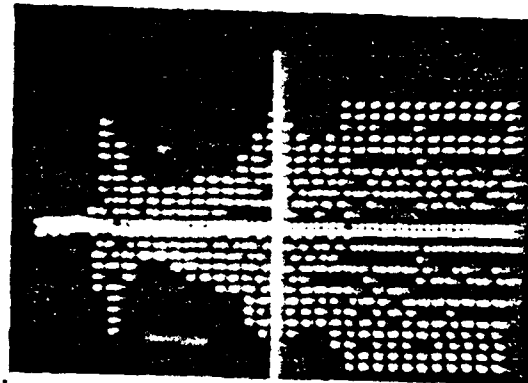


Fig 2b

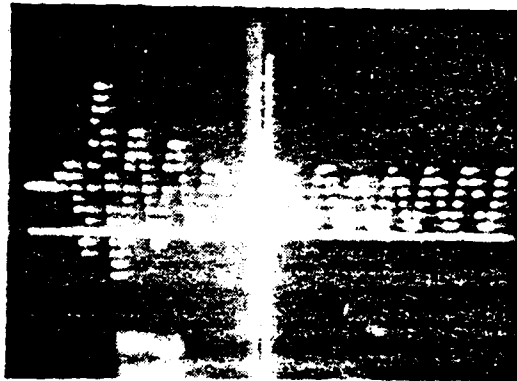
2 17 17 17



(a)



(b)

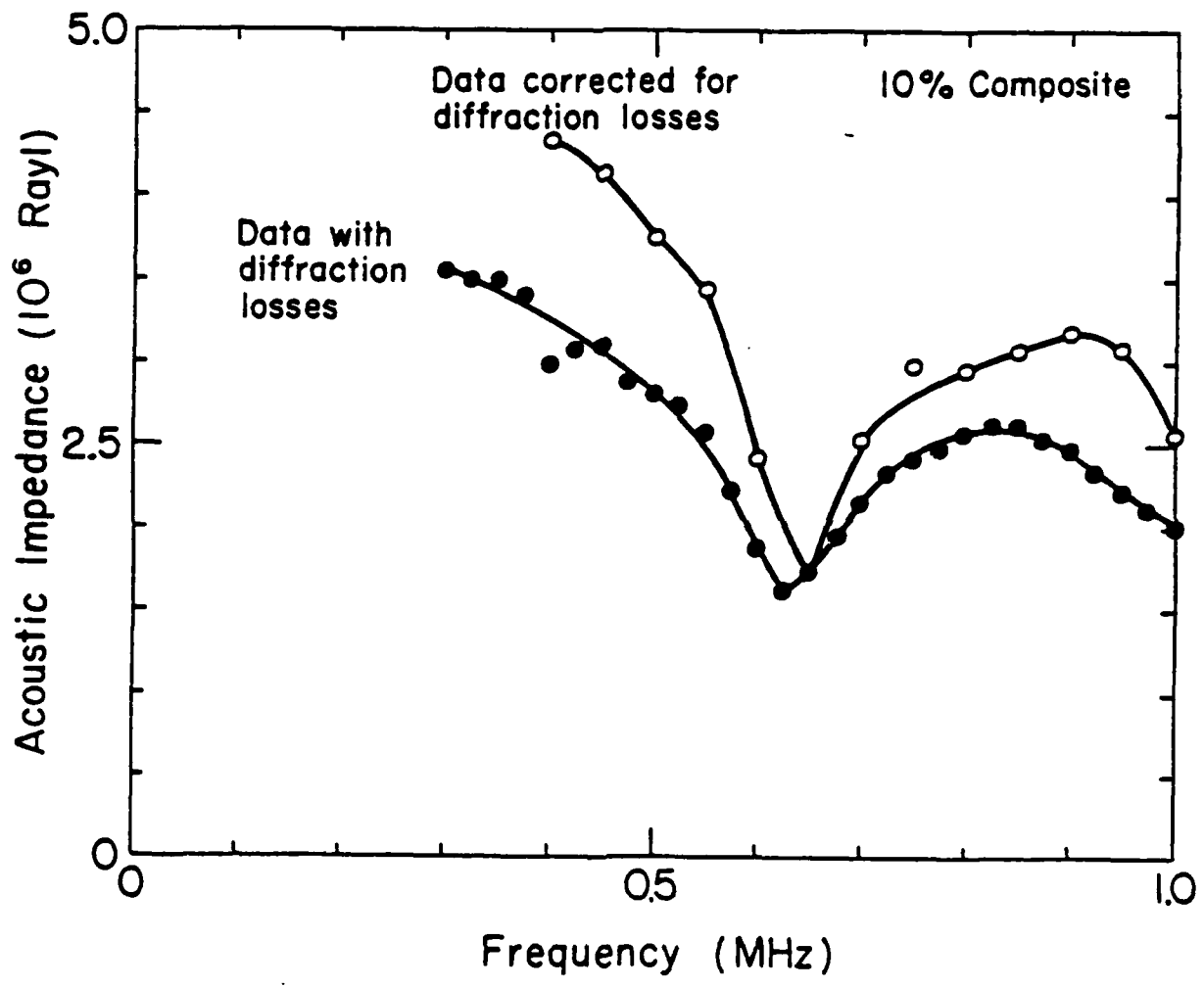


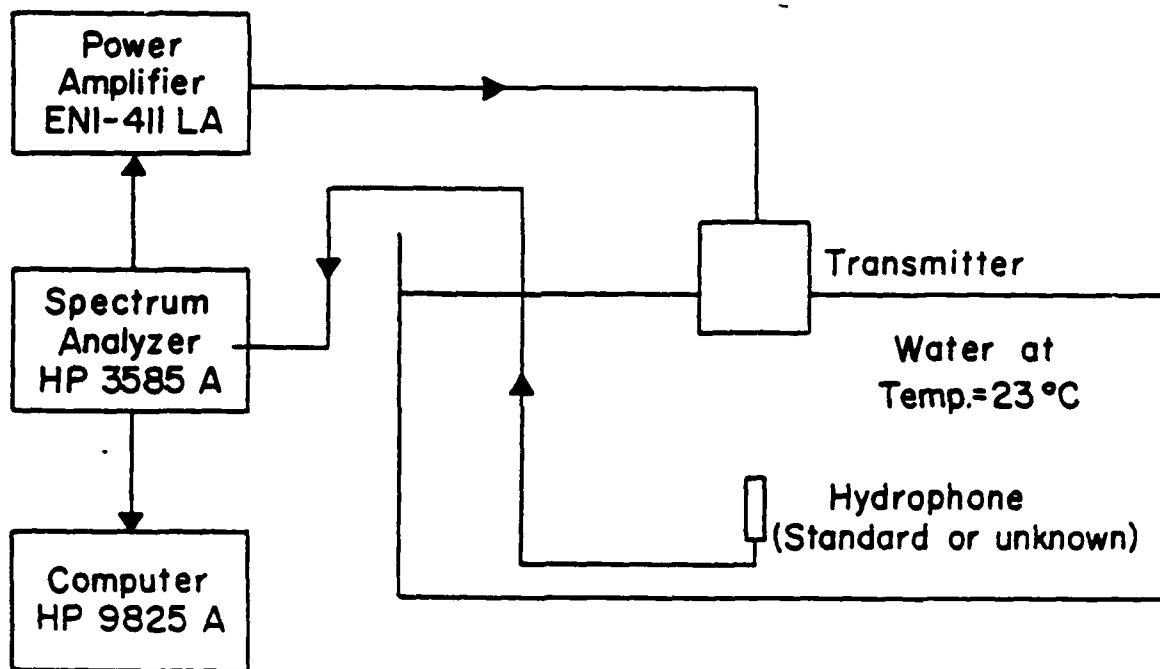
(c)

→ amplitude

→ time

3.4.18.72





Suryaraja

Calibration Chart for PVDF Ultrasonic Probe

Free Field Frequency Response

MEDICOTEKNISK INSTITUT
The Danish Institute of Biomedical Engineering

End of Cable
Voltage Sensitivity
(dB re. 1V/ μ P_a)

Date: 29 Jan. 82
Skn: CAL
Diameter: 1.0
Serial no.: 465

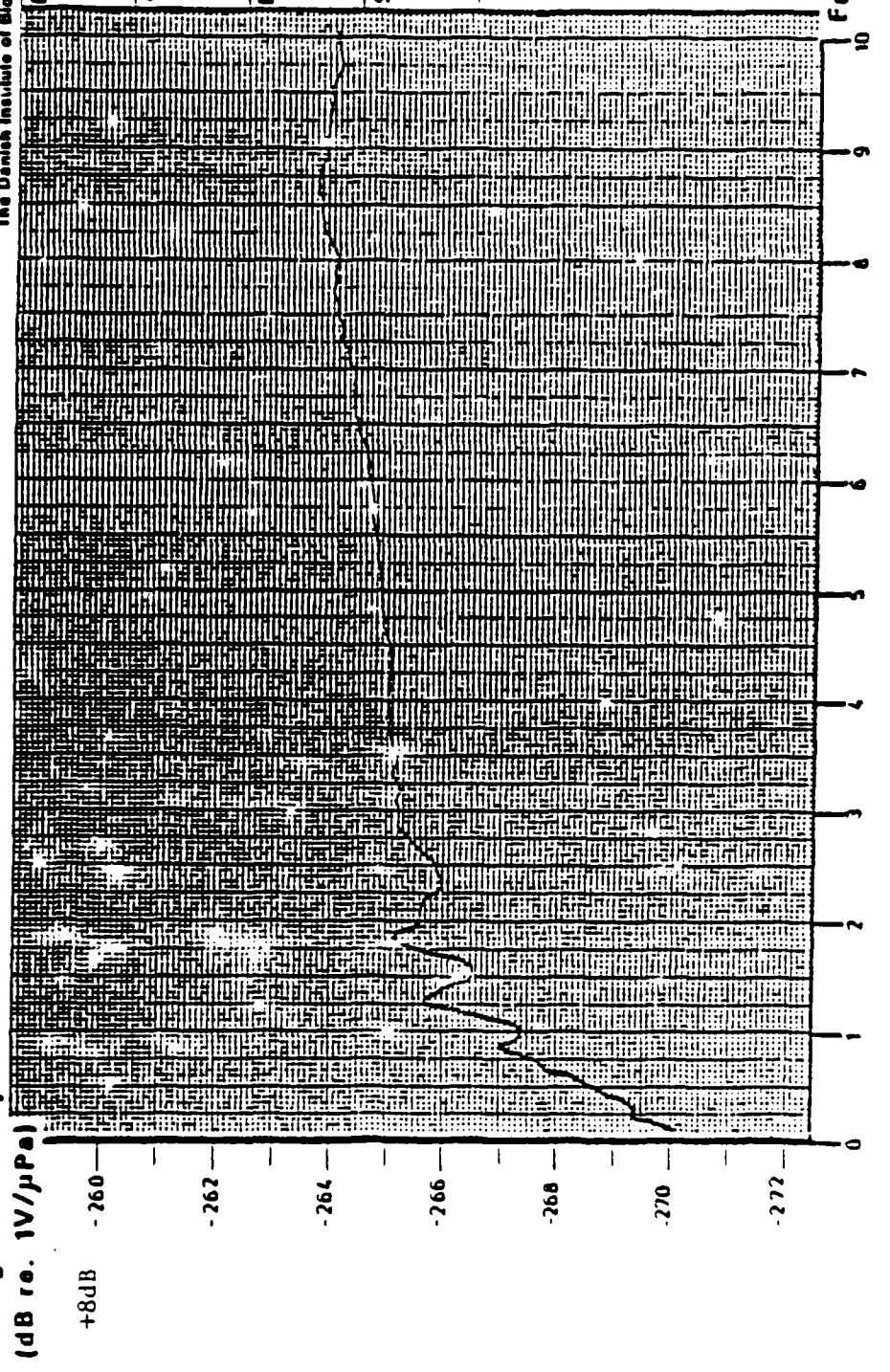


Fig. 7

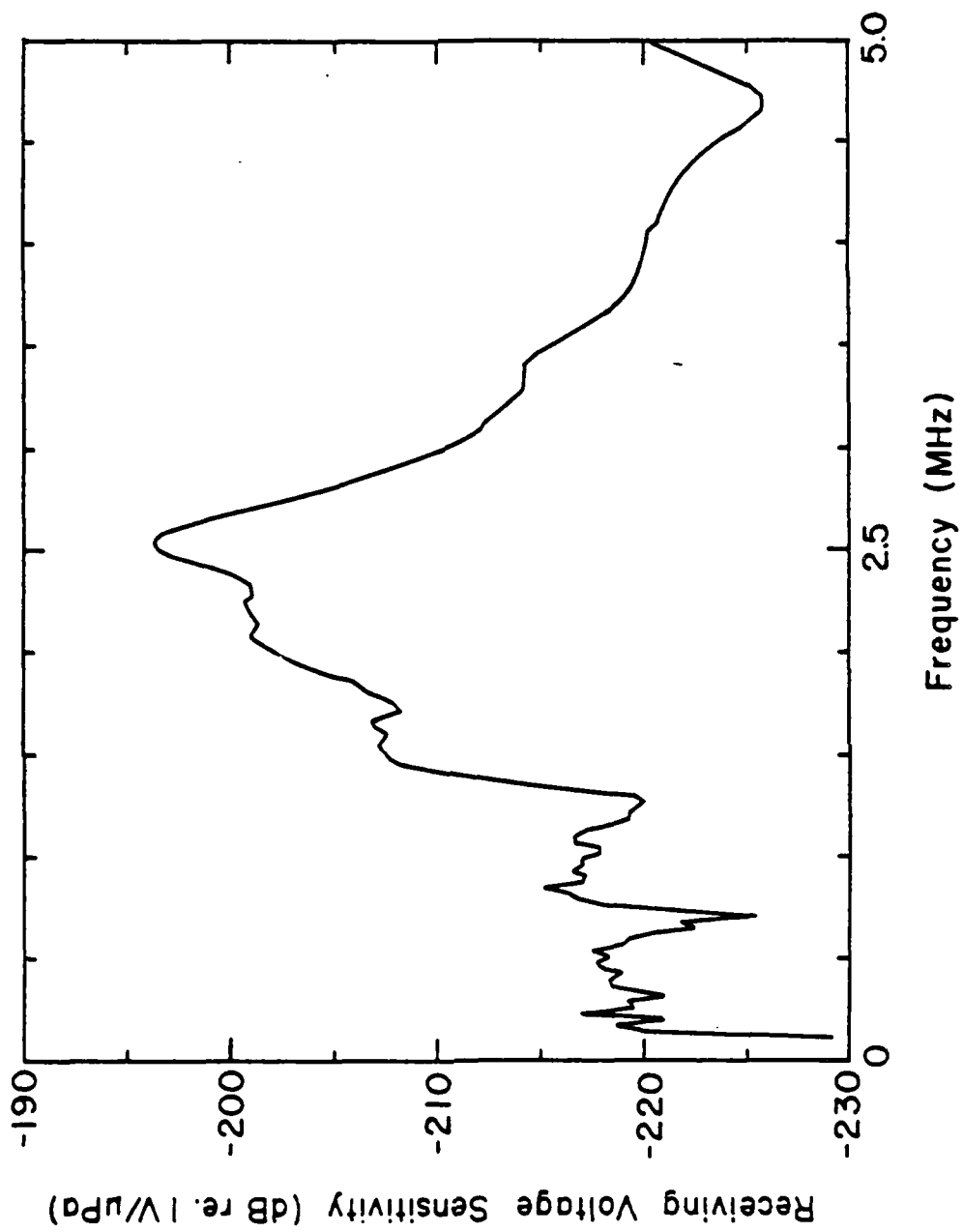
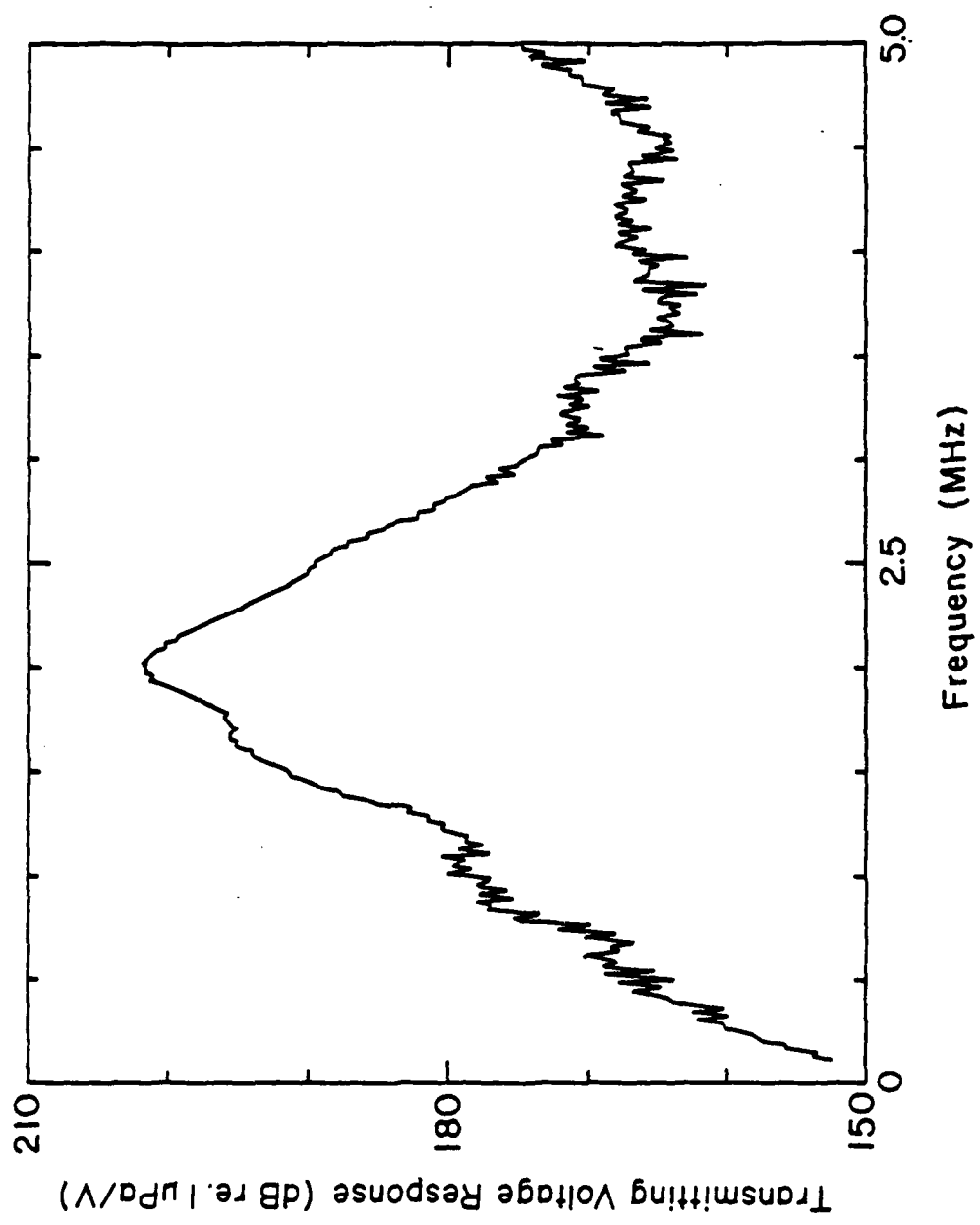
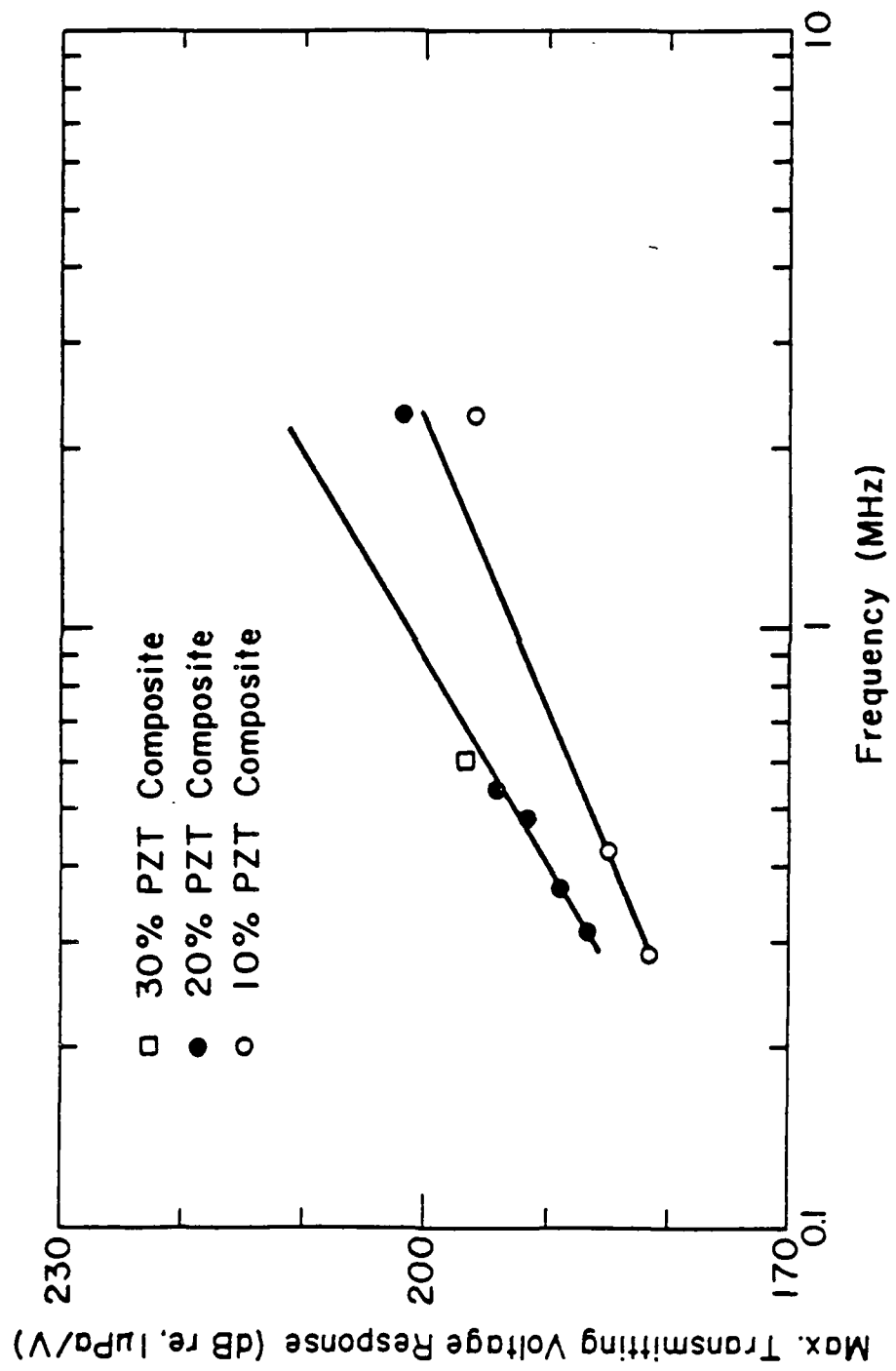


FIG 7

Surveys

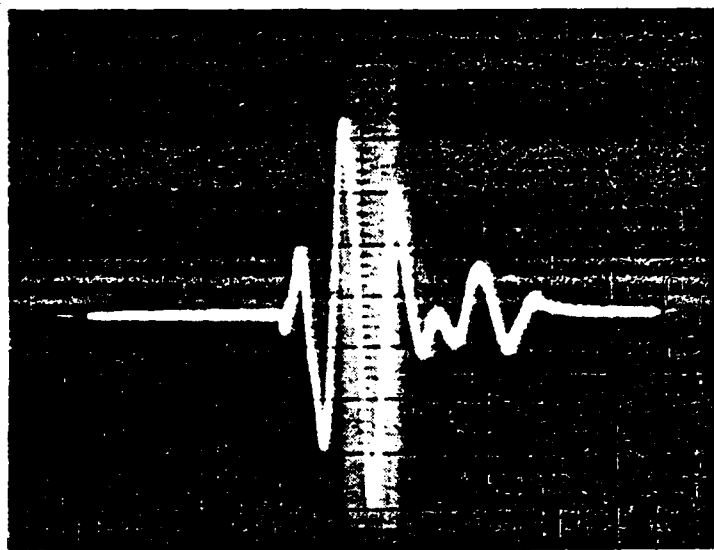


f 3 2



5-17-77

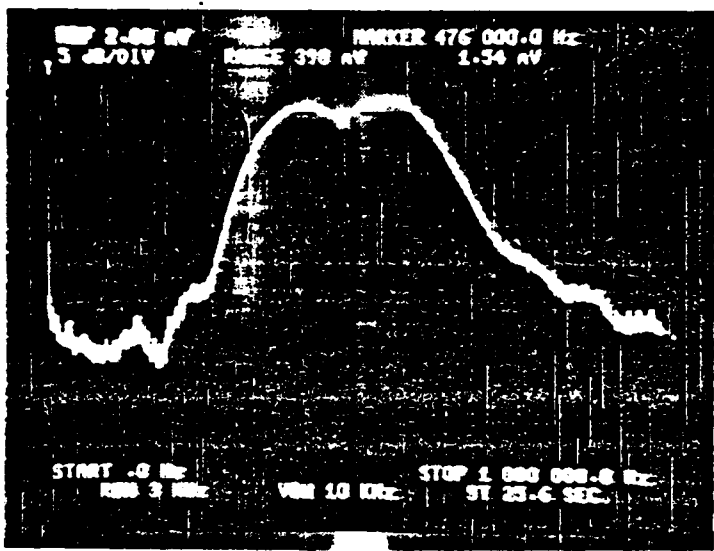
→ amplitude (50 mV/div)



(a)

→ time (2 μs/div)

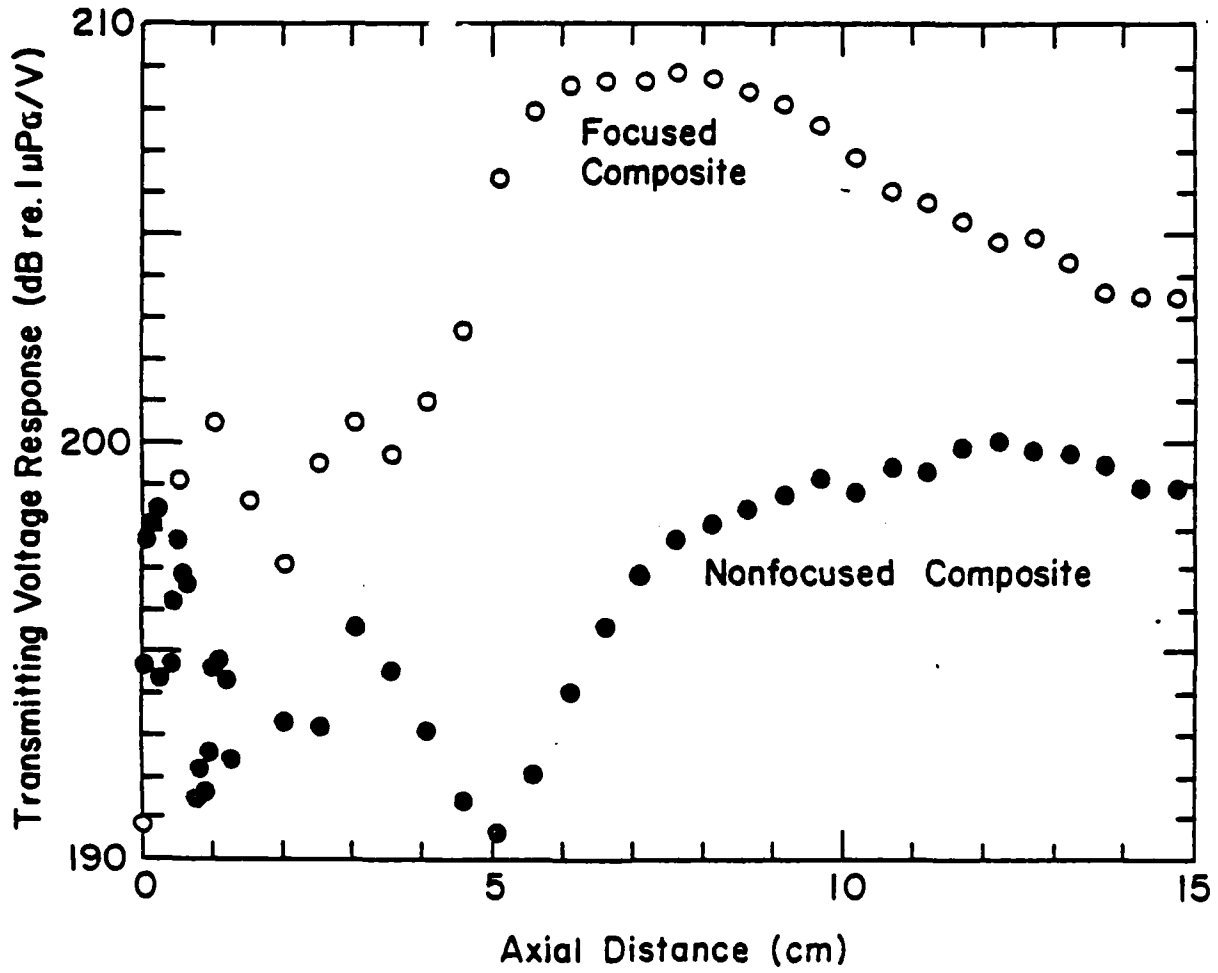
→ amplitude (dB)



(b)

→ frequency

f 11



Ph.D. Thesis

STUDY OF THE PIEZOELECTRIC AND PYROELECTRIC PROPERTIES
OF POLAR GLASS CERAMICS

A. Halliyal

The Pennsylvania State University

The Graduate School

Study of the Piezoelectric and Pyroelectric
Properties of Polar Glass-Ceramics

A Thesis in

Solid State Science

by

Arvind Halliyal

Submitted in Partial Fulfillment
of the Requirements
for the Degree of

Doctor of Philosophy

May 1984

I grant The Pennsylvania State University the nonexclusive right to use this work for the University's own purposes and to make single copies of the work available to the public on a not-for-profit basis if copies are not otherwise available.

A. Halliyal

Arvind Halliyal

ABSTRACT

This thesis deals with a new class of polycrystalline ceramic materials, the oriented polar glass-ceramics. Very recently it has been realized through work in this laboratory (Gardopee, 1980) that by suitable thermal processing, a glass which can be recrystallized into a polar crystalline phase may be treated in such a manner that the crystallites which develop are in parallel polar array. The macroscopic polarity thus developed gives rise to both pyroelectric and piezoelectric activity with characteristics markedly different to those which can be realized in poled ferroelectric ceramics or glass-ceramics.

The present thesis work explores a number of glass-forming systems, the preparation methods needed to give controlled oriented polar microstructure and an evaluation of the usefulness of these different glass-ceramics for piezoelectric and pyroelectric device applications.

In this study grain-oriented polar glass-ceramics have been prepared by recrystallizing glasses of several compositions from the systems $\text{BaO-SiO}_2\text{-TiO}_2$, $\text{BaO-GeO}_2\text{-TiO}_2$, $\text{SrO-SiO}_2\text{-TiO}_2$, $\text{Li}_2\text{O-SiO}_2$ and $\text{Li}_2\text{O-SiO}_2\text{-B}_2\text{O}_3$. The crystallization was carried out in a strong temperature gradient to promote oriented growth of crystallites. The crystalline phases identified in the glass-ceramics were $\text{Ba}_2\text{TiSi}_2\text{O}_8$, $\text{Ba}_2\text{TiGe}_2\text{O}_8$, $\text{Sr}_2\text{TiSi}_2\text{O}_8$, $\text{Li}_2\text{Si}_2\text{O}_5$ or $\text{Li}_2\text{B}_4\text{O}_7$, all of which are polar but nonferroelectric. X-ray diffraction and microstructure studies showed that the needle-like crystals grow from the surface, parallel to the direction of temperature gradient.

A major part of the effort in this study was devoted to the evaluation of dielectric, pyroelectric and piezoelectric properties of polar glass-ceramics. The glass-ceramics showed high pyroelectric

figures of merit (50 to 60% of that of lithium tantalate single crystals). The electromechanical coupling coefficients k_p and k_t were 15 to 25% with comparatively low temperature coefficients of resonance (50 to 100 ppm). Magnitudes of hydrostatic piezoelectric coefficient d_h (~ 10 pC/N), hydrostatic voltage coefficient g_h ($\sim 100 \times 10^{-3}$ Vm/N) and dielectric constant (~ 10) of glass-ceramics were comparable to the corresponding values of the ferroelectric polymer, polyvinylidene fluoride $(CH_2CF_2)_n$. Glass-ceramics with a wide range of pyroelectric and piezoelectric properties could be prepared by modifying the composition of glasses. Properties of $Ba_2TiSi_2O_8$ and $Ba_2TiGe_2O_8$ single crystals were also studied for comparison; from which it was concluded that the piezoelectric and pyroelectric properties of glass-ceramics are in good agreement with the respective single crystal properties.

During the present study an interesting behavior was evident in the polar orientation of different crystalline phases in the glass-ceramics. It was observed that the sign of piezoelectric coefficient d_{33} and the polar orientation of crystalline phases were dependent on the composition of the parent glass matrix. It was shown that the growth behavior of individual crystalline phases can be exploited to tailor the piezoelectric and pyroelectric properties of glass-ceramics. By considering the glass-ceramic as a microscopic composite of one or more crystalline phases and an amorphous glassy matrix, connectivity models were developed to predict the properties of grain-oriented polar glass-ceramics.

Ph.D. Thesis

PIEZOELECTRIC COMPOSITE MATERIALS FOR ULTRASONIC TRANSDUCER APPLICATIONS

T.R. Gururaja

The Pennsylvania State University

The Graduate School

Piezoelectric Composite Materials for Ultrasonic
Transducer Applications

A Thesis in
Solid State Science

by

Turuvekere Ramarao Gururaja

Submitted in Partial Fulfillment
of the Requirements
for the Degree of

Doctor of Philosophy

May 1984

I grant The Pennsylvania State University the nonexclusive right to use this work for the University's own purposes and to make single copies of the work available to the public on a not-for-profit basis if copies are not otherwise available.



T.R. Gururaja

ABSTRACT

The aim of the present work was to extend the understanding and usefulness of the piezoelectric composite materials developed previously for low frequency hydrophone applications to higher frequency (low megahertz) applications such as biomedical diagnosis. Among all the various composites, those with PZT rods embedded in Spurr's epoxy with a regular periodicity (1-3 connectivity) appeared to be especially favorable. An extensive investigation of the PZT rod-Spurr's epoxy composites was carried out to understand their high frequency dynamic behavior. This knowledge was then used to evaluate their performance as an ultrasonic transducer with water load.

The high frequency electromechanical properties of the composites were characterized in terms of the various resonance modes. The three principal resonances observed in a circularly shaped composite are the planar mode, the thickness mode, and the lateral modes. The thickness mode resonance was of greatest importance in this study as it is the one utilized for transmitting and receiving ultrasonic waves. The observed resonance behavior of the composite as a function of frequency and temperature was found to be a result of lateral interaction in the composite through the epoxy medium.

The acoustic impedance of the composite material was measured by three different techniques in the frequency range from 0.3 to 3.5 MHz. The dependence of acoustic impedance as a function of volume fraction PZT and frequency were theoretically modeled.

The composites were initially characterized by the pulse-echo method. The pulse-echo figure of merit of some of the composites compared favorably with that of commercial transducers. For a

complete understanding of the performance, the transmitting and receiving voltage responses of the composite transducers were characterized separately. The figure of merit in the receiving mode of a 20 percent PZT composite operating at 0.3 MHz was three times that of the single phase PZT.

The performance of the composite transducer was further improved by the use of quarter wavelength thickness matching layer of lucite mounted between the transducer and load. The figure of merit of the composite transducer in the receiving mode was increased by approximately 50 percent when the matching layer was used. The Q of the matched composite transducer was less than two which is advantageous in achieving a good axial resolution. The composite transducer was focused by a relatively simple technique to narrow the beam width in order to improve the lateral resolution. These results demonstrate that the 1-3 composite materials are excellent candidates for medical diagnostic transducer applications. However, it should be noted that the improved performance of the composite as a transducer demonstrated below 0.5 MHz should be extended to higher frequencies (2-5 MHz) typical for ultrasonic diagnostic applications. Several suggestions of practical techniques to increase the operating frequency of the composite transducers are made.

Ph.D. Thesis

ELECTROSTRICTION IN CUBIC HALIDE COMPOUNDS

Kurt M. Rittenmyer

The Pennsylvania State University

The Graduate School

Electrostriction in Cubic Halide Compounds

A Thesis in
Solid State Science .

by

Kurt M. Rittenmyer

Submitted in Partial Fulfillment
of the Requirements
for the Degree of

Doctor of Philosophy

May 1984

I grant The Pennsylvania State University of nonexclusive right to use this work for the University's own purposes and to make single copies of the work available to the public on a not-for-profit basis if copies are not otherwise available.

Kurt M. Rittenmyer
Kurt M. Rittenmyer

ABSTRACT

The electrostrictive properties have been reported previously for very few materials with low dielectric constants. They can be measured by using either the direct or converse electrostrictive effect. The converse effect involves measuring the stress dependence of the dielectric constant of the material. The direct effect is measured by determining the strain produced in a material by an applied electric field.

The hydrostatic electrostriction coefficients of several fluoride perovskite single crystals were determined from measurements of the converse effect using hydrostatic pressure. Non-linear behavior was observed in the dielectric constant-versus-pressure relationship. This indicates that higher-order electrostriction coefficients, ϕ_{ijk} , are significant. The quadratic hydrostatic electrostriction coefficients, Q_h , of the fluoride perovskite materials are similar to those of other fluoride materials such as LiF and CaF₂. This comparison suggests that crystal structure is less important in determining the electrostrictive properties of a simple material than the kinds of ions in the structure.

An ultrasensitive dilatometer, which had been previously constructed, was modified to allow correct measurement of the electrostriction coefficients of single crystal materials with low dielectric permittivities. In order to obtain reliable results, it was necessary to rigidly mount the crystal between stiff metal electrodes.

The complete electrostriction tensor of CaF₂ was calculated from measurements of the electrostriction coefficients of single crystals cut perpendicular to the (100), (110), and (111) crystallographic

directions. These measurements were used in conjunction with the value of the hydrostatic electrostriction coefficient obtained from the literature to calculate the values of the electrostriction tensor coefficients M_{11} , M_{12} , and M_{44} using a least-squares method. The magnitude of the M_{11} coefficient is similar to those reported for alkali halide crystals. The values of M_{12} and M_{44} are relatively different from those determined by previous authors. However, the values in these previous papers are incorrect because of a calculation error.

Attempts at measuring electrostriction in sodium chloride were unsuccessful. The measured electrostriction coefficient was found to vary sharply with the frequency of the applied electric field. Subsequent investigations to determine the cause of this behavior were carried out. Electrostriction measurements were performed on a NaCl crystal which had been hot-forged and also on a crystal which had been irradiated with neutrons. Both of these measurements in addition to the experiments performed on CaF_2 suggest that the movement of charged dislocations substantially increases the measured electrostriction coefficients of sodium chloride.

Measurements of other physical properties of several fluoride perovskite materials were completed. The measured properties include thermal expansion coefficients, temperature coefficients of the dielectric constants, and elastic constants. Values of these properties were used in conjunction with other published values of properties for a variety of materials to empirically relate electrostriction to other physical properties. Power-law relationships between isothermal compressibility, thermal expansion, and electrostriction were demonstrated. A linear relationship was observed between

electrostriction and the pressure coefficient of isothermal compressibility. These empirical results are discussed in terms of the theory of anharmonic solids.

M.S. Thesis

AN ANALYSIS OF THE REACTION OF PbO and Nb_2O_5 IN THE PRESENCE
OF MOLTEN SALTS FOR USE IN GRAIN-ORIENTED PIEZOELECTRIC 0-3 COMPOSITES

Mary Bliss

The Pennsylvania State University
The Graduate School
Department of Materials Science and Engineering

An Analysis of the Reaction of PbO and Nb₂O₅
in the Presence of Molten Salts for Use
in Grain-Oriented Piezoelectric 0-3 Composites

A Thesis in
Ceramic Science

by

Mary Bliss

Submitted in Partial Fulfillment
of the Requirements
for the Degree of

Master of Science

August 1984

I grant The Pennsylvania State University the nonexclusive right to use this work for the University's own purposes and to make single copies of the work available to the public on a not-for-profit basis if copies are not otherwise available.



Mary Bliss

ABSTRACT

Unconstrained acicular particles (typically $0.5 \times 0.5 \times 5-15 \mu\text{m}$) suitable for the fabrication of grain-oriented ceramics and composites were produced by molten salt synthesis. For orthorhombic lead meta-niobate (PbNb_2O_6) based compositions, the technique involved dry mixing of lead oxide (PbO) and niobium pentoxide (Nb_2O_5) with a soluble flux. The oxide-flux mixtures yielded grains with the desired morphology when reacted in air within the temperature range of $800-900^\circ\text{C}$ for a duration of 3-4 h. After cooling, the insoluble products were separated by dissolving the flux and filtering. Alkali-halide and alkali-free fluxes were used.

The acicular grains were identified as an alkali-doped orthorhombic ferroelectric PbNb_2O_6 based phase. This orthorhombic phase could not be obtained from the alkali-free flux (B_2O_3). A pure B_2O_3 flux yields only the rhombohedral form of PbNb_2O_6 ; additions of KCl to the B_2O_3 flux result in increased production of the orthorhombic alkali-doped PbNb_2O_6 phase. There is a strong correlation between reaction temperature, alkali content, and Curie temperature of $\text{PbO}\cdot\text{Nb}_2\text{O}_5$ reacted in a $0.25\text{B}_2\text{O}_3\cdot 0.75\text{KCl}$ flux.

When PbO and Nb_2O_5 were reacted in a $\text{NaCl}\cdot\text{KCl}$ flux, the alkali-doped orthorhombic PbNb_2O_6 phase was produced along with $\text{Pb}_3\text{Nb}_4\text{O}_{13}$ and possibly $(\text{Na},\text{K})\text{NbO}_3$. The contaminant phases were identified as small ($<1 \mu\text{m}$) equiaxed grains in the scanning electron

microscope images. The amount of the contaminant phases was reduced by making the initial charge deficient in lead oxide. The relationship of processing temperature and alkali content with Curie temperature indicates that there may be a mixed alkali effect on electrical properties.

All of the molten salt synthesized powders--equimolar $\text{PbO-Nb}_2\text{O}_5$ in NaCl-KCl or $\text{B}_2\text{O}_3\text{-KCl}$ fluxes and lead-oxide deficient mixtures in $\text{NaCl}\cdot\text{KCl}$ flux--were suitable for further processing as sintered ceramics. The lead-oxide deficient material was selected for use in an 0-3 polymer/ceramic composite because of its higher phase purity. Current available forming methods were found to be only moderately successful in producing grain-oriented piezoelectric 0-3 composites.

BASIC DISTRIBUTION LIST

Technical and Summary Reports

<u>Organization</u>	<u>Copies</u>	<u>Organization</u>	<u>Copies</u>
Defense Documentation Center Cameron Station Alexandria, VA 22314	12	Naval Air Propulsion Test Center Trenton, NJ 08628 ATTN: Library	1
Office of Naval Research Department of the Navy 300 N. Quincy Street Arlington, VA 22217 ATTN: Code 471 Code 470	1 1	Naval Construction Battalion Civil Engineering Laboratory Port Hueneme, CA 93043 ATTN: Materials Division	1
Commanding Officer Office of Naval Research Branch Office Building 114, Section D 666 Summer Street Boston, MA 02210	1	Naval Electronics Laboratory San Diego, CA 92152 ATTN: Electron Materials Sciences Division	1
Commanding Officer Office of Naval Research Branch Office 536 South Clark Street Chicago, IL 60605	1	Naval Missile Center Materials Consultant Code 3312-1 Point Hugu, CA 92041	1
Office of Naval Research San Francisco Area Office One Hallidie Plaza Suite 601 San Francisco, CA 94102	1	Commanding Officer Naval Surface Weapons Center White Oak Laboratory Silver Spring, MD 10910 ATTN: Library	1
Naval Research Laboratory Washington, DC 20375 ATTN: Codes 6000 6100 6300 2607	1 1 1 1	Commander David W. Taylor Naval Ship Research and Development Center Bethesda, MD 10084	1
Naval Air Development Center Code 606 Warminster, PA 18974 ATTN: Mr. F.S. Williams	1	Naval Oceans Systems Center San Diego, CA 92132 ATTN: Library	1
Naval Weapons Center China Lake, CA 93555 ATTN: Library	1	Naval Underwater System Center Newport, RI 02840 ATTN: Library	1
		Naval Postgraduate School Monterey, CA 93940 ATTN: Mechanical Engineering Dept.	1

<u>Organization</u>	<u>Copies</u>	<u>Organization</u>	<u>Copies</u>
Naval Air Systems Command Washington, DC 20360 ATTN: Codes 52031 52032	1 1	NASA Lewis Research Center 21000 Brookpark Road Cleveland, OH 44135 ATTN: Library	1
Naval Sea System Command Washington, DC 20362 ATTN: Code 05E	1	National Bureau of Standards Washington, DC 20234 ATTN: Metals Science and Standards Division	1
Naval Facilities Engineering Command Alexandria, VA 22331 ATTN: Code 03	1	Ceramics Class and Solid State Science Division Fracture and Deformation Division	1 1 1
Scientific Advisor Commandant of the Marine Corps Washington, DC 20380 ATTN: Code AX	1	Director Applied Physics Laboratory University of Washington 1013 Northeast Fortlieth Street Seattle, WA 98105	1
Army Research Office P.O. Box 12211 Triangle Park, NC 27709 ATTN: Metallurgy and Ceramics Program	1	Defense Metals and Ceramics Information Center Dattelle Memorial Institute 505 King Avenue Columbus, OH 43201	1
Army Materials and Mechanics Research Center Watertown, MA 02172 ATTN: Research Programs Office	1	Metals and Ceramics Division Oak Ridge National Laboratory P.O. Box X Oak Ridge, TN 37830	1
Air Force Office of Scientific Research/NE Building 410 Walloping Air Force Base Washington, DC 20332 ATTN: Chemical Science Directorate Electronics and Materials Sciences Directorate	1 1	Los Alamos Scientific Laboratory P.O. Box 1663 Los Alamos, NM 87544 ATTN: Report Librarian	1
Air Force Materials Laboratory Wright-Patterson AFB Dayton, OH 45433	1	Argonne National Laboratory Metallurgy Division P.O. Box 229 Lemont, IL 60439	1
Library Building 50, Room 134 Lawrence Radiation Laboratory Berkeley, CA 94720	1	Brockhaven National Laboratory Technical Information Division Upton, Long Island New York 11973 ATTN: Research Library	1
NASA Headquarters Washington, DC 20546 ATTN: Code 33X	1	Office of Naval Research Branch Office 1030 East Green Street Pasadena, CA 91106	1

SUPPLEMENTARY DISTRIBUTION LIST A

Electronic, Magnetic, and Optical Ceramics

Advanced Research Project Agency
Materials Science Director
1400 Wilson Boulevard
Arlington, VA 22209

Dr. Gene Haertling
Motorola Corporation
3434 Vassar, NE
Albuquerque, NM 87107

Dr. Don Earlincourt
Channel products
10722 Park Circle Drive W.
Chagrin Falls, OH 44022

Dr. W.E. Harrison
Honeywell Ceramics Center
1885 Douglas Drive
Golden Valley, MN 55422

Dr. J.V. Biggers
The Pennsylvania State University
Materials Research Laboratory
University Park, PA 16802

Dr. C.M. Stickley, V.P.
The BDM Corporation
7915 Jones Branch Drive
McLean, VA 22102

Mr. George Boyer
Sensor Systems Program
Office of Naval Research
Code 222
Arlington, VA 22217

Dr. L.L. Menck
Department of Metallurgy
University of Florida
Gainesville, FL 32603

Dr. Dean Buchner
Piezo Products Division
Gulton Industries
P.O. Box 4300
Fullerton, CA 92634

Dr. E.F. Eider
Rockwell International
400 Collins Road NE
Cedar Rapids, IA 52406

Dr. Robert Callahan
Channel Products
800 Ward Drive
Box 0660
Santa Barbara, CA 93105

Dr. F. Robert Hill
Marine Resources
755 Highway 17 and 92
Fern Park, FL 32730

Professor L.E. Cross
Materials Research Laboratory
The Pennsylvania State University
University Park, PA 16802

Dr. E.G. Koepke
Honeywell, Inc.
Corporate Research Center
10701 Lyndale Avenue South
Bloomington, MN 55420

Mr. H. Gada
Vice President for Engineering
Eric Technological Products
West College Avenue
State College, PA 16801

Dr. D. Lapetina
Edo Western Corporation
2645 South 300 West
Salt Lake City, UT 84115

Dr. M. Ferrone
Code 474
Office of Naval Research
600 M. Quincy Street
Arlington, VA 22217

Mr. C. LeBlanc
Naval Underwater Systems Center
TD 121
Newport, RI 02840

Professor R. Poy
Materials Research Laboratory
The Pennsylvania State University
University Park, PA 16802

Dr. Sam R. Deary
General Electric
Court Street
Plant Building C
Box 1122
Syracuse, NY 13201

Dr. J.F. Foscolowski
General Electric Company
Research and Development Center
P.O. Box 2
Schenectady, NY 02301

Dr. P.L. Smith
Naval Research Laboratory
Code 6361
Washington, DC 20375

Dr. R.W. Timme
Naval Research Laboratory
Code 2275
Underwater Sound Reference Division
P.O. Box 8337
Orlando, FL 32806

Dr. Charles C. Walker
Naval Sea Systems Command
National Center #3
2531 Jefferson Davis Highway
Arlington, VA 20390

Dr. Paul D. Wilcox
Sandia Laboratories
Division 2521
Albuquerque, NM 87115

The State University of New York
at Alfred
Materials Science Division
Alfred, NY 14602

Dr. R. Rice
Naval Research Laboratory
Code 3360

Dr. David C. Hill
Member, Technical Staff
Terns Instruments, Inc.
Attleboro, MA 02703

Dr. S.Z. Kurtz, V.P.
Clairel, Inc.
2 Blachley Road
Stamford, CT 06902

Dr. M. Tallan
AFML Wright-Patterson AFB
Dayton, OH 45433

Dr. H.E. Bennett
Naval Weapons Center
Code 3818
China Lake, CA 93555

Dr. Michael Bell
Inorganic Materials Division
National Bureau of Standards
Washington, DC 20234

Dr. R. Bratton
Westinghouse Research Laboratory
Pittsburgh, PA 15235

Dr. Joe Dougherty, Dir. Eng.
Gulton Industries
212 Durham Avenue
Metuchen, NJ 08840

Dr. James Pappis
Raytheon Co.
Research Division
28 Seyon Street
Waltham, MA 02154

Dr. Perry A. Files
Raytheon Co., Res. Div.
28 Seyon Street
Waltham, MA 02154

Dr. P.E.B. Morgan
Rockwell Science Center
1049 Camino Dos Rios
P.O. Box 1025
Thousand Oaks, CA 91360

Dr. G. Ewell
MSG-D163
Hughes Aircraft Company
Centinela and Teale Streets
Culver City, CA 90230

Dr. George W. Taylor
Princeton Resources, Inc.
P.O. Box 211
Princeton, NJ 08540

Mr. John J. Thiermann
Physics International
2700 Merced Street
San Leandro, CA 94577

Dr. Herb Moss
RCA Laboratories
Princeton, NJ 08540

Dr. E.E. Newham
Materials Research Laboratory
The Pennsylvania State University
University Park, PA 16802

Dr. Charles S. Sahagian, Chief
EM Technology Branch, SSS Division
HQ Rome Air Dev. Center (AFSC)
Deputy for Electronic Technology
Wanscon AFB, MA 01731

Dr. J. Smith
CDE Sylvania
100 Endicott Street
Danvers, MA 01923

Dr. Wallace A. Smith
North American Philips Laboratories
345 Scarborough Road
Briarcliff Manor, NY 10510

Mr. Raymond E. Sparks
Technology Library R220
Bellco Electronics Division/GMC
P.O. Box 1104
Zekomo, IN 46901

Dr. Manfred Zahn
Senior Scientist, Prod. Dev.
AVC Ceramics
Myrtle Beach, SC 29577

Mr. G. Goodman, Manager
Cooperation of Applied Research Group
Globe-Union, Inc.
5757 North Green Bay Avenue
Milwaukee, WI 53201

Dr. A.E. Clark
Naval Surface Weapons Center
White Oak Laboratory
Silver Spring, MD 20910

Director
Applied Research Laboratory
The Pennsylvania State University
University Park, PA 16802

Dr. D. Carson
Code 7122
Naval Ocean Systems Center
San Diego, CA 92152

Dr. C. Nicks
Code 631
Naval Ocean Systems Center
San Diego, CA 92152

Dr. F. Smith
Code 7122
Naval Ocean Systems Center
San Diego, CA 92152

Professor R. Buchanan
Department of Ceramic Eng.
University of Illinois
Urbana, IL 61801

Professor E.A. Auld
Stanford University
W.W. Hansen Laboratories
of Physics
Stanford, CA 94306

Dr. S. Musikant
General Electric Co.
3188 Chestnut Street
Philadelphia, PA 19101

Dr. A. Gentile
Hughes Research Labs
3011 Malibu Canyon Road

Dr. J. Harrington
Hughes Res. Labs.
3011 Malibu Canyon Road
Malibu, CA 90265

Professor G. Kino
Stanford University
Stanford, CA 94305

Dr. Gordon Martin
2627 Burgener
San Diego, CA 92110

Deborah Graves
Ceramic Engineer
Endevco
Rancho Vie Jo Road
San Juan Capistrano, CA 92675

Army Research Office
Box 211, Duke Station
ATRI: Met. and Ceram. Div.
Durham, NC 27706

National Bureau of Standards
Inorganic Matls. Division
Washington, DC 20234

National Bureau of Standards
Metallurgy Division
Washington, DC 20234

Naval Air Systems Command
Code 320
Washington, DC 20360

Pacific Missile Test Center
Materials Consultant
Code 4121
Pt. Mugu, CA 93042

Naval Research Lab
Code 6100
Washington, DC 20390

Naval Sea System Command
Code 035
Washington, DC 20362

Naval Ship Engr. Center
Code 6101, CTR BC #2
3700 East-West Highway
Prince Georges Plaza
Hyattsville, MD 20782

Office of Naval Research
Department of the Navy
Code 102
Arlington, VA 22217

Dr. G. Bansal
Battelle Laboratories
505 King Avenue
Columbus, OH 43201

Dr. F.F. Lange
eRockwell International
P.O. Box 1085
1049 Camino Dos Rios
Thousand Oaks, CA 91360

Dr. C. Benman, Code LPS
AFML, Wright-Patterson AFB
Dayton, OH 45433

Sheldon Detwiler, Disp. Mgr.
Adv. Technol. Laboratories
13200 Northrup Way
P.O. Box 6639
Bellevue, WA 98007

Dr. W.G.D. Frederick
AFML, Wright-Patterson AFB
Dayton, OH 45433

Dr. P. Gielisse
University of Rhode Island
Kingston, RI 02881

Mr. G. Hayes
Naval Weapons Center
China Lake, CA 93555

Dr. E.M. Katz
Army Materials and Mechanics
Research Center
Watertown, MA 02171

Dr. P.L. Lall
Office of Naval Research
666 Summer Street
Boston, MA 02210

Dr. P. Land
AFML, Wright-Patterson AFB
Dayton, OH 45433

Dr. Eugene A. Larson, Pres.
Blue River Laboratories
P.O. Box 442
Lewistown, PA 17044

Dr. George Bentzien
Naval Ocean Systems Center
Code 212
San Diego, CA 92152

Mr. E. Letson
Redstone Arsenal
Huntsville, AL 35899

Mr. G. Schmitt
AFML, Wright-Patterson AFB
Dayton, OH 45433

Dr. N. Macmillan
Materials Research Laboratory
The Pennsylvania State University
University Park, PA 16802

Mr. F. Markarian
Naval Weapons Center
China Lake, CA 93555

Mr. E.D. McHenry
Honeywell Corp. Tech. Center
16701 Lyndale Avenue South
Bloomington, MN 55420

Dr. E.R. Neurgaonkar
Rockwell International Science Ctr.
1649 Camino Dos Rios
P.O. Box 1685
Thousand Oaks, CA 91360

Horton Company - Library
Industrial Ceramics Division
Worcester, MA 01606

James W. Pell
Manager of Development
Tome Scientific Corporation
2722 S. Fairview Street
Santa Ana, CA 92704

Dr. R.C. Pohanka
Room 619 Ballston Tower
800 N. Quincy Street
Arlington, VA 22217

Dr. F.A. Queeney
126 Hammond Building
The Pennsylvania State University
University Park, PA 16802

J.J. Rasmussen, Manager
Applied Research Division
Montana Energy and MHD R and D
P.O. Box 3309
Butte, MT 59701

Dr. R. Ruh
AFML, Wright-Patterson AFB
Dayton, OH 45433

James Runt
318 Steidle Bldg.
The Pennsylvania State University
University Park, PA 16802

Dr. T. Senteientes
GTE Sylvania
100 Endicott Street
Danvers, MA 01923

State University of New York
College of Ceramics
Alfred University
ATTN: Library
Alfred, NY 14802

Dr. R.E. Tressler
Ceramic Science Section
226 Steidle Building
The Pennsylvania State Univ.
University Park, PA 16802

Eric Udd
McDonnell Douglas Astron.
5301 Eolisa Avenue
Huntington Beach, CA 92647

Dr. T. Vasilos
AVCO R and Adv. Dev. Div.
201 Lowell Street
Wilmington, MA 01887

Mr. J.D. Walton
Engineering Experiment Station
Georgia Institute of Technol.
Atlanta, GA 30332

Mr. L.D. Weckesser
Applied Physics Laboratory
Johns Hopkins Road
Laurel, MD 20810

Mertan Brooks
Sandia National Labs
Division 7472
P.O. Box 5800
Albuquerque, NM 87185

Darrall P. Durks
Sprague Electric Company
Ceramic Capacitor Operations
P.O. Box 5327
Wichita Falls, TX 76307

Dr. Kim Ritchie
AVX Corporation
P.O. Box 267
Myrtle Beach, SC 29577

Roger T. Birstine
Unitrode Corporation
590 Pleasant Street
Watertown, MA 02172

END

FILMED

12-85

DTIC